

# Coherence, dynamics and polarization properties of polariton condensates in single and coupled micropillars

Cohérence, dynamique et propriétés de polarisation de condensats de polaritons dans des micropiliers simples et couplés

Présentée par:

**Vera Giulia Sala**

LPN/CNRS, Laboratoire de Photonique et Nanostructures  
LKB, Laboratoire Kastler Brossel, Université Pierre et Marie Curie, CNRS

**Thèse de Doctorat en Physique**

de l'Université Pierre et Marie Curie

École doctorale: Physique de la Région Parisienne - ED 107

Soutenance le 13 Décembre 2013

Jury:

RAPPORTEURS:	Jeremy Baumberg Jean-Michel Gérard
EXAMINATEURS:	Michiel Wouters Valia Voliotis Christoph Westbrook
DIRECTEUR DE THÈSE:	Alberto Bramati
MEMBRES INVITÉS:	Alberto Amo Jacqueline Bloch



# Contents

<b>1</b>	<b>Introduction to microcavity polaritons</b>	<b>9</b>
1.1	Light-matter coupling: strong and weak coupling . . . . .	9
1.2	Exciton-polaritons: strong coupling in semiconductor microcavities . . . . .	10
1.3	Properties of microcavity polaritons . . . . .	24
1.3.1	Polaritons as a bosonic system with a very low effective mass: polariton condensation . . . . .	24
1.3.2	Polaritons as a highly nonlinear optical system . . . . .	28
1.3.3	Polaritons as a spinor system . . . . .	32
<b>2</b>	<b>Polaritons in low dimensional structures</b>	<b>39</b>
<b>3</b>	<b>Temporal correlation properties of 0D polariton condensates in micropillars: dynamical <math>g^{(2)}</math> measurements</b>	<b>47</b>
3.1	Introduction . . . . .	47
3.2	Our system: polaritons in micropillars . . . . .	51
3.3	Experimental setup: single shot streak camera measurements . . . . .	52
3.3.1	Experimental setup . . . . .	52
3.3.2	Single shot streak camera measurements . . . . .	53
3.4	Data analysis: software g2 . . . . .	55
3.5	Test of the software with artificial signals . . . . .	57
3.6	Test of the software with HeNe laser . . . . .	60
3.7	Experimental study of the g2 function of a polariton condensate . . . . .	64
3.8	Polarization resolved measurements . . . . .	70
3.9	Conclusion and perspectives . . . . .	78
3.10	Appendix . . . . .	79
<b>4</b>	<b>Macroscopic self-trapping and Josephson oscillations in polaritonic diatomic molecules</b>	<b>85</b>
4.1	Introduction . . . . .	85
4.2	Josephson oscillations . . . . .	87
4.3	Our system: a polaritonic diatomic molecule . . . . .	89
4.4	Experimental setup . . . . .	91
4.5	Measurements in the linear regime: $UN_{R,L} \sim 0$ . . . . .	93
4.5.1	Rabi oscillation regime . . . . .	95
4.5.2	a.c. Josephson regime . . . . .	96
4.6	Measurements in the nonlinear regime: $UN_{R,L} \gg J$ . . . . .	97
4.6.1	Anharmonic oscillations . . . . .	97
4.6.2	Macroscopic self-trapping . . . . .	100
4.7	Polarization rotation . . . . .	101
4.8	Conclusion and perspectives . . . . .	103

<b>5</b>	<b>Spin-orbit coupling in a benzene-like polaritonic molecule</b>	<b>105</b>
5.1	Introduction . . . . .	105
5.2	Our system: a polaritonic benzene-like molecule . . . . .	106
5.3	Experimental setup . . . . .	108
5.4	Low power measurements: characterization of the system . . . . .	109
5.5	High power measurements: polariton condensation in the molecule . .	112
	5.5.1 Condensation on the first excited level: a polarization vortex of order 1 . . . . .	115
	5.5.2 Condensation on a polarization vortex of order 2 . . . . .	116
5.6	Polarization degree of freedom: real eigenmodes . . . . .	118
5.7	Polarization splitting as an effective spin-orbit coupling . . . . .	124
5.8	Spin-orbit coupling in solids . . . . .	127
5.9	Conclusion and perspectives . . . . .	130

# Introduction

Microcavity polaritons are mixed half light-matter particles, arising from the strong coupling of an exciton and a photon. They can be excited in semiconductor based heterostructures, obtained by embedding a semiconductor quantum well in a high quality microcavity with the optical mode quasi-resonant with the excitonic transition in the quantum well. Thanks to their double light-matter nature, polaritons share properties with both atomic physics and optics. They are bosons with a very low effective mass (of the order  $10^{-5}m_e$ ,  $m_e$  being the mass of the electron), inherited from their photonic component, allowing them to undergo bosonic condensation at much higher temperatures if compared to atomic gases, from few K up to room temperature. On the other hand, they are a photonic system characterized by very strong nonlinearities, thanks to the exciton-exciton Coulomb repulsive interactions. Therefore they are a suitable system where  $\chi^{(3)}$  nonlinear optics can be studied, with nonlinearities much higher than in standard nonlinear optical media.

Since their first experimental observation in 1992 [1], microcavity polaritons have been the subject of an intense research [2, 3]. In particular, the experimental demonstration of polariton condensation in 2006 [4] opened the way to many studies related to the properties of this macroscopic coherent state. Macroscopic coherence [5, 6, 7, 8, 9, 10, 11, 12, 13], superfluidity [14, 15], topological excitations such as quantum vortices [16, 17, 18] and solitons [19, 20, 21, 22], spin properties [23, 24, 25], coherent propagation [26] have for example been observed.

Polaritons are a suitable system where the physics of bosonic gases can be studied, not only because the typical temperatures allow easier experimental conditions, but also because of the possibility to have a direct access to the parameters of the system. This is related to the short polariton lifetimes (typically few ps), corresponding to photons continuously leaking out of the cavity. Thanks to the one-to-one correspondence of photons outside the cavity with polaritons inside the cavity, the properties of the polariton population can be fully reconstructed by analyzing photons outside the cavity. The properties of the system, such as energy, real- and k-space intensity and phase profiles, temporal evolution, can be measured by optical means.

The low polariton lifetime allows also to address the study of out-of-equilibrium Bose gases, with the possibility of observing effects not easily observable with atomic condensates, such as the build-up of macroscopic coherence [9, 10, 11].

Many effects analogous to  $\chi^3$  nonlinear optics have also been observed, such as optical parametric oscillations (OPO) [27, 28, 29, 30], squeezing [31], optical bistability [32, 33] and multistability [34, 35].

Different theoretical works have proposed to exploit the high nonlinearity related to exciton-exciton repulsive interaction, to achieve a regime of single photon nonlinearities. Effects such as polariton blockade [36] and nonequilibrium strongly correlated polariton gases [37, 38] have been predicted.

An important degree of freedom is the possibility to act on polaritons with a lat-

erally confining potential. This can be done in different ways, for example by optical means or in a more drastic way, by etching the microcavity down to 1D or 0D structures. This possibility has stimulated many theoretical and experimental works where the coherent propagation of polaritons [26], together with the possibility of optically controlling them, can be used to realize polaritonic circuits [39, 40, 41, 42, 43, 44, 45, 46, 47].

Another possibility, as we will discuss throughout this thesis, is to confine polaritons in 0D structures, inducing a quantization of the polaritonic energy levels. These structures behave as polaritonic atoms and they can be coupled together to form polaritonic molecules. While in 2D systems, polariton-polariton repulsive interactions lead polaritons to propagate away from each other, in 0D confined structures, they are forced to stay in the same spatial region. Therefore nonlinearities are enhanced. Moreover the freedom given by the etching technique, allows to use the single micropillars as fundamental bricks to build molecular, 1D or 2D structures with a freedom in the choice of the geometry. As we will see, this opens the possibility to study effects that combine polariton properties to nontrivial geometries. This thesis deals with GaAs based micropillars and coupled pillar molecules. More specifically:

**Chapter 1** gives a general introduction on microcavity polaritons, with an overview on their properties. Polariton condensation, nonlinearities and spin degree of freedom are briefly discussed.

**Chapter 2** gives an overview on the physics of polaritons in low dimensional structures. The single micropillars and molecular structures used in this thesis are introduced.

Chapters 3, 4 and 5 are the three experimental chapters that describe the three main experimental results obtained during this thesis. In particular:

**Chapter 3** describes the experimental study on the temporal  $g^2(t, \tau)$  correlation function of a polariton condensate in a micropillar. We implemented in our laboratory a technique recently developed in the group of M. Bayer, allowing to measure the  $g^2(t, \tau)$  function by means of a streak camera working in the single shot regime, with a time resolution of  $\sim 4$  ps. We have built a software allowing to calculate the  $g^2(t, \tau)$  from the raw streak camera data. Different tests, both with artificial signals and real signals, have been performed to confirm that the software was working properly. By means of this technique we studied the temporal correlation properties of a polariton condensate in a micropillar. In particular we studied how the coherence properties of the polariton condensate evolve as we change the density of polaritons in the system, i.e. (i) how the  $g^2$  function changes in the transition from the linear regime to the polariton condensate regime, (ii) if the coherence is affected by polariton-polariton repulsive interactions in the condensate regime, and (iii) the transition from polariton condensation to photon laser in the weak coupling regime. Our measurements show that at low excitation power the system displays a statistics compatible with thermal emission, while at higher excitation powers the system displays a coherent statistics. Our measurements indicates that interactions play a negligible role on the intensity correlations of a polariton condensate. With this work, we contribute to the understanding of the temporal correlation properties of polariton condensates, which is still an open question.

The same technique has been used also to study the dynamical single shot polarization properties of a polariton condensate. We provide a new picture in the understanding of the polarization dynamics of polariton condensates in confined geometries.

**Chapter 4** describes the experimental study of the temporal dynamics of a polaritonic diatomic molecule made of two coupled micropillars. The system is shown to display a Josephson like dynamics, which can be controlled by optical means. In particular we studied the linear regimes of oscillation: the Rabi oscillation regime and the a.c. Josephson regime. In both cases, coherent oscillations of population between the two pillars take place. By exploiting the high nonlinearities related to polariton-polariton repulsive interactions, we could attain the nonlinear regimes of anharmonic oscillations and macroscopic self-trapping. In the macroscopic self-trapping regime, nonlinearities affects the dynamics so strongly that oscillations are inhibited and the system is found in a quasi-metastable state, where most of the particles stay in one of the two pillars. We also observe the dynamical decrease of the nonlinearities in time, due to the progressive decrease in the global population density, related to photons escaping out of the cavity. We could observe the transition from the self-trapped state to the linear regime, where coherent oscillations are recovered. This study highlights polaritonic molecules as a suitable system where highly nonlinear optical effects can be studied.

**Chapter 5** describes the experimental study of the properties of a benzene-like polaritonic molecule, made of six coupled pillars placed in a hexagonal structure. We studied both the linear regime and polariton condensation. First we fully characterized the molecular modes by low power measurements, measuring the intensity and phase profiles of the modes in the real- and k-space. Then we studied polariton condensation, at higher excitation powers. We showed that condensation takes place in excited modes, characterized by peculiar polarization patterns in the real-space. In particular two thresholds are present: the first corresponding to condensation on the second excited level, characterized by a polarization vortex of order two, the second corresponding to condensation on the first excited level, characterized by a polarization vortex of order one. We interpreted the experimental observations by considering a polarization energy splitting of the modes. In particular two terms contribute to this splitting: a polarization dependent tunneling term (for adjacent pillars) and an on-site polarization splitting, related to the global ring symmetry. The polarization splitting acts on the system as an effective spin-orbit coupling, which couples together modes with different spin (polarization) and orbital momentum. This work opens the way to the engineering of spin-orbit coupling in polaritonic systems. In particular the scalability of coupled micropillar systems, allows to extend the spin-orbit coupling to 2D lattices.



# Chapter 1

## Introduction to microcavity polaritons

### 1.1 Light-matter coupling: strong and weak coupling

The light absorption and emission properties of an emitter are strongly influenced by the environment in which it is placed. In most experimental situations, light-matter interaction is not a reversible process. This is related to the fact that, usually, optical transitions couple a matter state, as for example a two-level atom, to a continuum of final states [48]. It follows that, once the system has left its initial state, the probability to find it in the same initial state after a certain time  $t$  is practically zero, i.e. the probability of finding the system in the initial state decreases exponentially in time. It is the case for example of spontaneous emission from an excited atom: the interaction with the electromagnetic field couples the initial atomic state to a continuum of final states, constituted by the atom in a lower energy level and a photon with a direction and polarization which can take a continuum of possible values. In this situation, light-matter interactions take place in what is called *weak coupling regime*.

Nevertheless, it is possible to create experimental conditions in which emission and absorption of light become reversible processes, i.e. conditions in which the *strong coupling regime* can take place. One way to obtain strong coupling is to create a situation in which one matter mode is coupled with just one light mode. Experimentally, strong coupling has been realized by putting an atom (two-level system) inside an optical cavity, characterized by just one mode resonant with the atomic transition [49]. In this regime, a photon can be absorbed and reemitted several times by the atom before leaving the cavity. The probability to find the atom in the excited state does not decrease exponentially in time, but it follows a sinusoidal law. In particular, the probability to find it in the excited state takes the value one at fixed intervals of time. In other words, the system oscillates in time between two states: 1) atom in the excited state and 2) atom in the ground state plus one photon. These oscillations are called *Rabi oscillations*. In this regime, the eigenstates of the system are mixed half light-matter modes and they inherit properties from both components, as we will discuss throughout this thesis.

In 1992 Weisbuch and collaborators [1] showed that the light-matter strong coupling regime could be achieved also in semiconductor based structures. In particular the strong coupling regime can be obtained by embedding a semiconductor quantum well inside a microcavity, in which one longitudinal optical mode is resonant with

the excitonic transition in the quantum well. If the typical lifetimes of the photon and the exciton are long enough if compared to the typical interaction strength, the system is in the strong coupling regime, and the photon is absorbed and reemitted several times before leaving the cavity. As their atomic counterpart, semiconductor microcavities in the strong coupling regime are characterized by mixed half light-matter eigenstates, which are called *microcavity exciton-polaritons*.

## 1.2 Exciton-polaritons: strong coupling in semiconductor microcavities

In this section we introduce the physical system which allows to attain the strong coupling regime. First, we introduce excitons in quantum wells, which provide the two-level matter transition. Secondly, we introduce the optical microcavity, which provides the one-to-one coupling between the two-level matter transition and one optical mode. We show that in such a strongly coupled regime, the eigenmodes of the system are mixed exciton-photon particles, called *exciton-polaritons*.

### Excitons in quantum wells

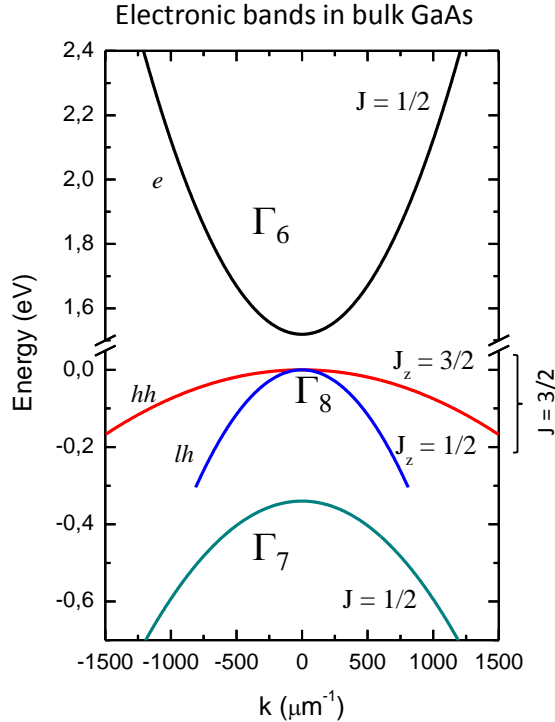


Figure 1.1: Conduction and valence band dispersions of bulk GaAs, close to the fundamental gap, corresponding to the  $\Gamma$  point, well approximated by parabolas.

We start by considering excitons in bulk semiconductors. Fig. 1.1 shows the dispersion curves for electrons in the conduction and valence bands in a bulk direct band gap semiconductor (GaAs), close to the fundamental gap ( $\Gamma$  in GaAs). Close to  $k = 0$  (starting from the  $\Gamma$  point) the dispersion curves can be approximated by parabolas and electrons can be described as free electrons with an effective mass  $m^*$

which is related to the curvature of the band through the relation

$$\frac{1}{m^*} = \frac{1}{\hbar^2} \frac{\partial^2 E}{\partial k^2}(k=0). \quad (1.1)$$

The dispersion curve can be written as

$$E(k) = E(k=0) + \frac{\hbar^2 k^2}{2m^*}. \quad (1.2)$$

In a semiconductor at zero temperature the valence bands are completely filled with electrons, while the conduction band is completely empty. This is the ground state of the system. The fundamental excitation consists on the promotion of an electron from the top of the valence band to the bottom of the conduction band. In this way all the valence band states except one remain occupied. It is convenient to picture this empty state as a positive charge in an empty valence band. This is the definition of *hole* and its description as a positive charge enables us to consider the valence band masses as positive in all practical calculations, despite the fact that from the single electron picture they have negative curvature.

For the most part of semiconductors, the conduction band (coming from the coupling of single atoms s orbitals, with  $l = 0$ ) is unique, while for the valence band (coming from the coupling of single atom p orbitals, with orbital angular momentum  $l = 1$ ) spin-orbit coupling lifts the degeneracy of states with total angular momentum  $J = \frac{1}{2}$  and  $J = \frac{3}{2}$ . In particular, the band corresponding to  $J = \frac{1}{2}$  has a lower energy (split-off band), while the band corresponding to  $J = \frac{3}{2}$  is at higher energy and it is divided in two subbands with projections on the quantization axis  $J_z = \pm\frac{3}{2}$  and  $J_z = \pm\frac{1}{2}$ . These two bands are degenerate at  $k = 0$ , but they are splitted in energy at  $k \neq 0$ , i.e. the two parabolic dispersions have different curvatures. It corresponds to holes with different effective masses: heavier for the  $J_z = \pm\frac{3}{2}$  band (*heavy holes*), lighter for  $J_z = \pm\frac{1}{2}$  (*light holes*).

Negatively charged electrons in the conduction band and positively charged holes in the valence band are subject to Coulomb attraction, through which they can form bound states, called *excitons*. Excitons are somehow analogues of hydrogen atoms, holes playing the role of protons. The Hamiltonians of both systems have the same expression and the structure of the energy levels and eigenmodes is the same, giving exciton levels 1s, 2s, 2p and so on.

The energy of the excitonic resonance can be written as

$$E_{exc} = E_{gap} - E_b + \frac{\hbar^2 K^2}{2m}, \quad (1.3)$$

where  $E_b$  is the electron-hole binding energy,  $\hbar\mathbf{K}$  is the exciton momentum, defined as the momentum of the center of mass of the electron-hole pair, and  $m$  is the exciton effective mass, given by the sum of the effective masses of electron and hole, which gives to the exciton its own parabolic band. Since there are two kinds of holes, there are also two kind of excitons: *light excitons* and *heavy excitons*, characterized by different effective masses.

The excitonic ground state energy is located at an energy  $E_b$  below the band gap energy. Therefore, the fundamental excitation in the system does not correspond to an electron and a hole created at the band edges, but by the formation of a 1s exciton at rest.

Excitons inherit their spin properties from their constituent electron and hole. In

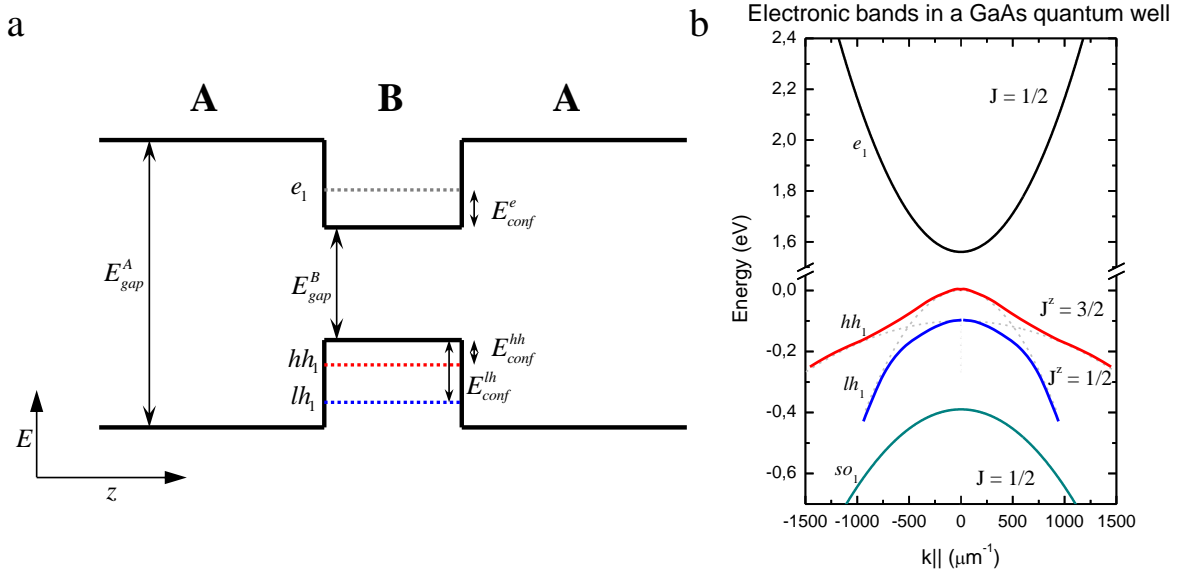


Figure 1.2: Semiconductor quantum well. (a) Extrema of the valence and conduction bands as a function of the growth direction  $z$ . The first confined energy levels for electrons and holes (light and heavy) are represented by dotted lines. (b) In-plane conduction and valence bands dispersions for a GaAs/AlGaAs quantum well, close to the fundamental gap.

particular, for heavy excitons, the combination of the electronic spin, with spin projections on the  $z$  quantization axis  $J_z^{(e)} = \pm\frac{1}{2}$ , and the heavy hole spin, with  $J_z^{(hh)} = \pm\frac{3}{2}$ , gives rise to two possible values for the excitonic spin,  $J_{exc} = 1$  and  $J_{exc} = 2$ . Note that the fundamental state of the crystal has  $J = 0$ .

The excitonic transition can be induced in many different ways. In this context, we are interested particularly in optically induced transitions. In particular, a photon whose energy exceeds the bandgap energy ( $\hbar\omega > E_{gap}$ ), can be absorbed inducing a transition from the fundamental state of the crystal to a state where one exciton with wavevector  $\mathbf{K}_{exc}$  and angular momentum  $J_{exc}$  is created. Some selection rules need to be satisfied in order for the optical transition to take place. In a dipolar approximation, conservation of the total linear momentum and angular momentum is required. In particular, since photons have total intrinsic angular momentum equal to one, it follows that just excitons with  $J = 1$  can be optically excited. Excitons with  $J = 2$  can not interact with light and they are therefore called *dark excitons*.

In a bulk semiconductor, the excitonic spectrum is a 3D continuum of states  $|\mathbf{K}, J_z\rangle$  and the selection rules induce a one-to-one correspondence with the modes of the electromagnetic field  $|\mathbf{k}, \sigma\rangle$ .

A semiconductor quantum well is a heterostructure where excitons result to be confined in the growth direction  $z$ , while they are free to move in the  $(x,y)$  2D plane perpendicular to  $z$ . A quantum well can be fabricated by growing a sequence of three thin 2D layers of semiconductors, where a material B, with a typical thickness of  $\sim 10$  nm is sandwiched between two layers of a material A characterized by a higher energy gap. Figure 1.2 (a) shows the extrema of the valence and conduction bands as a function of the growth direction  $z$ , displaying an abrupt discontinuity, when crossing the A-B interfaces. This discontinuity creates a quantum well in which excitons are confined. The thickness of the B layer is chosen on the order of the size of the exciton. The direct consequence of the confinement is the splitting of

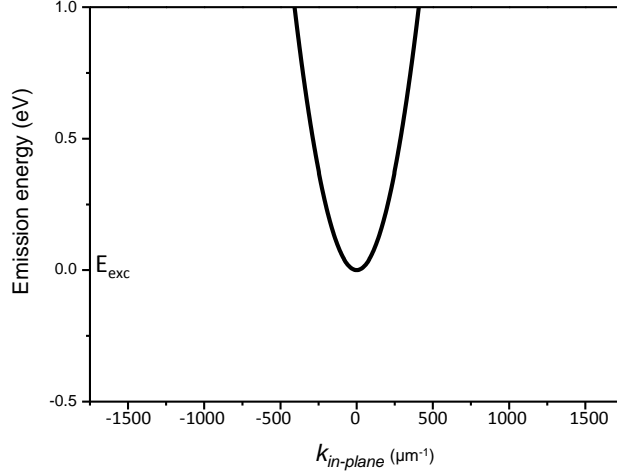


Figure 1.3: Exciton dispersion curve in a semiconductor quantum well, renormalized to the bottom of the band.

each band in different confined states. The eigenenergies in the growth direction are quantized, while in the in-plane directions show parabolic dispersions (Fig. 1.2 (b)). It means that, while excitons are confined in the  $z$  direction, they are free to move in the in-plane direction.

In the in-plane direction, the band structure of a quantum well displays a remarkable difference with respect to bulk materials: the bands of heavy and light holes are no more degenerate at  $k_{\parallel} = 0$ , as shown in Fig. 1.2 (b). This is due to the fact that, in a quantum well, the confining energy depends on the mass of the particle (different for light and heavy holes). Usually this splitting is quite large, i.e. the fundamental energy level of the system is well separated in energy from all the other levels. Therefore we can account just for it (heavy holes) in our experiments. In particular we will deal with 1s heavy hole excitons and in most situations we can neglect all the other excitations.

In the in-plane direction, the dispersion curve for quantum well excitons can be written

$$E_{K_{\parallel}} = E_{exc} + \frac{\hbar^2 K_{\parallel}^2}{2m_{exc}}, \quad (1.4)$$

with  $E_{exc} = E_{gap} + E_{conf}^e + E_{conf}^{hh} + E_{1s}$ , where  $E_{conf}^e$  and  $E_{conf}^{hh}$  are the confining energies of the first electron and hole levels (Fig.1.2 (a)) and  $E_{1s}$  is the binding energy.  $\hbar\mathbf{K}_{\parallel}$  is the in-plane momentum and  $m_{exc}$  is the effective in-plane mass of the exciton, given by the sum of the electron and hole effective in-plane masses. In GaAs based quantum wells, the exciton effective mass is of the order of  $m_{exc} \sim 10^{-1} m_e$ , where  $m_e$  is the mass of electrons. The exciton dispersion is shown in Fig. 1.3. In quantum wells, the selection rule regarding momentum conservation is modified with respect to bulk semiconductors: conservation of the in-plane momentum  $\hbar\mathbf{K}_{\parallel}$  is required, instead of conservation of the total momentum. As a consequence, an exciton is coupled to a continuum of modes of the electromagnetic field, since, once energy, spin and in-plane momentum are conserved, light with any  $k_z$  component can excite the system.

Nevertheless, energy conservation during exciton-photon interaction requires the

following condition to be satisfied

$$E_{exc} + \frac{\hbar^2 K_{\parallel}^2}{2m_{exc}} = \frac{\hbar c}{n} \sqrt{K_{\parallel}^2 + k_z^2}, \quad (1.5)$$

where the second term corresponds to the energy of a photon having wavevector  $\mathbf{k}_{\parallel} = \mathbf{K}_{\parallel}$  moving in the quantum well characterized by refractive index  $n$ . This relation implies

$$E_{exc} + \frac{\hbar^2 K_{\parallel}^2}{2m_{exc}} \geq \frac{\hbar c}{n} K_{\parallel}. \quad (1.6)$$

For small  $K_{\parallel}$ , i.e. close to the bottom of the band, where we are working, it gives the condition

$$K_{\parallel} \lesssim \frac{nE_{exc}}{\hbar c}, \quad (1.7)$$

which for III-V materials corresponds to values  $K_{\parallel} \lesssim 30 \mu\text{m}^{-1}$ . If we consider the dispersion curve in Fig. 1.3, we note that only excitonic states which are very close to the bottom of the band are coupled to light.

The angular momentum conservation condition remains the same as found for bulk semiconductors. Nevertheless, for a quantum well, the quantization axis coincides with the growth axis, which in general is not coincident with the propagation axis of light (except at  $K_{\parallel} = 0$ ), as it was the case in bulk semiconductors. This means that if a circularly polarized light wave has  $K_{\parallel} \neq 0$ , it will not excite a pure spin state, but a mix of  $J_z = 1$  and  $J_z = -1$  states.

In a quantum well in free space, as we have seen, an exciton is coupled to a continuum of optical modes. In the region of the dispersion curve in which excitons are coupled to light, the radiative emission of a photon through exciton recombination is an irreversible process (i.e. the probability of finding the exciton in the excited state decreases exponentially in time), which can be described by the Fermi golden rule, and which takes place on typical timescales of some tens of ps (in 10 nm GaAs based quantum wells the radiative lifetime is  $\sim 10$  ps [50]). This radiative decay corresponds to a radiative broadening of the excitonic line.

As we will discuss in the following sections, the radiative broadening of the excitonic line is strongly modified as we embed the quantum well in a microcavity. In this case in fact the excitonic transition is not coupled to a continuum of modes, but it is coupled to just one longitudinal optical mode, i.e. the mode resonant with the cavity. In the approximation of a perfect cavity, the exciton displays an infinite radiative lifetime.

Nevertheless, nonradiative relaxation mechanisms take place in the quantum well (both in free space and when it is embedded in a cavity), causing broadening of the excitonic linewidth and giving rise to a finite excitonic lifetime  $\tau_{exc}$ . The main causes of broadening are disorder related to imperfections in the material, interaction with phonons of the crystal lattice and exciton-exciton interactions. The typical exciton lifetimes (related to nonradiative decay) are of the order of some hundreds of ps [51]. One advantage of using a quantum well instead of a bulk semiconductor, is that the overlap of the electron and hole wavefunctions constituting the exciton is greatly enhanced due to the confinement in the growth direction. This has important consequences in the optical properties. In particular, it results in an increased oscillator strength, i.e. an increasing in the coefficient describing exciton-photon interaction. As we will discuss later, this is a fundamental property necessary to reach the strong coupling regime.

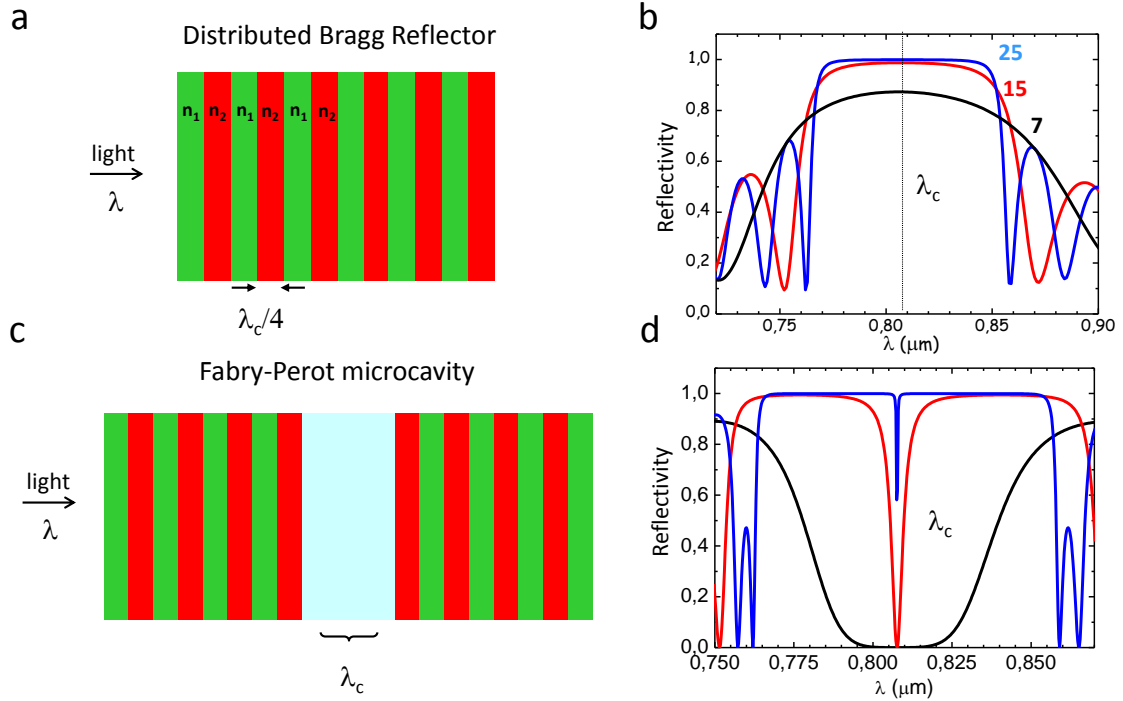


Figure 1.4: (a) Schematic representation of a Distributed Bragg Reflector (DBR). (b) Typical DBR reflectivity spectrum for three different numbers of  $(n_1, n_2)$  pairs. (c) Schematic representation of a Fabry-Perot microcavity made by coupling two DBRs. (d) Reflectivity spectrum of the microcavity, displaying a dip at the center of the stop-band, corresponding to the optical mode resonant with the cavity.

## Optical microcavities

In order to reach the strong coupling regime in a quantum well, we need to couple the excitonic transition to one single resonant optical mode. This is done by means of a semiconductor microcavity. A semiconductor microcavity is a heterostructure made of two parallel Distributed Bragg Reflectors (DBR), separated by an optical distance  $L = p\lambda_c/2$  with  $p$  integer number, forming a Fabry-Perot cavity with a resonance at the wavelength  $\lambda_c$ , when the cavity is excited at normal incidence.

In particular each Distributed Bragg Reflector is composed of layers of two alternating materials of different refractive indices  $n_1$  and  $n_2$ , as shown in Fig. 1.4 (a). Each layer has the same optical thickness, i.e.  $L_1 n_1 = L_2 n_2 = \lambda_c/4$ . Radiation incident on the DBR will be subjected to multiple reflections (transmissions) as it propagates along the structure, giving rise to an interference process which will be globally constructive or destructive depending on the radiation wavelength and incidence angle. A typical reflectivity spectrum of a DBR at normal incidence is shown in Fig. 1.4 (b), for three different numbers of pairs of layers  $(n_1, n_2)$ . At the center of the stop-band (at normal incidence), the reflectivity can be approximated by the expression

$$R = 1 - 4 \frac{n_{out}}{n_{sub}} \left( \frac{n_1}{n_2} \right)^{2N_{pairs}}, \quad (1.8)$$

where  $n_{out}$  and  $n_{sub}$  are the refractive indices of the external medium and the substrate on which the DBR is grown and  $N_{pairs}$  is the number of pairs of layers  $(n_1, n_2)$ . The reflectivity of the mirror grows rapidly with the number of layers and it is characterized by a high reflectivity band, called stop-band, centered on  $\lambda_c$ . For the DBRs typically used in our experiments, made of alternating layers of GaAs/AlAs,

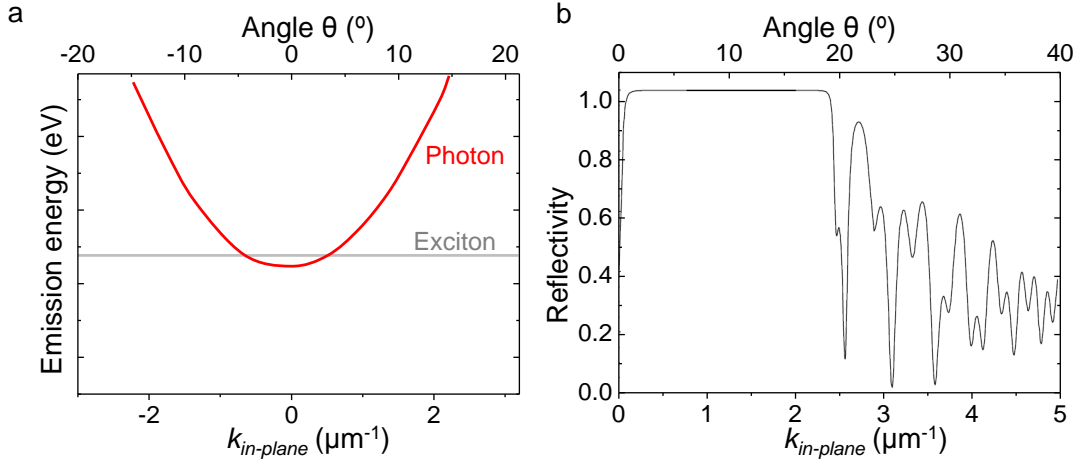


Figure 1.5: (a) Parabolic dispersion curve of photons in the in-plane direction of the microcavity (red). On the same scale, the excitonic dispersion curve appears to be flat (gray curve). (b) Angle dependence of the cavity reflectivity at the resonant wavelength  $\lambda_c$ .

25 pairs are enough to reach values of reflectivity very close to one ( $R \sim 0.9997$ ). Typically the stop-band has a bandwidth of  $\sim 100$  nm. For incident radiation with wavelength within the stop-band, the DBR behaves as a very high quality mirror.

As we couple two DBRs together, separated by a distance  $L = p\lambda_c/2$ , we form a Fabry-Perot cavity with resonance at  $\lambda_c$ . Its reflectivity spectrum shows a very narrow dip at the center of the stop-band (a narrow peak in transmission spectrum), corresponding to an optical mode resonant with the Fabry-Perot cavity.

Since in semiconductor microcavities the cavity length  $L_{cav}$  is of the order of  $\lambda_c$  and since the separation in energy of the longitudinal optical modes in a cavity is inversely proportional to  $L_{cav}$ , it follows that longitudinal modes in a semiconductor microcavity are well separated in energy. In particular it happens that the spectral width of the stop band is narrower than the typical spectral distance between two Fabry-Perot modes. Therefore just one optical mode appears within the stop-band (corresponding to one of the first Fabry-Perot resonances).

The high reflectivity of DBRs at the stop-band makes of semiconductor microcavities very high quality cavities, with Q factors up to 100000, corresponding to photonic lifetimes up to tens of ps.

When the cavity is excited not at normal incidence but at an angle  $\theta$  with respect to the normal, the interference condition defining the cavity mode resonance changes slightly. More explicitly, the cavity imposes the quantization condition on the  $k_z$  component of the wavevector

$$k_z = \frac{2\pi n_c}{\lambda_c}. \quad (1.9)$$

If we introduce the energy of the photon

$$E(k) = \frac{\hbar c}{n_c} \sqrt{k_z^2 + k_{\parallel}^2}, \quad (1.10)$$

and we consider the limit in which  $k_z \gg k_{\parallel}$ , which is the situation we are interested in, this relation reduces to

$$E(k) \approx \frac{\hbar c}{n_c} \left( k_z + \frac{1}{2k_z} k_{\parallel}^2 \right). \quad (1.11)$$

With the quantization condition 1.9, it corresponds to a parabolic dispersion relation in the in-plane direction, as shown in Fig. 1.5 (a). The parabolic dispersion

allows to define an effective mass for photons, through relation 1.1. In the same way as for excitons, we can consider photons as particles with an effective mass moving freely in the 2D plane of the cavity, with a momentum given by  $\hbar\mathbf{k}_{\parallel}$ .

Nevertheless, the curvature of the dispersion curve for photons is much higher than the curvature typical of the excitonic dispersion. If we put the two curves on the same scale, the exciton dispersion appear to be flat, as shown in Fig. 1.5 (a) (in gray). The corresponding effective mass for photons is of the order of  $m_{ph} \sim 10^{-5}m_e$  where  $m_e$  is the mass of electrons, four orders of magnitude less than the excitonic mass ( $m_{exc} \sim 10^{-1}m_e$ ).

Fig. 1.5 (b) shows the angle dependence of the cavity reflectivity at the resonant wavelength  $\lambda_c$ . For  $k_{\parallel}$  vectors exceeding  $\sim 2.5 \mu\text{m}^{-1}$ , oscillations of the reflectivity as a function of  $k_{\parallel}$  take place. In particular the dips in the reflectivity can be interpreted as secondary modes of the cavity, with a much lower lifetime (wider linewidth) than the principal mode, being well coupled with free space. These modes limit the working region (in which we can expect to attain strong coupling) to  $k_{\parallel}$  vectors smaller than few  $\mu\text{m}^{-1}$ . We expect that for higher  $k_{\parallel}$  vectors, the system will be in any case in the weak coupling regime.

Semiconductor microcavities are particularly suited systems where the strong coupling regime can be achieved. On one hand they are characterized by an optical mode with a very long lifetime, corresponding to a very narrow peak in the energy spectrum and this mode is well separated in energy from the other longitudinal modes. It is therefore a good approximation of a single optical mode. On the other hand they can confine the optical mode to very small volumes. This is another requirement necessary to reach the strong coupling regime, since, as we will see, the strength of the exciton-photon coupling is inversely proportional to the volume in which the optical mode is confined.

### Strong coupling between quantum well excitons and microcavity photons

The strong coupling regime is obtained by embedding one or more semiconductor quantum wells in a microcavity, with the optical mode quasi-resonant with the excitonic transition. In particular, the quantum wells are placed in correspondence to antinodes of the electromagnetic field, in order to maximize the coupling, as shown schematically in Fig. 1.6.

When we discussed the quantum well excitons, we saw that for a quantum well in the free space, one excitonic transition is coupled to a continuum of modes of the electromagnetic field, each mode having a different  $k_z$  component. Since the microcavity imposes the quantization of motion in the growth direction  $z$ , it selects one specific value of  $k_z$ , i.e. just one optical mode. In that way the coupling between two discrete modes is realized. Of course this would be strictly true, only if both exciton and photon had infinite lifetime. The finite lifetime introduces a broadening of the linewidths, meaning that we do not have exactly two single modes. We will see under which conditions the two-mode approximation, leading to the strong coupling regime, remains a good approximation.

For the moment, we suppose the coupling of two modes with infinite lifetimes, i.e. delta functions in energy. We also suppose that we excite just few particles in the system. This allows neglecting interactions between excitons, i.e. nonlinear terms in the Hamiltonian. We also consider excitons in pure states of spin (normal incidence, for circularly polarized light), which allows to use a scalar theory.

Under these approximations, the system is equivalent to two coupled harmonic os-

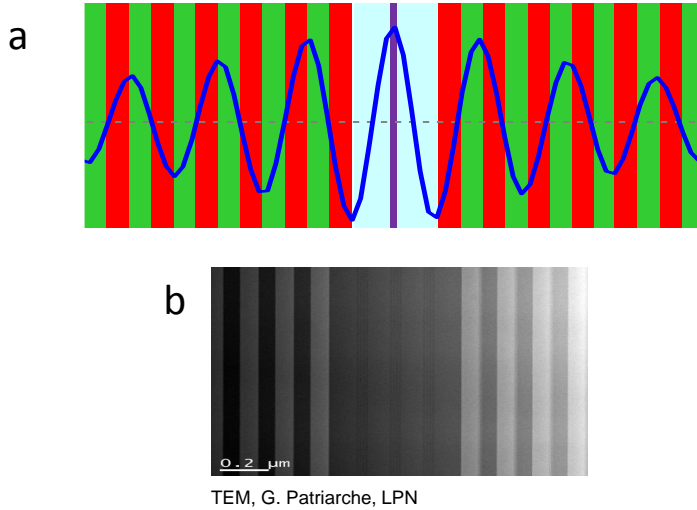


Figure 1.6: (a) Schematic representation of a semiconductor microcavity with one embedded quantum well. Its position corresponds to an antinode of the electromagnetic field inside the cavity. (b) TEM image taken from a real microcavity, with three sets of four quantum wells placed inside the cavity.

cillators, one oscillator being the excitonic transition with wavevector  $\mathbf{K}_{\parallel}$ , the other a quasi-resonant optical mode with  $\mathbf{k}_{\parallel} = \mathbf{K}_{\parallel}$ . From now on, we will omit the index  $\parallel$  to simplify notations,  $\mathbf{k} \equiv \mathbf{k}_{\parallel}$ .

We write the Hamiltonian using a quantum approach, even if a mean-field classical approach would give equivalent results [2]

$$H_{\mathbf{k}} = E_{exc}(k)b_{\mathbf{k}}^{\dagger}b_{\mathbf{k}} + E_{cav}(k)a_{\mathbf{k}}^{\dagger}a_{\mathbf{k}} + \frac{\Omega_R}{2}(a_{\mathbf{k}}^{\dagger}b_{\mathbf{k}} + b_{\mathbf{k}}^{\dagger}a_{\mathbf{k}}), \quad (1.12)$$

where  $b_{\mathbf{k}}^{\dagger}, b_{\mathbf{k}}$  and  $a_{\mathbf{k}}^{\dagger}, a_{\mathbf{k}}$  are respectively the creation and annihilation operators for an exciton and a photon with wavevector  $\mathbf{k}$  in the 2D plane transversal to the growth axis. They satisfy the bosonic commutation relations.  $E_{exc}(k)$  and  $E_{cav}(k)$  correspond to the energies of excitons and photons, given by the dispersion relations 1.4 and 1.11. The last term in 1.12 corresponds to the coupling term. In particular it contains one term corresponding to the simultaneous creation of a photon and annihilation of an exciton (emission term) and a term corresponding to the simultaneous creation of an exciton and annihilation of a photon (absorption term).

The coefficient  $\Omega_R/2$  is the coupling energy ( $\Omega_R$  is the *Rabi splitting*) and it has the expression

$$\Omega_R = 2g = 2\sqrt{\frac{2c\Gamma_0}{n_{cav}L_{eff}}} \propto \sqrt{\frac{f_{osc}}{L_{eff}}}, \quad (1.13)$$

where  $\Gamma_0$  is the radiative lifetime of excitons in  $\mathbf{k} = 0$  in the absence of the cavity.  $L_{eff}$  is the effective length in which the optical mode is confined,  $L_{eff} = L_{cav} + 2L_{Bragg}$ , where  $L_{Bragg}$  is the length over which the electromagnetic field decays exponentially inside each Bragg mirror (typically  $L_{Bragg} \approx \lambda_c$ ).  $f_{osc}$  is the oscillator strength of the excitonic transition, characterizing the strength of its dipolar coupling to the electromagnetic field. Therefore, the coupling constant depends on one hand on the oscillator strength of the exciton, which is increased in a quantum well, due to the enhanced overlap of the electron and hole wavefunctions, on the other hand to the

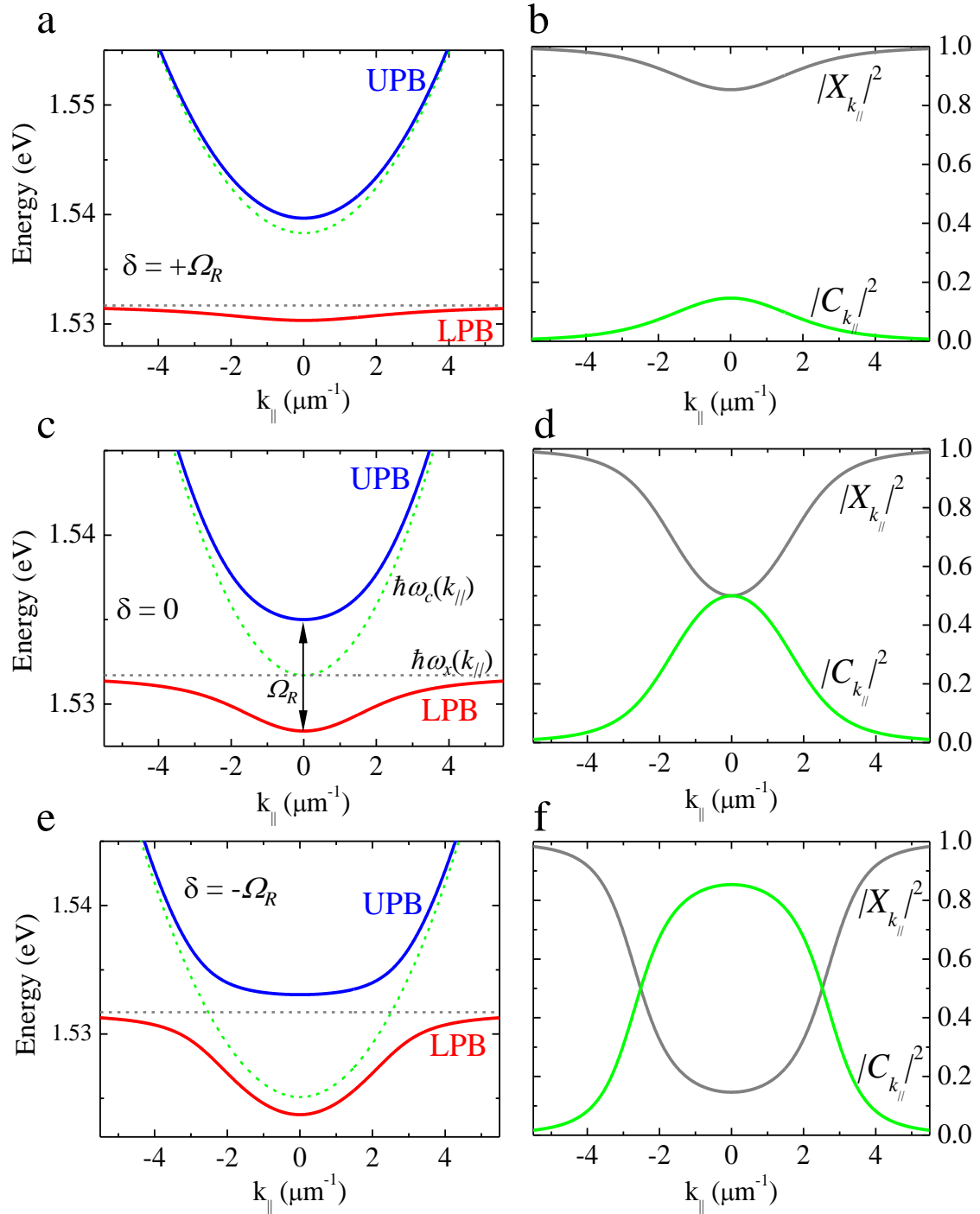


Figure 1.7: Left panels: calculated bare exciton and cavity mode dispersions (dashed lines) as well as polariton dispersions (solid lines) for different cavity-exciton detunings  $\delta$  in a microcavity with a Rabi splitting  $\Omega_R = 6.6$  meV. Right panels: corresponding Hopfield coefficients obtained from Eqs. 1.16, 1.17. Detunings: (a)-(b)  $+\Omega_R$ , (c)-(d) zero, (e)-(f)  $-\Omega_R$ .

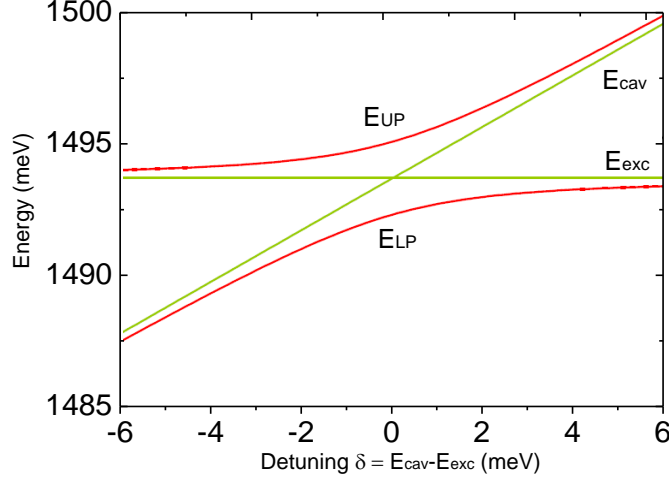


Figure 1.8: Energies of the upper and lower polariton branches at  $k = 0$ , as a function of the cavity-exciton detuning  $\delta$ , showing anticrossing at  $\delta = 0$ .

volume over which the electromagnetic field is confined. This volume is particularly small in semiconductor microcavities. Both contribute to achieve high values of  $\Omega_R$ , typically of the order of  $\sim 15$  meV in our GaAs based samples, and even higher for CdTe and GaN based microcavities.

The Hamiltonian 1.12 is diagonalized in the following way

$$H_{\mathbf{k}} = E_{UP}(k)p_{\mathbf{k}}^{(UP)\dagger}p_{\mathbf{k}}^{(UP)} + E_{LP}(k)p_{\mathbf{k}}^{(LP)\dagger}p_{\mathbf{k}}^{(LP)}, \quad (1.14)$$

where the operators  $p_{\mathbf{k}}$  are found by applying to the photon and exciton operators  $a_{\mathbf{k}}$  and  $b_{\mathbf{k}}$ , the unitary transformation

$$\begin{pmatrix} p_{\mathbf{k}}^{(LP)} \\ p_{\mathbf{k}}^{(UP)} \end{pmatrix} = \begin{pmatrix} -C_k & X_k \\ X_k & C_k \end{pmatrix} \begin{pmatrix} a_{\mathbf{k}} \\ b_{\mathbf{k}} \end{pmatrix}. \quad (1.15)$$

$C_k$  and  $X_k$  are the Hopfield coefficients [52], real positive coefficients defined as

$$X_k^2 = \frac{\delta_k + \sqrt{\delta_k^2 + \Omega_R^2}}{2\sqrt{\delta_k^2 + \Omega_R^2}} \quad (1.16)$$

$$C_k^2 = \frac{\Omega_R^2}{2\sqrt{\delta_k^2 + \Omega_R^2}(\delta_k + \sqrt{\delta_k^2 + \Omega_R^2})}, \quad (1.17)$$

where  $\delta_k$  is the cavity-exciton detuning, given by  $\delta_k = E_{cav}(k) - E_{exc}(k)$ . The Hopfield coefficients satisfy the relation  $X_k^2 + C_k^2 = 1$ .

The new eigenstates of the system are called *exciton-polaritons*, in particular *upper polaritons* and *lower polaritons*, and, as explicitly written in 1.15, they are mixed particles composed by a photonic fraction and an excitonic fraction.  $X_k^2$  and  $C_k^2$  represent respectively the excitonic and photonic fractions. At zero detuning ( $\delta_k = 0$ ) upper and lower polaritons are both composed by an equal amount of photonic and excitonic components ( $X_k^2 = C_k^2 = 1/2$ ).

The energies of the lower and upper polaritons are given by

$$E_{UP,LP}(k) = \frac{1}{2}(E_{exc}(k) + E_{cav}(k) \pm \sqrt{\delta_k^2 + \Omega_R^2}), \quad (1.18)$$

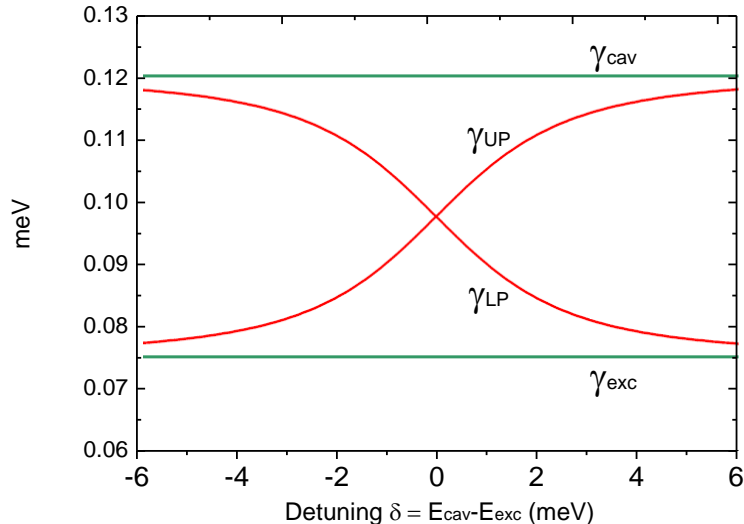


Figure 1.9: Upper and lower polariton linewidths as a function of the cavity-exciton detuning  $\delta$ .

corresponding to the dispersion curves shown in Fig. 1.7, for three different values of the cavity-exciton detuning  $\delta_k$ .

At zero detuning (Fig. 1.7 (c)-(d)) and at  $k = 0$ , where the excitonic transition and the optical mode have the same energy, the coupling lifts the degeneracy of modes, opening an energy gap between the polaritonic states equal to the Rabi splitting  $\Omega_R$ . This energy gap is the signature of the strong coupling regime.

Note that if we consider the photon-exciton basis, instead of the upper-lower polariton basis, this situation corresponds to coherent oscillations between the excitonic and photonic modes, with a frequency given by  $\Omega_R$ , called *Rabi oscillations*.

Close to  $k = 0$ , the polaritonic dispersion (Fig. 1.7 (c)) can be approximated by a parabola, with a curvature similar to the curvature of the photonic dispersion curve. Polaritons can be therefore approximated by free particles, moving in the 2D plane of the cavity, characterized by a very small effective mass, of the order of the bare cavity photon mass,  $m_{pol} \approx 10^{-5}m_e$ .

Figures 1.7 (a)-(b) show the dispersion curves and the corresponding Hopfield coefficients in the case of positive detuning ( $\delta_k = \Omega_R$ ), while Figs. 1.7 (e)-(f) show the case of negative detuning ( $\delta_k = -\Omega_R$ ). We observe that in the case of positive detuning, the upper polariton branch has a higher photonic weight, while the lower polariton branch is mostly excitonic. In the case of negative detuning, the situation is inverted. We also note that, as the detuning between the excitonic transition and the optical mode is increased, the effect of the coupling becomes less and less important, up to a point in which the eigenmodes of the system are the bare cavity and excitonic modes (i.e. the polaritonic modes coincide with photonic and excitonic modes). This is explicitly shown in Fig. 1.8, where the energies of the upper and lower polariton branches at  $k = 0$  are plotted as a function of the cavity-exciton detuning. The anticrossing behaviour is clear at  $\delta = 0$ .

Up to now we have considered exciton and photons to have an infinite lifetime. For finite lifetimes, photons and excitons are no more single modes, but they are characterized by a finite homogeneous linewidth in the spectral domain. The comparison of this homogeneous linewidth with the magnitude of the exciton-photon coupling tells us if the system can be with a good approximation described by the

two-mode description, i.e. if it is in the strong coupling regime. In particular we can describe the finite lifetime by introducing the complex energies,  $E_{cav}(k) - i\gamma_{cav}$  and  $E_{exc}(k) - i\gamma_{exc}$ . The polariton energies take the form

$$E_{UP,LP}(k) = \frac{E_{cav}(k) + E_{exc}(k)}{2} - i\frac{\gamma_{cav}(k) + \gamma_{exc}(k)}{2} \pm \frac{1}{2}\sqrt{(\delta_k - i(\gamma_{cav}(k) - \gamma_{exc}(k)))^2 + \Omega_R^2}, \quad (1.19)$$

which gives, at zero detuning,

$$E_{UP,LP}(k) = E(k) - i\frac{\gamma_{cav}(k) + \gamma_{exc}(k)}{2} \pm \frac{1}{2}\sqrt{\Omega_R^2 - (\gamma_{cav}(k) - \gamma_{exc}(k))^2}. \quad (1.20)$$

From this expression, we note that the existence of two separate energies for polaritons depends on the relative values of  $\Omega_R$  and  $|\gamma_{cav}(k) - \gamma_{exc}(k)|$ . If  $\Omega_R$  is smaller than  $|\gamma_{cav}(k) - \gamma_{exc}(k)|$ , the two energies have the same real part and the degeneracy between photon and exciton is not lifted. In this case the system is in the weak coupling regime. If  $\Omega_R$  is larger than  $|\gamma_{cav}(k) - \gamma_{exc}(k)|$  the two energies are separated by the quantity

$$\Omega'_R = \sqrt{\Omega_R^2 - (\gamma_{cav}(k) - \gamma_{exc}(k))^2} \quad (1.21)$$

and the system is in the strong coupling regime.

More explicitly the strong coupling regime is attained if the coupling between excitons and photons is strong enough if compared to the typical photon and exciton lifetimes. Under this condition a photon can be absorbed and reemitted more times, through the excitonic transition, before leaving the cavity.

The imaginary part of expression 1.19 gives the homogeneous linewidths of the upper and lower polaritonic modes, which can be related to the bare photon and exciton homogeneous linewidths through the relations

$$\gamma_{LP}(k) = X_k^2\gamma_{exc}(k) + C_k^2\gamma_{cav}(k) \quad (1.22)$$

$$\gamma_{UP}(k) = C_k^2\gamma_{exc}(k) + X_k^2\gamma_{cav}(k). \quad (1.23)$$

Their values, as a function of the cavity-exciton detuning  $\delta$ , are shown in Fig. 1.9. In particular, at zero detuning, the upper and lower polaritons have the same linewidth which is equal to  $\gamma_{pol}(k) = (\gamma_{exc}(k) + \gamma_{cav}(k))/2$ . Since usually  $\gamma_{exc}(k) \ll \gamma_{cav}(k)$ , we can approximate  $\gamma_{pol}(k) \approx \gamma_{cav}(k)/2$ . That is, at zero detuning, we can approximate the polariton lifetime as being twice the bare cavity lifetime. It follows that polaritons are characterized by quite short lifetimes, of the order of some tens of ps, at best.

The short polariton lifetime is responsible for some features characterizing specifically polaritonic systems. First of all, it defines polaritons as an intrinsically out-of-equilibrium system, characterized by a continuous decay of the population corresponding to photons leaking out of the cavity. This property on one hand is an obstacle in the reaching of the thermodynamical equilibrium, on the other hand, it represents a great advantage, since it allows a direct way of detection. In fact, since photons out of the cavity are in a one-to-one correspondence with polaritons inside the cavity, the properties of polaritons can be fully reconstructed by analyzing photons outside of the cavity. Moreover polaritons result to be a suitable system to study out-of-equilibrium quantum gases.

To conclude this section, we would like to introduce the polariton Hamiltonian in

a mean-field approximation, since in most of experimental situations, a quantum description is not necessary.

First of all we introduce the total field operator  $\hat{\Psi}(\mathbf{r})$  in a quantum picture, which has the expression [53]

$$\hat{\Psi}(\mathbf{r}) = \sum_{\mathbf{k}} \hat{p}_{\mathbf{k}} \frac{1}{\sqrt{V}} e^{i\mathbf{k}\cdot\mathbf{r}}, \quad (1.24)$$

where  $\hat{p}_{\mathbf{k}}$  is the polariton operator annihilating a polariton with wavevector  $\mathbf{k}$ . The Hamiltonian can be written

$$\hat{H} = \sum \frac{\hbar^2 k^2}{2m} \hat{p}_{\mathbf{k}}^\dagger \hat{p}_{\mathbf{k}} = \int \frac{\hbar^2}{2m} \nabla \hat{\Psi}^\dagger \nabla \hat{\Psi} d\mathbf{r} \quad (1.25)$$

and the dynamics of the system is described by

$$i\hbar \frac{\partial}{\partial t} \hat{\Psi}(\mathbf{r}, t) = [\hat{\Psi}(\mathbf{r}, t), \hat{H}] = -\frac{\hbar^2 \nabla^2}{2m} \hat{\Psi}(\mathbf{r}, t). \quad (1.26)$$

As already mentioned, in lots of experimental situations, is it possible to replace the field operator  $\hat{\Psi}(\mathbf{r}, t)$  with a classical field  $\Psi(\mathbf{r}, t)$ , i.e. to use a mean-field approximation. This is allowed any time that we deal with macroscopic occupation of particles in the quantum states. In this case we can safely describe the dynamics of the system by considering the mean values of the field (neglecting quantum fluctuations).

In terms of mean-field, the dynamics of the system is described by the equation

$$i\hbar \frac{\partial}{\partial t} \Psi(\mathbf{r}, t) = -\frac{\hbar^2 \nabla^2}{2m} \Psi(\mathbf{r}, t). \quad (1.27)$$

If we now account also for exciton-exciton Coulomb repulsive interactions (introducing the nonlinear term  $g |\Psi(\mathbf{r}, t)|^2 \Psi(\mathbf{r}, t)$ ) and for the presence of an external potential  $V_{ext}$ , we find that equation 1.27 is extended to

$$i\hbar \frac{\partial}{\partial t} \Psi(\mathbf{r}, t) = \left( -\frac{\hbar^2 \nabla^2}{2m} + V_{ext}(\mathbf{r}, t) + g |\Psi(\mathbf{r}, t)|^2 \right) \Psi(\mathbf{r}, t), \quad (1.28)$$

which is used to describe the polariton dynamics in many situations. This equation is formally equivalent both to the Gross-Pitaevskii equation [53], the main theoretical tool for investigating dilute Bose gases at low temperatures (equation for the order parameter  $\Psi(\mathbf{r}, t)$  of a Bose-Einstein condensate), and to the nonlinear Maxwell equations in  $\chi^{(3)}$  media. In the next sections, we will highlight some properties of microcavity polaritons, related to their double light-matter nature. In particular we will discuss more in detail the origin and consequences of the nonlinear term  $g |\Psi(\mathbf{r}, t)|^2 \Psi(\mathbf{r}, t)$  (section 1.3.2) and the introduction of an external lateral potential  $V_{ext}(\mathbf{r}, t)$  (section 2).

As a final observation, we would like to mention that, due to the low polariton lifetime, in most of the experimental situations, a decay and a pumping term need to be included in equation 1.28 in order to describe fully the dynamics of the system. The resulting equation is the driven-dissipative Gross-Pitaevskii equation

$$i\hbar \frac{\partial}{\partial t} \Psi(\mathbf{r}, t) = \left( -\frac{\hbar^2 \nabla^2}{2m} + V_{ext}(\mathbf{r}, t) + g |\Psi(\mathbf{r}, t)|^2 - i \frac{\gamma_{LP}}{2} \right) \Psi(\mathbf{r}, t) + F_p, \quad (1.29)$$

where  $\gamma_{LP}$  is the homogeneous broadening of the polariton line, taking into account the finite polariton lifetime, while  $F_P$  is a very general pumping term. This term can be related to different mechanisms as for example direct injection of resonant polaritons, in a resonant pumping configuration, or a scattering term from the excitonic reservoir (as we will discuss in the next section), in a out-of-resonance pumping configuration.

### 1.3 Properties of microcavity polaritons

Due to their half light-matter nature, polaritons share many properties both with atomic condensates and  $\chi^{(3)}$  nonlinear optics, many of which can be described by the Gross-Pitaevskii equation 1.28 introduced in the previous section. In this view, we can consider them as a system lying in between this two big fields of physics. On one hand we can look at them as a bosonic matter system with a very low effective mass, which therefore is expected to undergo Bose-Einstein condensation at much higher temperatures if compared to atomic condensates. On the other hand we can consider them as a photonic system with strong nonlinearities, thanks to exciton-exciton Coulomb interactions. As an additional property, polaritons are spinor particles, introducing in the dynamics another degree of freedom.

In the next three sections we will introduce three properties of polaritons: condensation, nonlinearity and spin. These three properties are fundamental in the experiments reported in this thesis (Chapters 3, 4, 5).

#### 1.3.1 Polaritons as a bosonic system with a very low effective mass: polariton condensation

One of the most interesting properties of microcavity polaritons is their capability to undergo condensation. This property arises from the bosonic character of polaritons, which is inherited from the bosonic nature of their constituents: photons and excitons.

Bose-Einstein condensation is a phase transition characterizing in general bosonic gases, which is expected to take place at a critical temperature  $T_c$ , corresponding to the de Broglie wavelength of the single particles

$$\lambda_T(T) \equiv \sqrt{\frac{2\pi\hbar^2}{mK_B T}} \quad (1.30)$$

becoming comparable or larger than the average interparticle distance. The critical temperature is related to the particle density through the relation (considering a three dimensional gas of free particles of mass  $m$ )

$$n_c \lambda_T^3(T_c) = 2.612. \quad (1.31)$$

Close to the critical temperature, particles start to “feel each other” as bosons and the Bose statistics starts to play a role in determining the properties of the gas. When the occupation number of one energy level exceeds one (usually the ground state), bosonic stimulation from the other levels towards that level starts to take place, leading to more and more particles occupying the level. This stimulated process ends up with the formation of a macroscopic population of particles in a single quantum state, a Bose-Einstein condensate. In the condensate state, quantum

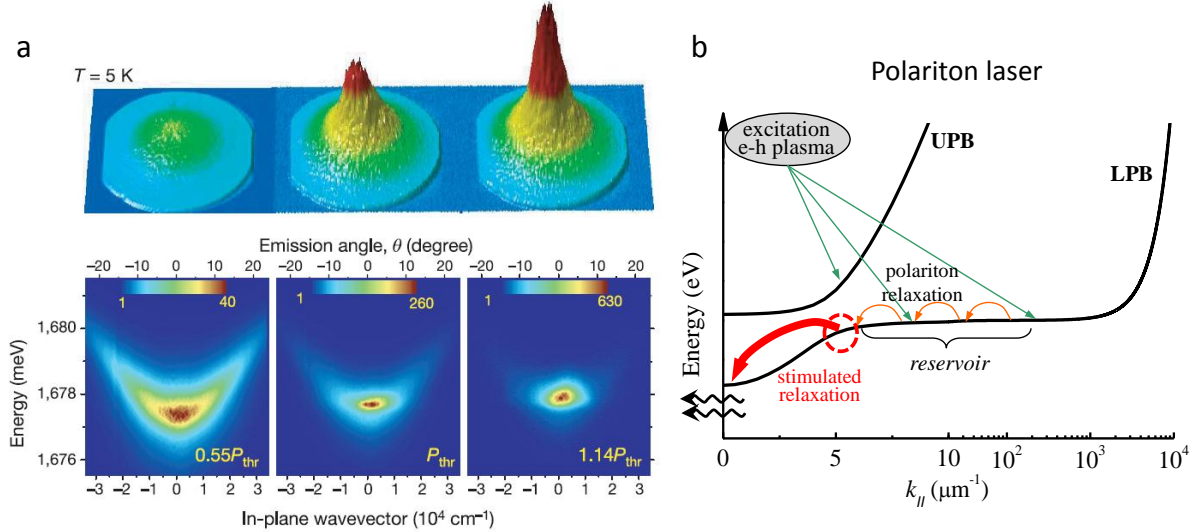


Figure 1.10: (a) Experimental observation of polariton condensation in a CdTe based microcavity (reported from [4]). Upper panels: far-field emission ( $k_x$  and  $k_y$  momentum space) from the lower polariton branch under nonresonant excitation at 5 K at different polariton densities. Above threshold (last two densities), macroscopic occupation of a single momentum state ( $k = 0$ ) takes place. Lower panels: same as upper panels for  $k_y = 0$  and energy resolution. (b) Schematic representation of the relaxation processes leading to polariton condensation, when the microcavity is excited out-of-resonance. After the condensation process has taken place, light emitted from the cavity displays high coherence (polariton laser).

Systems	Atomic gases	Excitons	Polaritons
Effective mass $m^*/m_e$	$10^3$	$10^{-1}$	$10^{-5}$
Bohr radius $a_B$	$10^{-1} \text{ \AA}$	$10^2 \text{ \AA}$	$10^2 \text{ \AA}$
Particle spacing: $n^{-1/d}$	$10^3 \text{ \AA}$	$10^2 \text{ \AA}$	$1 \text{ \mu m}$
Critical temperature $T_c$	1 nK–1 $\mu$ K	1 mK–1 K	1–>300 K
Thermalization time/Lifetime	1 ms/1 s $\sim 10^{-3}$	10 ps/1 ns $\sim 10^{-2}$	(1–10 ps)/(1–10 ps)=0.1–10

Figure 1.11: Parameter comparison of BEC systems (taken from [57]).

correlation properties, that are usually characteristic of microscopic systems, can manifest on a macroscopic scale, giving rise to macroscopic quantum coherence effects, in which the phase of the wavefunction is coherent over distances much longer than the separation between individual particles.

Bose-Einstein condensation has been thoroughly studied in dilute atomic systems [54], since its milestone experimental demonstration in 1995 [55, 56].

Condensation of microcavity polaritons [58, 59] has been demonstrated more recently [4, 60, 6, 61], providing a new and rich framework to the study Bose-Einstein condensation phenomena in a semiconductor based system.

A remarkable advantage of microcavity polaritons, if compared to cold atoms, is that they have a very small effective mass due to their photonic component, of the order of  $10^{-9}$  times smaller than that of atoms. For this reason, the transition to a Bose-condensate phase can take place at much higher temperatures (lower densities), from few Kelvins up to room temperature [62, 63], as shown in Table 1.11.

Not only this simplifies the experimental setups for polariton research, but it also makes polaritons a natural and practical candidate for quantum device applications. Many properties associated to the formation of condensates of polaritons in microcavities have been observed in many different experiments in the past decade, like spatial and temporal coherence [5, 6, 7, 8, 9, 10, 11, 12, 13], the observation of integer and half quantum vortices [16, 17], and superfluidity [14, 15]. One of the most common configurations used to obtain polariton condensation is sketched in Fig. 1.10 (b). The system is excited out-of-resonance, i.e. at an energy well above the energy of the polariton modes, creating a plasma of free hot electrons and holes. First an ultrafast nonradiative relaxation of free carriers takes place, through optical-phonon emission, towards the lower polaritonic branch (green arrows). Part of these electron and hole pairs bind and form polaritons at large  $k$ -vectors, populating the so-called *excitonic reservoir*. Then polaritons relax energy and momentum (orange arrows) until they reach the momentum bottleneck region (red dashed circle). The relaxation from the bottleneck region to the bottom of the lower polariton branch is a slow process at low excitation densities, as it requires the simultaneous relaxation of significant amounts of energy and momentum. Optical-phonon assisted scattering processes cannot participate due to energy conservation constraints, and only polariton-polariton and acoustic phonon-polariton interactions can mediate in the polariton relaxation. If this relaxation process is efficient enough, allowing to reach an occupation number greater than one in the ground state, bosonic stimulation from the bottleneck to the ground state takes place, accelerating strongly the relaxation towards the ground state and allowing the formation of the condensate at the bottom of the lower polariton branch.

Figure 1.10 reports the results obtained by the groups of Le Si Dang in Grenoble and B. Deveaud in Lausanne in which spontaneous Bose-Einstein condensation of microcavity polaritons has been demonstrated in a CdTe based microcavity [4]. As it is usually the case in polariton condensation measurements, the temperature is kept constant (in this experiment  $T = 5$  K) and the density of particles is varied. A critical density, corresponding to a critical pumping power, determines the threshold for polariton condensation.

Figure 1.11 depicts the momentum distribution for three different pumping power, below (a) and above (b)-(c) the condensation threshold for the condensate state. In the last two cases the macroscopic occupation of a single momentum state ( $k = 0$ ) is obtained. The formation of the condensate corresponds also to a nonlinear increase in the emitted intensity, spectral narrowing of the emission and build-up of macroscopic coherence. Note that the out-of-resonance pumping configuration guarantees that the coherence built-up in the system is solely related to the spontaneous condensation and not to the coherence properties of the excitation laser, which are lost during the spontaneous relaxation process.

A remarkable difference with respect to atomic BEC, is that polaritons are an intrinsically out-of-equilibrium system. Since polariton lifetimes are of the order of 1-100 ps, once the condensate is formed at the bottom of the lower polariton branch, a continuous leaking of the condensate population takes place through photons which escape out of the cavity. At the same time the population is continuously replenished through stimulated scattering from the bottleneck. Therefore a polariton condensate is not obtained at thermodynamic equilibrium (differently from atomic BEC), but as a steady state established between stimulated pumping and losses. In particular, depending on the relative strength between scattering rates and polariton lifetime,

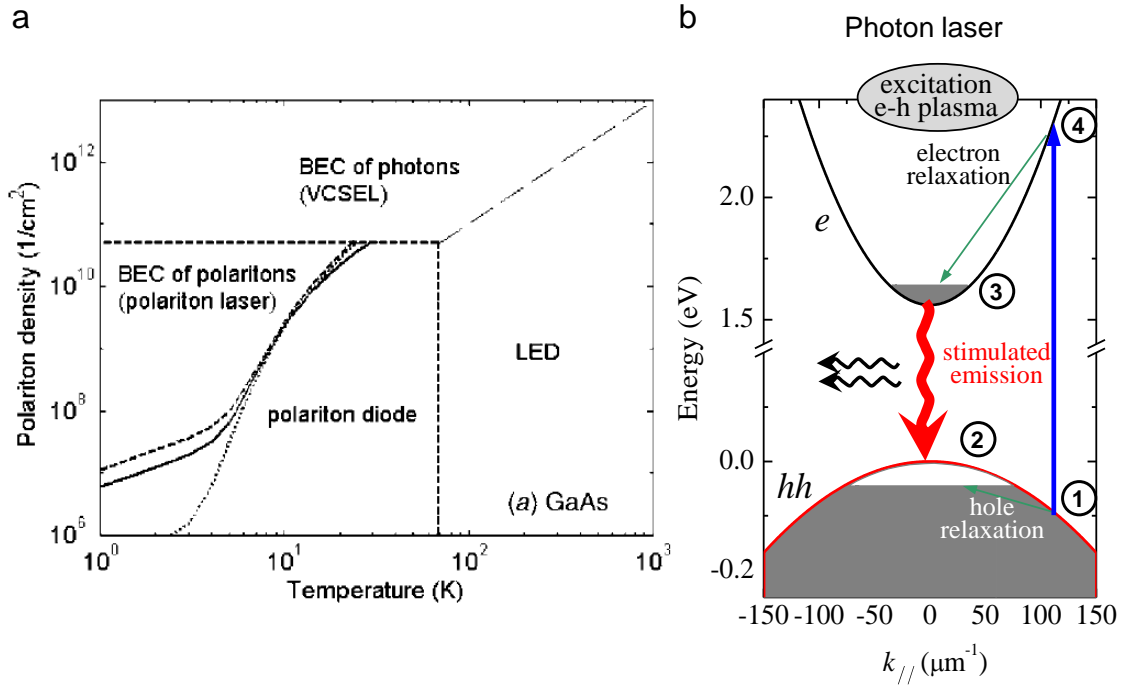


Figure 1.12: (a) Phase diagram for a GaAs based microcavity. The vertical and horizontal dashed lines show the limits of the strong coupling regime imposed by the exciton thermal broadening and screening, respectively. The dotted and dashed lines show the critical densities for condensation in finite size systems (lateral sizes of  $100 \mu\text{m}$  and  $1 \text{m}$ , respectively). Taken from [64]. (b) Carrier relaxation and light emission in the weak coupling regime above the threshold for photon lasing (VCSEL regime). The numbers indicate the leveling of the 4-level lasing system.

the steady state distribution can be almost thermalized or highly out-of-equilibrium.

The finite polariton lifetime has represented at the beginning an obstacle for the achievement of condensation. In fact, in order for condensation to take place, relaxation towards the bottom of the polaritonic band needs to take place at higher rates if compared to the rate at which the condensate is depleted (corresponding to polariton lifetime). This condition needs to be compatible with keeping the density of polaritons in the system relatively low, in order to maintain the system in the strong coupling regime. In fact, at high excitation densities, free carriers injected nonresonantly start to screen the excitonic transition, up to a point in which the strong coupling is broken and just free carriers populate the system. Under this condition the pumping drives the system into the VCSEL regime, where photon lasing takes place under weak coupling. This situation is sketched in Fig. 1.12 (b), together with the phase diagram in the (density, temperature) space characterizing a GaAs microcavity.

The finite polariton lifetime and low density constraint have been the major obstacles for the observation of the BEC phase transition in GaAs based microcavities, where, due to the reduced electron-hole binding energy ( $\lesssim 10 \text{meV}$ ) the exciton can be ionized (and the polariton destroyed) at relatively small carrier densities. This is not the case in CdTe based microcavities, where condensation has first been observed, since in these systems the exciton binding energy is much larger. Two strategies have been followed in order to observe polariton condensation in GaAs microcavities under non-resonant excitation [61]: on one hand the increase of the polariton lifetime, by increasing the microcavity quality factor, on the other hand the insertion in the microcavity of more quantum wells placed in different antinodes

of the electromagnetic field, in order to increase the highest density of particles in the system, compatible with the strong coupling regime.

While having constituted an obstacle for the realization of polariton condensation, the out-of-equilibrium nature of polaritonic condensates presents also remarkable advantages. First of all, it allows to follow in time the dynamics of the system and reconstruct the properties, by analyzing photons which escape out of the cavity, thanks to the one-to-one correspondence between polaritons inside the cavity and photons outside the cavity. Moreover, the typical lifetimes in which the polaritonic condensate is formed allow to study the transient behaviour and the build-up of the coherence [9, 10, 11], difficult to study in atomic BEC, due to the short relative timescales in which the thermodynamic equilibrium is reached. Also, polaritons allow to study the physics related to out-of-equilibrium condensation, which displays different properties if compared to condensates at thermodynamical equilibrium. For example, in polaritonic systems, condensation is allowed to take place on excited energy levels, as we will discuss in Chapter 5.

The macroscopic coherence properties of the polariton condensate inside the cavity are directly reflected into coherence properties of photons emitted by the cavity. Similarly as for a photon laser, the emitted light displays a high coherence, what has led people to speak about *polariton laser*. Nevertheless, the mechanism leading to photon coherence is totally different in the two cases: in the polariton laser the basic principle is the bosonic stimulation of exciton scattering induced by the macroscopic population in the condensate state, while in the photon laser the basic principle is the stimulated emission of photons, once the population inversion condition is satisfied. Polariton lasers have been proposed as a new class of lasers, characterized by a lower lasing threshold [58, 59].

Analogously as for atomic condensates, since polariton condensates are characterized by a macroscopic population on a single quantum level, they can be described through a macroscopic classical wavefunction, which satisfies the Gross-Pitaevskii equation 1.29 introduced in the previous section.

### 1.3.2 Polaritons as a highly nonlinear optical system

In Section 1.2 we mostly concentrated on the linear properties of polaritons, which is a good approximation when we excite a low density of particles in the system. As the number of particles is increased, polariton-polariton interactions start to play an important role in the dynamics. In particular interactions are related to the polariton excitonic component: excitons interact repulsively through Coulomb interactions. To first order approximation, these interactions can be described by introducing in the Hamiltonian 1.25 a contact two-body interaction potential term [53, 3, 65] of the form

$$H_{exc-exc} = \frac{1}{2V} \sum_{\mathbf{k}, \mathbf{k}', \mathbf{q}} V_{\mathbf{q}} p_{\mathbf{k}+\mathbf{q}}^\dagger p_{\mathbf{k}'-\mathbf{q}}^\dagger p_{\mathbf{k}} p_{\mathbf{k}'} = \frac{1}{2} \int \hat{\Psi}^\dagger \hat{\Psi}^{\dagger'} V(\mathbf{r}' - \mathbf{r}) \hat{\Psi} \hat{\Psi}' d\mathbf{r}' d\mathbf{r}, \quad (1.32)$$

giving the dynamical equation

$$i\hbar \frac{\partial}{\partial t} \hat{\Psi}(\mathbf{r}, t) = [\hat{\Psi}(\mathbf{r}, t), \hat{H}] = \left[ -\frac{\hbar^2 \nabla^2}{2m} + \int \hat{\Psi}^\dagger(\mathbf{r}', t) V(\mathbf{r}' - \mathbf{r}) \hat{\Psi}(\mathbf{r}', t) d\mathbf{r}' \right] \hat{\Psi}(\mathbf{r}, t). \quad (1.33)$$

As discussed at the end of Section 1.2, in most situations we can use a mean-field approximation and replace the field operator  $\hat{\Psi}(\mathbf{r}, t)$  with its mean value  $\Psi(\mathbf{r}, t)$ . In the hypothesis of diluteness, it is possible to replace the microscopic potential  $V$  with an effective soft potential which takes into account the average interaction of one particle with all the others. Under these approximations, equation 1.33 takes the form

$$i\hbar \frac{\partial}{\partial t} \Psi(\mathbf{r}, t) = \left( -\frac{\hbar^2 \nabla^2}{2m} + V_{ext}(\mathbf{r}, t) + g |\Psi(\mathbf{r}, t)|^2 \right) \Psi(\mathbf{r}, t), \quad (1.34)$$

where  $g$  is a constant and where an additional external potential  $V_{ext}$  has been introduced. This is the equation already introduced at the end of Section 1.2, formally equivalent to the Gross-Pitaevskii equation, the main theoretical tool for investigating atomic condensates, and the nonlinear Maxwell equations in  $\chi^{(3)}$  media.

The nonlinear term leads to many physical effects, some of which are close to what is observed in  $\chi^{(3)}$  nonlinear optics. For example optical parametric oscillations (OPO) [27, 28, 29, 30] (Fig.1.13 (d)), squeezing [31], optical bistability [32, 33] and multistability [34, 35] have been observed.

In this context, polaritons display a great advantage if compared to typical  $\chi^{(3)}$  nonlinear optical media. In usual  $\chi^{(3)}$  media, the nonlinear term is proportional to the third order polarizability of the medium, which is strongest as much as we go close to the optical resonances. Unfortunately close to resonances, absorption is also large. Therefore, minimization of absorption losses causes also a nonnegligible reduction in the optical nonlinearity. Nonresonant optical nonlinearity have the serious drawback of being generally very small and requiring a large number of photons to be observable.

As described in the previous sections, polaritons overcome this problem by working exactly at resonance, in a situation of strong coupling between the excitonic transition and a single optical mode. Being half light-matter particles, they inherit directly from their excitonic component strong repulsive interactions. The advantage is that nonlinearities can be observed in principle on the single particle level, what is not possible in standard nonlinear optics.

In this perspective, polaritons display a behaviour closer to atoms, in which single particle nonlinearities have been observed [66].

In Section 1.3.1 we described the formation of a macroscopic population of particles, through stimulated relaxation, at the bottom of the polaritonic branch, i.e. in  $k = 0$ . In this case polaritons are created at rest.

Nevertheless, it is possible to create situations in which a macroscopic population of particles is created with a  $k \neq 0$ , giving rise to a moving condensate. In particular we can consider two main ways in which it is usually done. One way is to inject polaritons resonantly, with a given  $k$ -vector [15, 19]. In this case the excitation laser is resonant with the polariton branch, and it excites the cavity at an angle different from zero. A similar configuration is obtained by using the OPO mechanism [68]. Another way is to use an out-of-resonance pumping configuration, as the one described in Section 1.3.1, and exploit the repulsive interaction of the condensate polaritons with the local potential created by the optically induced excitonic reservoir [26]. This potential tends to expel polaritons from the excitation region, thus converting potential energy in kinetic energy and giving rise therefore to a moving condensate. The spontaneous coherence of the condensate is preserved during the propagation [26].

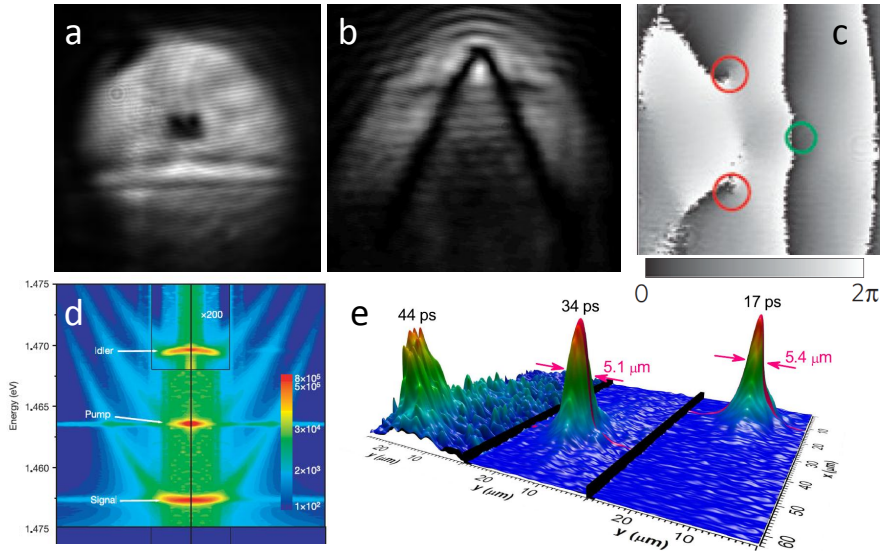


Figure 1.13: Experimental observation of: (a) superfluidity [15], (b) oblique dark solitons [19], (c) hydrodynamic vortices [67], (d) optical parametric oscillation [29], (e) bright solitons [21].

The possibility of creating moving condensates, has led to an intense study on the hydrodynamical nonlinear properties of polaritons [3], which can be most of times described by equation 1.34. The study of the interaction of a polaritonic fluid with a defect has led to the observation of superfluidity [15] (Fig.1.13 (a)) and the nucleation of topological defects in the wake of the defect, such as integer vortices [67, 69] (Fig.1.13 (c)) or dark solitons [19, 20] (Fig.1.13 (b)). Bright solitons have also been observed [21, 22] (Fig.1.13 (e)).

Note that, depending on the specific configuration used in the experiment, the nonlinear term can be related to different effects: in the nonresonant excitation, for example, the main contribution is given by the Coulomb interaction of condensate polaritons with excitons in the excitonic reservoir (see previous section), while in the resonant excitation it is mostly related to polariton-polariton interactions within the condensate. Nevertheless, the nonlinear and hydrodynamics effects are mostly described by the same physical principles.

The physics of most of these experiments is well described by a mean-field approximation, where many particles contribute to the nonlinear effect.

A recent interest in the polaritonic nonlinear properties is related to the possible observation of single particle nonlinearities. Effects such as polariton blockade [36] and nonequilibrium strongly correlated polariton gases [37, 38] have been predicted.

To conclude this section we would like to briefly describe a specific experiment to which I contributed in the earliest stages of my PhD work, showing very spectacular nonlinear effects in a 2D microcavity. It is the experimental observation of oblique dark solitons [19].

### Hydrodynamic dark solitons in polariton superfluids

A polariton superfluid with a finite speed  $v_f$  is created by resonantly injecting polaritons at nonzero  $k$ -vector in the lower polariton branch of a GaAs based microcavity kept at 10 K. The fluid propagates against an obstacle spontaneously present in

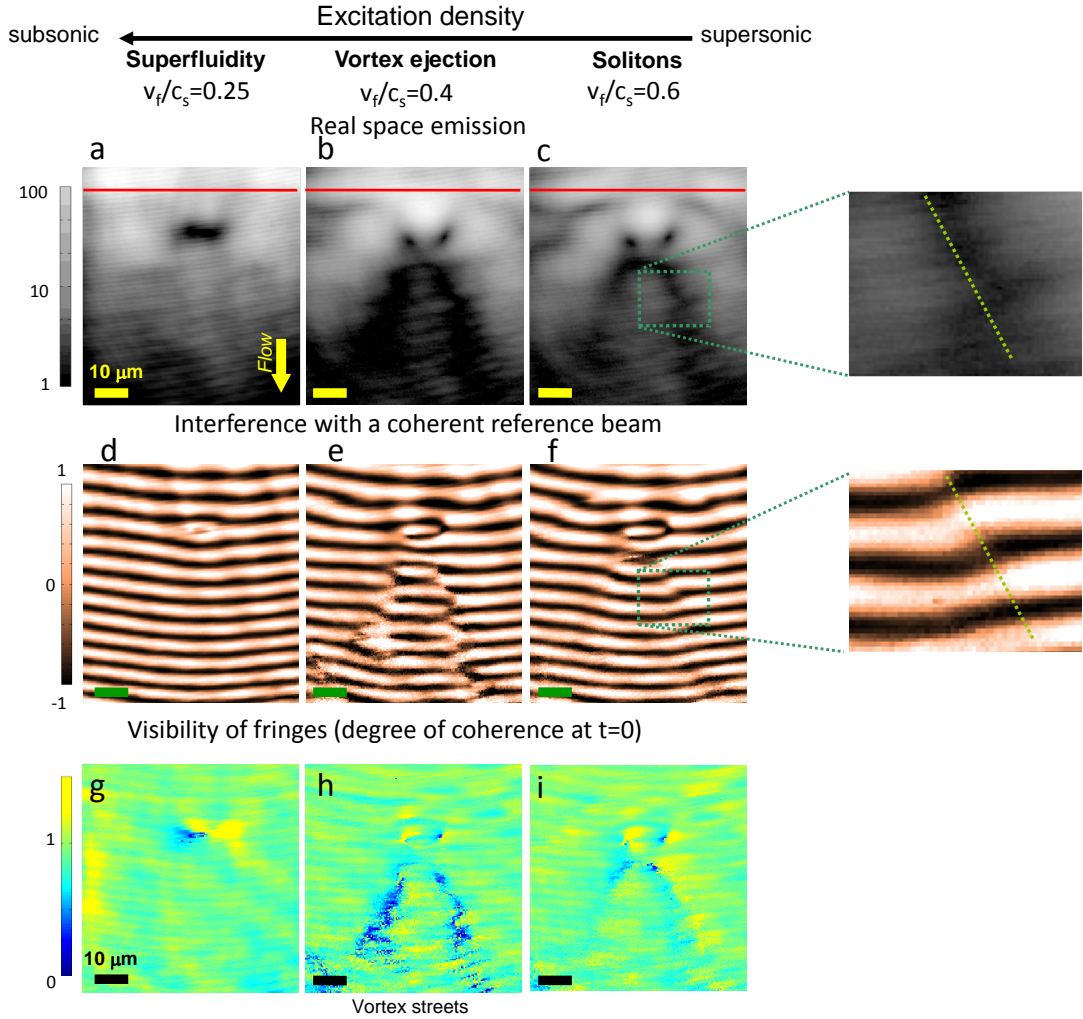


Figure 1.14: Different regimes of flow as the polariton superfluid flows against a big obstacle. Depending on the excitation density, the ratio between the speed of the fluid  $v_f$  and the speed of sound  $c_s$  is changed and different regimes are found. Left column: superfluid regime ( $v_f = 0.25 c_s$ ). Central column: turbulent regime characterized by the continuous emission of vortices and antivortices in the wake of the defect ( $v_f = 0.4 c_s$ ). Right column: stationary regime characterized by oblique dark solitons ( $v_f = 0.6 c_s$ ). Upper panels: real-space. Middle panels: corresponding interferograms. Bottom panels: corresponding degree of first order coherence  $g^{(1)}$ .

the cavity, giving rise to different topological excitations in the wake of the defect. Different regimes were found, depending on the ratio between the speed of the fluid  $v_f$  and the speed of sound  $c_s$ , defined by the relation

$$c_s = \sqrt{\frac{\hbar g |\Psi|^2}{m}}. \quad (1.35)$$

In particular, in the experiment, the speed of the fluid is kept fixed, while the speed of sound is varied, by varying the density of polaritons  $|\Psi|^2$  in the system (changing the pumping power).

Figure 1.14 shows the transition between three different regimes: a superfluid regime (left column), a turbulent regime (central column) and a regime characterized by two oblique dark solitons (right column). For each regime, the real-space intensity of the emission is shown (upper panels) together with the interferogram obtained by making the signal interfere with a constant phase reference beam (central panels).

The lower panels show the visibility of the fringes.

For small ratios of  $v_f/c_s$  the system is in the superfluid regime (left column) and it flows around the obstacle without any perturbation. The real-space image shows a flat density (a) and phase (d) profile around the obstacle (black area in the figure). As the ratio  $v_f/c_s$  is increased to the value 0.4, a transition takes place from the superfluid regime to a turbulent regime (central column), characterized by the continuous emission of quantized vortices and antivortices in the wake of the defect. The real-space is characterized by two low-density channels (b) corresponding to a low visibility in the interferogram (e,h). The density profile can be explained by considering that quantized vortices are characterized by a zero of the density in the core. Regarding the phase, they are characterized by a phase turning by  $2\pi$  around the vortex core. Nevertheless, since the measurements are integrated over many independent realizations, the continuous emission of vortices in the two channels causes a blurring in the interferograms. This is evident if we look at the visibility of fringes, which displays values close to zero corresponding to the two low-density channels. By further increasing the ratio  $v_f/c_s$  to the value 0.6 we reach a new stationary regime characterized by two dark oblique solitons in the wake of the defect (right column).

The intensity of the emission displays a dip in correspondence of the solitons (Fig. 1.14 (c) and Fig. 1.15 (a)), while the phase is well defined and shows a jump of  $\pi$  across the density dip (Fig. 1.14 (f), Fig. 1.15 (b) and red triangles of Fig. 1.15 (d)), as expected theoretically.

### 1.3.3 Polaritons as a spinor system

Up to now, we considered a scalar theory for polaritons. Actually polaritons are characterized also by a spin degree of freedom, which is inherited by their constituent particles: exciton and photon. In particular, as already mentioned in Section 1.2, quantum well excitons are composite bosons (getting their spin properties from their constituents electron and heavy hole) and they are characterized by two possible values for their total internal angular momentum  $J = 1$  and  $J = 2$ . Nevertheless, due to the selection rules for electromagnetic interaction, only  $J = 1$  excitons can couple to light, while  $J = 2$  constitute the so called *dark-excitons*. Therefore polaritons are characterized by  $J = 1$ , and by only two possible projections of the angular momentum on the quantization axis  $z$  (perpendicular to the growth axis of the microcavity)  $J_z = +1$  and  $J_z = -1$ , as shown schematically in Fig. 1.16 (a). Having just two possible projections of the total angular momentum, polaritons behave effectively as  $1/2$  spin particles, whose pseudospin state can be represented on a Bloch sphere (Fig. 1.16 (b)). Thanks to the one-to-one relation between polaritons inside the cavity and photons outside the cavity, each spin state of polaritons corresponds to a well defined polarization of light outside the cavity. The spin-polarization one-to-one correspondence is written explicitly in Fig. 1.16 (b). Therefore, by studying the polarization properties of light emitted from the cavity, we can fully reconstruct the pseudospin properties of polaritons inside the cavity.

Two main properties of polaritons can be associated to the spin degree of freedom. A first property is related to the fact that the nonlinear term in eq. 1.34 is actually spin dependent: it has a much higher magnitude for polaritons with parallel spins than for polaritons with opposite spins. This fact is related to the particular way in which two excitons interact depending on their relative spin projections. Theoretical studies [65] have shown that the most important exciton-exciton scattering

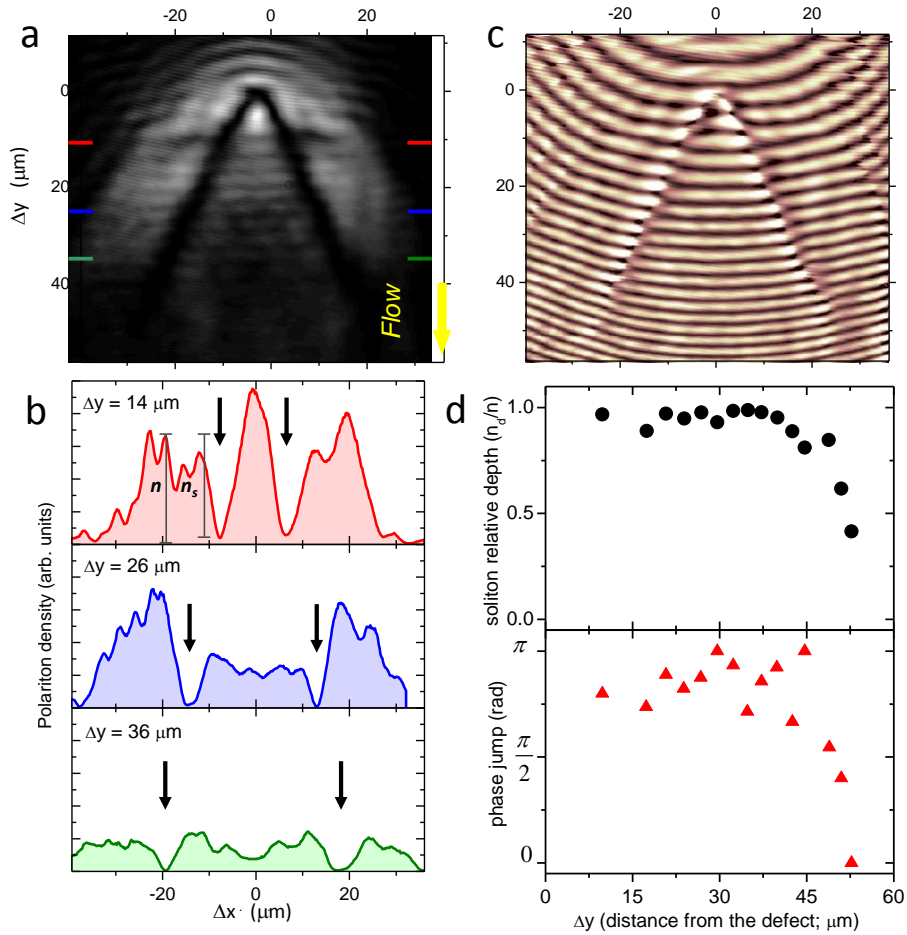


Figure 1.15: (a) Real-space emission showing a soliton doublet nucleated in the wake of a photonic defect located at the origin. (b) Horizontal profiles at different downflow distances from the defect  $\Delta y$ . Arrows indicate the soliton position. (c) Interference between the emitted intensity and a constant-phase reference beam, showing phase jumps along the solitons. The curved shape of the fringes and the decreasing interfringe distance arise from the geometry of the reference beam. (d) Soliton depth (black circles) and phase jump (filled triangles), showing a strong correlation.

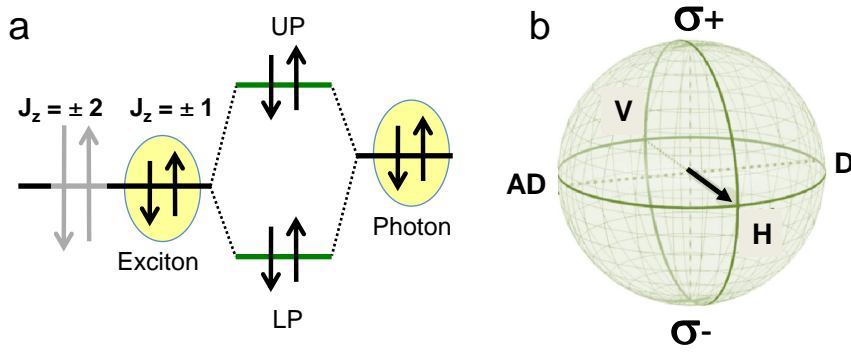
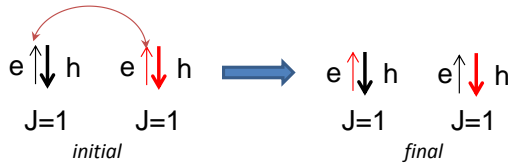
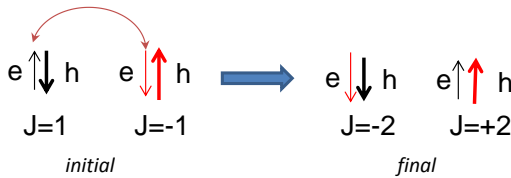


Figure 1.16: (a) Schematic representation of the polariton pseudospin: since just  $J = 1$  excitons are coupled to light, polaritons have just two possible pseudospin projections  $J_z = \pm 1$ , i.e. they behave effectively as  $1/2$  spin particles. (b) Representation on a Bloch sphere of the polariton pseudospin, in a one-to-one correspondence with the polarization of light outside the cavity. The poles represent circularly polarized states, while the equator describes linearly polarized states.

**Parallel spins :**



**Opposite spins :**



- Parallel spin  $\alpha_1$
- Anti-parallel  $\alpha_2$

$$\alpha_1 \gg |\alpha_2|$$

Figure 1.17: Schematic representation showing the main mechanism contributing to the exciton-exciton scattering process: electron/hole exchange. This mechanism induces a nonlinear term in the Gross-Pitaevskii equation which has a much stronger magnitude ( $\alpha_1$ ) for excitons with parallel spins with respect to excitons with antiparallel spins ( $\alpha_2$ ).

processes are the one corresponding to the exchange of electrons/holes between the two excitons. This situation is depicted schematically in Fig. 1.17. We observe that, while interaction of two excitons with parallel spins gives rise to two excitons of total angular momentum  $J = 1$ , the interaction of two excitons with antiparallel spins, gives rise to two excitons of total angular momentum  $J = 2$ , which are not coupled to light (dark excitons). It follows that two polaritons can interact directly just if they have parallel spins, while if they have antiparallel spins, the interaction has to be mediated via dark excitons intermediate states. Due to the strong light-matter interaction, the dark exciton states are at a different energy than the lower polariton branch. Therefore, the latter process is significantly inhibited compared to parallel spin interactions, which is a resonant process. The Gross-Pitaevskii equation for one

spin component can be written therefore in the form

$$i\hbar \frac{\partial}{\partial t} \Psi_{\uparrow}(\mathbf{r}, t) = \left( -\frac{\hbar^2 \nabla^2}{2m} + V_{ext}(\mathbf{r}, t) + \alpha_1 |\Psi_{\uparrow}(\mathbf{r}, t)|^2 + \alpha_2 |\Psi_{\downarrow}(\mathbf{r}, t)|^2 \right) \Psi_{\uparrow}(\mathbf{r}, t), \quad (1.36)$$

where  $\alpha_1 \gg \alpha_2$ .

The spin-dependent nonlinearity is responsible for example for the fact that polariton condensates are linearly polarized [4, 10, 9]. In fact the energy of the system is minimized for an equal amount of spin-up and spin-down particles [70], corresponding to an equal amount of  $\sigma+$  and  $\sigma-$  photons out of the cavity (equivalent to linear polarization).

The spin dependent nonlinearity has led for example to the realization of all optical switches [71] (Fig. 1.19 (b)), spin rings [72, 73] and polarization multistability [35].

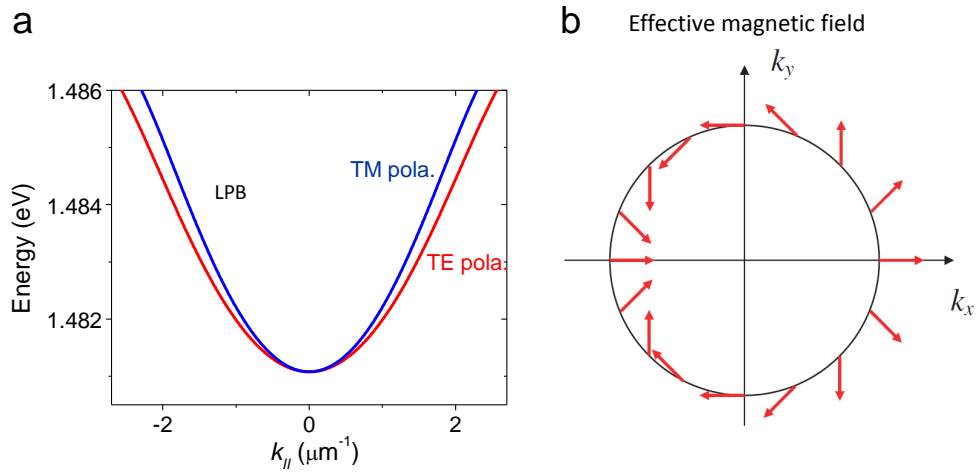


Figure 1.18: (a) TE-TM splitting of the lower polariton branch in a 2D microcavity. (b) Corresponding effective magnetic field, with a texture in the  $(k_x, k_y)$  plane (taken from [24]).

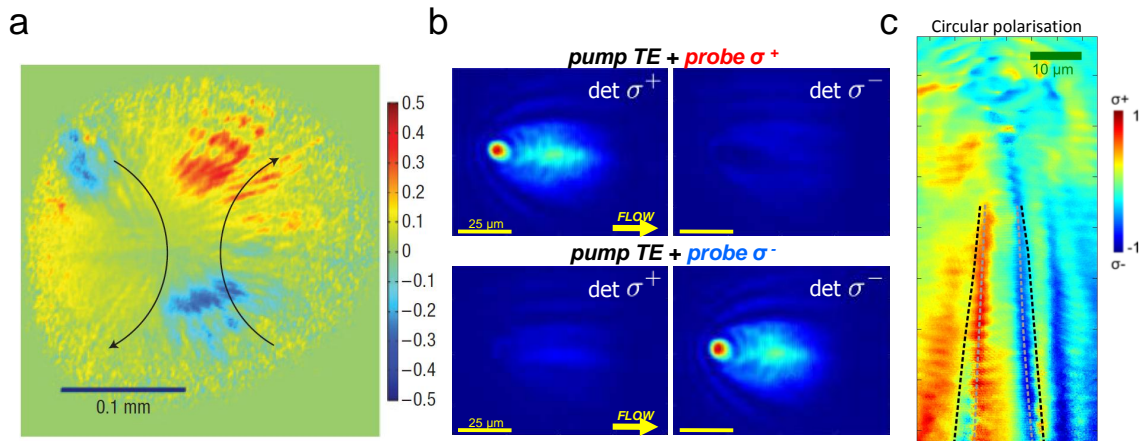


Figure 1.19: Experimental demonstration of: (a) optical spin Hall effect in a semiconductor microcavity (reported from [23]), (b) exciton-polariton spin switches [71], (c) half-solitons [25].

Another property, characterizing polaritons in the linear regime, is related to the

presence of a polarization energy splitting of the polaritonic modes [74]. In a dielectric microcavity a TE-TM polarization splitting is always present. This splitting is present in the photonic component of polaritons [75] and it is related to the boundary conditions determining the reflection and transmission components of the electromagnetic field at each interface of the cavity, which are dependent on the polarization of light. In particular the coefficients are slightly different for light polarized transversally to the plane of incidence (TE) (i.e. polarized in the 2D plane of the cavity) or in the plane of incidence (TM).

The TE-TM splitting is zero at normal incidence and it gives rise to a  $k$ -dependent spin splitting of the polaritonic bands, as shown in Fig. 1.18 (a). Such a splitting can be interpreted as an effective spin-orbit term [74], which couples the orbital ( $k$ -vector) and pseudospin degree of freedoms

$$\hat{H}_{SO} = \frac{cost}{k^2}((k_x^2 - k_y^2)\sigma_x + 2k_x k_y \sigma_y) \quad (1.37)$$

and which can be described through an effective magnetic field lying in the microcavity plane and having the explicit expression

$$\begin{aligned} \Omega_x &= \frac{\Omega}{k^2}(k_x^2 - k_y^2) \\ \Omega_y &= \frac{2\Omega}{k^2}k_x k_y. \end{aligned} \quad (1.38)$$

The texture of  $\Omega$  in the  $(k_x, k_y)$  plane is shown in Fig. 1.18 (b). The pseudospin dynamics is characterized by the typical behaviour of a  $1/2$  spin particle in a magnetic field. In particular, if the system is not prepared in one of its pseudospin eigenstates (TE, TM), it will undergo spin precession around the direction of the magnetic field, following the relation

$$\frac{\partial \mathbf{s}}{\partial t} = \mathbf{s} \times \mathbf{\Omega}_{\mathbf{k}}. \quad (1.39)$$

Since the magnetic field has a texture in the  $(k_x, k_y)$  plane, the precession will be different for different propagation directions. This is the principle which led to the observation of the optical spin hall effect in a semiconductor microcavity [23, 24]. In this experiment, a polariton wave packet is injected resonantly in the cavity, with fixed momentum and a linear polarization. As it propagates, it scatters on the structural disorder of the microcavity in every in-plane direction. The  $k$ -dependent precession of the spin around the effective magnetic field results in the appearance, in both real and reciprocal space, of circular polarization domains in the four quarters of the plane, as reported in Fig. 1.19 (a).

The same effect has led also to the observation half solitons [25] (Fig. 1.19 (c)).

As we will discuss in the next chapter, a polarization splitting arise in low dimensional structures, as microwires and molecules, characterized by a much higher magnitude. In wires it corresponds to a longitudinal-transversal splitting with respect to the elongated structure, and corresponds to the fact the electromagnetic field polarized along the structure results to be less confined (lower in energy) than the transversally polarized electromagnetic field. In these structures, the TE-TM splitting typical of 2D microcavities is still present, but it is negligible if compared to the splitting related to the lateral confinement. Note that, although the TE-TM splitting we have just introduced is related to the photonic component of polaritons, and additional linear polarization splitting can appear originating in the exciton component. This splitting does not have a  $k$  dependence and it is usually related to strain

or axial disorder in the microcavity. Both splittings are usually present in microcavities [76]. As we will see, the excitonic related splitting will play a non-negligible role in the polarization emission properties of polariton microstructures.



# Chapter 2

## Polaritons in low dimensional structures

In the previous chapter we introduced microcavity polaritons and we discussed some properties which make them a rich platform to study Bose gases and optical nonlinearities. In this chapter we will introduce another degree of freedom which makes this system even richer: the possibility to manipulate polaritons introducing a lateral confining potential. In particular we will deal with the term  $V_{ext}$  that we introduced in Eq. 1.28. In this chapter and throughout this thesis we will see how the polariton properties described in the previous chapter, combined with a lateral confinement, give rise to a class of new effects.

Two main strategies can be used to create a lateral confining potential, by acting respectively on the polariton photonic component or on the excitonic component. Different techniques have been developed in different groups, following either strategy.

### Excitonic confining potential

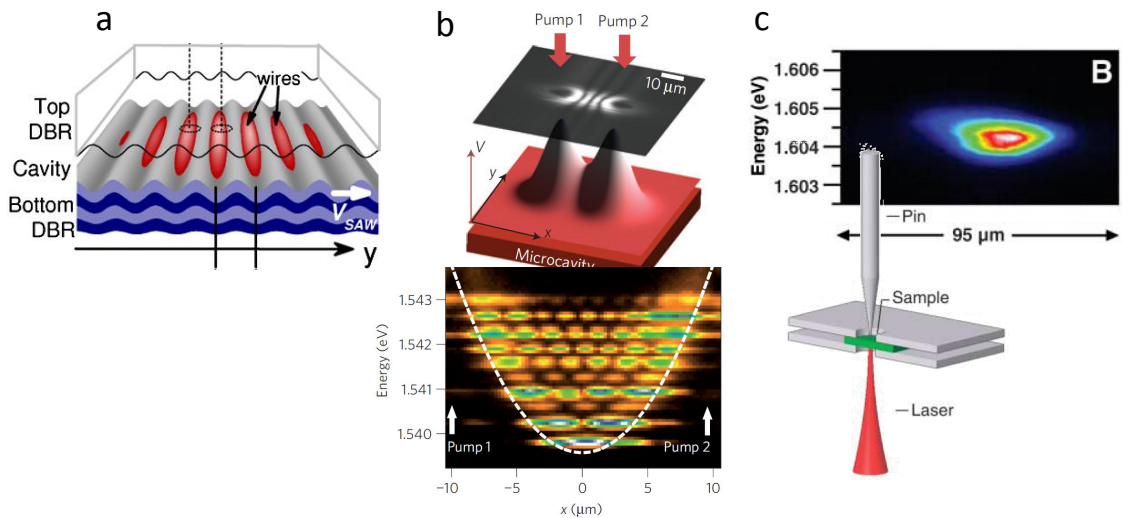


Figure 2.1: Techniques to create an excitonic confining potential. (a) Surface acoustic waves [77]. (b) Optical manipulation [78]. (c) Pressure induced traps [6].

In Fig. 2.1 we report some techniques used to create a potential acting on the excitonic component:

- (a) **Surface acoustic waves.** The technique, developed in the group of P. Santos in Berlin, allows to modulate the exciton energy via a deformation potential produced by the surface acoustic wave strain field (it also affects the photonic component by introducing a change in the thickness and refractive index of the cavity layer). One or two trains of surface acoustic waves can be used to create 1D or 2D lattices. Polariton condensation in a dynamic acoustic lattice has for example been obtained using this technique [77, 79].
- (b) **Optical manipulation.** Optical manipulation has been developed in different groups and uses different strategies [80, 26, 78, 81, 69]. One successful strategy is to create an excitonic potential by using an out-of-resonance pump which induces a local blueshift due to excitons in the excitonic reservoir in correspondence to the pump spot [26, 78]. This technique has been used for example, in the group of J. Baumberg in Cambridge, to create a harmonic oscillator trap for polaritons [78].
- (c) **Pressure induced traps.** The technique, developed in the group of D. Snoke in Pittsburgh, allows to change the exciton energy by using a tip which pushes on the back side of the sample. A local trap in the real-space has for example been realized, forcing polaritons to flow to its minimum. [6].

## Photonic confining potential

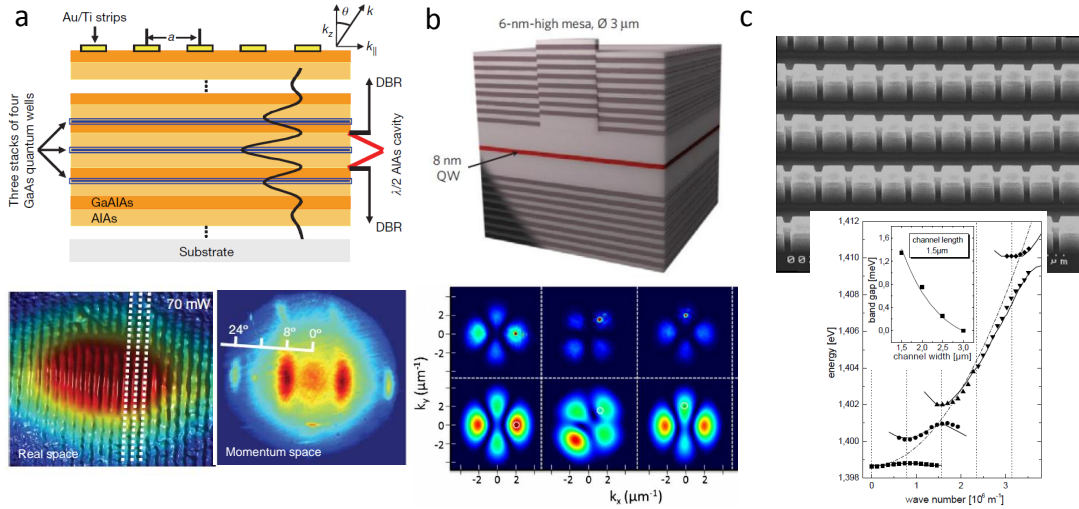


Figure 2.2: Techniques to create a photonic confining potential. (a) Metallic deposition [12]. (b) Etching before top mirror growth [82]. (c) Post growth etching [83].

In Fig. 2.2 we illustrate some techniques used to create a potential acting on the photonic component:

- (a) **Metallic deposition.** This technique, developed in the group of Y. Yamamoto in Stanford, introduces a local change in the dielectric constant of a cavity by depositing a patterned thin metallic layer on top of the sample. 1D and 2D periodic potentials can be obtained [12, 13, 84]. The spontaneous build-up of coherence in an array of polariton condensates (both 0-state and  $\pi$ -state) has for example been observed [12].
- (b) **Etching before top mirror growth.** This technique, developed in the group of B. Deveaud in Lausanne, consists in locally changing the thickness

of the cavity layer, during the growth process. In particular this is done prior to the growth of the top mirror. 0D confining structures (mesas), as the one shown in Fig. 2.2 (b) have been realized [85, 86]. Optical control of the quantized polaritonic modes in a mesa has for example been realized [82].

- (c) **Post growth etching.** This technique consists in the deep etching of the microcavity structure after the growth process, with an etching involving all the layers forming the top mirror, the cavity layer and the lower mirror down to the substrate. This technique is the one used in our group at LPN and we will describe it more in details in the next paragraphs. A similar technique has been implemented also in the group of M. Bayer in Dortmund and A. Forchel in Würzburg [87]. For example, a chain of coupled micronsized cavities has been shown to display crystal band structure [83].

### Etching technique at LPN

Our samples are obtained by a post growth etching of a GaAs based microcavity. First the GaAs based microcavity is grown by molecular beam epitaxy. Then the structure is designed and realized by etching away all the layers constituting the top mirror, the cavity, and the bottom mirror down to the substrate. In particular first electron beam lithography is performed. It involves a photoresist layer spin coated on top of the cavity. The resist is developed by using an electron beam in a pattern corresponding to our desired design. Then reactive ion dry etching allows to etch away all the layers of the microcavity down to the substrate in every shined area, imprinting the desired geometry into the cavity sample.

We would like to mention here the work done by the people involved in the fabrication of our samples. In particular A. Lemaitre and E. Galopin for what concerns the growth of the microcavities and I. Sagnes for the etching procedure. The etching technique developed by I. Sagnes allows to obtain low dimensional structures which preserve the high quality optical properties of the 2D microcavity: high Q, low defects density.

This technique allows to obtain structures with a strong lateral confinement, thanks to the large refractive index difference between air and semiconductor. Moreover it does not impose any restriction on the shape of the structures, except that their lateral dimension should not be too small (typically lateral dimension should be larger than  $1.5 \mu\text{m}$ ) to avoid non-radiative recombinations on the side walls of the etched structures, which would strongly degrade the optical properties of the system. 0D, 1D and patterned 2D structures can be realized with a high degree of freedom in choosing the desired geometry.

### 1D structures: microwires and circuits

As an example of the power of this technique, cavity samples can be processed in the shape of elongated photonic wires [88, 89]. Typically the lateral size  $L_x$  of the wires is of a few microns, while their extension along the (y) direction exceeds a few hundreds of microns. As a result, the  $k_x$  component of the polariton wavevector becomes quantized because of lateral confinement of the photonic mode, while free motion along the (y) direction is preserved. Thus  $k_x = (p_x\pi)/L_x$ , where  $p_x$  is an integer. Moreover, due to the lateral confinement, a splitting develops between the photon mode with linear polarization parallel to the wire (TE) and the photon mode with polarization orthogonal to the wire axis (TM mode polarized along the

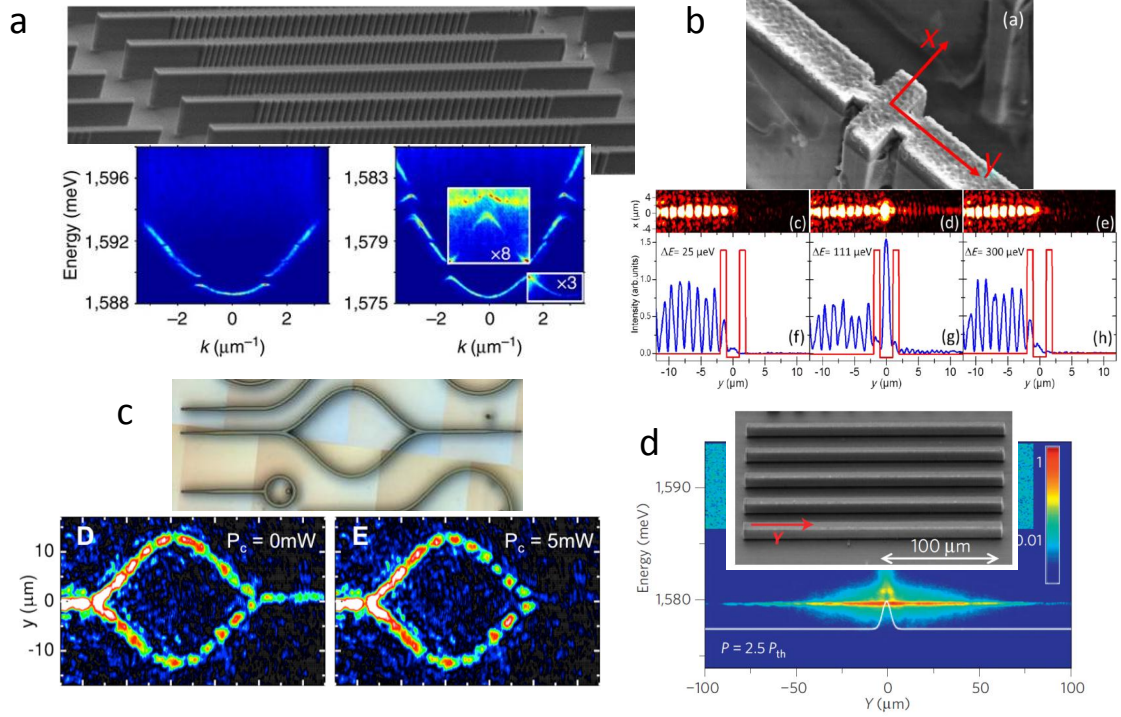


Figure 2.3: Examples of 1D structures processed at LPN. (a) Periodically modulated wires [90]. (b) Resonant tunneling diode [40]. (c) Polaritonic Mach-Zehnder interferometer [39]. (d) Microwires [26].

(x) direction). Thus each subband of given index  $p_x$  is split into two bands, one TE and the other one TM polarized.

In microwires, optical manipulation and coherent propagation of polariton condensates over long distances (full length of the wire,  $\sim 100 \mu\text{m}$ ) has been demonstrated [26] (Fig. 2.3 (d)).

This demonstration has opened the way to the design of more complex structures, with the aim of realizing polaritonic circuits and devices, where polaritons can propagate over long distances in a coherent way and their propagation can be controlled by optical means. In this context, a Mach-Zehnder polariton interferometer [39] (Fig.2.3 (c)) and a double-barrier resonant tunneling diode [40] (Fig.2.3 (b)) have recently been realized. These experiments are among the first realizations of polaritonic devices (polariton transistors have also been recently implemented [41, 42, 43]) and go together with many theoretical works which propose to make use of polaritonic platforms to develop new nonlinear photonic devices [44, 45, 46, 47].

Other kind of effects can be obtained by modulating the lateral size of the wire. An example is shown on Fig. 2.3 (a), where a periodically modulated wire gives rise to bands characterized by the formation of mini-Brillouin zones together with the opening of minigaps. The widths of both the mini-bands and mini-gaps are fully controlled by the geometrical dimensions of the wire. In the nonlinear regime, the formation of gap solitons has recently been observed [90].

## 0D structures: micropillars

The microcavity can be etched also into 0D micropillars, with a typical lateral size of few  $\mu\text{m}$ . Micropillars provide a strong 3D confinement of the optical mode: in the longitudinal direction it is obtained thanks to the Bragg mirrors, in the lateral

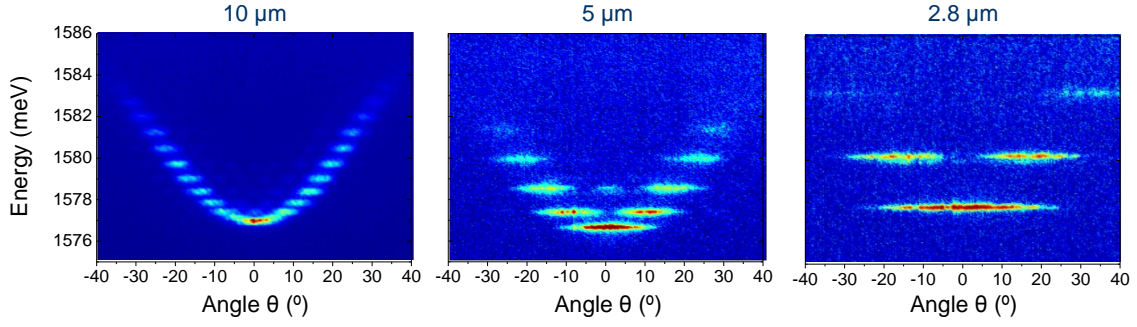


Figure 2.4: Energy spectrum of cylindrical micropillars, for three different pillar diameters: 10  $\mu\text{m}$ , 5  $\mu\text{m}$  and 2.8  $\mu\text{m}$ .

directions thanks to the difference in the refractive index between the semiconductor and air. The 3D confinement of the optical mode results in a full discretization of the polaritonic energy spectrum, since both the in-plane wavevector components  $k_x$  and  $k_y$  are quantized. Figure 2.4 shows the energy spectrum for three different pillar sizes. The energy levels are more separated in energy as we consider pillar of smaller lateral size.

If we consider squared shaped micropillars, the quantization condition has the easy

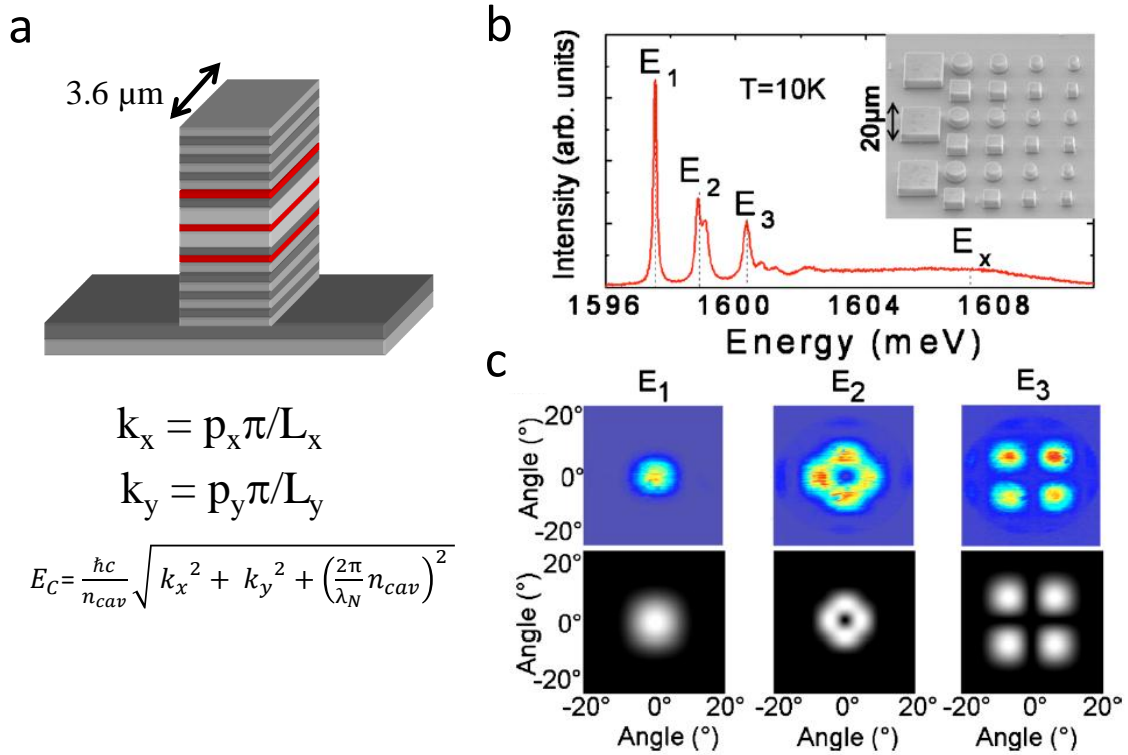


Figure 2.5: (a) Schematic representation of a square pillar and corresponding quantization condition. (b) Experimental spectrum for a pillar with lateral size of 3.6  $\mu\text{m}$ . (c) Intensity profiles of the modes in the  $k$ -space, corresponding to the first three energy levels. Upper panel: experimental data. Lower panel: numerical simulations (taken from [91]).

expression  $k_x = p_x \pi / L_x$ ,  $k_y = p_y \pi / L_y$ , where  $p_x$  and  $p_y$  are integer numbers and  $L_x$  and  $L_y$  are the pillar lateral sizes in the  $x$  and  $y$  directions. The energy of the modes

can be written explicitly

$$E_c = \frac{\hbar c}{n_{cav}} \sqrt{k_x^2 + k_y^2 + \left(\frac{2\pi n_{cav}}{\lambda_N}\right)^2}. \quad (2.1)$$

The experimental energy spectrum for a square pillar with lateral size of  $3.6 \mu\text{m}$  is shown in Fig. 2.5, together with the intensity profile of the modes in the  $k$ -space corresponding to the first three energy levels (taken from [91]). The first energy level  $E_1$  corresponds to one mode with  $p_x = p_y = 0$ , the second energy level  $E_2$  corresponds to four degenerate modes ( $p_x = +1, p_y = 0$ ;  $p_x = -1, p_y = 0$ ;  $p_x = 0, p_y = +1$ ;  $p_x = 0, p_y = -1$ ), the third level  $E_3$  corresponds to four degenerate modes ( $p_x = +1, p_y = -1$ ;  $p_x = +1, p_y = +1$ ;  $p_x = -1, p_y = -1$ ;  $p_x = -1, p_y = +1$ ), as it is clear if we look at the experimental data (upper panel) and numerical simulations (lower panel) in Fig. 2.5 (c).

Polariton condensation has been experimentally demonstrated in micropillars [61] and the effects of interactions with the excitonic reservoir have been shown to strongly affect the spatial distribution of condensates in micropillars with sufficiently large lateral size [92].

In the following chapter we will study the dynamical properties of micropillar polariton condensates, namely the temporal intensity correlation properties ( $g_2(t, \tau)$  function) and the dynamical polarization properties. We provide new indications in the understanding of the temporal correlation properties of polariton condensates, which is still an open question. We provide also a new picture in the understanding of the polarization dynamics of the condensates.

Single pillars can be considered as polaritonic analogues of single atoms. In the same way as for real atoms, we can couple them together to form polaritonic molecules.

### Coupled micropillars: from molecules to 2D lattices

Micropillars are the building blocks for more complex systems made by the coupling of several of them. In particular two or more pillars can be etched one close to the other in order to induce the photonic coupling of the single pillar optical modes. The coupling is determined by the evanescent tail of one single pillar optical mode overlapping with the optical mode of an adjacent pillar.

In most of the situations, as we will see throughout this thesis, we can model our system using a tight-binding approximation, analogously to what is usually done for real molecules. The molecular eigenstates are written as linear superpositions of the single pillar eigenmodes, and the coupling is described in the Hamiltonian through a linear term, with coefficient  $J$ , which couples each pillar with the first neighbours. The coupling coefficient  $J$  describes the strength of the coupling and it is dependent on the parameters of the system (center-to-center distance of the pillars).

Many different molecules can be realized, together with 1D chains and 2D lattices.

The simplest molecule that can be realized is a diatomic molecule (Fig. 2.6 (a)), defined by two micropillars with center-to-center distance smaller than their diameter. The coupling gives rise to molecular modes, which arise from the hybridization of the single pillars modes, delocalized over the entire molecule. Condensation in polariton diatomic molecules has been studied [94] under nonresonant excitation. The condensation process is strongly affected by the interaction with the cloud of uncondensed excitons and thus strongly depends on the exact localization of these excitons within the molecule. This is a result of the high confinement which enhances nonlinearities.

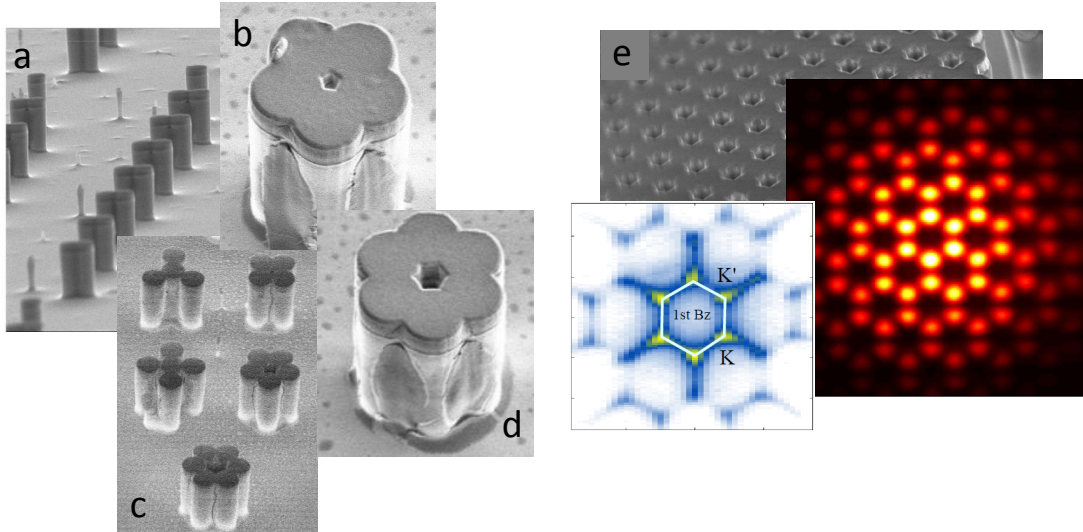


Figure 2.6: Examples of structures made of coupled micropillars processed at LPN. Left side: polaritonic molecules. Right side: honeycomb 2D lattice [93].

Chapter 4 is dedicated to the experimental study of the dynamics of a polariton diatomic molecule under resonant excitation conditions. We will show that a Josephson like physics takes place and that confinement allows to reach strongly nonlinear regimes, in which the dynamics of the system is highly affected by polariton-polariton interactions. This has led to the first observation in a photonic system of the macroscopic self-trapping regime [95].

Chapter 5 is dedicated to the study of a more complex molecule, made of six coupled micropillars in a hexagonal geometry (Fig. 2.6 (d)), constituting a polaritonic analogue of a benzene molecule. We will show that this molecule displays a nontrivial polarization splitting, that can be modeled through the presence of a polarization dependent coupling coefficient  $J$  and an additional on-site splitting. This polarization splitting acts as an effective spin-orbit coupling, which lifts the degeneracy of modes displaying nontrivial polarization patterns. As we will discuss, condensation allows to have access to these modes.

These two experiments, described in Chapter 4 and 5, show the potentiality of these kind of molecular structures. On one hand they give the possibility to study highly nonlinear optical effects, where the nonlinearity is enhanced thanks to the high lateral confinement. On the other hand they allow to study spin-orbit coupling effects. In particular, we will show that spin-orbit coupling arises as an effect of the lateral confinement on polarization and, thus, it can be engineered by choosing the geometry of the system.

These two properties add up with the high freedom in the design of the geometry of the structure and the high scalability, which allows to easily extend the few pillar molecules to 1D chains and 2D lattices.

In this view, a honeycomb lattice has been recently realized in our group [93] (Fig. 2.6 (e)). Dirac cones have been directly observed in the energy spectrum, together with higher energy p orbital bands, one of them with the non-dispersive character of a flat band.



# Chapter 3

## Temporal correlation properties of 0D polariton condensates in micropillars: dynamical $g^{(2)}$ measurements

### 3.1 Introduction

One of the most striking properties of polaritons is their ability to undergo bosonic condensation [4, 60, 6]. Differently from atomic BEC, in which this phase transition occurs at thermal equilibrium [55, 56], polariton condensates are an intrinsically out-of-equilibrium system, in which the condensate population is the result of the dynamical balance between pump and losses. Despite their nonequilibrium nature, polariton condensates share many properties with their atomic counterparts, in particular related to the establishment of temporal and spatial macroscopic coherence. Long-range spatial coherence [5, 6, 7] and increasing of the temporal coherence [8] have, for example, been observed. Despite the fact that many studies have been performed in order to characterize the coherence properties of polariton condensates, there are still many open questions on their specific characteristics in relation not only to atomic condensates, but also to photon lasers, the most common system in which light manifests macroscopic coherence.

In this context a crucial measurement (which has been for example of crucial importance in characterizing the coherence properties of laser light) is the temporal second order correlation function  $g_2(t, \tau)$ . First introduced by Glauber [96], it can be written, in a quantum picture, in the form

$$g_2(t, \tau) = \frac{\langle n(t)n(t + \tau) \rangle}{\langle n(t) \rangle \langle n(t + \tau) \rangle}, \quad (3.1)$$

where  $n(t)$  and  $n(t + \tau)$  are respectively the number of photons arrived at time  $t$  and  $t + \tau$ .  $g_2(t, \tau)$  corresponds to the average number of coincidences of photons arrived at time  $t$  and  $t + \tau$ , normalized by the average number of photons arrived at  $t$  and the average number of photons arrived at  $t + \tau$ , where the average is performed over many independent configurations. The  $g_2$  function gives a measure of the statistical distribution of photons in time. In a classical picture, it gives a measure of temporal intensity fluctuations.

Fig. 3.1 shows the  $g_2(\tau)$  function for three typical examples of photons statistics: a thermal signal (a), a coherent signal (b) and an antibunched signal (c). A ther-

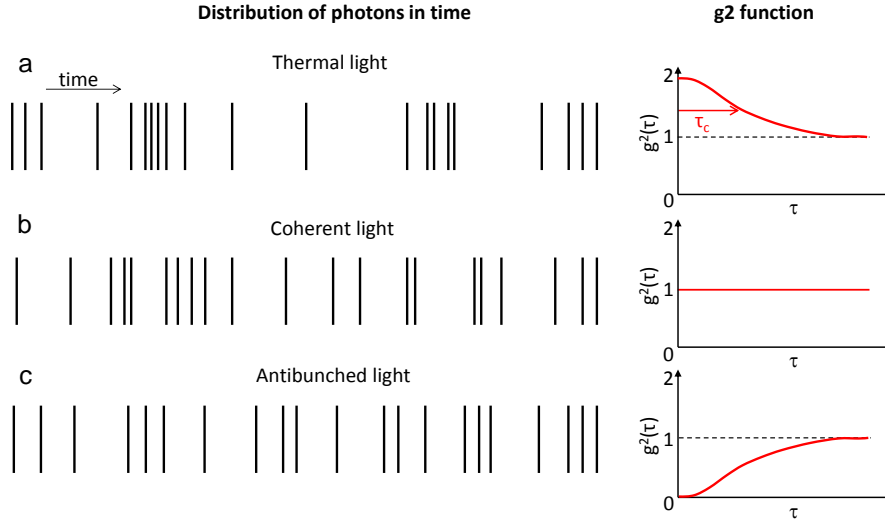


Figure 3.1: Sketch showing three typical examples of photons statistics. (a) Thermal light, characterized by a bunched distribution of photons in time.  $g^2(\tau) = 2$  in  $\tau = 0$  and it decays towards one on a time corresponding to the coherence time  $\tau_c$ . (b) Coherent light, characterized by a random distribution of photons in time.  $g^2(\tau) = 1$  at any  $\tau$ . (c) Antibunched light, characterized by photons which are distributed in time more likely far from each other.  $g^2(\tau)$  takes values below one at  $\tau=0$ .

mal signal (a) is characterized by photons which are more likely emitted in bunches and the  $g^2(\tau)$  function is characterized by a gaussian which has its maximum value  $g^2(\tau = 0) = 2$  in  $\tau = 0$  and decays towards one on a timescale corresponding to the coherence time. A coherent signal, such as the laser emission, is characterized by photons which are distributed randomly in time, and  $g^2(\tau) = 1$  at any  $\tau$ . Another possible signal, which does not have a classical counterpart, is an antibunched signal. It is characterized by photons which are more likely emitted separated in time, like in a single photon source, and the  $g^2$  function is characterized by values below one for times  $\tau$  close to 0.

The temporal  $g^2$  function of polariton condensates has been studied both theoretically [97, 98, 99, 100] and experimentally [60, 5, 8, 101]. It has been predicted in particular that the threshold for polariton condensation should correspond to a transition of the  $g^2$  function from a thermal one, with  $g^2(\tau = 0) = 2$  to a coherent one,  $g^2(\tau = 0) = 1$ , i.e. the same behaviour characterizing the photon laser threshold. Some theoretical works [99, 100] have predicted that well above the polariton laser threshold, polariton-polariton interactions could introduce some decoherence in the system, leading to an increase of the  $g^2(\tau = 0)$  above one. This behaviour would be a signature of the polariton laser in which, differently from the photon laser, the coherence could be affected by interactions in the system. Anyway, the presence and magnitude of such a decoherence effect seems not to be a general signature and it seems to be related to the characteristics of the specific system. Also from an experimental point of view, the results are contradictory [60, 5, 8, 101] and they all suffer from the same crucial drawback: the very low resolution time of the detectors used in the measurements compared to the polariton lifetime (few ps). In fact the mentioned works report  $g^2$  measurements using a classical Hanbury Brown-Twiss setup [102], mainly consisting of a 50/50 beam splitter and two single-photon counters, whose best temporal resolution is  $\sim 50$  ps. The detector time resolution is higher than the typical polariton lifetimes, and affects strongly the  $g^2$  measurements, giving rise to variations in the  $g^2$  functions that never exceed

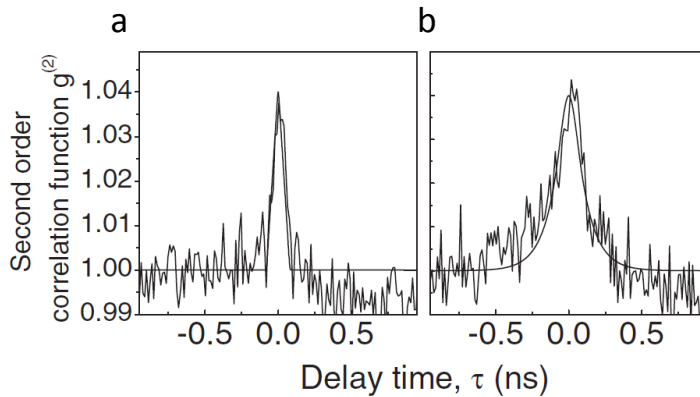


Figure 3.2: Measured second order correlation function  $g_2(\tau)$  of a polariton condensate in a CdTe microcavity, performed with a Hanbury Brown and Twiss setup (taken from [8]), (a) below threshold (b) above threshold. In both cases the  $g_2$  function exceeds only slightly one at  $\tau = 0$ . This is related to the resolution time of the HBT setup,  $\sim 40$  ps in this case, much higher than the typical time scales involved in the polariton dynamics.

substantially the value of one, as shown in Fig. 3.2. Therefore in the experiments the real value of the  $g_2$  is usually found not by a direct measurement but by an a posteriori reconstruction. An accurate measurement and a complete understanding of the  $g_2$  function of a polariton condensate is still an open problem.

A remarkable characteristics of polariton condensates, related to their out-of-equilibrium nature, is that the temporal dynamics of the system can be easily detected, analyzing photons emitted at each time out of the cavity. The typical timescales of this dynamics allow in particular to study the transient time during which the condensate is formed and study how coherence is built. This dynamics is not easily detectable in atomic BEC, due to the very short timescales in which cold atoms reach thermal equilibrium. To this end, different experiments have been performed in a pulsed configuration by means of streak camera measurements (time resolution of few ps). They have shown in particular the spontaneous build-up of linear polarization of the condensate [9, 10] and of first order spatial coherence [11].

More recently a new technique has been implemented by the group of M. Bayer in Dortmund, which allows to reconstruct the temporal  $g_2(t, \tau)$  function with a time resolution of few ps, by means of a streak camera operating in the single shot regime [104, 105]. This technique on one hand overcomes the temporal resolution limit of the HBT setups usually used for the temporal  $g_2(t, \tau)$  measurements, on the other hand it allows to have access to the temporal dynamics of the  $g_2(t, \tau)$  function (i.e. how the  $g_2(t, \tau)$  function evolves during the temporal evolution of the system).

This technique has been already used to measure directly second and higher order photon correlations in a micropillar laser with semiconductor quantum dots as active material [104] and higher-order photon bunching in a semiconductor microcavity [105]. The same technique has been used very recently to study the power dependence of the  $g_2(t, \tau = 0)$  function, averaged over all times  $t$ , in a GaAs semiconductor microcavity [103, 106].

In [103], the authors observe a two-threshold behaviour in the intensity vs excitation power curve (shown in Fig. 3.3 (a)). They associate the first threshold to the onset of polariton laser and the second to the transition towards photon laser. They measure a corresponding  $g_2(\tau = 0)$  that decreases from a value of  $\sim 1.8$  to

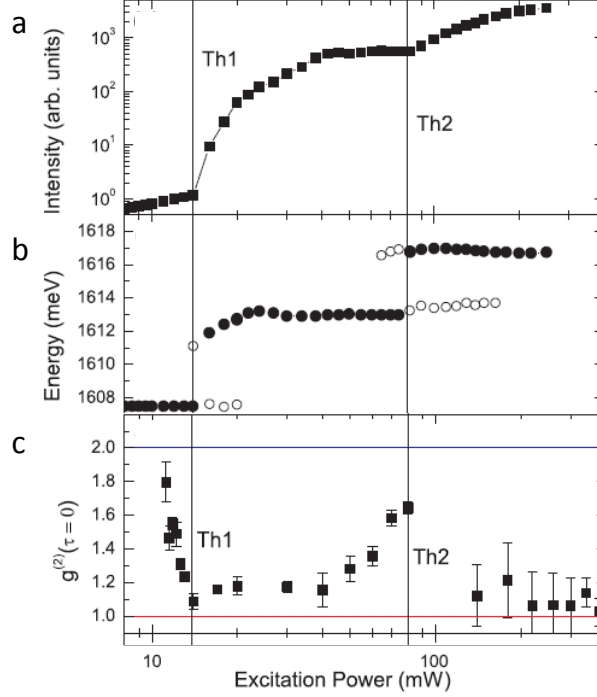


Figure 3.3: Measured second order correlation function  $g_2(\tau = 0)$  in a GaAs microcavity, experiment performed with a streak camera working in the single shot regime. The microcavity is pumped out-of-resonance at increasingly excitation powers (taken from [103]). (a) Measured emitted intensity vs excitation power, displaying a two-threshold behaviour. The authors associate the first threshold to the onset of polariton laser, the second to the onset of photon laser. (b) Energy vs excitation power dependence, showing two abrupt jumps in correspondence to both the thresholds. (c) Measured  $g_2(\tau = 0)$ , which is shown to drop towards one in correspondence to both the thresholds.

$\sim 1$  corresponding to the first threshold. The successive increase of  $g_2(\tau = 0)$  with excitation power is associated to polariton-polariton repulsive interactions, which introduce decoherence in the system [100]. The second threshold is characterized by a new drop of  $g_2(\tau = 0)$  to values close to one. However, a careful analysis of the curve showing the energy vs excitation power dependence, shown in Fig. 3.3 (b), seems not to be compatible with the picture given by the authors. In correspondence to both thresholds, two clear jumps in the emission energy are visible. Such a jump is expected in correspondence of the photon laser threshold at weak coupling, which is characterized by the polariton mode suddenly switching to the cavity mode. This is not what we expect when crossing the polariton laser threshold, in which the emission energy should constantly increase with excitation power, due to increasing polariton-polariton and polariton-exciton interactions. It is possible that the two-threshold behaviour could be related to photon laser mode competition inside the cavity, i.e. it is possible that the first threshold corresponds to a first photon laser threshold, while the second corresponds to a threshold in which the system lases on another mode.

In this chapter, we will experimentally study the  $g_2(t, \tau)$  characteristic of a polariton condensate in a single micropillar. In order to do so, we have implemented the same technique as the one introduced by the group of M. Bayer. In a micropillar, thanks to the 3D confinement of the optical modes, different modes are well separated in

energy (especially for pillars of small diameter). Therefore the problem of mode competition could be easily identified. Moreover the high Q microcavities with large Rabi splitting used in this work allow a clear discrimination of the polariton laser threshold from the photon laser threshold [61].

### 3.2 Our system: polaritons in micropillars

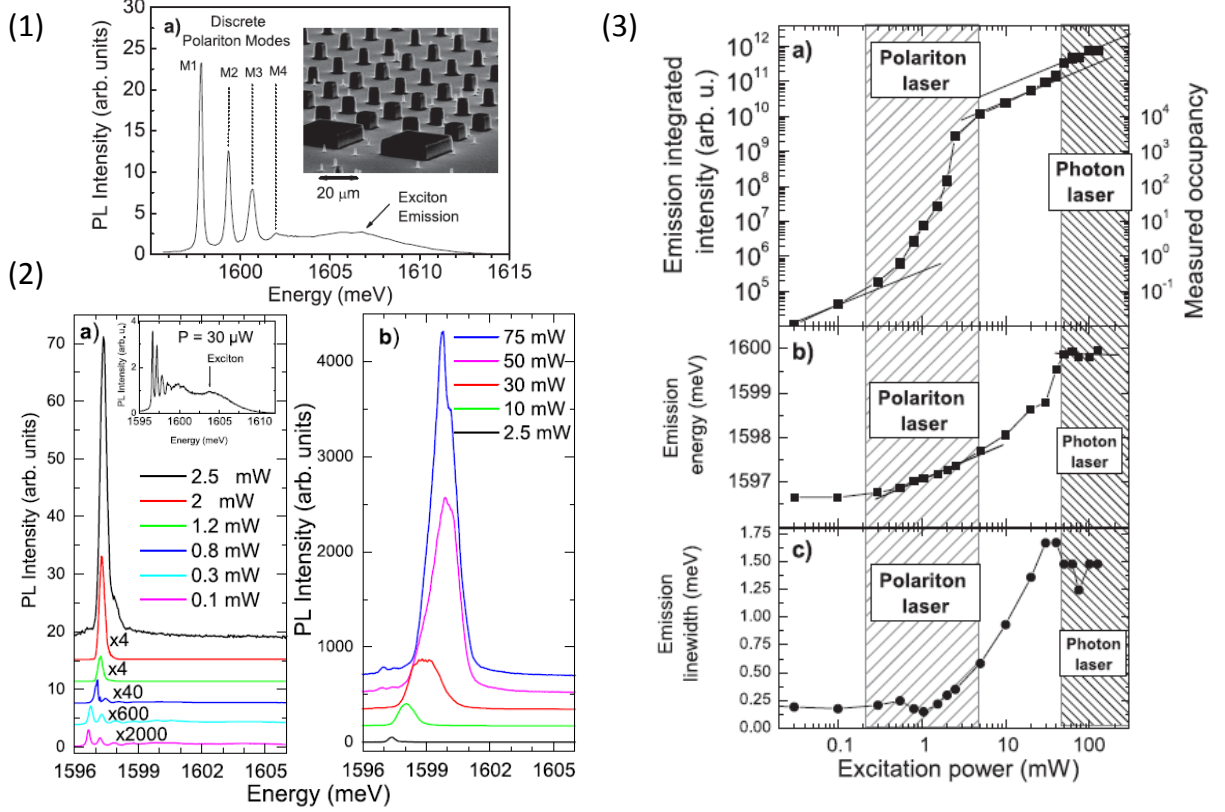


Figure 3.4: Experimental demonstration of polariton laser in a GaAs micropillar (taken from [61]). (1) Low power excitation spectrum showing the micropillar quantized energy levels. The inset shows a scanning electron micrography of a micropillar array. (2) Emission spectra measured for increasing excitation powers. (a) Corresponds to the polariton lasing regime, (b) corresponds to the loss of the strong coupling regime and the onset of photon lasing. (3)(a) Integrated intensity and measured occupancy, (3)(b) emission energy and (3)(c) emission linewidth measured on the lowest energy emission line as a function of the excitation power; dashed areas highlight the excitation range for polariton lasing or photon lasing.

Our system is a semiconductor cylindrical micropillar as those shown in the inset of Fig. 3.4 (1). 3D confinement of the optical modes is provided, in the longitudinal direction, by the Bragg mirrors, while in the transverse directions it is obtained through the refractive index difference between GaAs and air. The 3D confinement gives rise to the quantization of the polaritonic modes, with energy levels which are more and more separated in energy as we reduce the micropillar lateral size. An example of the spectrum for a 4 μm pillar is shown in Fig. 3.4 (1), together with the scanning electron micrography of a micropillar array.

In GaAs micropillars, polariton condensation has been demonstrated in [61], as shown in Fig. 3.4 (2) and (3). In the experiment reported in that work, the micropillar is excited out-of-resonance with a CW pumping laser at increasing excita-

tion powers, and photoluminescence from the pillar is analyzed both in intensity and energy. The emitted intensity vs power is reported in Fig. 3.4 (3a) and it displays a two-threshold behaviour, in which the emission intensity becomes highly nonlinear. The first threshold corresponds to the onset of polariton laser, in which stimulated relaxation towards to ground state takes place. Across the threshold, a soft continuous blueshift of the energy of that level is observed (Fig. 3.4 (3b)) with increasing pumping power. This blueshift originates from the repulsive interactions between condensate polaritons and reservoir excitons. The second threshold corresponds to the onset of photon laser, in which the high density of injected carriers screens the excitonic resonance and the strong coupling is lost. The photon laser threshold corresponds to the emitted intensity vs power dependence becoming nonlinear again, and to a jump in the energy of the level: at the photon laser threshold, the system jumps from the polaritonic mode to a bare cavity mode (higher in energy).

In GaAs micropillars polariton condensation has been studied and clear signatures for polariton laser threshold and photon laser threshold have been identified. It is therefore a suitable system in which  $g^2(t, \tau)$  measurements can be performed and provide information on the coherence characteristics when crossing the two thresholds.

In this chapter we will experimentally study the intensity correlations in the emission of a polariton condensate in a micropillar. We will implement and use a streak camera based technique that allows measuring  $g^2(t, \tau)$  with a time resolution of  $\sim 4$  ps.

### 3.3 Experimental setup: single shot streak camera measurements

#### 3.3.1 Experimental setup

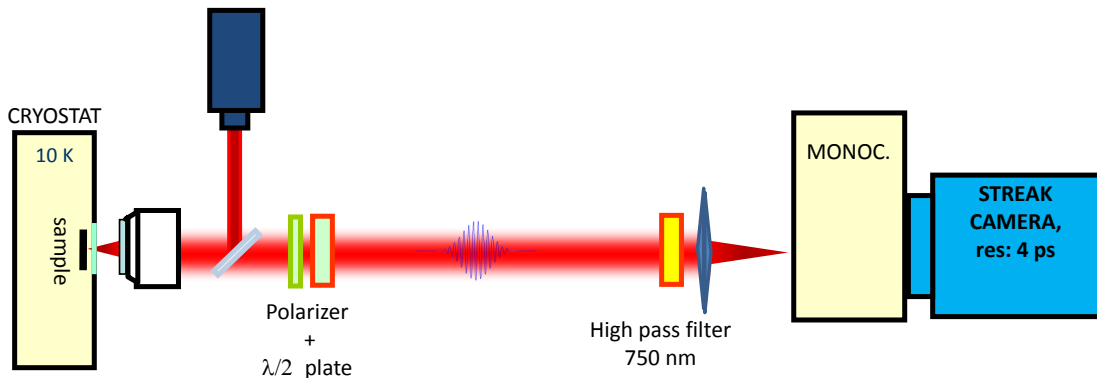


Figure 3.5: Experimental setup.

The micropillar is etched out of a planar microcavity, which is grown by molecular beam epitaxy and it is made out of Bragg reflectors with 28 and 40 pairs of alternating  $\text{Al}_{0.95}\text{Ga}_{0.05}\text{As}/\text{Al}_{0.20}\text{Ga}_{0.80}\text{As}$   $\lambda/4$  layers that define a  $\lambda/2$  cavity. Three sets of four GaAs quantum wells of  $70 \text{ \AA}$  in width are distributed at the three central maxima of the confined electromagnetic field. The coupling between the quantum well 1s excitons and the fundamental longitudinal cavity mode results in a Rabi splitting of  $15 \text{ meV}$  at  $10\text{K}$ . The measured polariton lifetime is  $\sim 50 \text{ ps}$  at zero photon-exciton

detuning (see Section 5.4).

The experimental setup is shown in Fig. 3.5. We excite the micropillar with a 1.7 ps pulsed laser at 735 nm, at the first reflectivity minimum of the stop band defined by the Bragg mirrors. The sample is kept inside a cryostat cooled down to 10K. The laser is well out-of-resonance with respect to the polaritonic modes, which are at  $\sim 780$  nm. An objective focuses the excitation laser on the sample to a spot which fully and symmetrically covers the pillar (few microns in diameter). The micropillar photoluminescence is collected back through the same objective and focused on the entrance slit of a spectrometer coupled to a streak camera. Two high pass interferential filters with cut-off wavelength 750 nm are placed before the spectrometer entrance slit, in order to filter out the residual excitation signal from the photoluminescence signal. By putting a half-waveplate followed by a polarizing cube on the detection line, we can filter the photoluminescence signal in its linear polarization components.

Our setup allows to resolve the temporal dynamics of the photoluminescence signal with a time resolution of 4 ps. In particular, it allows simultaneous energy and time resolved measurements.

### 3.3.2 Single shot streak camera measurements

In order to perform the  $g^2(t, \tau)$  measurement, the streak camera operates in the single shot regime, by means of the dual base configuration sketched in Fig. 3.6. First the photoluminescence signal is focused on the photocathode, where photons are converted into electrons. Electrons are accelerated and then deflected by two couples of sweep electrodes. A fast sweep voltage is applied in the vertical direction, synchronized with our 1.7 ps pump laser, with a repetition rate of  $\sim 80$  MHz (synchroscan mode). In particular the vertical sweep is synchronized with our photoluminescence signal, since the photoluminescence emission is also triggered by the excitation laser. The vertical voltage deflects the signal on the y axis, separating spatially, along the y coordinate, photons which arrive at different times on the photocathode. In the dual base configuration, an additional sweep voltage is applied in the horizontal direction, much slower than the vertical one. This voltage induces a small horizontal deflection which allows the spatial separation, on the x coordinate, of successive pulses. In this way each vertical streak carries information related just to one single pulse. Once passed the deflecting electrodes, electrons are multiplied in a multichannel plate, which enhances the signal introducing some gain. Then they are reconverted into photons thanks to a phosphor screen and they are recorded by means of a cooled CCD camera, whose acquisition is synchronized with the horizontal sweep and whose maximum rate is 150 Hz. The repetition rate is limited by the phosphor screen remanescence: in order to avoid cross talking between different CCD shots, we need to wait for the complete de-excitation of the phosphor screen before registering the next shot. The phosphor has an emission lifetime of  $\sim 7$  ms, giving a maximum repetition rate of  $\sim 150$  Hz.

Five different time ranges can be chosen, corresponding to different speeds for the vertical sweep. Each time range corresponds to a different time window and therefore to a different time resolution, the best time resolution being  $\sim 4$  ps (TR2, vertical window  $\sim 145$  ps). In the same way, different Blanking Amplitudes can be chosen corresponding to different speeds for the horizontal sweep. The choice of a particular Blanking Amplitude determines the number of pulses we can see in a sin-

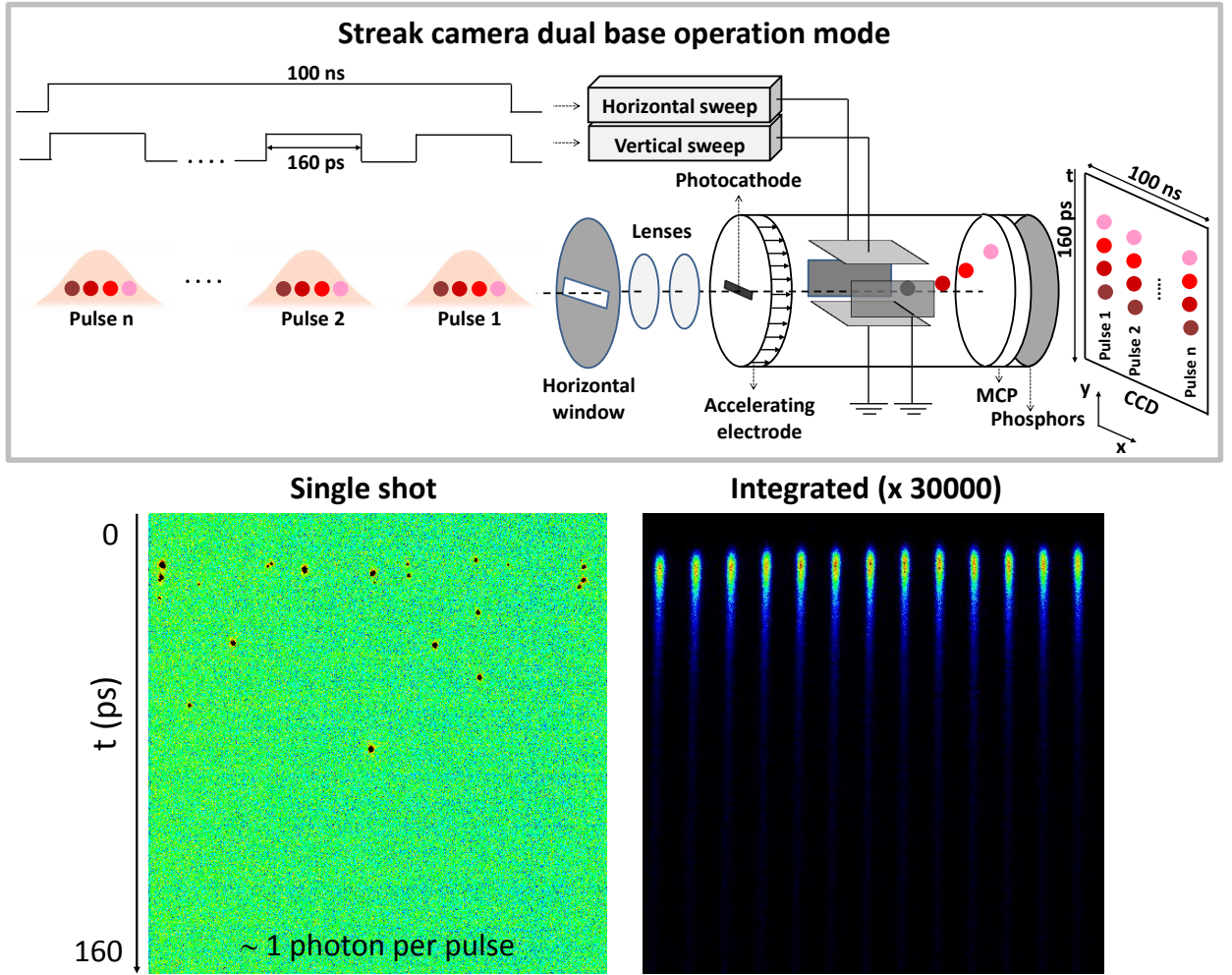


Figure 3.6: Upper panel: sketch showing the operating principle of a streak camera working in the dual base configuration. Lower panel: typical single shot image (left) and corresponding image integrated over 30000 frames (right). In the single shot image each spot corresponds to one photon.

gle acquisition. The Blanking Amplitudes is chosen in order to have the maximum number of distinguishable pulses in a single acquisition. The horizontal sweep is also synchronized with the laser pulse repetition frequency, such that in every frame the individual pulses always fall in the same region of the CCD.

A typical single shot measurement is shown in Fig. 3.6 (left side), each dark spot corresponding to one photon. The corresponding integrated measurement, integration done over 30000 frames, is shown on the right side. In the single shot image we do not have access to the temporal profile of the emission, since the single shot signal has, on average, only few photons per pulse. It is as we integrate over many single shot acquisitions, that we have access to the pulse profiles and temporal dynamics.

The dual base operation mode allows to have direct access to the position in time of photons emitted within a single pulse. The reconstruction of the  $g_2(t, \tau)$  function is based on counting coincidences of photons within a single pulse and then doing an ensemble average over many pulses. To this purpose, the streak camera photon counting operation mode provides an efficient algorithm which allows to record many tracks of photons with low memory consumption. The photon counting operation mode is based on the definition of an intensity threshold, which is found through

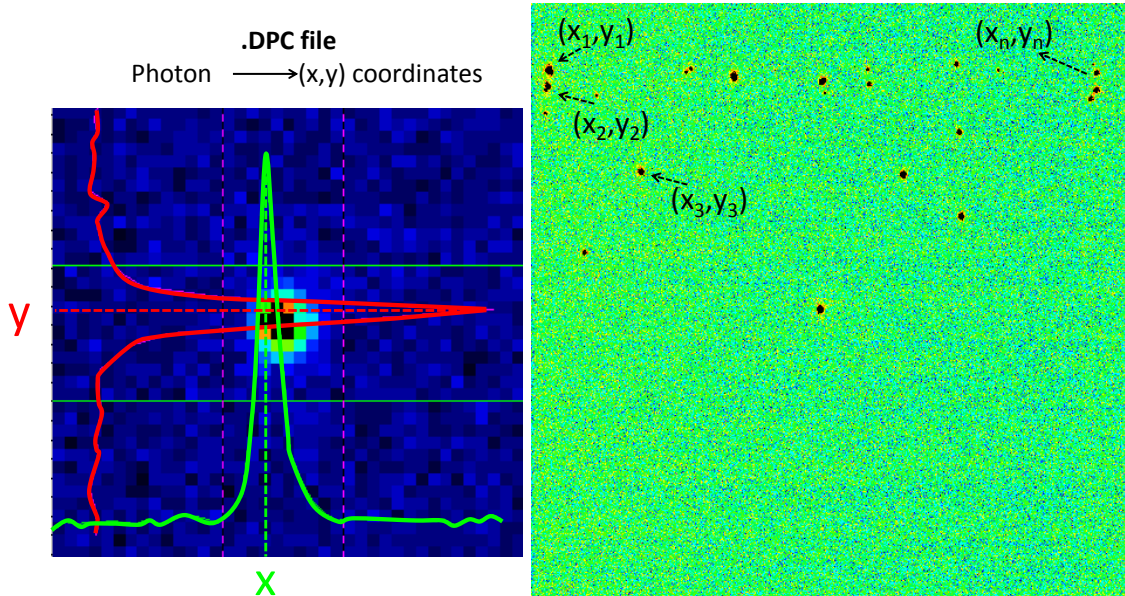


Figure 3.7: Schematic representation of the streak camera algorithm which allows to record the temporal track of photons in a dynamic photon counting (.dpc) format. Each signal whose intensity exceeds a certain threshold is considered as a photon. For each photon the center of gravity is found and a couple of coordinates  $(x,y)$  are assigned. The resulting .dpc file contains the coordinates  $(x,y)$  of all the photons arrived, divided frame by frame.

a noise measurement (measurement without signal), in order to discriminate signal from dark count noise. If we consider the single shot image of Fig. 3.6, the threshold discriminates the spots corresponding to real photons from those corresponding to noise. The signals whose intensity exceeds the threshold are considered as real photons. For each of these photons, an algorithm calculates the center of mass of the signal, as shown in Fig. 3.7, and the corresponding coordinates  $(x,y)$  are registered. The resulting .dpc (dynamic photon counting) file, is a two column matrix which contains the coordinates  $(x,y)$  of each photon, classified by frame (shot).

### 3.4 Data analysis: software g2

As mentioned in the introduction of this chapter, the  $g2(t,\tau)$  function is defined in the following way

$$g2(t,\tau) = \frac{\langle n(t)n(t+\tau) \rangle}{\langle n(t) \rangle \langle n(t+\tau) \rangle} \quad (3.2)$$

and corresponds to the average number of coincidences of photons arrived at time  $t$  and  $t+\tau$  (i.e. first photon arrived in  $t$ , second in  $t+\tau$ ), divided by the average number of photons arrived in  $t$  and the average number of photons arrived in  $t+\tau$ . The average is performed over many independent configurations.

Following the technique proposed by the group of M. Bayer [104, 105], we implemented in our laboratory a software which allows to reconstruct the  $g2(t,\tau)$  function starting from the raw .dpc streak camera data. Figure 3.8 shows a schematic representation of the technique. The .dpc file contains the  $(x,y)$  coordinates of photons divided frame by frame, which we can represent on a 2D matrix, as shown in Fig. 3.8 (a), for a single frame. Each point corresponds to one photon. Figure 3.8 (b) is obtained if we plot all the acquired frames together. From the integrated image we can define the area of arrival of emitted photons corresponding to a single pulse, and

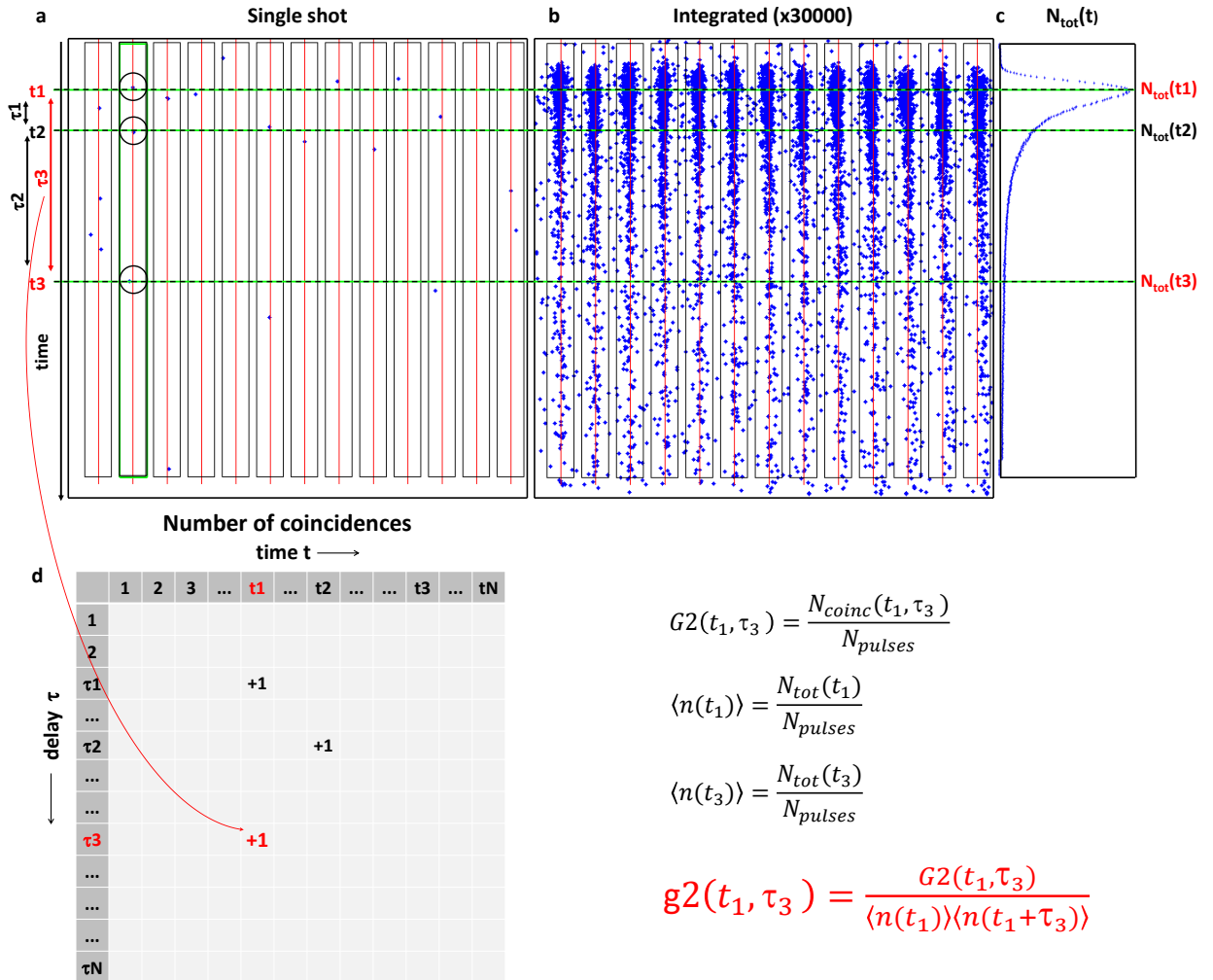


Figure 3.8: Schematic representation of the working principle of our software, which allows to reconstruct the  $g2(t, \tau)$  function starting from the raw streak camera data. (a) and (b) are the reconstructed single shot and integrated images, in which each point represents one photon. From the integrated image we define the area corresponding to one single pulse, indicated by rectangles in (a) and (b). Within each rectangle we count the coincidences. This is shown explicitly for the second pulse: for each photon arrived at a certain  $t$ , we consider all the photons arrived after a certain delay  $\tau$ , and we fill the matrix (d) containing the number of coincidences. This procedure is repeated for every pulse and every frame. The total number of coincidences is then renormalized by the total number of photons arrived in  $t$  and  $t+\tau$ , shown in (c). As an example, the explicit expression of  $g2(t, \tau)$  is written for a particular choice  $t = t_1$  and  $\tau = \tau_3$ .

define for each pulse the corresponding rectangle, as shown in Fig. 3.8 (a) and (b). In each frame, each rectangle is considered as an independent configuration. The y coordinate corresponds to the time coordinate. Within a rectangle, two photons with the same y coordinate and different x coordinates, are considered as simultaneous events. Within each rectangle, we count the coincidences, for each arrival time  $t$  of the first photon and for each delay  $\tau$  between the first and the following photons. As an example, if we consider the second pulse in Fig. 3.8 (a), we count the three coincidences  $(t_1, \tau_1)$ ,  $(t_1, \tau_2)$  and  $(t_2, \tau_3)$ , as sketched in Fig. 3.8 (d). We repeat the same procedure for all the rectangles and all the frames, therefore obtaining a matrix containing all the coincidences. If we divide this matrix by the total number of independent configurations (total number of pulses, 13 pulses per frame multiplied

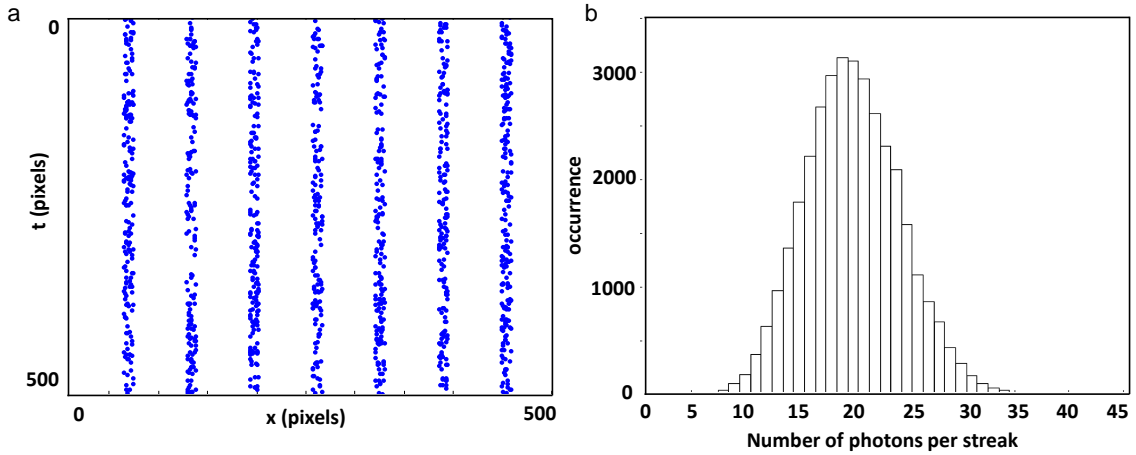


Figure 3.9: (a) Simulated CW coherent signal: photons are distributed randomly in time (image integrated over few frames). (b) Occurrence of a fixed number of photons in a streak, showing the poissonian distribution (centered on the mean value of photons, 20 in this case) typical of a coherent signal.

by 30000 frames in the example of Fig. 3.8), we obtain the numerator of Eq. 3.2 which is commonly called  $G2(t, \tau)$ . The  $g2(t, \tau)$  function is found by normalizing  $G2(t, \tau)$ , i.e.

$$g2(t, \tau) = \frac{G2(t, \tau)}{\langle n(t) \rangle \langle n(t + \tau) \rangle}, \quad (3.3)$$

where  $\langle n(t) \rangle$  and  $\langle n(t + \tau) \rangle$  correspond respectively to the average number of photons arrived at time  $t$  and at time  $t + \tau$ . We find the total number of photons arrived at time  $t$  and at time  $t + \tau$  by considering the sum of all the independent configurations, as shown in Fig. 3.8 (c), and then dividing by the number of independent configurations.

The resulting  $g2(t, \tau)$  is the time dependent second order correlation function.

## 3.5 Test of the software with artificial signals

### CW coherent artificial signal

As a test for the  $g2$  software, we simulated numerically a CW coherent signal. The artificial signal is simply characterized by a random distribution of photons in time. In order to perform the most meaningful test, we create a matrix with the same structure as the .dpc file generated by the streak camera, as the one shown in Fig. 3.8 (b). The random arrival of photons in time is generated using the random routine of Matlab. Since the artificial signal is a CW signal, the integrated image will be characterized by streaks with constant average intensity in time, as shown in Fig. 3.9 (a). In our artificial signal we do not fix the total number of photons per streak, but the mean number of photons.

If we plot the occurrence of a fixed number of photons in a streak we find a poissonian distribution centered on the mean number of photons, as shown in Fig. 3.9 (b), as we expect for a coherent signal.

We calculate  $g2$  with our software. In Fig. 3.10 (a) it is shown the total number of photons  $N_{tot}$  vs time, found by adding up all the independent streaks. As expected  $N_{tot}$  is in average constant in time. Fig. 3.10 (b) shows the calculated  $g2(t = 10, \tau)$ , which gives the probability to find a photon at a certain delay  $\tau$ , if a photon was recorded at  $t = 10$ . The calculated  $g2$  function is in average around one for every

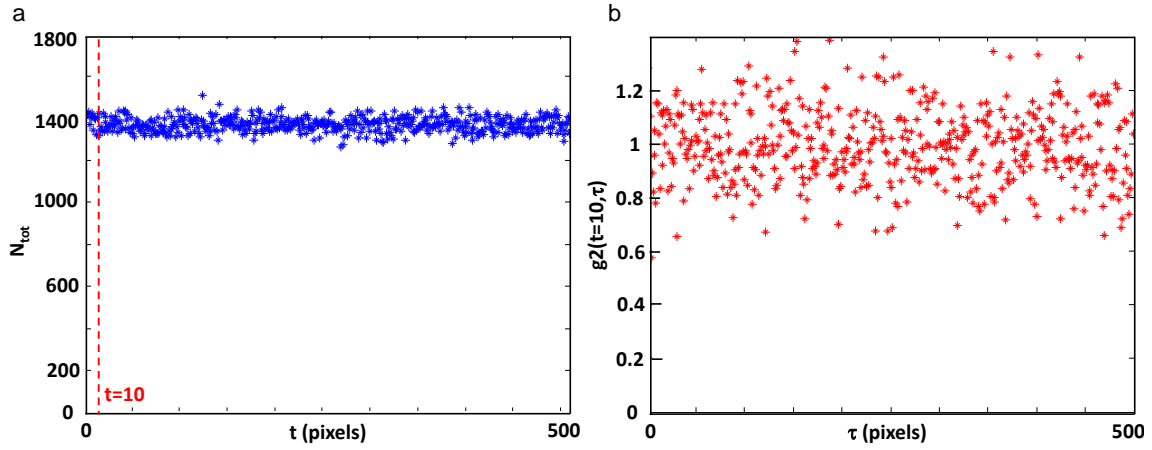


Figure 3.10: Simulated CW coherent signal. (a) Total number of photons vs time. (b)  $g_2(t, \tau)$  calculated from the starting time  $t = 10$  pixels.  $g_2(t, \tau)$  is centered around one at any  $\tau$ , as expected for a coherent signal. Fluctuations around this value are quite big, of the order of 20%.

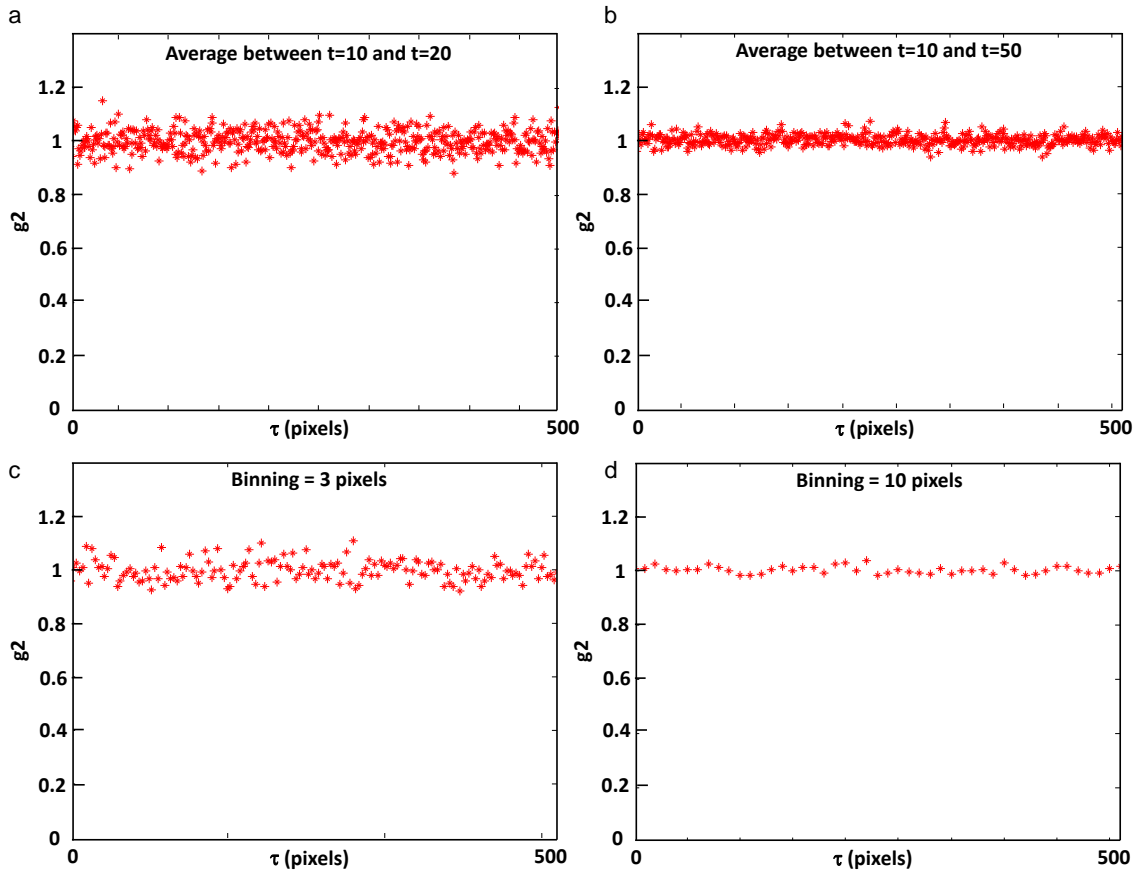


Figure 3.11: Simulated CW coherent signal. Two ways of improving the statistics, without increasing the number of independent configurations constituting the statistical ensemble: (a), (b) weighted average of the  $g_2(t, \tau)$  over a time interval; (c), (d) time binning.

$\tau$ , as we expect for a coherent signal. Despite that, we remark that fluctuations around this value are quite big. In order to improve the result, we should increase the statistical sample, i.e. increasing the total number of independent configurations. On the other hand, for a given number of independent configurations, we have two ways to improve the statistics. One way is to define a time binning: we define an

interval of time, for example 3 pixels, and we consider that all the photons arrived within this interval are simultaneous. It is meaningful to define a time binning, since the streak camera resolution is limited to  $\sim 10$  pixels and therefore it is not meaningful to discriminate photons arrived within such interval.

The other way is to do a weighted average of  $g_2(t, \tau)$  over a time window. This procedure is meaningful every time we suppose photons to have the same statistics within the chosen time window. In case the photons statistics changes within the time window, the average process would wash out the  $g_2$  features.

Fig. 3.11 shows the results after application of the two methods on our artificial signal. We see that fluctuations around the mean value reduce as we perform the time binning (Fig. 3.11 (c) and (d)) and the weighted average (Fig. 3.11 (a) and (b)).

### Pulsed coherent artificial signal

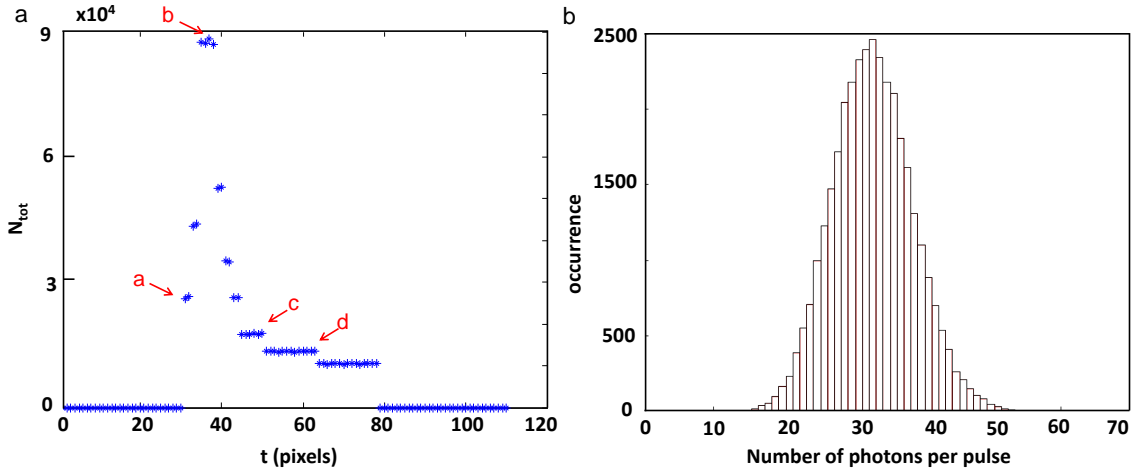


Figure 3.12: Simulated pulsed coherent signal. (a) Total number of photons vs time. (b) Occurrence of a fixed number of photons in a pulse, showing the poissonian distribution typical of a coherent signal.

Since we will mostly work with pulsed signals, we test the software with a pulsed coherent artificial signal. Similarly to the CW case, we define a random distribution of photons in time but differently from before, the average number of photons is not constant along the  $y$  time window (i.e. we create an average photon distribution similar to that shown in Fig. 3.8 (b)). The integrated signal is shown in Fig. 3.12 (a). Fig. 3.12 (b) shows the statistics of the number of photons per pulse, which is poissonian as expected for a coherent signal. Figure 3.13 shows the calculated  $g_2(t, \tau)$  for four different fixed times  $t$  along the pulse. We observe that, as expected,  $g_2(t, \tau) = 1$  at any  $\tau$  for each considered time  $t$ .

This result tells us that the normalization process we defined in Section 3.4 is well performed and that there are not effects on the calculated  $g_2(t, \tau)$  function related to the temporal dynamics of the signal, only to the statistics of the emission.

We remark that the fact that the  $g_2(t, \tau)$  drops to zero at a certain  $\tau$  does not have any physical meaning and it is just related to the fact that we consider a signal which has a finite duration in time. In the software,  $g_2(t, \tau)$  is set by default equal to zero any time that the intensity of the signal drops to zero.

More tests with artificial signals are reported in the appendix of this chapter.

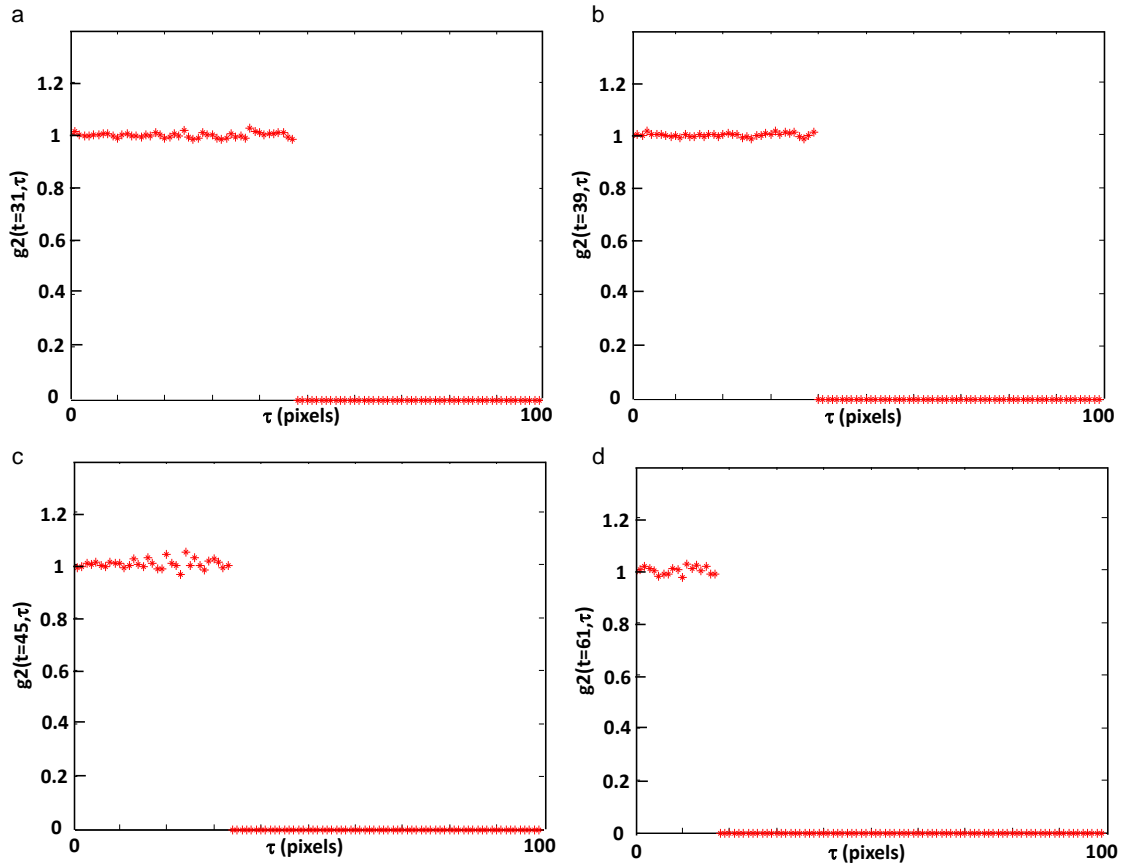


Figure 3.13: Simulated pulsed coherent signal. Calculated  $g_2(t, \tau)$  function, corresponding to four different starting times along the pulse: (a)  $t = 31$ , (b)  $t = 39$ , (c)  $t = 45$ , (d)  $t = 61$ . The fact that the  $g_2(t, \tau)$  drops to zero at a certain  $\tau$  is just related to the fact that we consider a signal which has a finite duration in time.

### 3.6 Test of the software with HeNe laser

As a second step, we test the software with a real signal. We use a CW HeNe laser which provides a real CW coherent signal (in principle analogous to the CW signal defined in Section 3.5). Fig. 3.14 shows a typical single shot image (a) and the corresponding integrated image (b), taken directly from the streak camera software. Fig. 3.15 (a) corresponds to a reconstruction of Fig. 3.14 (b), after data analysis with our software. The total number of photons detected vs time is shown in Fig. 3.15 (b), and we see that it is almost constant in time. The slight variation is due to the position dependent gain in the multichannel plate. This is not an issue, since the renormalization procedure described in Section 3.4, results in an extracted  $g_2(t, \tau)$  function which is not dependent on global variations in the intensity of the signal (i.e. variations in the global temporal profile, which affect in the same way each single shot measurement). For the same reason, the procedure can be safely used for pulsed signals, as the artificial signal described in the previous section.

The results of the  $g_2$  calculations are shown in Fig. 3.16 for two different laser powers. Fig. 3.16 (a) corresponds to a signal with an average of  $\sim 7$  photons per streak, while Fig. 3.16 (c) corresponds to a case with  $\sim 1$  photon per streak. We observe that in both cases the signal is well centered around one for every  $\tau$ , as expected for a coherent signal. In Fig. 3.16 (a) the fluctuations around one are smaller if compared to Fig. 3.16 (c), because the total number of photons is higher and therefore the statistics is better.

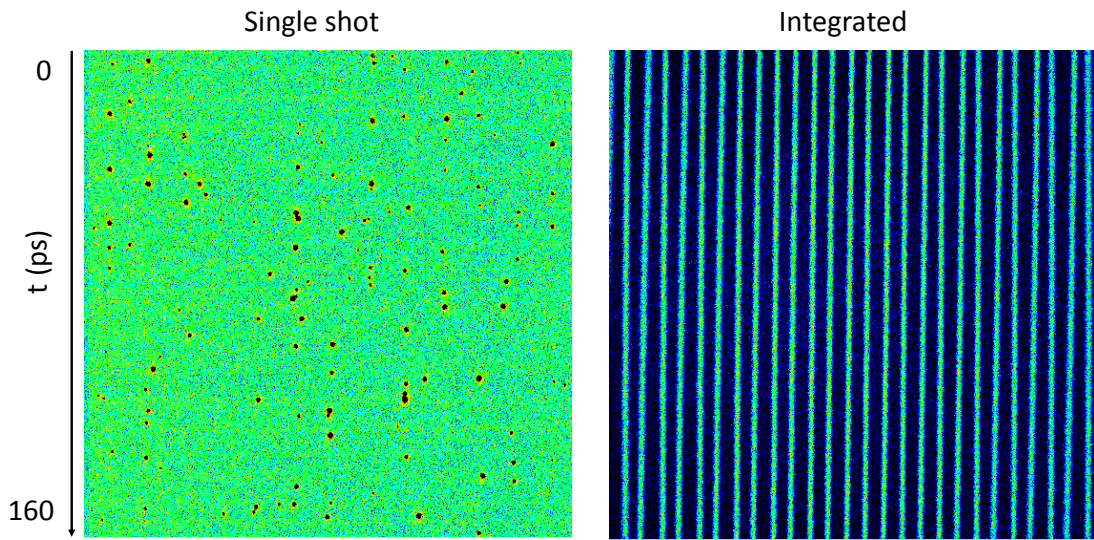


Figure 3.14: HeNe measurements. (a) Single shot image. (b) Integrated image.

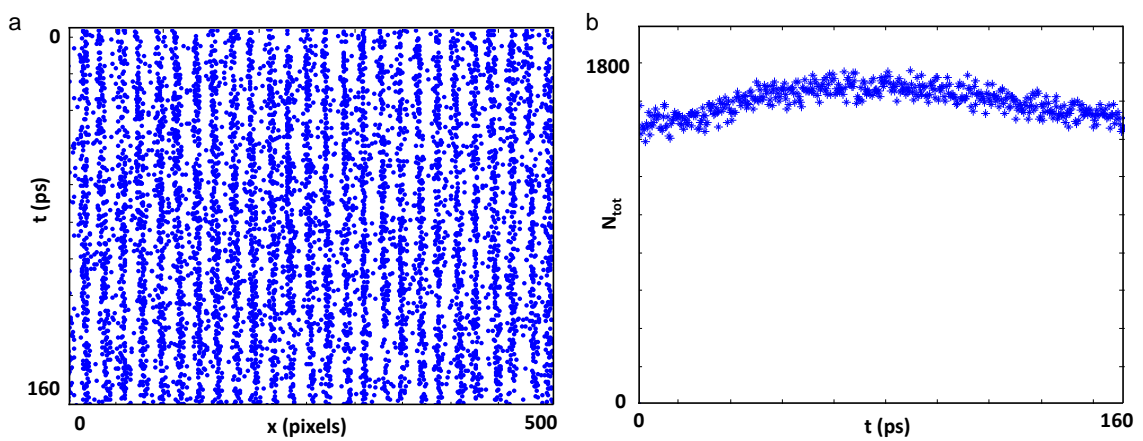


Figure 3.15: HeNe measurements. (a) Software reconstruction of Fig. 3.14 (b). (b) Total number of photons vs time.

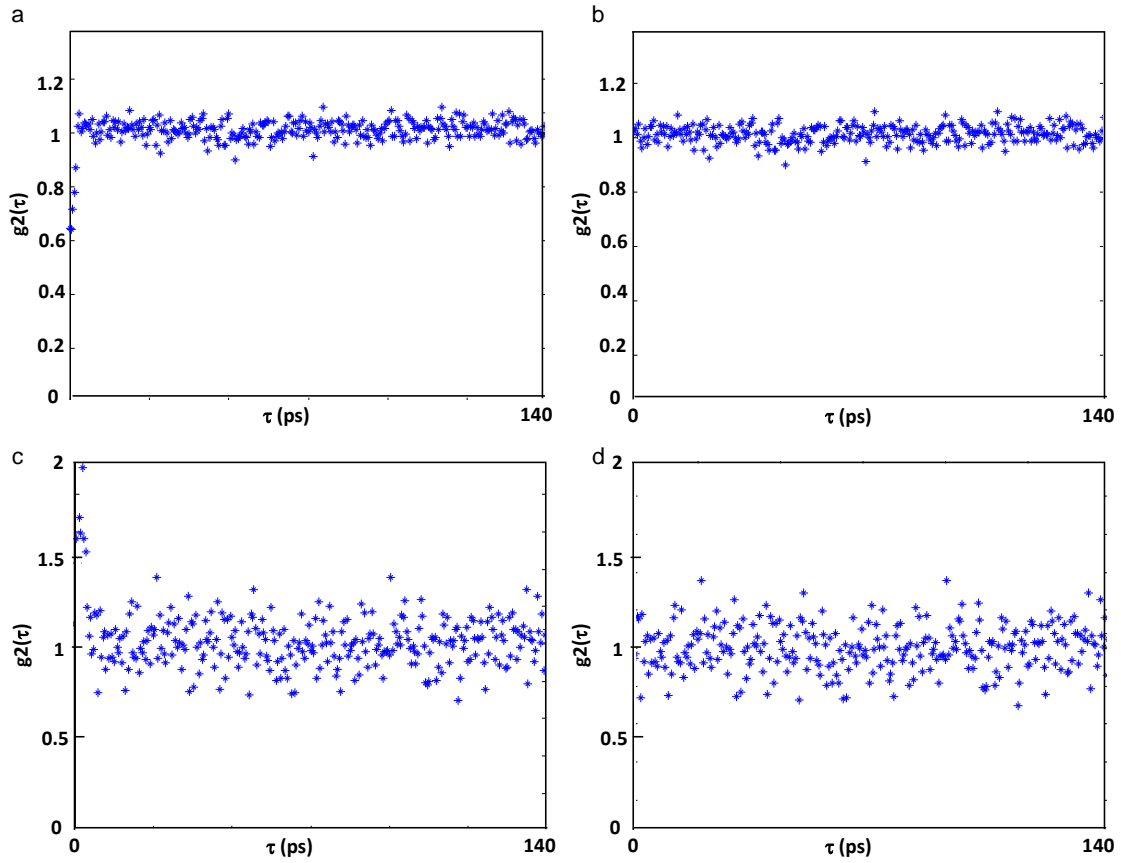


Figure 3.16: HeNe measurements. (a), (c) Calculated  $g_2(t,\tau)$  for two different average numbers of photons. (a) corresponds to  $\sim 7$  photons per streak, (c) corresponds to  $\sim 1$  photon per streak. (b), (d) respectively the same than (a), (c) after removing the first 10 points, in which the  $g_2$  function is affected by the finite effective photon size.

In both cases we remark a deviation from one for values of  $\tau$  close to zero and we observe that this deviation has opposite signs in the two cases. A zoom over these points is shown respectively in Fig. 3.17 (b) and (d) and a possible explanation of this effect is represented. We can associate such an artificial bunching/antibunching of the  $g_2$  function at small  $\tau$  to the finite effective size of photons hitting the CCD, which is related to the amplification and detection properties of the streak camera measurement. As shown in Fig. 3.7, the photons have an effective size of few pixels on the CCD. Such a finite size can lead to artifacts during the photon discrimination process of the photon counting algorithm, in which a coordinate (x,y) is associated to each signal which exceeds the defined threshold, as described in Section 3.3. Two possible situations are shown in Fig. 3.17 (a) and (c). In (a) two photons arrive very close to each other and they are registered as a single photon. In (c) a single photon presents a double peak structure on the CCD and it can be counted as two photons. Situation (a) gives rise to an artificial antibunching effect in the  $g_2$  function, as the one shown in (b), while situation (c) gives rise to an artificial bunching effect, as the one shown in (d). We remark that the scales typical of the bunching/antibunching peaks are compatible with the typical photons size.

The prevalence of one effect or the other seems to be related to the fluence of the signal. Situation (a) seems to be the dominant one for intense signals, while (c) seems to dominate for low power signals.

We get rid of this effect simply by eliminating the first ten points in the calculated

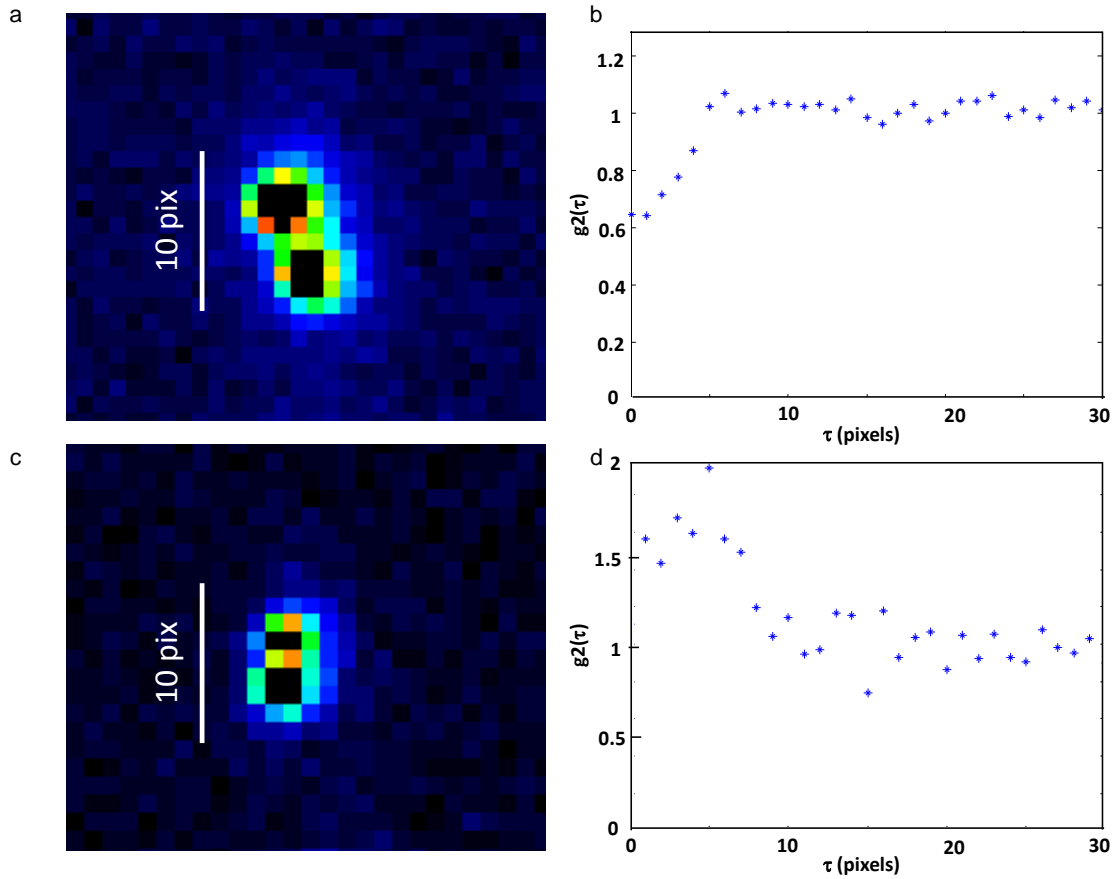


Figure 3.17: Two possible artifacts in the  $g^2$  function related to the effective photon size on the CCD camera. (a), (b) Two photons arriving one close to the other can be considered as a single photon, giving rise to an antibunching in the  $g^2$  function. (c), (d) A single photon with a double peak structure can be counted as two photons, giving rise to a bunching in the  $g^2$  function.

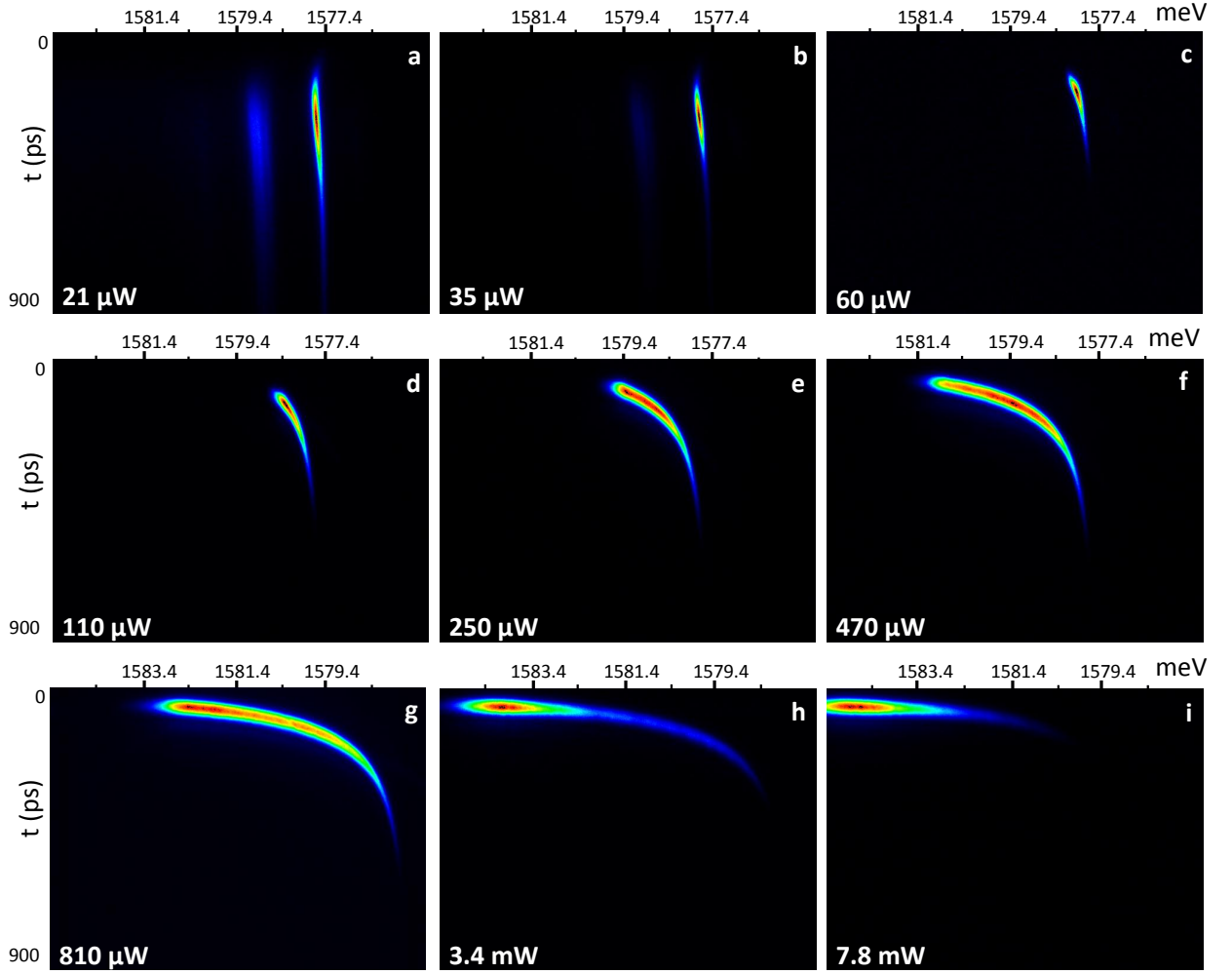


Figure 3.18: Energy-time resolved emission from the micropillar as it is excited out-of-resonance at increasing excitation powers. (a) corresponds to the linear regime in which emission from both the ground state and the first excited state is visible. (c) corresponds to the threshold for polariton laser. From (d) to (g), the increasing of particles in the system leads to stronger polariton-exciton interactions, leading to an increasing in the energy blueshift. (h) corresponds to the threshold for the photon laser.

$g_2$  function. For the HeNe data in Fig. 3.16 (a) and (c), this procedure leads to (b) and (d). This data correspond exactly to what we expect for a coherent CW signal. All the tests we have done confirm that the software we have built is working properly.

### 3.7 Experimental study of the $g_2$ function of a polariton condensate

We use the technique we have just described to study the  $g_2(t, \tau)$  temporal correlation function of a single pillar polariton condensate. In particular we study how the coherence properties of the polariton condensate evolve as we change the density of polaritons in the system, i.e. (i) how the  $g_2$  function changes in the transition from the linear regime to the polariton condensate regime, (ii) if the coherence is affected

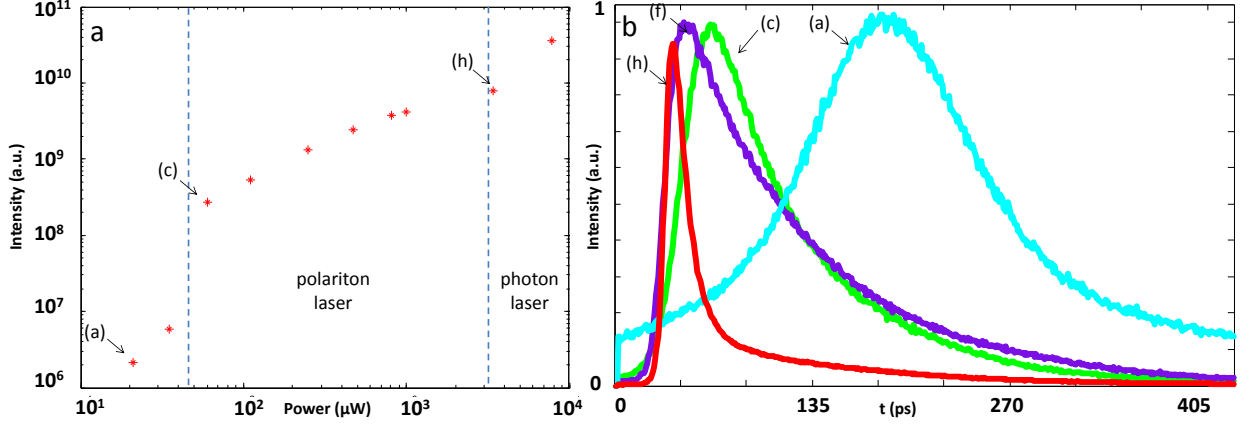


Figure 3.19: (a) Integrated intensity of the emission from the micropillar vs excitation power, displaying two thresholds in which the emission becomes highly nonlinear, corresponding respectively to the threshold for polariton laser and for photon laser. (b) shows how the temporal profile of the photoluminescence changes at the different excitation powers.

by polariton-polariton repulsive interactions in the condensate regime, and (iii) the transition from polariton condensation to photon laser in the weak coupling regime. Moreover, since we excite the system with a pulsed excitation, we have access to the temporal dynamics. For each regime of excitation, we can therefore study the evolution in time of the  $g_2$  function.

The system is excited out-of-resonance, with a 1.7 ps pulsed laser, which is under the streak camera resolution time ( $\sim 4$  ps). The excitation laser injects in a short time a lot of hot carriers. These carriers relax down to form excitons and finally polaritons that accumulate at the bare exciton energy, where the density of states is large. From those energy states, polaritons relax down towards the bottom of the lower polariton branch via polariton-polariton and polariton-phonon scattering. The photoluminescence dynamics reflects the combination of all these relaxation processes and it is strongly determined by the excitation density [107]. Figure 3.18 shows the energy-time resolved photoluminescence emission for different excitation powers. Note that the excitation pulse is eliminated from the detection by means of two high-pass interference filters with a cut-off wavelength of 750 nm (the laser excitation wavelength is 735 nm). Each image in Fig. 3.18 is renormalized to a different value to improve the visibility of the traces, whose profiles are plotted in Fig. 3.19 (b). The measured integrated intensity for each power is shown in Fig. 3.19 (a).

At low power (Fig. 3.18 (a)) emission from both the ground state ( $\sim 1577.5$  meV) and first excited state ( $\sim 1579$  meV) is visible. The energy of both signals remains almost constant in time, meaning negligible interactions in the system. The emitted photoluminescence dynamics (Fig. 3.19 (b), light blue curve) is quite long,  $\sim 130$  ps, with a profile symmetric in time. In this regime all the micropillar energy levels are slowly populated through spontaneous scattering processes.

As we increase the excitation power ( $\sim 60 \mu\text{W}$ , Fig. 3.18 (c)), the emission starts to come mostly from the ground state mode, the first excited mode being no more visible. The dynamics is strongly accelerated and the emitted intensity increases by several orders of magnitude (Fig. 3.19 (a)). This corresponds to the threshold for polariton laser, at which stimulated relaxation towards the ground state starts to take place. A slight energy blueshift is visible at short times, showing that interac-

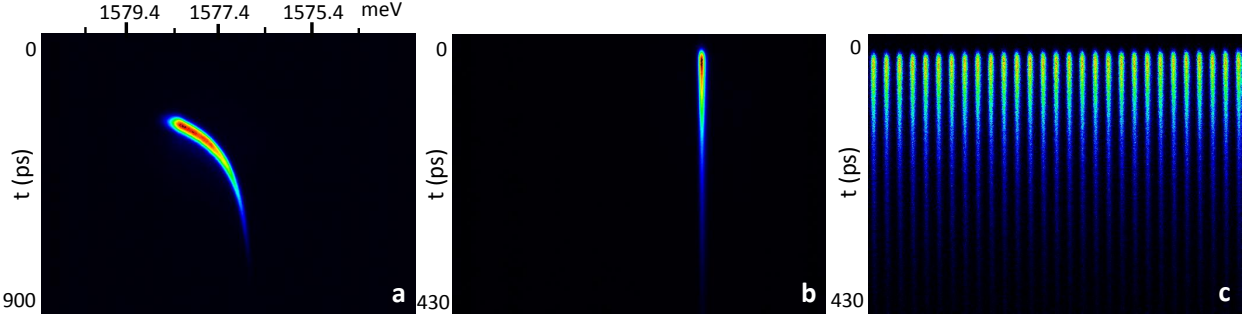


Figure 3.20: Configuration used to perform the  $g^2$  experiment. (a) Example of a time-energy resolved measurement. Corresponding signal when we replace the grating with a mirror (b) and when we use the dual base operation mode (c). This is the configuration used for the  $g^2$  experiment.

tions between polaritons and the excitonic reservoir [26, 92] start to play a role in the dynamics. The stimulation process leads also to the observed faster dynamics (Fig. 3.19 (b), green curve), most of the signal is emitted within  $\sim 80$  ps, and the emission starts to be asymmetric, with a steeper rising edge.

As we further increase the excitation power, polariton-exciton repulsive interactions become more and more important (Fig. 3.18 (d) to (g)), leading to a continuously increasing energy blueshift at short times, which reaches values of up to 6 meV (g). The emitted intensity grows linearly vs excitation power, as shown in Fig. 3.19 (a) and the temporal profile does not change substantially (Fig. 3.19 (b), green and blue curves).

At  $\sim 3.5$  mW (Fig. 3.18 (h)) we reach the photon laser threshold. The high density of electrons and holes injected in the quantum wells screens the excitons, strongly reducing their oscillator strength, and resulting in the break-up of the strong coupling. In this situation, the photoinjected electrons and holes provide a population inversion and the system turns into a standard photon laser. As the strong coupling is broken, the system jumps from the polaritonic mode to the bare cavity mode, which is at a higher energy (Fig. 3.18 (h)). At the same time the photon laser regime is characterized by a very fast dynamics, since the system is inverted no relaxation is needed, and the stimulated lasing process is very fast. Most of the signal is emitted within  $\sim 20$  ps (Fig. 3.19 (b), red curve).

We remark that in all regimes, even after most part of the emission has occurred, the system continues to emit, up to a point in which it is completely depleted. The progressive depletion of the micropillar leads to the progressive decrease of the blueshift (Fig. 3.18). The emission finally takes place at the energy of the unrenormalized polariton mode.

In order to perform the  $g^2$  measurement we replace the grating in the spectrometer with a mirror. In a signal as the one shown in Fig. 3.20 (a), all the energy components will be superimposed as we work in the mirror configuration, giving a signal as the one shown in (b). In the dual base streak camera operation mode (Blanking Amplitude 500 ns) this signal looks like (c). Our  $g^2$  measurements are taken in the single shot regime, as explained previously.

The results of the  $g^2$  measurement are shown in Figs. 3.21 and 3.22. Figure 3.21 shows the results at low excitation power (corresponding to Fig. 3.18 (a)). The total number of photons emitted vs time is shown in Fig. 3.21 (a). The inset shows

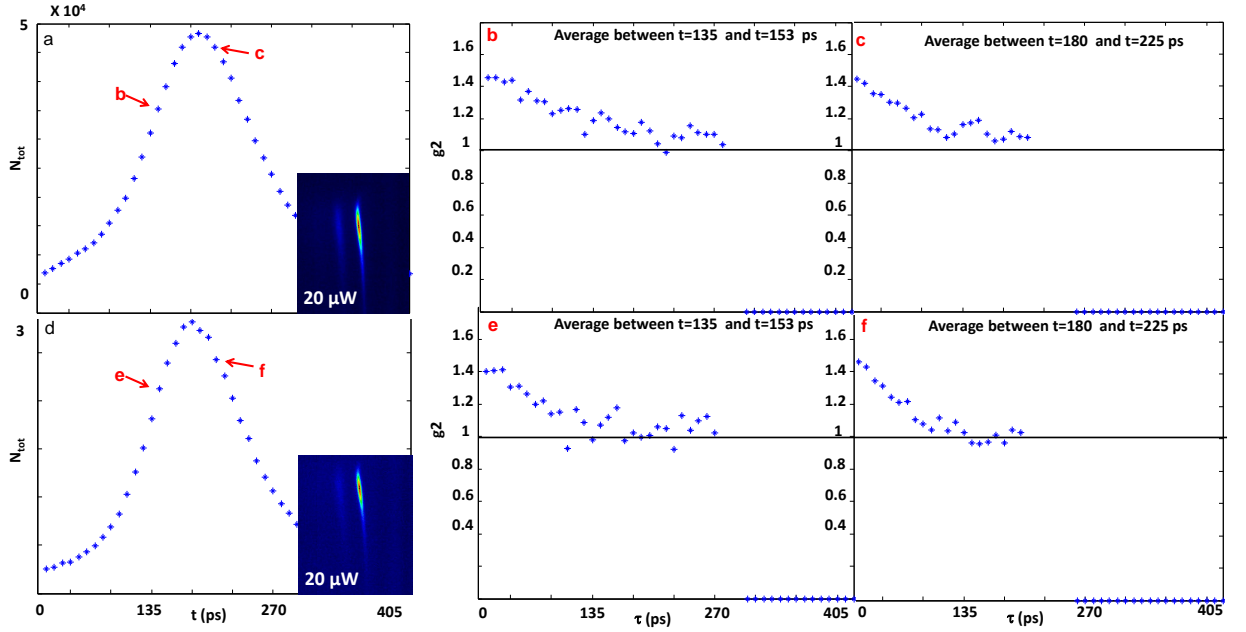


Figure 3.21:  $g_2$  measurement as the micropillar is excited at low power. (a) Total number of photons vs time. The inset shows the energy-time resolved measurement, highlighting that we are in the low power regime. (b) and (c)  $g_2(t, \tau)$  measurement for two different starting times  $t$ , indicated by red arrows in (a), showing a behaviour compatible with a thermal signal. (d) to (f) Same measurements as in the upper panel, in case the signal is filtered in linear polarization.

the energy-time resolved measurement. The measured  $g_2(t, \tau)$  function is shown in Fig. 3.21 (b) and (c), for two different starting times  $t$ , indicated by red arrows in (a). We observe that  $g_2(t, \tau = 0)$  is well above one,  $g_2(t, \tau = 0) \sim 1.4$ , and it decays in time towards one on a timescale of  $\sim 90$  ps (half width at half maximum). This result is compatible with the behaviour expected for a non-polarized thermal signal with a coherence time of  $\sim 90$  ps. In fact for non-polarized thermal light the value of  $g_2(\tau = 0)$  is expected to be 1.5, lower with respect to the typical value  $g_2(\tau = 0) = 2$ , characteristic of polarized thermal light [108]. Our result is therefore compatible with what is predicted theoretically [97, 98, 99, 100].

On the contrary, the coherence time extracted from these data  $\tau_c \sim 90$  ps seems to be quite long if compared to the measured polariton lifetime of  $\tau_{\text{lifetime}} \sim 50$  ps (see Section 5.4). One possible reason for this is that the excitation density in the experiment shown in Fig. 3.21 (a) is close to the polariton lasing threshold. In this case, we would expect some enhanced relaxation from the bosonic effect and, consequently, an extended coherence time. This explanation is compatible also with the fact that we measure a  $g_2(t, \tau = 0)$  slightly smaller than 1.5, the expected value from an unpolarized thermal source. Experiments at lower power were not possible due to the low quantum efficiency of the streak camera, resulting in low signal-to-noise ratios at low fluences, even in the case of long measurements (i.e. big statistical ensembles).

Figure 3.22 shows the results of the  $g_2$  measurement for higher excitation powers. Data corresponding to four different excitation powers are reported, starting from the polariton laser threshold (a-c) up to the threshold for the photon laser regime (j-l). In the left column the energy-time resolved measurements are reported: they allow to easily identify the regime we are considering, looking at the signal energy

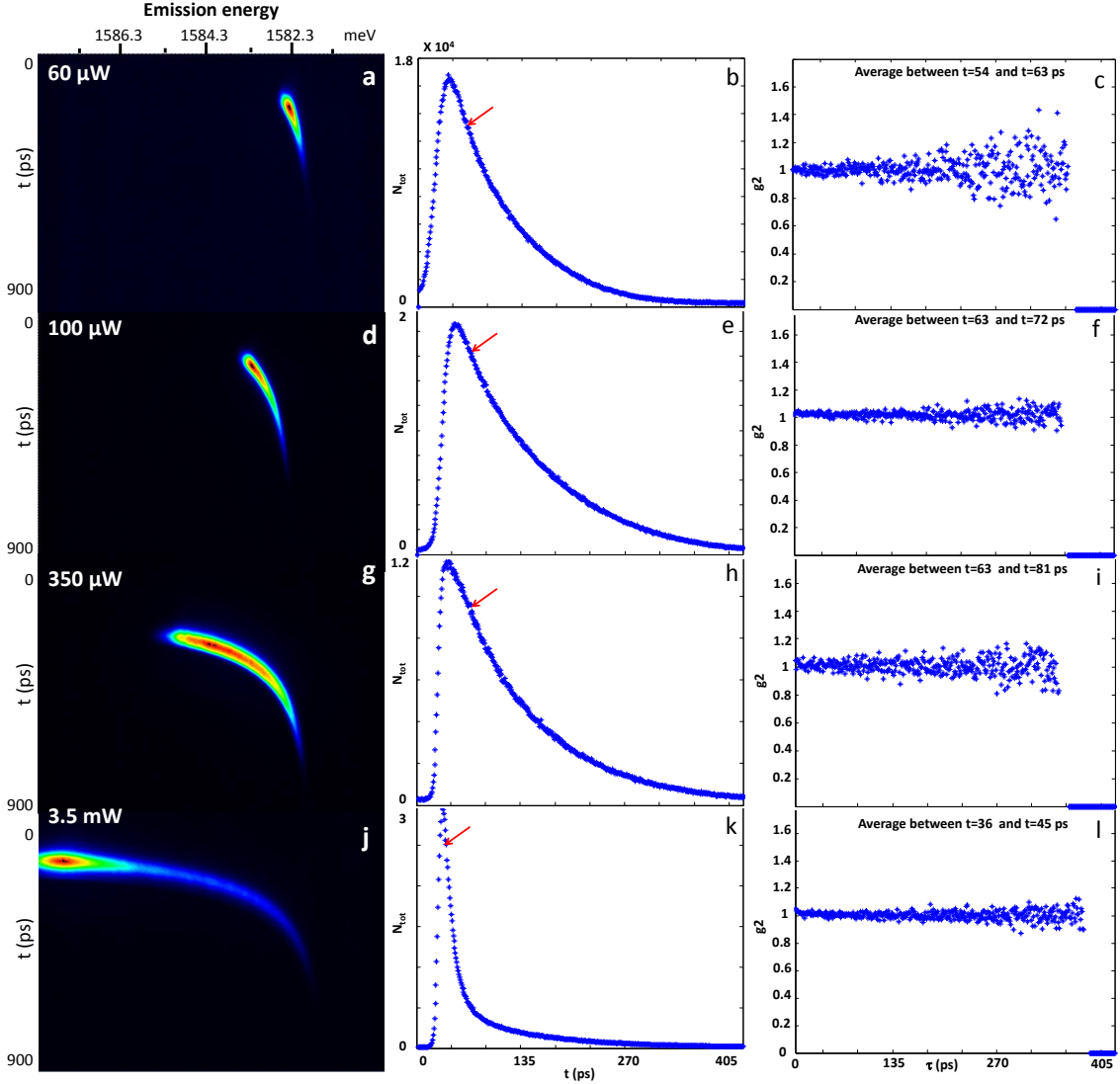


Figure 3.22:  $g_2$  measurements at higher power, starting from the polariton laser threshold (a-c) up to the photon laser threshold (j-l). Left column: energy-time resolved measurements, allowing to easily identify the regime, looking at the energy blueshift. Central column: total number of photons vs time. Right column:  $g_2(t, \tau)$  measurements for the starting time  $t$  indicated by the red arrow. The emission is coherent in all regimes ( $g_2(t, \tau) = 1$  at any  $\tau$ ).

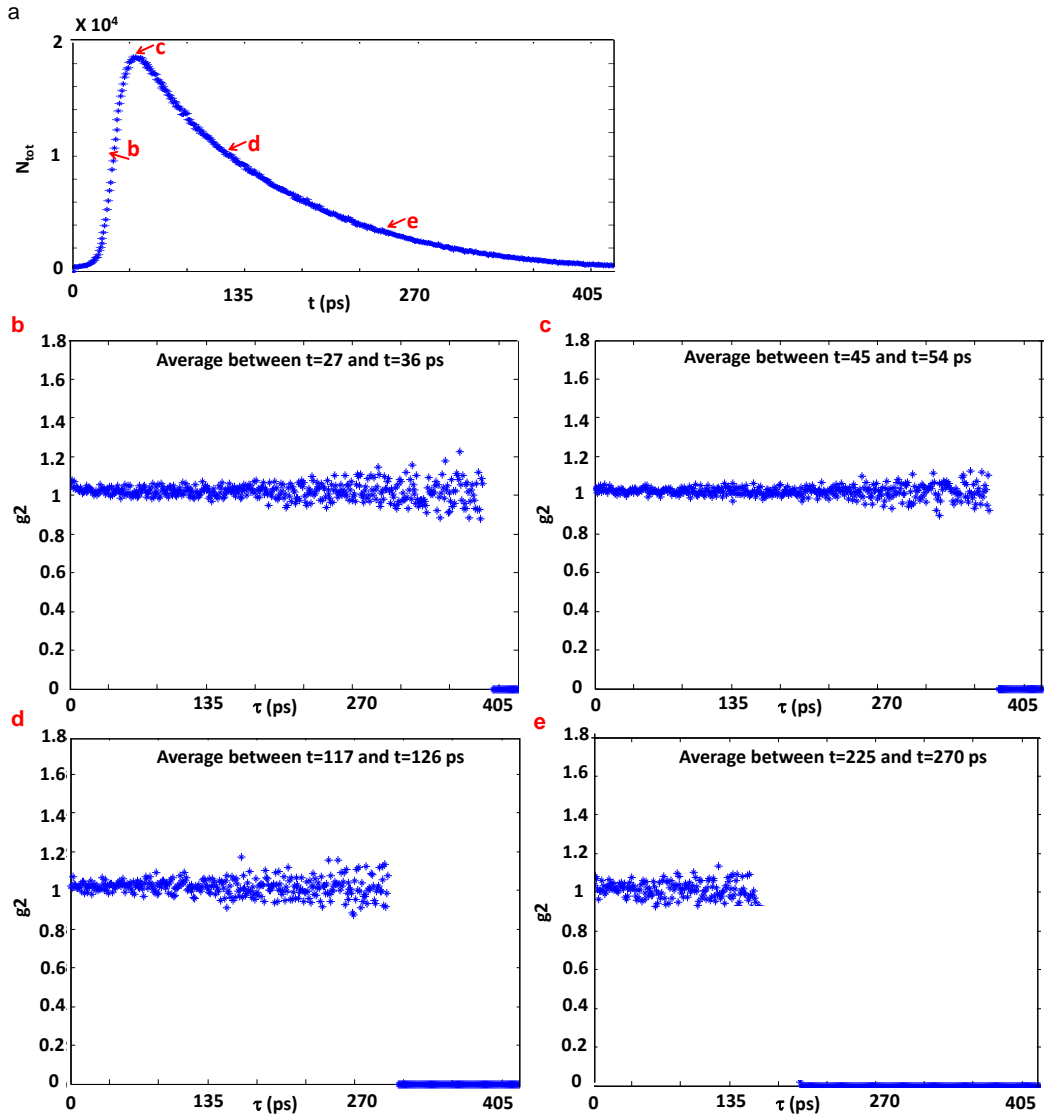


Figure 3.23:  $g_2(t, \tau)$  function calculated for four different starting times  $t$  (indicated by red arrows), in the polariton laser regime (excitation power  $100 \mu\text{W}$ , Fig. 3.22 (d-f)), showing that the signal is coherent at any time of the emission.

blueshift. In the central column it is shown, for each regime, the total number of photons vs time.

The results of the  $g_2(t, \tau)$  measurements are shown in the right column of Fig. 3.22, for the times  $t$  indicated by the red arrows. We see that  $g_2(t, \tau) = 1$  for all delays  $\tau$  in each regime. This means in particular that the polariton laser emits coherent light. If we concentrate at a specific excitation power, we can measure  $g_2(t, \tau)$  at different times  $t$  after the arrival of the pulse. Figure 3.23 shows the  $g_2(t, \tau)$  function measured for four different starting times  $t$  (indicated by red arrows), in the polariton laser regime (Fig. 3.22 (d-f)). The signal is coherent at any time of the emission.

The power dependent results depicted in Fig. 3.22 (f)-(i) show that the coherence built above the polariton laser threshold is not affected by polariton-polariton interactions. This seems to be at odds with theoretical calculations [99, 100], which predict that polariton-polariton interactions could introduce some decoherence in the system, giving rise to an increase of the  $g_2$  function above one. Reference [100] predicts that decoherence should arise as a consequence of two-mode parametric scattering. This mechanism is possible in polariton condensates in 2D microcavities, but it is highly inhibited in our system in which modes are quantized and separated in energy due to confinement. The other decoherence mechanism, proposed by [99], should arise as a consequence of the interaction with the excitonic reservoir. An explicit evaluation of this effect shows that, in our system, extremely strong interactions should take place in order to observe a non-negligible decoherence. The strong coupling is broken, before we can reach such regime.

As expected, the signal is coherent also in the photon laser regime (Fig. 3.22 (l)). We remark that, in any of the regimes, as the cavity is progressively depleted, going towards the linear regime, we expect the emission to become thermal. In our measurements this transition is not visible, since as the system reaches the linear regime, the emission is characterized by a very low signal-to-noise ratio. Since noise is characterized by  $g_2(\tau) = 1$ , even considering a large statistical sample, we would not be able to retrieve the typical  $g_2$  thermal behaviour. This is also the reason why we are not able to observe the build-up of coherence at the rising edge of the signal.

### 3.8 Polarization resolved measurements

The same technique used to measure the  $g_2(t, \tau)$  function can be used to study the polarization properties of the polariton condensate. To this end, we perform the same kind of measurements shown in the previous section, filtering the signal in polarization. In particular we filter the emission in the linear polarization cross-polarized with the excitation laser. The results of the measurement are shown in Fig. 3.24, for the same regimes of excitation considered in Fig. 3.22. We observe that the  $g_2(t, \tau)$  function displays an oscillatory behaviour in all regimes. Its value at  $\tau = 0$  is around 1.4 and then, at longer  $\tau$ , oscillations take place around  $g_2 = 1$ , with a period which depends on the regime we are considering. The smallest oscillation period is found to correspond to the polariton laser threshold,  $T \sim 160$  ps (Fig. (c)) and it increases progressively as we increase the excitation power going towards the photon laser regime. We observe that the oscillations are damped in time.

The oscillating behaviour in the  $g_2$  function can be related to the polarization properties of our polariton condensate. In collaboration with Michiel Wouters from Universiteit Antwerpen (Belgium), we have developed a preliminary theoretical model,

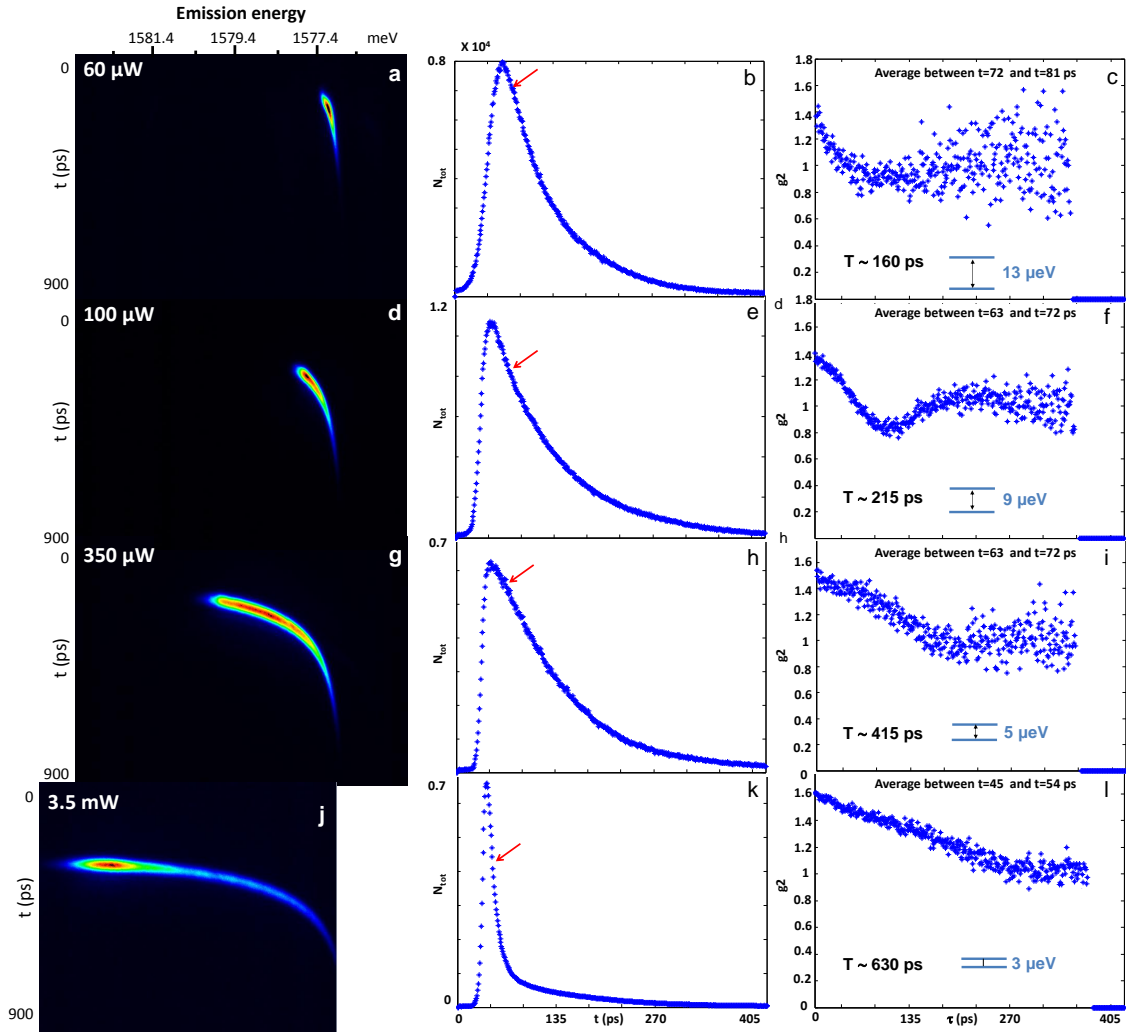


Figure 3.24: Polarization resolved measurements in the same four regimes considered in Fig. 3.22. Left column: energy-time resolved measurements, allowing to identify the regime looking at the energy blueshift. Central column: total number of photons vs time. Right column:  $g_2(t, \tau)$  measurements for the starting time indicated by the red arrow. The  $g_2$  function is characterized by oscillations in  $\tau$  around  $g_2 = 1$ , whose period increases as we increase the excitation power. The period of oscillations is reported explicitly for each regime, together with the corresponding value of the calculated polarization energy splitting (indicated in light blue).

which provides a simple picture to understand our observations.

The first assumption of the model is that our micropillar displays a small linear polarization splitting along a nontrivial direction, that is a direction not necessarily related to the crystallographic directions. The splitting could be induced by structural disorder due to some strain arising in the growth process. As we will see in the next chapter, this kind of polarization splitting affects the dynamics of the Josephson oscillations in two-pillar molecules. The second assumption is that, since condensation takes place very quickly and the energy splitting between the two polarized eigenstates is very small, the system does not have enough time to “probe” the energy levels and to condense on the lowest one. Therefore it condenses on a linearly polarized state whose polarization direction changes randomly from shot to shot. Later in time the polarization splitting induces a precession of the polarization [24, 23], with a frequency which is related to the magnitude of the splitting by the relation  $T = h/\Delta E$ .

We can reproduce qualitatively our data within this model assuming a coherent polariton condensate, whose initial polarization direction is chosen randomly for different independent realizations of the condensate. The linear polarization precesses linearly in time with a fixed period given by the energy splitting. A diffusion term is included to take into account any process inducing a polarization dephasing (damping term). As in the experiment, we project the linear polarization direction onto a fixed linear polarization direction representing our detection polarizer. In the absence of decay, the average number of polaritons is constant on time and Eq. 3.1 can be written

$$g2(t, \tau) = \frac{\langle n(t)n(t + \tau) \rangle}{\langle n(t) \rangle^2}. \quad (3.4)$$

We can write  $\langle n(t)n(t + \tau) \rangle$  in terms of probability distributions in the form

$$\langle n(t)n(t + \tau) \rangle = \int n_t n_{t+\tau} P(n_t, n_{t+\tau}) dn_t dn_{t+\tau}, \quad (3.5)$$

where  $P(n_t, n_{t+\tau})$  is the joint probability to find a photon in  $t$  and another in  $t + \tau$ . With the previous assumptions, this joint probability depends only on the angle of linear polarization  $\theta$  of the signal at  $t$  and at  $t + \tau$  (angle taken with respect to the optical axis of the linear polarizer). We can express  $P$  in the form

$$P(\theta_t, \theta_{t+\tau}) = \frac{1}{\pi\sqrt{\pi}\sigma} \exp \left[ -\frac{(\theta_{t+\tau} - \theta_t - \Theta_{pr}(\tau))^2}{\sigma^2} \right]. \quad (3.6)$$

This expression describes an uniform distribution of angles at initial time  $t$ . In fact

$$P(\theta_t) = \int d\theta_{t+\tau} P(\theta_t, \theta_{t+\tau}) = \frac{1}{\pi}, \quad (3.7)$$

which accounts for the random initial linear polarization.

The angle  $\Theta_{pr}(\tau)$  gives the average precession of the axis of polarization in the time interval  $\tau$ , while the width  $\sigma$  is a measure of the diffusion of the orientation (damping term). Note that in the limit where  $\sigma$  goes to zero, the probability distribution of  $\theta_{t+\tau}$  is a  $\delta$ -function around  $\theta_t + \Theta_{pr}(\tau)$ .

If we filter the signal with a polarizer, we have that  $n_t$  and  $n_{t+\tau}$  in Eq. 3.5 can be written as

$$n_t = I \cos^2(\theta_t), \quad (3.8)$$

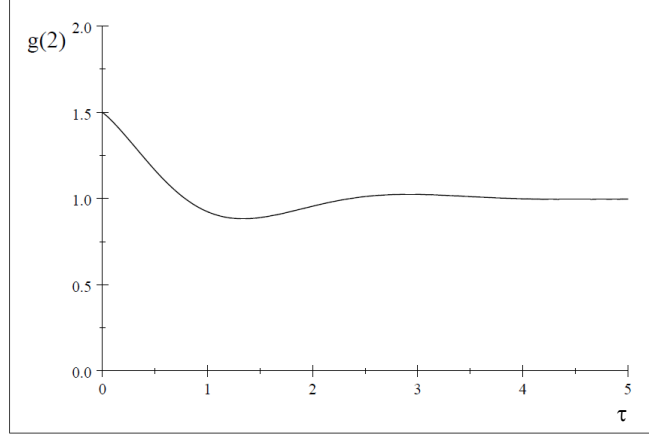


Figure 3.25: Simulated behaviour of  $g2(\tau)$  for a coherent polariton condensate without losses, with initial random linear polarization and characterized by a linear precession of the polarization in time. The linear polarization of the signal is projected onto a fixed linear polarization direction representing our detection polarizer. The calculated  $g2$  shows a high qualitative agreement with our measurements.

where  $I$  is the constant intensity of the signal.

Therefore Eq. 3.4 takes the form

$$g2(t, \tau) = \frac{\int \cos^2(\theta_t) \cos^2(\theta_{t+\tau}) P(\theta_t, \theta_{t+\tau}) d\theta_t d\theta_{t+\tau}}{(\int \cos^2(\theta_t) P(\theta_t, \theta_t) d\theta_t)^2}, \quad (3.9)$$

which gives explicitly

$$g2(\tau) = 1 + \frac{1}{2} e^{-\sigma^2 \tau} \cos(2\Theta_{pr}(\tau)). \quad (3.10)$$

First of all we observe that  $g2(\tau = 0) = 1.5$ . This is a consequence of the random direction of the linear polarization at  $\tau = 0$  combined to the filtering imposed by the polarizer.

If we suppose a precession linear in time ( $\Theta_{pr} = \Omega_{rot} \tau$ ) and the width  $\sigma$  of the distribution following  $\sigma \propto \sqrt{\tau}$  (according to a Brownian motion), we find a behaviour of the  $g2$  function as the one shown in Fig. 3.25, which is qualitatively very close to our experimental observations.

In agreement with the experimental data,  $g2(\tau)$  starts from a value 1.5 and then displays oscillations which are damped in time. The frequency of oscillations is  $2\Omega_{rot}$ , where  $\Omega_{rot}$  is the frequency of the polarization rotation.  $\Omega_{rot}$  corresponds to the polarization energy splitting  $\Delta E_{pol} = \hbar \Omega_{rot}$ . Therefore, through Eq. 3.10, the period of oscillations  $T$  is related to  $\Delta E_{pol}$  by the relation

$$T = \frac{h}{2\Delta E_{pol}}. \quad (3.11)$$

From the period of oscillations estimated from the experimental data, we can calculate the corresponding polarization energy splitting. The values are reported in Fig. 3.24 for each measurement, together with the period of oscillations  $T$ . We see that the polarization energy splitting ranges from few  $\mu\text{eV}$  to  $\sim 13 \mu\text{eV}$ , and the splitting decreases progressively as we increase the excitation power.

We can explain these observations by considering a power dependent excitonic screening effect which takes place as we increase the number of particles in the

system. As stated above, in our model the polarization splitting originates in the directional strain or any kind of asymmetry in the quantum well. This results in a potential that confines slightly differently excitons linearly polarized in different directions. Even an asymmetry in the growth direction can give rise to this kind of splitting [109]. As we increase the excitation density, free carriers and excitons gradually screen this asymmetric potential, resulting in a decrease of the polarization splitting.

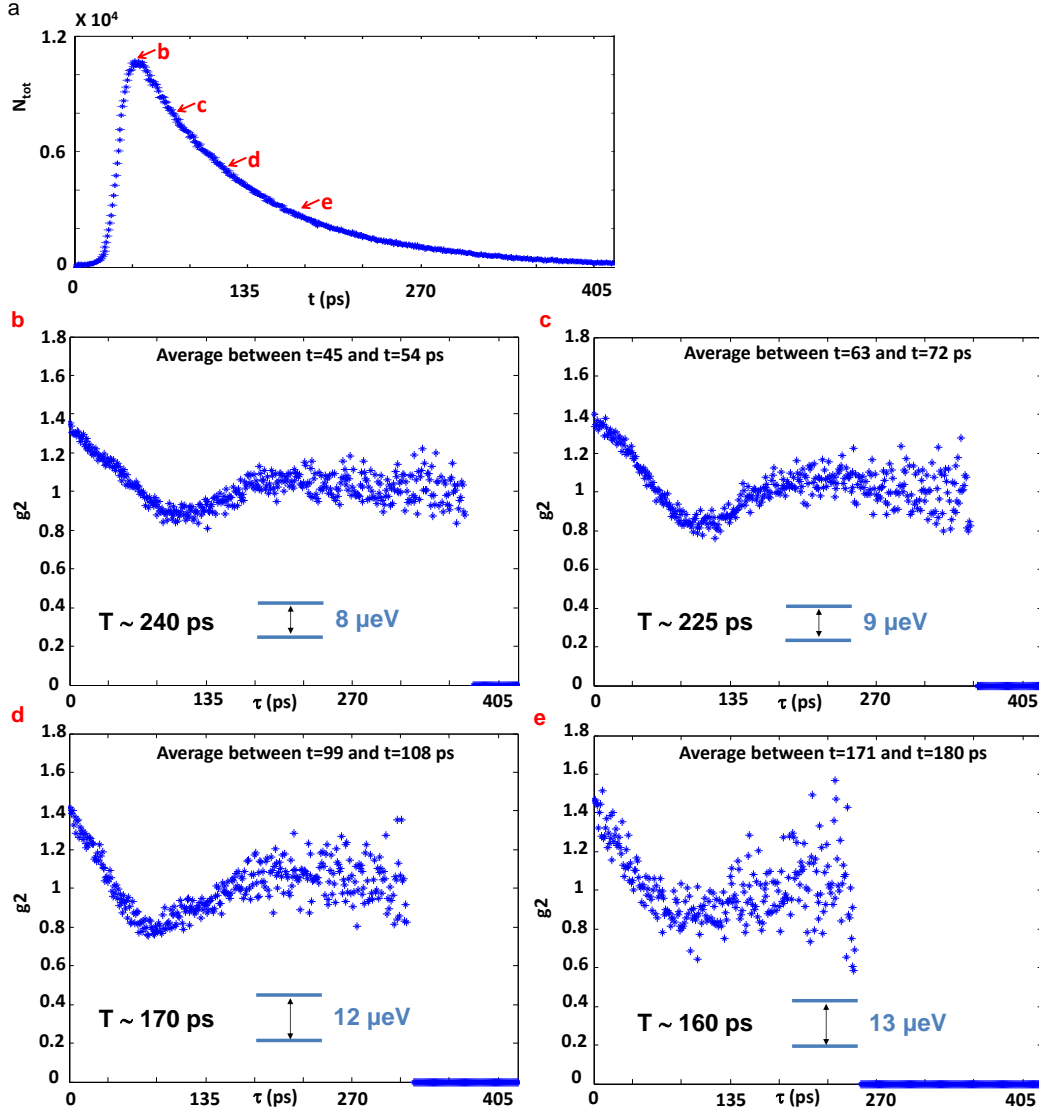


Figure 3.26: Data corresponding to the excitation power  $100 \mu W$  (Fig. 3.24 (d,e,f)), where the  $g_2(t, \tau)$  function is calculated for four different starting times (indicated by red arrows), showing that the period of oscillations reduces as we consider initial times which are more and more far away from the peak of the emission. This corresponds to an increasing of the polarization energy splitting as the cavity is progressively depleted.

In order to further test the predictions of the model, we analyze the  $g_2(t, \tau)$  function measured at different times  $t$  for fixed excitation densities. Figures 3.26 and 3.27 show the  $g_2(t, \tau)$  measured at different times  $t$  for the excitation powers corresponding to Fig. 3.24 (d) and 3.24 (g), respectively. In both cases we observe that the period of oscillations is reduced as we consider initial times further away from the

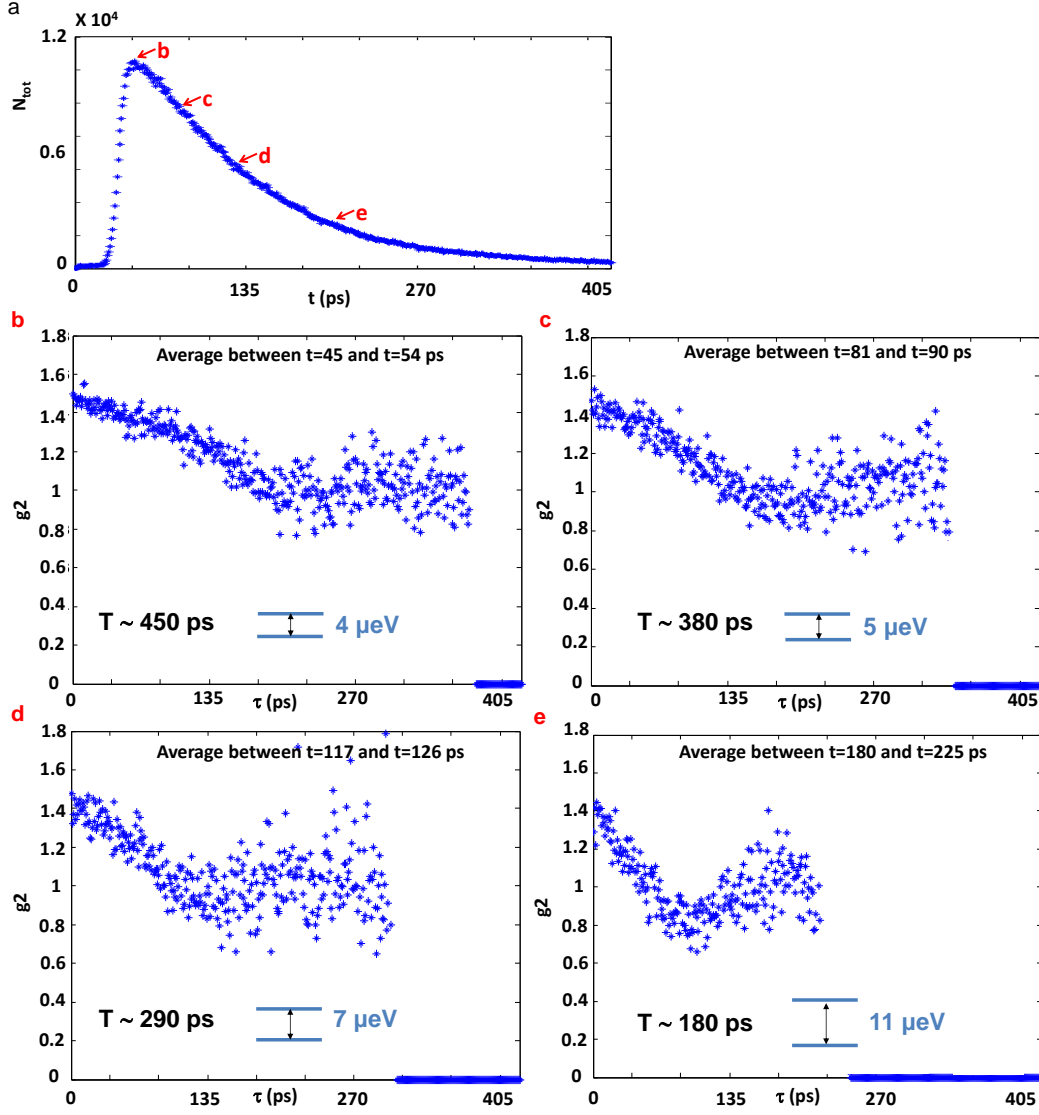


Figure 3.27: Same as Fig. 3.26, for the excitation power  $350 \mu\text{W}$  (Fig. 3.24 (g,h,i)).

maximum of the emission. This corresponds to a progressive increase in the polarization energy splitting with time. We can understand this in the framework of our model in the following way. At short times  $t$ , the large injected density of carriers partially screens the polarization splitting, reducing its value. At longer times  $t$ , the micropillar is progressively depleted, the screening decreases, and the polarization splitting recovers its unperturbed value. This results in a reduction in the period of oscillations with time, as can be seen when comparing Fig. 3.26 (b) and Fig. 3.26 (d), or Fig. 3.27 (b) and Fig. 3.27 (e). In both cases the splitting ends up to the same value of  $\sim 13 \mu\text{eV}$ .

At even higher powers (Fig. 3.18 (i)), the system gets into the photon lasing regime in the weak coupling. This regime is studied in detail in Fig. 3.28. At short times (Fig. 3.28 (b)), close to the maximum of emission, we measure a long decay time of the  $g^2(t, \tau)$  and no oscillations take place within the time of emission. In this regime, photons are decoupled from excitons (which are replaced by a bath of electrons and holes) and the lasing mode is not sensitive to the polarization splitting previously present for polaritons. The direction of the initial polarization still changes from shot to shot, resulting in a value of  $g^2(t, 0) > 1$ . However, the fact that the actual

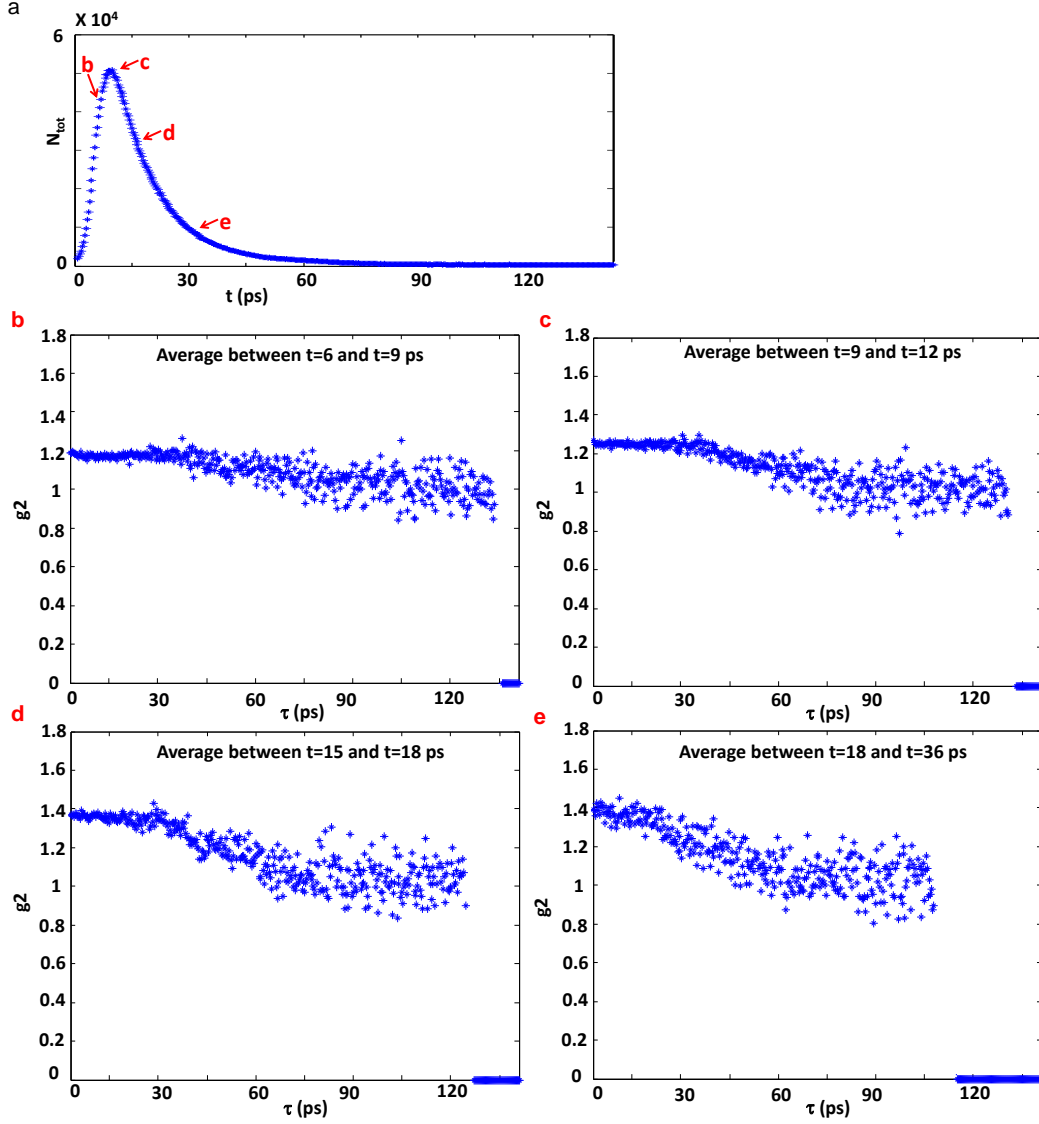


Figure 3.28: Same as Fig. 3.26 and Fig. 3.27, for the highest excitation regime, excitation power 7.8 mW (Fig. 3.18 (i)). Note that the horizontal scale spans over a reduced time delay if compared to Fig. 3.27.

value of  $g_2(t, 0)$  at short times is smaller than 1.5 (Fig. 3.28 (b)), might indicate that the system chooses preferentially a polarization direction. This direction might be given by the crystallographic axis, as it is the case in standard Vertical Cavity Surface Emitting Lasers in the weak coupling regime.

At later times  $t$ , the carriers de-excite and the system goes back to the strong coupling regime. Polaritons are again subject to the polarization splitting and  $g_2(t, \tau)$  should start to oscillate again. Indeed, the beginning of an oscillation can be guessed from the data reported in Fig. 3.28 (e).

Let us note that in the data shown in Fig. 3.24 we observe oscillations (even if damped) induced by the polarization precession, even at longer times after the peak of the emission. It indicates that the signal is still coherent even if most part of polaritons have left the cavity. On the other hand we should treat the data close the photon laser regime with some care (Fig. 3.24 (l)). In fact, in this case, emission takes place very fast and a very long decay of the  $g_2(t, \tau)$  function is observed. In this measurement we measure intensity correlations between photons emitted in very different regimes: at short times in the weak coupling photon laser regime, and

at longer times in a lower density regime, closer to the strong coupling linear regime.

On the light of this discussion we can consider again the low power measurements of Fig. 3.21. We observe that the data taken filtering in polarization (lower panels) are almost equivalent to the data taken without filtering in polarization (upper panel). We can make the following argument. In the low power regime, the two linearly polarized energy levels will be populated. Since they are very close in energy, we can suppose that they will be equally populated. We can also suppose that each one of the two levels displays a thermal statistics, completely independent from the other level. As we perform the  $g^2$  measurement without filtering in polarization, we mix two independent emitters with thermal statistics. As already mentioned, we expect therefore a  $g^2$  function equal to 1.5 in  $\tau = 0$  (lower than the value of 2 expected for a polarized thermal signal) [108]. As we filter in polarization, we will recover a statistics with  $g^2(\tau = 0) = 2$  only in the case we filter exactly along one of the two linear polarizations which constitute the eigenstates of the system. If not, we will still have the detection of two independent modes. This would reduce the value of the  $g^2(t, \tau)$  to 1.5 [108].

Although we have selected the polarization of the emission along a direction cross-polarized with that of the excitation laser, the results do not seem to be dependent on the choice of this direction. We performed some measurements filtering the signal co-polarized with the excitation laser and we found the same behaviour.

We would like now to comment on the magnitude of the polarization splitting assumed in our model, as compared to other microcavity systems. Our data show an initial polarization behaviour similar to the one observed in bulk GaN microcavities [10], in which the polariton condensate is shown to display a random direction of the linear polarization. In those systems, both the absence of quantum wells, which lowers the number of interfaces in the active region, and the bulk character of polaritons, reduce the in-plane anisotropic effects that could give rise to a polarization splitting.

This is quite different from what is observed in CdTe microcavities [110, 9], in which the polarization of the condensate is pinned to a given direction dependent on the position on the sample. We recall that a polariton condensate is expected to display a linear polarization. This is related to the fact that polaritons with aligned spins interacts more strongly if compared to polaritons with antialigned spins, therefore the lower energy state is made of an equal amount of spin-up ( $\sigma+$ ) and spin-down ( $\sigma-$ ) particles [70]. In [10], the bulk microcavity prevents the presence of a polarization splitting (all polarizations are degenerate in energy). This leads to the fact that, for any configuration, the polariton condensate “chooses” a random polarization direction in the condensation process (spontaneous symmetry breaking). On the other hand, the CdTe microcavities studied in [110, 9] display a very strong polarization splitting ( $\sim 200 \mu\text{eV}$ ) as a consequence of the strong photonic disorder typical of these heterostructures. The polarization of the condensate is therefore always pinned to the linear polarization corresponding to the lowest energy level. In our case the experimental results indicate that in the GaAs based samples we employ, the polarization splitting is very small, and the system chooses a random polarization direction in the condensation process. This is confirmed by the values for the energy splitting that we found experimentally, few  $\mu\text{eV}$ , much smaller than the  $\sim 200 \mu\text{eV}$  of [110, 9]. On the other hand, though small, the polarization splitting

is still present, inducing polarization precession.

### 3.9 Conclusion and perspectives

In this chapter we described our experimental study on the  $g_2(t, \tau)$  temporal correlation properties of a polariton condensate in a GaAs micropillar. In particular we implemented in our laboratory a technique recently developed in the group of M. Bayer, which makes use of a streak camera working in the single shot regime. This measurement allows to record directly the track in time of photons arrived within each single pulse, with a time resolution of  $\sim 4$  ps, and the  $g_2(t, \tau)$  function can be extracted by directly counting the photon coincidences. This technique overcomes the temporal resolution limit of the photodiode based HBT setups usually employed for the  $g_2$  measurements (best resolution  $\sim 50$  ps). However, contrary to the HBT technique using avalanche photodiodes, the streak camera technique lacks a high quantum efficiency.

In this chapter we described the working principle of the software we implemented in order to extract the  $g_2(t, \tau)$  function from raw streak camera data, and different tests we performed, both with artificial signals and real signals, which confirm that the software works properly.

Our  $g_2$  measurements performed on a micropillar polariton condensate show that at low excitation power the system displays a statistics compatible with a thermal emission, while at higher excitation powers the system displays a coherent statistics. This means, in particular, that the polariton laser is characterized by a coherent emission and that in our system coherence is not affected by polariton-polariton interactions, when the number of particles is increased. We observed also that coherence is maintained all along the emission, even at longer times after that the maximum of the emission has occurred.

By using the same technique we have also studied the polarization properties of the polariton condensate, by performing the same measurement, with the signal filtered in linear polarization. Our results show that, above the polariton laser threshold, the  $g_2(t, \tau)$  function displays temporal oscillations around  $g_2(t, \tau) = 1$ , with a period that depends on the excitation regime. We showed that our results can be explained if we suppose that our micropillar displays a small linear polarization splitting and that, since condensation takes place very quickly and the energy splitting between the two polarized eigenstates is very small, the system does not have enough time to condense on the lowest energy level. Therefore it condenses on a linearly polarized state whose polarization direction changes randomly from shot to shot. Later in time, the splitting induces a precession of the polarization with a frequency related to the energy splitting. We underline that our measurement is able to detect a polarization precession which occurs on the single shot configuration and which would be completely washed out if we performed a time integrated measurement, since the linear polarization on which the system condense changes randomly from shot to shot.

Our measurements indicate that interactions play a negligible role in the intensity correlation properties of a polariton condensate. Additionally we provide a new picture in the understanding of the polarization dynamics of the condensates. The possibility of exploring the single shot dynamics with a very short time resolu-

tion ( $\sim 4$  ps), opens the way to the study of temporal correlation functions of more complex systems, as for example cross correlations in multiple pillar systems. For instance, concepts like second order tunneling in coupled pillars [111] or intensity correlations in microwires [112] can be explored.

### 3.10 Appendix

In this Appendix we report some complementary tests we performed with artificial signals.

#### Antibunched artificial signal

We can easily create an antibunched signal. This is done by defining, as for the simulated CW coherent signal presented in Section 3.5, a random distribution of photons in time, but with a fixed average number of photons in each streak. The resulting  $g_2$  function is shown in Fig. 3.29 and it is characterized by an antibunching ( $g_2 < 1$ ) which is stronger and stronger as we reduce the fixed number  $n$  of photons per pulse. What we created is something analogue to a single photon source, with the difference that in this case we have the emission of packets of fix number of photons.

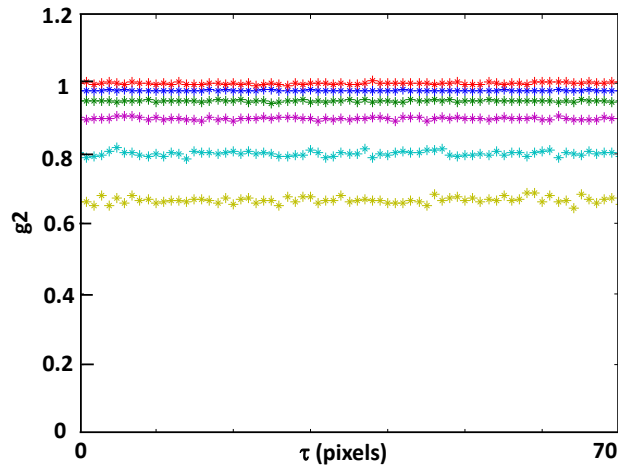


Figure 3.29: Antibunched artificial signal, created by fixing the number  $n$  of photon per streak. Calculated  $g_2(\tau)$  function for different  $n$ . Red:  $n$  not fixed (corresponding to a coherent signal), blue:  $n = 50$ , green:  $n = 20$ , pink:  $n = 10$ , light blue:  $n = 5$ , yellow:  $n = 3$ . The antibunching increases as we reduce  $n$ .

#### Simulation of some effects that can induce artificial changes in the $g_2$ function

We can use artificial signals to simulate possible experimental effects which can create non-physical artifacts in the  $g_2$  function. In particular we study the effect on the  $g_2$  function of intensity fluctuations and temporal jitter.

To study intensity fluctuations, we define, as described in Section 3.5, a random distribution of photons in time, but we impose that for a certain number of frames  $N_1$  the average number of photons has the value  $X_1$ , while for the rest of the frames  $N_2 = N_{tot} - N_1$  we impose it to have another value  $X_2$ . The results are shown in Fig. 3.30, for different values of the  $N_1/N_2$  ratio. We see that the statistics of the number

of photons per pulse is characterized by two poissonians, centered respectively on  $X_1$  and  $X_2$ , whose intensities depend on the  $N_1/N_2$  ratio. As shown in Fig. 3.30 (f) intensity fluctuations are always inducing a bunching in the  $g_2$  function. This is an artificial effect, not physical, which arises only as a consequence of a “not well done” statistical average. In fact, if we could look inside the signal (i.e. frame by frame), we would find a coherent signal with a random distribution of photons in time.

The same effect is found if we consider the pulsed coherent signal described in Section 3.5. In this case we simply suppose that for a certain number of frames the intensity of the signal goes to zero. The results are shown in Fig. 3.31 and we see that an artificial bunching is found at each considered time value along the pulse. These results tell us that we should suspect intensity fluctuations any time that we see a  $g_2$  function which is globally shifted to a value greater than one.

The last test that we want to do is related to time jitter, that can affect experimental results when we work in pulsed excitation. In our experiment, jitter is mostly related to instabilities in the streak camera trigger mechanism (but it can also be related to instabilities of the laser on its own), which cause the signal to arrive at slightly different times from shot to shot. Additionally to jitter, instability in the electronics, can cause a progressive drift of the signal in time. Both the effects affect the  $g_2$  in the same way.

In order to simulate jitter, we use the coherent pulsed signal described in Section 3.5, and we merge some frames where the signal is in a certain position in time with some other frames where the signal is in a shifted position in time, as shown in Fig. 3.32 (a) (blue and red signals, the black one being the resulting signal). The results of the calculations show that jitter affects strongly the  $g_2$  function in the rising part of the signal, while at longer times the effect is negligible. At short times, jitter causes a bunching effect followed by an antibunching effect, whose time scales are related to the jitter time scales.

We should suspect some jitter effects any time that, in a pulsed experiment, we have strong  $g_2$  modulations corresponding to the rising edge of the signal.

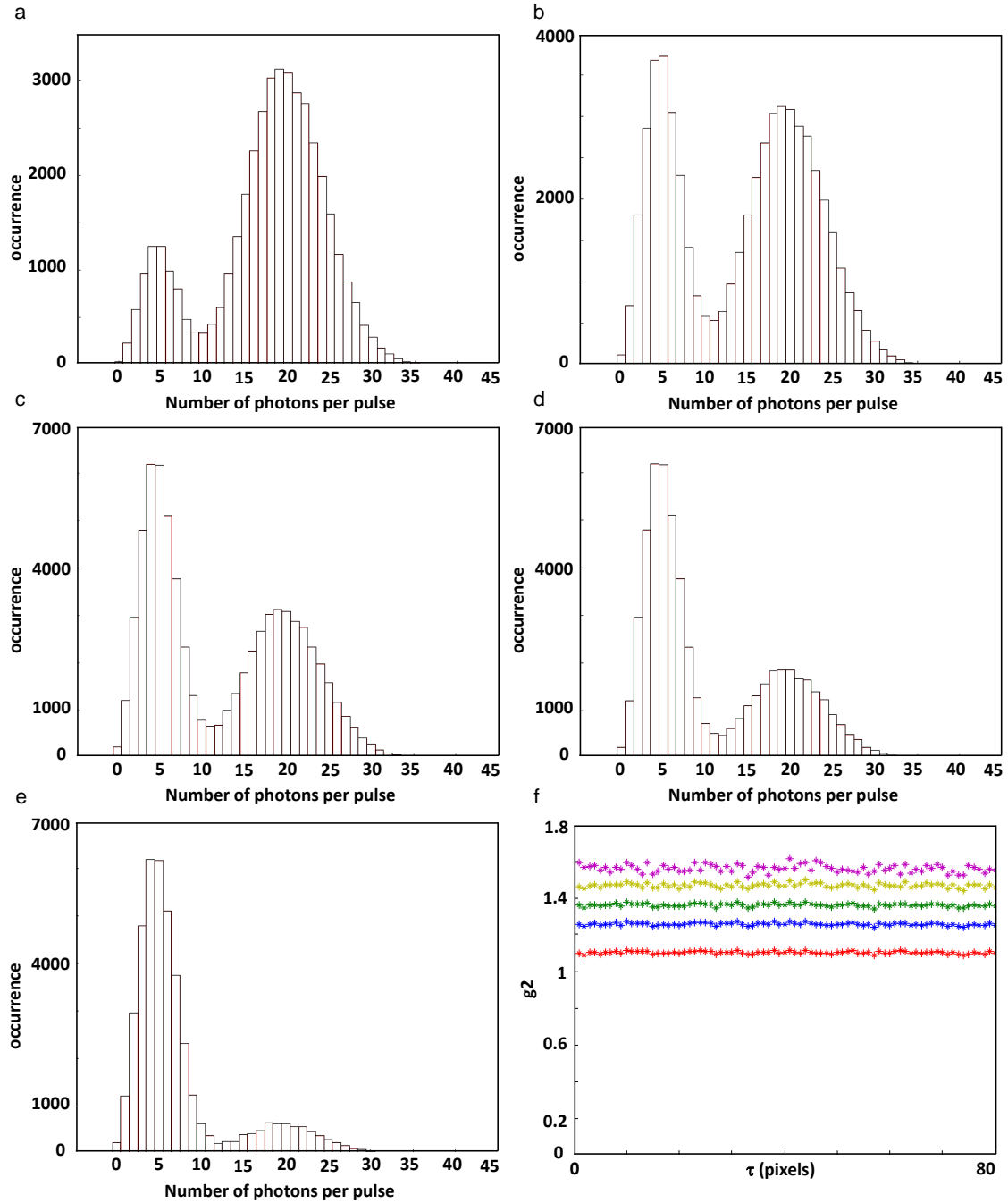


Figure 3.30: Simulated CW coherent signal with intensity fluctuations, created by merging  $N_1$  frames with  $X_1$  mean photons per streak with  $N_2$  frames with  $X_2$  mean photons per streak. The statistics of the number of photons per streak is shown in (a)-(e) for  $X_1 = 5$ ,  $X_2 = 20$ , and for different values of  $N_1$  and  $N_2$ . The signal is characterized by two poissonian distributions centered around  $X_1$  and  $X_2$ , with relative magnitudes depending on  $N_1$  and  $N_2$ . (f) shows the calculated  $g_2$  function for the different cases: red-(a):  $N_1 = 1000$ ,  $N_2 = 5000$ , blue-(b):  $N_1 = 3000$ ,  $N_2 = 5000$ , green-(c):  $N_1 = 5000$ ,  $N_2 = 5000$ , yellow-(d):  $N_1 = 5000$ ,  $N_2 = 3000$ , pink-(e):  $N_1 = 5000$ ,  $N_2 = 1000$ . The effect of intensity fluctuations is an artificial bunching of the  $g_2$  function.

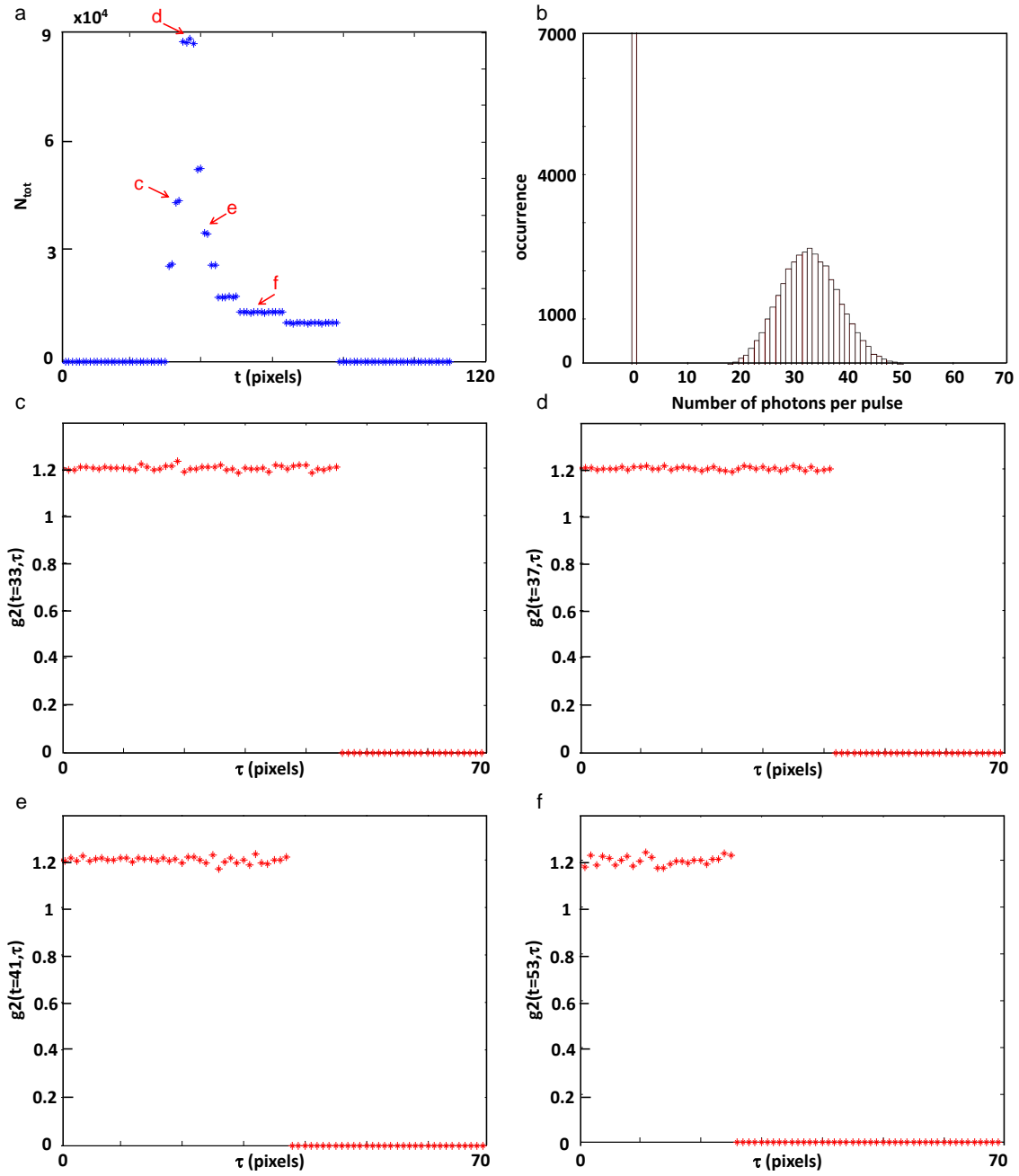


Figure 3.31: Simulated pulsed coherent signal with intensity fluctuations, created by merging 5000 frames with 20 mean photons per pulse and 1000 frames with 0 photons per pulse. (a) Total number of photons vs time. (b) Statistics of the number of photons per pulse. (c)-(f) Calculated  $g_2(\tau)$  function, corresponding to four different starting times along the pulse: (a)  $t = 33$ , (b)  $t = 37$ , (c)  $t = 41$ , (d)  $t = 53$ , showing an artificial bunching.

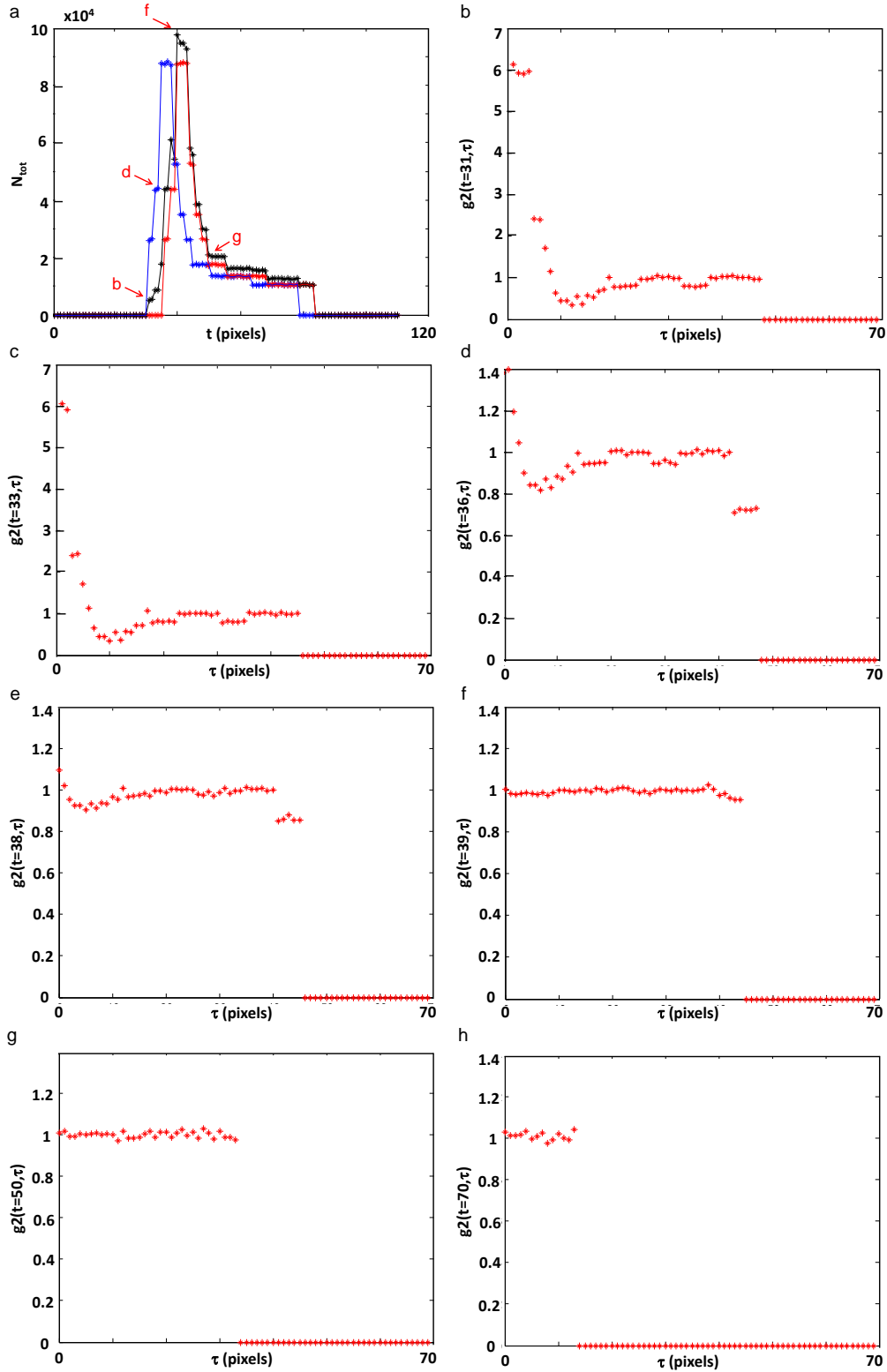


Figure 3.32: Simulated pulsed coherent signal with temporal jitter, created by merging 5000 frames of a coherent pulse (red signal) with 1000 frames of the same pulse shifted in time (blue signal) (shift in time = 5 pixels). The integrated signal is shown in black in (a). (b)-(h)  $g_2(\tau)$  function calculated for different starting times along the pulse: (b)  $t = 31$ , (c)  $t = 33$ , (d)  $t = 36$ , (e)  $t = 38$ , (f)  $t = 39$ , (g)  $t = 50$ , (h)  $t = 70$ . Jitter affects strongly the  $g_2$  function, mainly if we consider starting times in the rising part of the pulse.



# Chapter 4

## Macroscopic self-trapping and Josephson oscillations in polaritonic diatomic molecules

### 4.1 Introduction

In the previous chapter we have studied the temporal correlation properties of a single micropillar polariton condensate. We are now interested in the physics that arises as we couple two or more micropillars. As described in Chapter 2, two or more pillars can be etched one close to the other, such that they partially overlap. This gives rise to a weak photonic coupling, through the overlapping of the evanescent tails of the two single pillar optical modes. In this way we can build polaritonic analogues of diatomic molecules and polyatomic molecules. The system is easily scalable, allowing to design more complex structures, such as unidimensional chains or two dimensional lattices. Coupled micropillars arise as a flexible polaritonic platform in which the physics of nonlinear discrete systems can be studied.

The physics of nonlinear discrete systems deals in general with the dynamical behaviour of a chain of discrete coupled particles under the influence of nonlinearities. The first theoretical studies of this kind date back to the '50s, but it is starting from the '70s that they were objects of important theoretical studies, revealing fundamental differences between these discrete systems and their continuum counterparts [113]. In this context a model describing such discrete nonlinear systems was introduced, based on a discrete nonlinear Schrödinger-like equation (DNLS) [114]. The discrete nonlinear Schrödinger equation describes in a simple model a lattice of coupled harmonic oscillators with nonlinearity. In one spatial dimension, the equation has the form

$$i\frac{d\Psi_j}{dt} + U|\Psi_j|^2\Psi_j + J(\Psi_{j+1} + \Psi_{j-1}) = 0, \quad (4.1)$$

where  $\Psi_j$  is the complex mode amplitude of the oscillator at the site  $j$ , with  $j$  ranging over the 1D lattice, the term  $J(\Psi_{j+1} + \Psi_{j-1})$  accounts for the coupling of each site with the first neighbours and the term  $U|\Psi_j|^2\Psi_j$  accounts for the on-site nonlinearity.

This model is very general, and since many systems in nature are fundamentally discrete, it is expected to describe effects in systems of quite different origin. For example, this kind of physics was expected to have a role in describing energy transfer in  $\alpha$ -helical proteins [115] or the electric, optical, and magnetic properties of

polymer chains such as polyacetylene and polythiophene [116, 117].

Equation 4.1 is formally equivalent to the Bose-Hubbard model [118] originally proposed in the '60s to describe electrons in solids. It accounts for particle-particle on-site interactions, thus providing an extension of the tight-binding model (in which only the hopping term is considered) commonly used to calculate electronic bands in solids. This model is particularly interesting for high-temperature superconductivity and more recently for describing the behavior of ultracold atoms trapped in optical lattices. Moreover it is able to predict the existence of the so-called Mott insulators, in which strong repulsion between particles prevents conduction.

Yet, it is in the field of optics that nonlinear discrete systems have really found a fertile ground where they could be easily observed and studied, in particular in arrays or lattices of evanescently coupled waveguides [119, 113, 120].

These arrays consist of equally spaced identical waveguide elements, in which light hops from site to site through optical tunneling, and, in doing so, it profoundly alters the global diffraction characteristics. Since the end of the '90s, these systems have been intensively studied, both in the linear and in the nonlinear regime, with the observation of many effects in few coupled systems, 1D chains and 2D lattices. In the linear regime, these structures have provided the observation of discrete diffraction, anomalous diffraction, localization at defects, photonic Bloch oscillations, Zener tunneling, and diffractionless propagation due to dynamical localization [113, 119]. In the nonlinear regime many effects have been observed, such as the formation and propagation of discrete solitons (bright and dark) in 1D and 2D arrays, gap solitons and nonlinear Bloch oscillations (see [113, 119] for references).

More recently atomic BEC in optical lattices, have provided a new platform where the physics of discrete systems can be studied. Both the linear and the nonlinear regime have been explored, with the observation for example of Bloch oscillations and Landau-Zener tunneling, gap solitons or Josephson physics [121].

In atomic systems a good control of the collective properties is achievable, but on the other side it is challenging to access and control individual lattice sites, due to their small separation.

Optical based systems present the advantage that they allow a direct experimental access and control over individual lattice sites and they could be easily integrated in quantum opto-mechanical devices. In this context, there is a crucial drawback of photonic systems. It is related to the fact that, unlike charged particles, photons do not interact with each other and the effective interaction related to the propagation of photons in a dielectric medium ( $\chi^{(3)}$  nonlinearity) is very weak and proportional to the number of photons which are present in the system. Therefore lots of photons are needed in order to achieve observable effective interactions. Moreover the strongest optical nonlinearities are found in the vicinity of optical resonances, where absorption is usually large.

Another limitation of arrays of optical waveguides is that they don't give a direct access to the temporal dynamics, the temporal coordinate being simulated by the spatial direction of propagation [113, 119].

Polaritonic systems overcome the usual drawback of resonant absorption in optical media, by working exactly at resonance, in the regime of strong coupling between a cavity mode and a two-level emitter. In this case the nonlinearity is related to the nonlinear nature of the two-level emitter, like the exciton-exciton Coulomb repulsive interaction in a case of a quantum well embedded in the optical cavity, as it is our case. This nonlinearity is much higher than the usual optical  $\chi^{(3)}$  one, present in standard nonlinear media in the regime of transparency.

These enhanced nonlinearities are of particular interest in the system we treat here based on coupled micropillars. In fact in 1D and 2D polaritonic structures it has been demonstrated that repulsive interactions usually leads to polaritons propagating away from the excitation regions, making nonlinearities more difficult to observe [26, 78, 81]. In micropillars this drawback is overcome thanks to the lateral confinement, which forces excitons to stay in the same spatial point and therefore interact strongly [92].

At the same time polaritonic systems allow to have a direct access to the temporal dynamics. This possibility is related to the use of high quality microcavity resonators, in which light is confined for a long time in a small volume. The lifetime is long enough for the temporal dynamics to be observable. At the same time, the finite lifetime, related to photons that progressively escape out of the cavity, allows to reconstruct the state of the system at each time, since photons outside the cavity are related in a one-to-one relation with polaritons inside the cavity. The efficient optical coupling with free space is a remarkable advantage of our system, which allows not only an efficient dynamical detection, but also a high optical control of the parameters of the system, particularly over each single site.

In this chapter we describe our experimental study on the simplest system made out of two coupled micropillars: a polaritonic two-site molecule, building block for more complex discrete structures. We show that our system displays a Josephson-like dynamics typical of a two-mode coupled system. We show that in such a system highly nonlinear regimes can be reached. Moreover a high optical control over the single site parameters is achieved, which allows to externally control the dynamics. The temporal evolution of the system is imaged, with a time resolution of 4 ps, allowing a full dynamical measurement.

This study highlights the system we propose of polaritons in coupled micropillars as an interesting optical system in which the physics of nonlinear discrete system can be studied, and it shows that it is particularly suited for the study of highly nonlinear regimes.

## 4.2 Josephson oscillations

Josephson oscillations refer in general to the physics that arises as two macroscopically occupied quantum modes are coupled together through a weak barrier [123, 124]. This is actually the simplest discrete nonlinear system, in which the system of equations 4.1 reduces to two coupled equations.

In the simplest case of noninteracting particles the tunneling through the barrier gives rise to coherent oscillations in the population and phase between the two modes, widely known as Rabi oscillations. It's as we let particles interact that such a simple system starts to display more interesting behaviours. The nonlinearity induced by interactions leads to new dynamical regimes: from anharmonic oscillations up to situations in which the nonlinearity is so high that oscillations are inhibited and the system stays in a metastable regime known as macroscopic self-trapping regime. Going towards these highly nonlinear regimes a rich phenomenology is expected to take place, such as the appearance of polarization chaos [125], spontaneous symmetry breaking, pitchfork bifurcations [126, 127, 128] or the formation of highly squeezed macroscopic states [129].

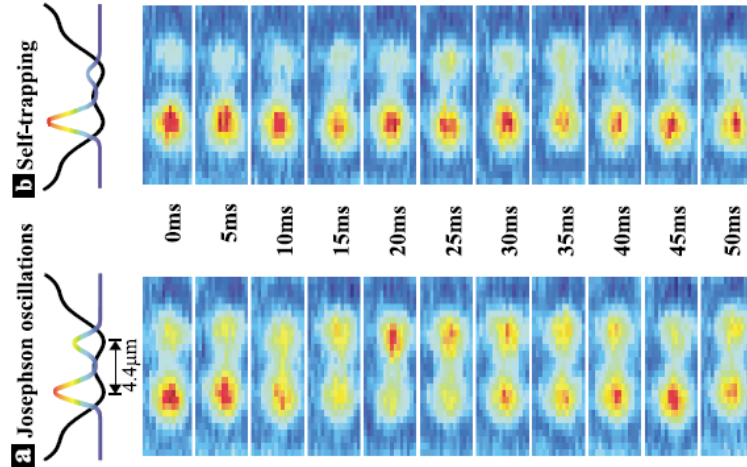


Figure 4.1: Data reproduced from [122], first experimental demonstration of macroscopic self-trapping. Two weakly linked Bose-Einstein condensates are created in a double-well potential with an initial population imbalance and the evolution in time of the population between left and right potential well is measured. By exceeding a critical threshold for the initial population imbalance, the authors could observe the transition from an oscillating regime (lower panel) to a self-trapped regime (upper panel), in which oscillations are quenched and most of the particles stay in one potential well.

Josephson oscillations were first predicted by B. D. Josephson for superconductors [130] and then observed in different bosonic systems. Harmonic oscillations in the linear regime have been observed in superconductor junctions [131, 132] or in nanoscale apertures connecting superfluid helium vessels [133].

In particular, Josephson physics has been predicted and observed in Bose-Einstein condensates of ultracold atoms in coupled traps [134, 135, 123, 124, 136], which have shown, in addition, macroscopic self-trapping [122], and collective phases in arrays of junctions [137, 138].

In Fig. 4.1 the main result of [122] obtained in the group of M. Oberthaler in Heidelberg is presented, in which the first experimental demonstration of the macroscopic self-trapping regime was obtained in a cold atomic gas. In this experiment two weakly linked Bose-Einstein condensates are created in a double-well potential. An initial population imbalance is created between the two wells and the time evolution of the population of the left and right potential well is reconstructed, through absorption technique over many experimental realizations. The data in Fig. 4.1 show the transition from an oscillating regime (lower panel) to a self-trapped regime (upper panel) as the initial population imbalance exceeds a certain threshold. In this latter case, oscillations are quenched and most of the particles stay in one potential well.

For photonic systems, mostly theoretical results have been obtained so far. Despite the observation of symmetry breaking in photonic  $\chi^{(3)}$  Kerr media [126, 139], a clear observation of nonlinear Josephson oscillations [140, 141, 142] has remained inaccessible. Just one experimental observation of linear Josephson oscillations has been reported up to now in photonic systems [143]. In this experiment, done in the group of B. Deveaud in Lausanne, two coupled polariton condensates are created under incoherent excitation in a double well potential naturally present in the random disorder of the structure of a planar CdTe microcavity (Fig. 4.2, left side). Coherent oscillations in the linear regime between the two condensates are shown to take place

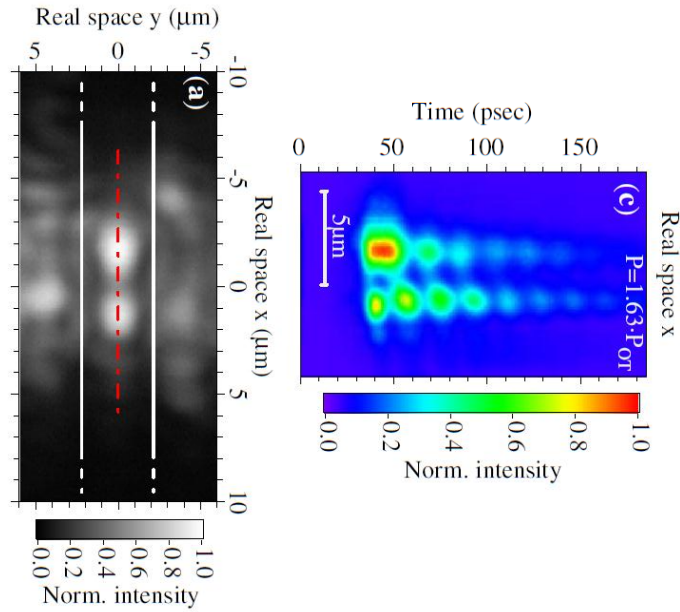


Figure 4.2: Data taken from [143], showing the first experimental demonstration of linear Josephson oscillations in an optical system. Two coupled polariton condensates are created under incoherent excitation in a double well potential naturally present in the random disorder of the structure of a planar CdTe microcavity. On the left side, an integrated real-space image of the luminescence shows the spatial profile of the two coupled condensates. On the right side the time-resolved photoluminescence is reported, showing coherent oscillations of population between the two wells.

(Fig. 4.2, right side). Despite this remarkable result, the authors couldn't achieve the nonlinear regime, probably due to their out-of-resonance pumping configuration.

In this chapter we describe our study on photonic Josephson effects in polaritonic molecules made of two coupled micropillars. Taking advantage of a resonant excitation configuration, we could exploit the high nonlinearity of polaritons, which arises from the exciton-exciton repulsive interaction and we could reach the nonlinear regimes of anharmonic oscillations and macroscopic self-trapping. The freedom in designing our molecule with the desired parameters, namely the coupling coefficient, and the possibility of fully controlling the system by optical means, gave us the possibility to explore a wide range of parameters and to study both linear and nonlinear regimes of oscillations.

### 4.3 Our system: a polaritonic diatomic molecule

Our system is a polaritonic diatomic molecule, made of two coupled micropillars, as shown in Fig.4.3 (a). As mentioned in Chapter 2, two pillars are etched one closed to the other so that they partially overlap. The narrow region between two pillars results in a tunnel barrier for the photonic component of the wavefunction. Thus polaritons can tunnel from one pillar to the other via their photonic component. The choice of the center-to-center distance determines the strength of the coupling, described by the coupling coefficient  $J$ . If we consider just the ground state modes of the right and left micropillar  $\psi_R$  and  $\psi_L$ , and we neglect polarization effects for

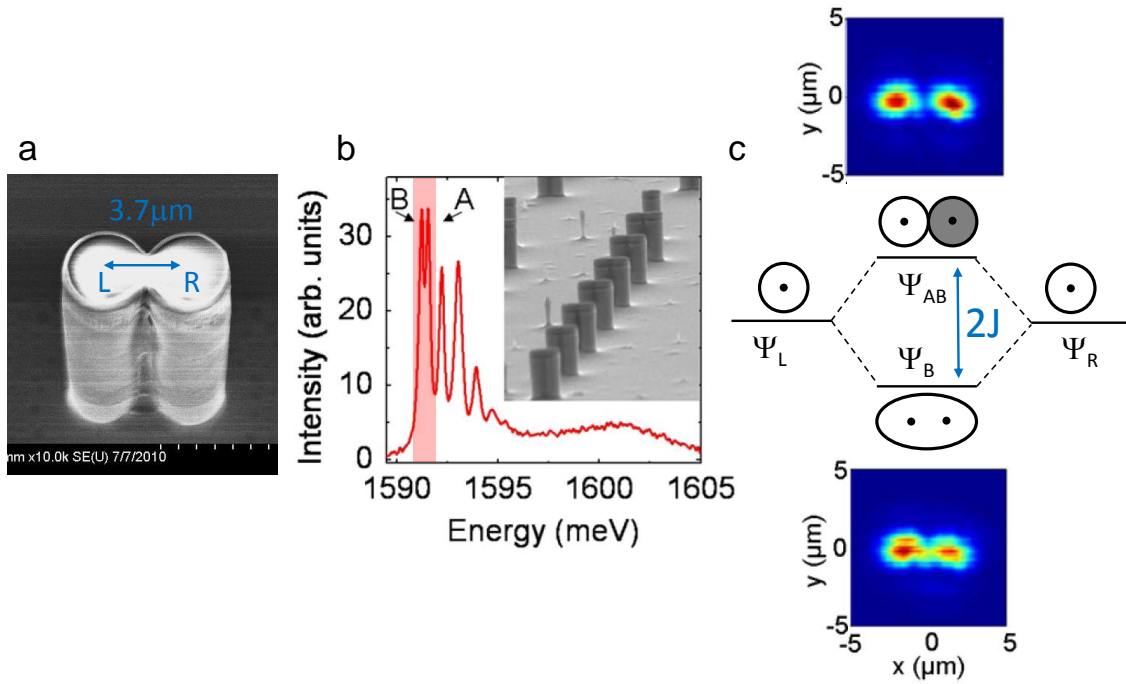


Figure 4.3: (a) Scanning electron microscope image of the diatomic molecule. (b) Experimental emission spectrum taken exciting the molecule out-of-resonance at low excitation power. In the highlighted region the levels corresponding to the ground state molecular bonding and antibonding modes are identified. Data taken from [94]. (c) Sketch showing the bonding-antibonding energy splitting equal to  $2J$  and the real-space image of the two modes. Data taken from [94].

the moment, the dynamics of our system can be described by the equations

$$i\hbar \frac{\delta\psi_L}{\delta t} = (E_L^0 + U |\psi_L|^2 - \frac{i\hbar}{2\tau})\psi_L - J\psi_R \quad (4.2)$$

$$i\hbar \frac{\delta\psi_R}{\delta t} = (E_R^0 + U |\psi_R|^2 - \frac{i\hbar}{2\tau})\psi_R - J\psi_L. \quad (4.3)$$

Apart from the decay term  $-\frac{i\hbar}{2\tau}$ , these are the two-mode coupled equations characteristic of a bosonic Josephson junction [123, 124] and correspond to equations 4.1, restricted to a two-site system.

As in Eqs. 4.1, the coupling is described by a linear term, where  $J$  is the coupling coefficient. The terms  $U |\psi_R|^2$  and  $U |\psi_L|^2$  are the nonlinear terms which account for particle-particle repulsive interactions and which are proportional to the number of particles  $N_L = |\psi_L|^2$  and  $N_R = |\psi_R|^2$  in the left and right pillars.  $E_L^0$  and  $E_R^0$  are the single particle energies of the left and right single pillar ground states and their presence into the equations takes into account the possibility in which the two pillars have different ground state energies. The additional term  $-\frac{i\hbar}{2\tau}$  is a decay term which accounts for the polariton losses due to photons escaping out of the cavity.

In the case of negligible interactions ( $U |\psi_{R,L}|^2 \sim 0$ ), and in the case the two pillars have the same ground state energy and infinite lifetime, the two equation reduces to

$$i\hbar \frac{\delta\psi_L}{\delta t} = -J\psi_R \quad (4.4)$$

$$i\hbar \frac{\delta\psi_R}{\delta t} = -J\psi_L. \quad (4.5)$$

These equations can be easily solved analytically, and give rise to the well known Rabi oscillations between the two coupled states  $\psi_R$  and  $\psi_L$ , with a frequency equal to  $2J$ . The eigenstate of the system are the bonding (symmetric)

$$\psi_B = \frac{1}{\sqrt{2}}(\psi_L + \psi_R) \quad (4.6)$$

and antibonding (antisymmetric)

$$\psi_{AB} = \frac{1}{\sqrt{2}}(\psi_L - \psi_R) \quad (4.7)$$

molecular eigenstates, which are separated in energy by an energy splitting  $2J$ , as shown in Fig. 4.3 (b) and (c). The two modes have equal densities on the two pillars, but different phase profiles, the antibonding state being characterized by a  $\pi$  phase difference between the two pillars. If the system is set in an initial condition which differs from one of the molecular eigenmodes, as for example a situation in which the initial state corresponds to a single pillar mode, it will start to oscillate coherently in time, with the particles tunneling in time between the left and right pillar. This is the main concept of Josephson oscillations.

If we include all the terms in Eqs. 4.2 and 4.3, the dynamics will be more complicated, in particular as nonlinearities and finite lifetime are taken into account, and the solution of the equations will be found numerically.

If we write  $\psi_{R,L}$  in the form

$$\psi_{R,L}(t) = \sqrt{N_{R,L}(t)}e^{i\theta_{R,L}(t)}, \quad (4.8)$$

and we define as new variables the population imbalance  $z(t) \equiv \frac{N_L(t) - N_R(t)}{N_T}$  and the phase difference  $\phi(t) \equiv \theta_L(t) - \theta_R(t)$ , we can rewrite Eq. 4.2 and Eq. 4.3 in the form

$$\frac{\hbar}{2J}\dot{z} = \sqrt{1 - z^2(t)} \sin \phi(t) \quad (4.9)$$

$$-\frac{\hbar}{2J}\dot{\phi} = \frac{\Delta E}{2J} + \frac{UN_t e^{-\frac{t}{\tau}}}{2J}z(t) + \frac{z(t)}{\sqrt{1 - z^2(t)}} \cos \phi(t). \quad (4.10)$$

Our experimental setup described in the next section gives direct access to both the population imbalance and phase difference.

## 4.4 Experimental setup

The molecule is etched out of a planar microcavity, grown by molecular beam epitaxy and made out of Bragg reflectors with 26 and 30 pairs of alternating  $\text{Al}_{0.95}\text{Ga}_{0.05}\text{As}/\text{Al}_{0.20}\text{Ga}_{0.80}\text{As}$   $\lambda/4$  layers that define a  $\lambda/2$  cavity. Three sets of four GaAs quantum wells of 70 Å in width are distributed at the three central maxima of the confined electromagnetic field. The coupling between the quantum well 1s excitons and the fundamental longitudinal cavity mode results in a Rabi splitting of 15 meV at 10K. The quality factor of the etched structure is 16000, resulting in a photon lifetime of 15 ps. We perform the experiments at zero photon-exciton detuning. The polariton lifetime is  $\sim 30$  ps.

The molecule we studied is shown in Fig. 4.3 (a). It is made of two pillars with a

diameter of  $4 \mu\text{m}$  and a center-to-center separation of  $3.7 \mu\text{m}$ , resulting in a polariton tunnel coupling of the single pillars ground states of  $J = 0.1 \text{ meV}$ .

We excite the system with a  $1.7 \text{ ps}$  pulsed laser resonant with the ground state energy of the micropillars ( $\sim 780 \text{ nm}$ ). The spectral width of the laser ( $0.4 \text{ meV} > 2J$ ) allows us to excite simultaneously the bonding and antibonding states, while preventing the excitation of the higher excited states which are much higher in energy. We use a  $10 \mu\text{m}$  wide gaussian excitation spot, covering the whole molecule. This excitation configuration allows to create a macroscopic population of polaritons simultaneously in the bonding and antibonding modes. The short pulsed excitation allows to set the initial conditions of the system which is then left to evolve spontaneously. In particular we can control the initial phase difference  $\phi(0)$  and the initial population imbalance  $z(0)$ , by changing the spot position over the molecule. As we excite the molecule slightly asymmetrically, we inject more polaritons in one pillar than in the other. In this way we set the system in an initial state which is not an eigenstate (the two eigenstate have symmetric population in the two pillars) but in a linear combination of the two. As the excitation pulse is gone, the system will start to evolve in time in a way which depends on the parameters of the system.

By changing the excitation power we can change the number of particles in the system, so we can optically control the nonlinearities and switch easily the system from the linear regime, in which  $J \gg UN_{R,L}$ , to the nonlinear regime in which  $J \ll UN_{R,L}$ .

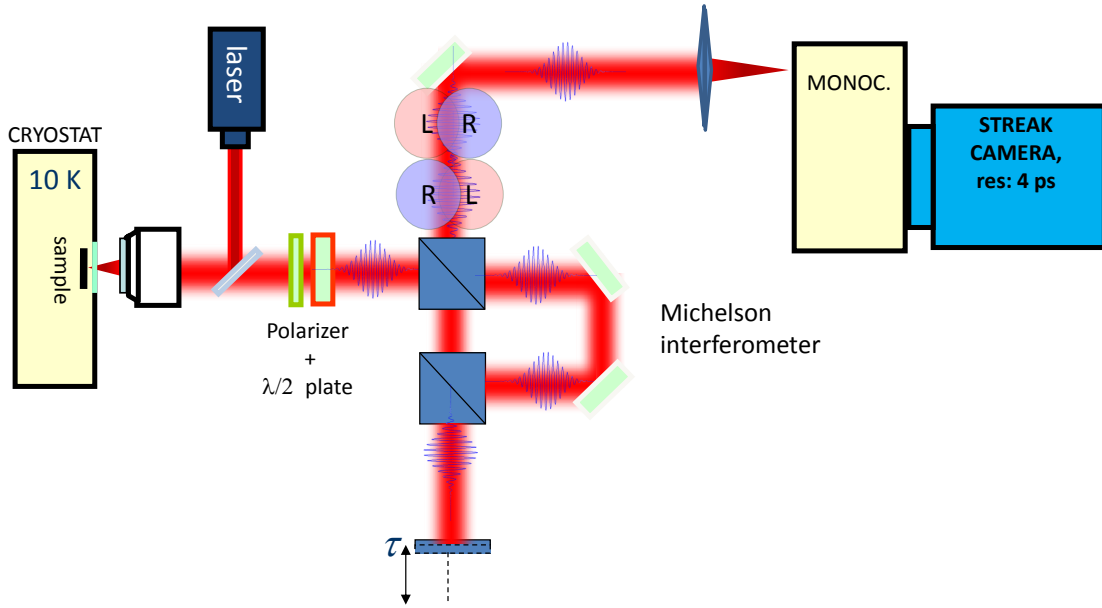


Figure 4.4: experimental setup.

The experimental setup is shown in Fig. 4.4. The pulsed laser is focused on the sample to a spot of  $\sim 10 \mu\text{m}$  by means of a microscopic objective. The sample is kept inside a cryostat cooled down to  $10\text{K}$ . We work in reflection geometry, collecting the signal emitted from the molecule with the same objective we use to excite it. The collected signal is then focused to the entrance slit of a spectrometer coupled to a streak camera with a  $4 \text{ ps}$  temporal resolution. In this way the signal is analyzed both in energy and in time. We record the evolution in time of the emitted intensity, from which we monitor the evolution of the population imbalance.

In order to get information on the phase difference, we add to our detection line a Michelson interferometer, as shown in Fig. 4.4. The signal is made interfere with a

mirror copy of itself: the signal coming from the right pillar (Fig. 4.5 (a)) interferes with the one coming from the left one (Fig. 4.5 (b)), creating an interferogram as shown in Fig. 4.5 (c). Constructive/destructive interferences appear depending on the phase difference between the emitted light from each micropillars and also from the delay between the two arms of the interferometer. By varying the delay of one of the arms with a piezoelectric stage by  $6\pi$ , we obtain an oscillating interference pattern from which we extract the phase difference  $\phi(t)$  at different delay times  $t$ , as shown in Fig. 4.5 (d). By taking a vertical slice of this phase plot (white dashed line of Fig. 4.5 (d)), we get the evolution in time of the phase difference between the right and left pillar.

Since we excite the system at resonance, we have to get rid of the laser light which is reflected by the sample and which can cover the signal emitted by the molecule. To minimize the laser stray light, we detect the signal in a cross-polarized configuration, by means of a half-waveplate and a polarizing beam splitter, as shown in Fig. 4.4. A discussion over the consequences of the cross-polarized detection is done in Section 4.7.

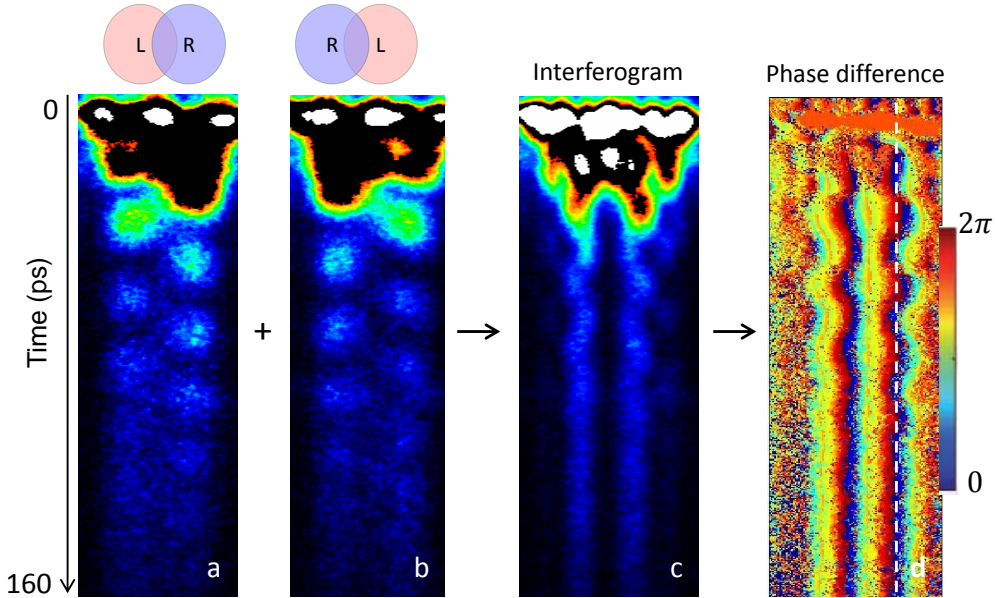


Figure 4.5: Interferometric technique allowing to reconstruct the phase information. (a) Streak camera measurement recording the evolution in time of the real-space signal emitted by the molecule. (b) Mirror copy of (a). (c) Interferogram obtained by the superposition of (a) and (b). (d) Reconstructed phase plot, showing the evolution in time of the phase difference between the right and left pillar  $\phi(t) = \phi_R(t) - \phi_L(t)$ .

## 4.5 Measurements in the linear regime: $UN_{R,L} \sim 0$

As we pump the system at low power (2.5 mW), we inject a small population of polaritons  $N_{R,L}$  in the molecule. In this case  $J \gg UN_{R,L}$  and we can neglect the nonlinear term  $UN_{R,L}$  in Eqs. 4.2, 4.3. In this linear regime there are two possible ways in which the system can evolve, depending on the value of  $\Delta E = E_R^0 - E_L^0$ .

If  $\Delta E = 0$ , which means that the two pillars have the same ground state energy, as in the sketch of Fig. 4.6 (a), we are in the Rabi oscillation regime.

If we solve numerically the coupled equations 4.9 and 4.10, we find that, as expected,

the Rabi oscillation regime is characterized by harmonic oscillation in time both in the population imbalance and in the phase difference, with a period of oscillation which is related to the coupling coefficient through the Heisenberg relation  $\tau \sim \frac{\hbar}{2J}$ . In Fig. 4.6 (b) we plot the numerical solution for the parameters  $z(0) = 0.45$ ,  $\phi(0) = 0$ ,  $\Delta E = 0$ . The period of oscillation is of the order of 21 ps, having set  $J = 0.1$  meV.

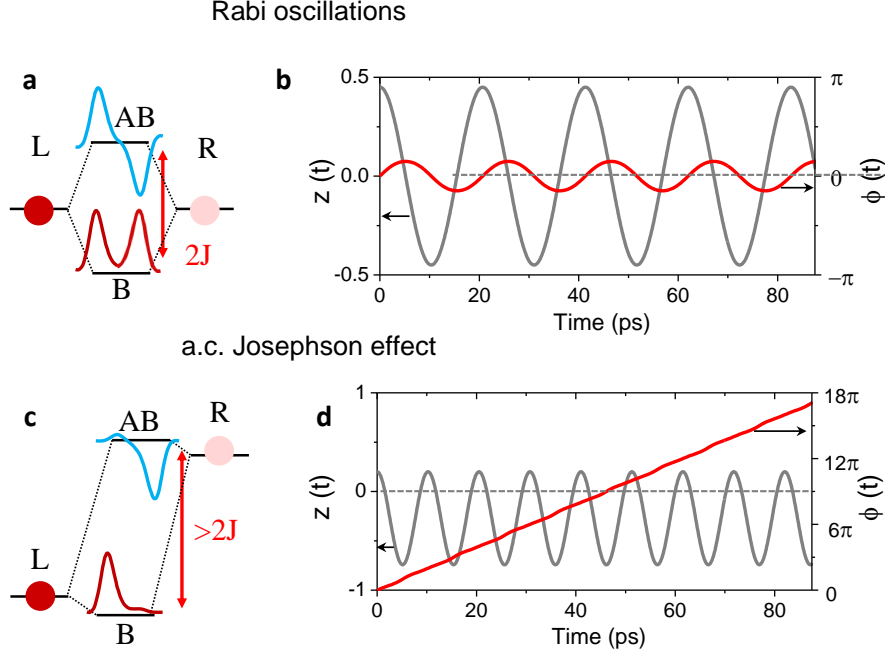


Figure 4.6: Numerical simulations for the Rabi and a.c. Josephson oscillation regimes. (a),(b) Rabi oscillation regime. (a) Sketch of the energy levels. (b) Numerical solution of Eqs. 4.9 and 4.10 with parameters  $z(0) = 0.45$ ,  $\phi(0) = 0$ ,  $\Delta E = 0$ . (c),(d) a.c. Josephson oscillation regime. (c) Sketch of the energy levels. (d) Numerical solution of Eqs. 4.9 and 4.10 with parameters  $z(0) = 0.2$ ,  $\phi(0) = 0$ ,  $\Delta E = 0.35$  meV. Gray lines: population imbalance; red lines: phase difference.

Another linear regime is found when the two single pillar ground states are at different energies  $E_R^0$  and  $E_L^0$ ,  $\Delta E > 2J$ , as in the sketch of Fig. 4.6 (c). In this case equations 4.2 and 4.3 have the expression

$$i\hbar \frac{\delta\psi_L}{\delta t} = E_L^0 \psi_L - J\psi_R \quad (4.11)$$

$$i\hbar \frac{\delta\psi_R}{\delta t} = E_R^0 \psi_R - J\psi_L. \quad (4.12)$$

If we calculate the eigenstates of the system, we find that they are asymmetric, the bonding state having a left pillar weight greater than the antibonding one, as schematically shown in Fig. 4.6 (c).

In this case the dynamics of the system is still characterized by coherent oscillations in the population imbalance, but the dynamics is accelerated. The period of oscillations is shorter, consistently with the increased bonding-antibonding splitting  $E_{AB} - E_B = \sqrt{4J^2 + (E_R^0 - E_L^0)^2}$ . Differently from the Rabi regime, this regime is characterized by a running phase difference, that is a phase difference which increases linearly in time. Figure 4.6 (d) shows the numerical solution for the choice of parameters  $z(0) = 0.2$ ,  $\phi(0) = 0$ ,  $\Delta E = 0.35$  meV, giving a period of oscillations

of  $\sim 16$  ps, shorter than in the Rabi oscillation regime.

This regime is equivalent to the so called a.c. Josephson effect, in which a constant voltage (analogous to our  $\Delta E$ ) across the superconductor junction gives rise to an alternated current through the barrier.

### 4.5.1 Rabi oscillation regime

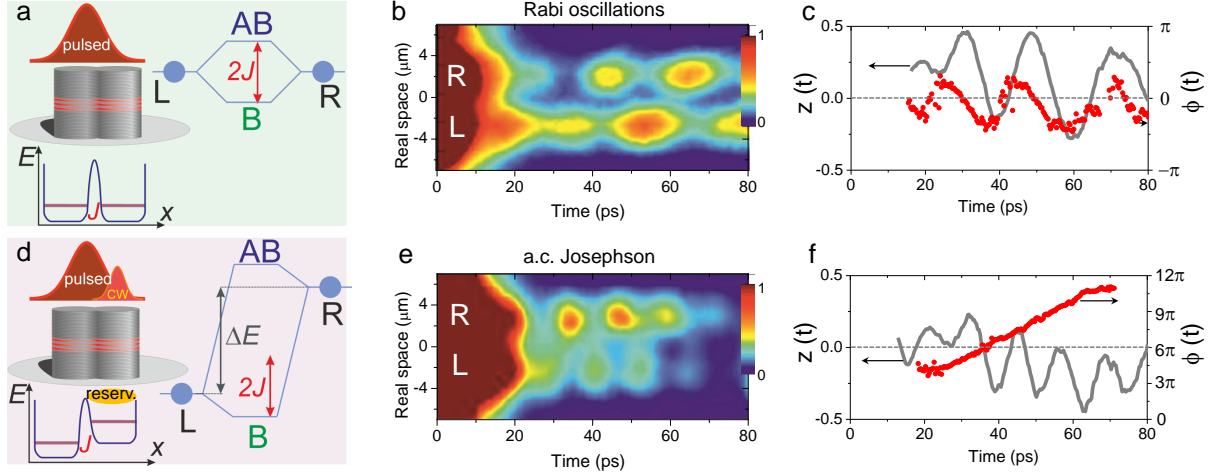


Figure 4.7: Experimental data for the Rabi ((a),(b),(c)) and a.c. ((d),(e),(f)) Josephson oscillation regimes. (a),(d) Sketches showing the excitation conditions. (b),(e) Evolution in time of the real-space emitted intensity. (c),(f) Measured population imbalance (grey) and phase difference (red). (c) shows harmonic oscillations with a frequency given by  $\hbar\omega = 2J$ . The slight asymmetry of the oscillations about  $z = 0$  might be caused by an unintentional difference in the size of the micropillars. (e),(f) The larger bonding-antibonding splitting results in faster intensity oscillations (e), and in a monotonously increasing phase difference (f, red points).

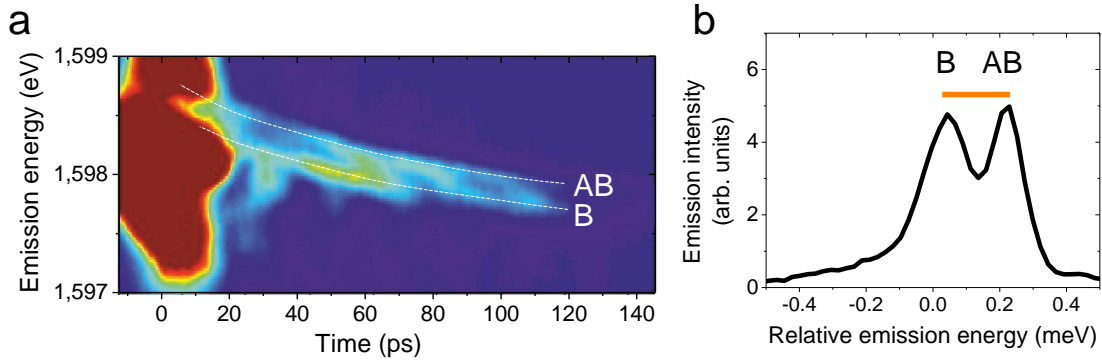


Figure 4.8: Energy resolved emission in the Rabi oscillations regime. The right panel shows a spectrum taken at 94 ps. A bonding-antibonding splitting of 0.2 meV is observed (orange bar).

As we pump our system at low power, it spontaneously oscillates in the Rabi oscillation regime. This is due to the fact that the right and left pillars are identical, so they have the same ground state energies  $E_R^0$  and  $E_L^0$ . Fig. 4.7 (b) shows the measured emitted intensity vs time, in which we clearly see the tunneling of polaritons in time from one pillar to the other. From this measurement we can extract the evolution in time of the population imbalance. By means of the interferometric

technique described in Section 4.4 we extract the evolution in time of the phase difference. Fig. 4.7 (c) shows the evolution in time of the population imbalance (in gray) and phase difference (in red). We see that both oscillate harmonically in time, with a period which is as expected  $\sim 21$  ps, corresponding to the nominal value  $J = 0.1$  meV. Our data are consistent with the numerical simulations of Fig. 4.6 (b). Figure 4.8 shows the emission resolved in time and energy, taken by imaging the emission of one of the micropillars through the spectrometer placed in front of the streak camera. As expected we observe the bonding and antibonding states with a splitting of 0.2 meV, corresponding to twice the nominal coupling energy (0.1 meV).

#### 4.5.2 a.c. Josephson regime

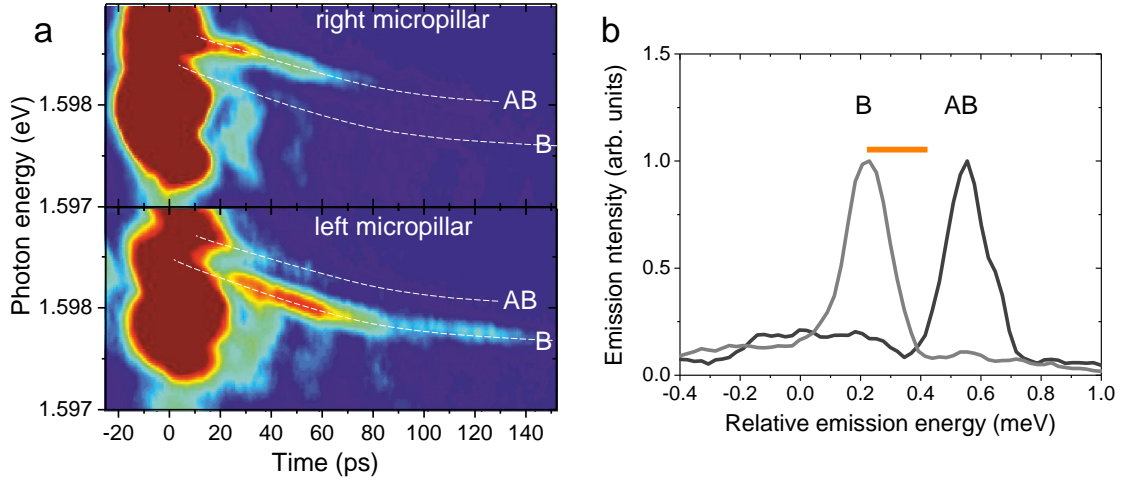


Figure 4.9: Energy resolved emission from the right and left micropillars in the a.c. Josephson oscillations regime. The right panel shows the spectra measured at a time delay of 72 ps for the left (grey) and right (black) micropillars. The orange bar indicates a splitting of 0.2 meV. A bonding-antibonding splitting of 0.38 meV is measured, from which we extract a  $E_L^0 - E_R^0$  splitting of 0.35 meV.

To have access to the a.c. Josephson regime, we need to change one of the two single pillar ground state energy levels, in order to induce an energy splitting  $\Delta E \neq 0$ . We could do this by fabricating a coupled molecule in which one of the two pillars is smaller than the other. The asymmetric confinement would make  $\Delta E \neq 0$ . Another strategy is to change the ground state energy of one of the pillars by inducing a localized blueshift by optical means. This can be done by injecting reservoir polaritons as demonstrated in [26]. In coupled polariton molecules, a previous work from our group showed that the eigenstate energy of one of the pillars can be modified by the presence of the reservoir [94]. To create such excitonic reservoir, we use a second CW laser, which is set out-of-resonance ( $\sim 730$  nm) and focused on just one of the two pillars, the right one in our case, as sketched in Fig. 4.7 (d). The induced reservoir is large enough to induce a blueshift on the right pillar, but small enough not to alter the population of the resonantly excited states. The induced blueshift is of about 0.35 meV. Fig. 4.7 (e) shows the measured emitted intensity vs time, in which we see that the dynamics is accelerated, the polaritons tunneling faster from one pillar to the other. In Fig. 4.7 (f) we extract the evolution in time of the population imbalance (in gray) and phase difference (in red). We see that the population imbalance oscillates harmonically with a period which is shorter than in the Rabi regime, while the phase difference grows linearly in time, as expected from

our numerical simulations (Fig. 4.6 (d)).

This data are analogous to the observations done by the group of Deveaud [143]. The difference is that in our experiment the energy splitting  $\Delta E$  is induced by the interaction with the excitonic reservoir created by the CW laser, while in the Deveaud's experiment the splitting is naturally present due to the spontaneous asymmetry of the double well potential. An advantage of our configuration is that we can tune the blueshift by changing the power of the CW excitation.

Another advantage of our system is that in our case the initial phase difference  $\phi(0)$  is well defined, since we excite the molecule resonantly, while in the results of [143], since the system is excited out-of-resonance, the initial phase changes randomly from shot to shot. This is affecting in particular their measurement of the phase difference, which display a more complicated behaviour if compared to what is expected from the theory.

In Fig. 4.9 we show the emission resolved in time and in energy for the right (upper panel) and left micropillar (lower panel). Emission from the bonding state is more clearly seen in the left micropillar while the antibonding emission is clearer in the right micropillar. This is due to the fact that, as highlighted in Section 4.5 and sketched in Fig. 4.6 (c), the wavefunction of the antibonding state has a right pillar weight greater than the bonding state (whose center of gravity is shifted towards the left pillar). This is the reason why oscillations in this regime are asymmetric (Fig. 4.7 (e),(f)). As expected, the bonding-antibonding splitting is greater than the value of 0.2 meV measured in the symmetric case of the Rabi oscillation regime. In this case we measure a bonding-antibonding splitting of 0.38 meV, which corresponds to a  $E_L^0 - E_R^0$  splitting of 0.35 meV. Note that the energy difference between bonding and antibonding states is constant all along the emission, evidencing negligible polariton interactions within the condensates.

## 4.6 Measurements in the nonlinear regime:

$$UN_{R,L} \gg J$$

As we increase the pump power (27 mW), we inject more and more polaritons in the system. As  $N_{R,L}$  grows, repulsive interactions between polaritons start to play a role in the dynamics, leading the system to the nonlinear regime, where  $UN_{R,L} \gg J$ . It is in this regime that the most interesting effects take place, with phenomena ranging from anharmonic oscillations up to situations in which the nonlinearity affects the system so strongly that oscillations are quenched. This is the case of the macroscopic self-trapping regime, in which the system stays in a metastable state where tunneling from one pillar to the other is strongly inhibited. It is in the nonlinear regime that the out-of-equilibrium nature of our system also plays a significant role. The finite lifetime of polaritons combined with the nonlinearity leads to new effects, which are difficult to observe in other systems.

### 4.6.1 Anharmonic oscillations

A first nonlinear regime can be obtained when we pump the system at high power, with a pump spot placed slightly asymmetrically on the molecule. The excitation conditions are similar to those of the Rabi regime described above, but the number of polaritons in the system is significantly larger and repulsive interactions between

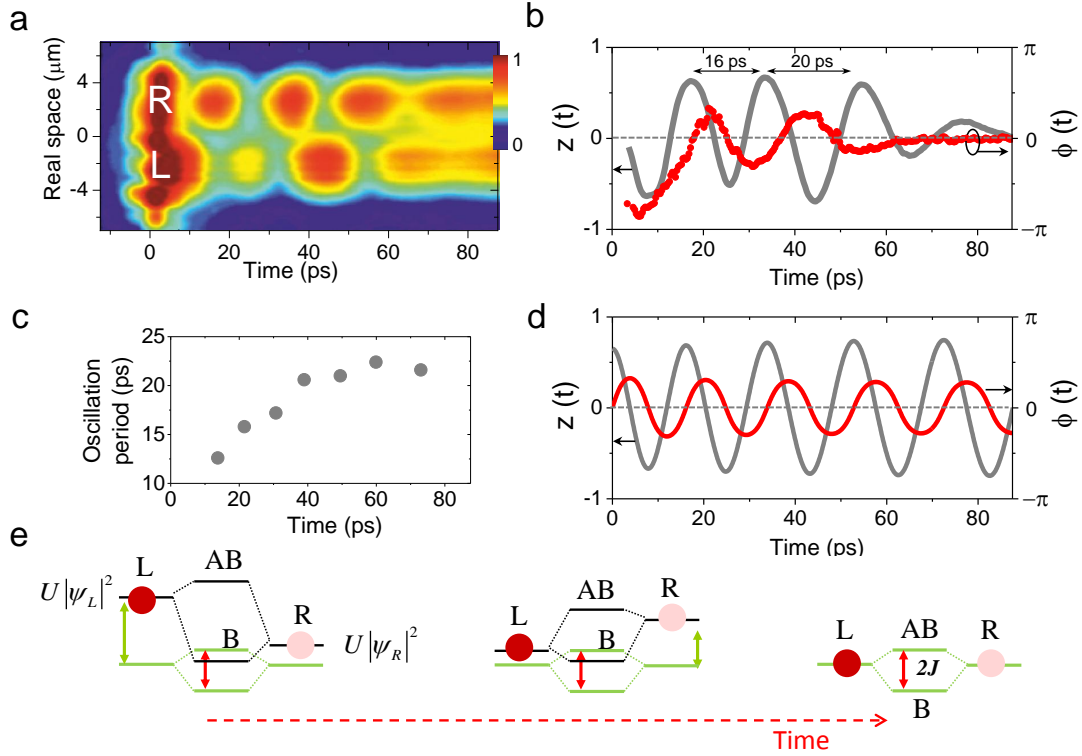


Figure 4.10: Anharmonic oscillation regime. (a) Evolution in time of the real-space emitted intensity. (b) Measured population imbalance (grey) and phase difference (red), evidencing a monotonously increasing oscillation period, explicitly reported in (c). The apparent damping of the oscillations observed in (a),(b) arises from pulse-to-pulse power fluctuations in the excitation laser. (d) Result of the simulations based on Eqs. 4.9 and 4.10 with initial parameters  $z(0) = 0.62$ ,  $\phi(0) = 0$ ,  $J = 0.1 \text{ meV}$ ,  $UN_T(t=0) = 1.2 \text{ meV}$ ,  $\tau = 30 \text{ ps}$ . (e) Sketch showing the evolution in time of the energy levels, finally recovering the linear condition.

them are no more negligible. Interactions within each pillar induce a local blueshift of the single pillar energy level which is proportional to the occupation number  $N_{R,L}$ . As sketched in Fig. 4.10 (e), this blueshift corresponds to an increased bonding-antibonding splitting ( $> 2J$ ), which results in faster oscillations in the population imbalance and phase difference. Moreover oscillations are anharmonic, because of the dynamical renormalization of the right and left energy levels as the particles tunnel from one pillar to the other. At longer time, the dynamics is affected by the finite polariton lifetime. The progressive reduction of the number of particles  $N_{R,L}$  in the system corresponds to the progressive reduction of the induced blueshift. The period of oscillations increases, finally recovering the linear regime, in which interactions are negligible (right side of Fig. 4.10 (e)). In Fig. 4.10 (a) and Fig. 4.10 (b) we see that as expected the dynamics is accelerated at shorter times, with a period of oscillations of about 16 ps, while at longer times the period increases, finally recovering the value  $\sim 21 \text{ ps}$  characteristic of the linear regime. The evolution in time of the period of oscillations is reported in Fig. 4.10 (c). Our experimental data are well reproduced by numerical simulations (Fig. 4.10 (d)) with parameters  $z(0) = 0.62$ ,  $\phi(0)=0$ ,  $UN_T(t=0) = 1.2 \text{ meV}$ ,  $\tau = 30 \text{ ps}$ .

The dynamical renormalization of the energy of each pillar when the population oscillates can be directly accessed in the energy resolved measurements shown in

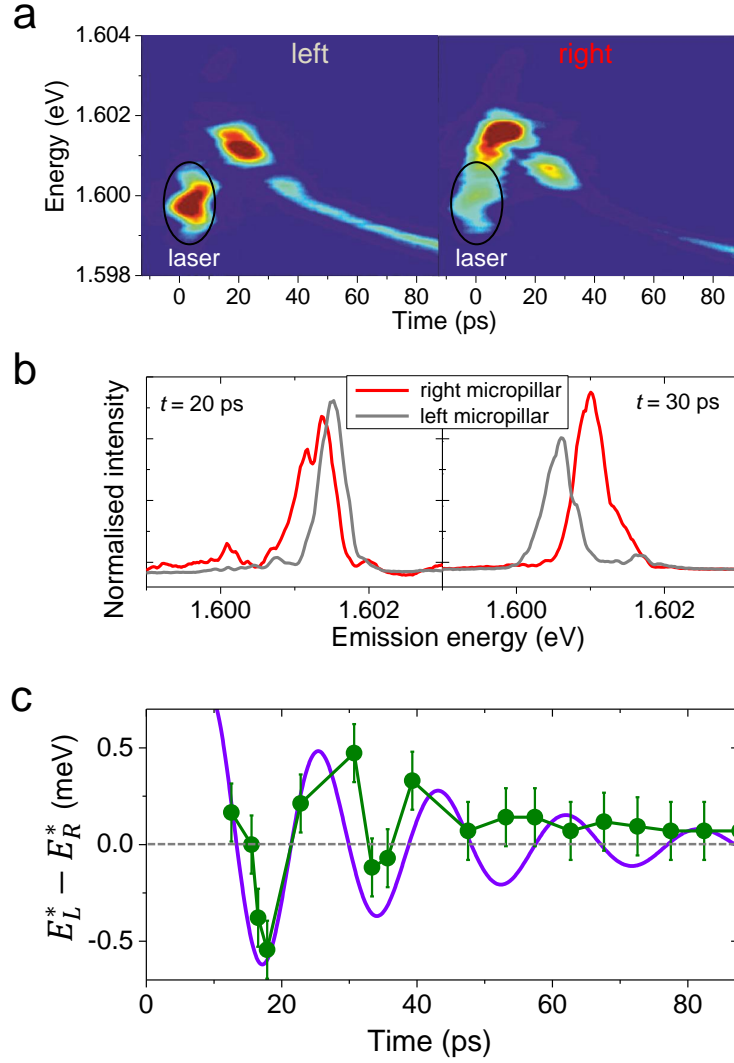


Figure 4.11: (a) Energy- and time-resolved emission from each micropillar in the anharmonic oscillation regime. The time-dependent energy splitting can be extracted from the position of the emission of the left and right micropillars at each time delay, as shown for  $t = 20$  and  $30$  ps in (b). (c) Energy difference between the ground state energies of each micropillar measured experimentally (dots) and simulated (solid line). Error bars show the spectral resolution of the experiment.

Fig. 4.11 (a). The oscillations in the energy resolved dynamics are related to the fact that, as explained in the case of the a.c. Josephson oscillations, the blueshifted pillar, in this case the one with the highest population, is closer to the antibonding state, while the less populated one is closer to the bonding state. We see that, at short times, the renormalization induced by interactions blueshift the ground state energy of both the micropillars above the energy of the excitation laser. From this measurement we can extract the renormalized energy levels  $E_L^*$  and  $E_R^*$  for the left and right pillar (as shown in Fig. 4.11 (b) for  $t = 20$  ps and  $t = 30$  ps). Fig. 4.11 (c) shows the oscillation in time of the energy difference  $E_L^* - E_R^*$  (green dots). We see that a dynamical renormalization takes place at short times, as the particles tunnel from one pillar to the other. The oscillations are damped in time as the system recovers the linear oscillation regime. The solution of Eqs. 4.9, 4.10 with the same parameters used for the simulation in Fig. 4.10 (d) reproduces well the experimental observations.

## 4.6.2 Macroscopic self-trapping

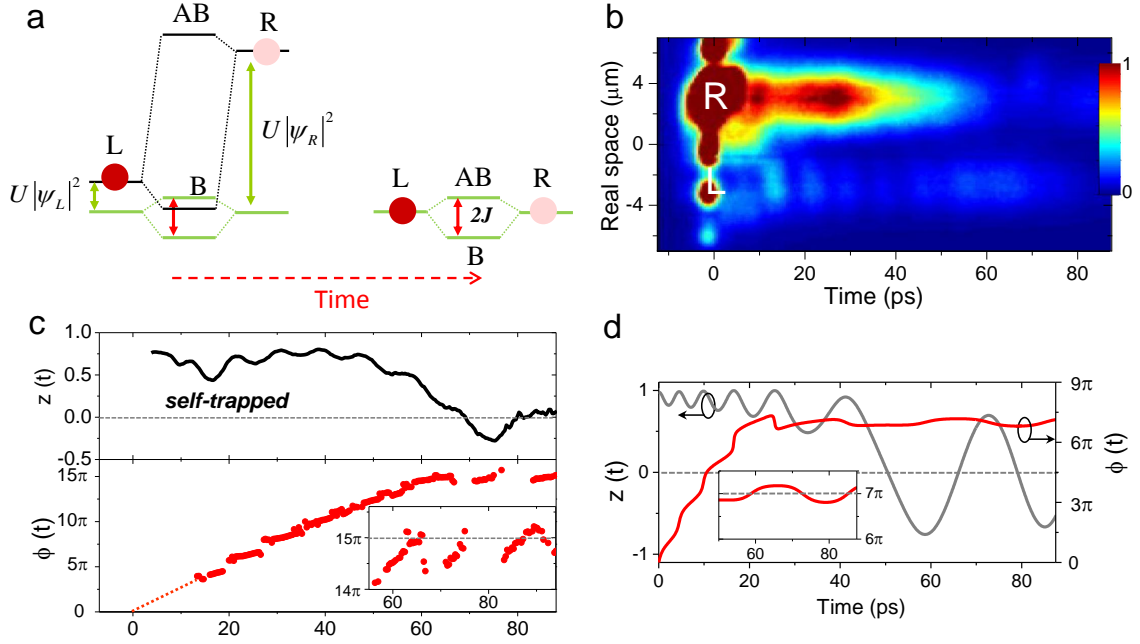


Figure 4.12: Macroscopic self-trapping regime. (a) Sketch showing the renormalized energy levels at short times (self-trapped) and long times (harmonic oscillations) for a highly asymmetric excitation at high density. (b) Evolution in time of the real-space emitted intensity. (c) Time evolution of the population imbalance and phase difference. At short times particles are self-trapped in the right micropillar, and the phase difference  $\phi(t)$  increases linearly with time. At  $t \sim 60$  ps, the escape of particles out of the microcavity induces a transition to an oscillating regime around  $\phi = 15\pi$  (the inset showing a zoom over the harmonic oscillations). The red dotted line is an extrapolation of the phase evolution towards  $t = 0$ . (d) Result of the simulations based on Eqs. 4.9 and 4.10 with initial parameters  $z(0) = 0.98$ ,  $\phi(0) = 0$ ,  $J = 0.1$  meV and  $UN_T(t=0) = 5.5$  meV.

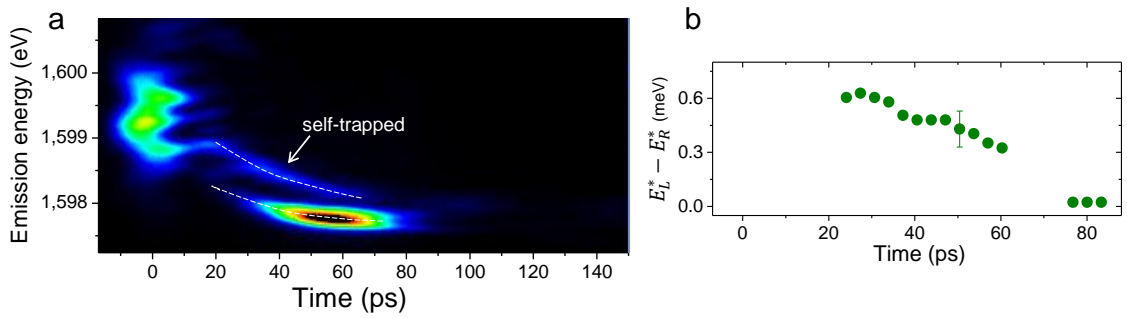


Figure 4.13: (a) Energy resolved emission in the self-trapping regime coming from the left micropillar (the low density one). (b) Energy difference between the ground states of the two micropillars extracted from (a). At short times a large bonding-antibonding splitting is observed. At around  $\sim 60$  ps, the splitting is reduced to  $2J$ , corresponding to the transition from the self-trapped state to harmonic oscillations. Error bars show the spectral resolution of the experiment.

The nonlinearity can also affect the dynamics so strongly that oscillations are inhibited. This is the case of the macroscopic self-trapping regime. In this case we pump the molecule still at high power but with the pump spot positioned highly asymmetrically on the molecule, so that mostly one of the two pillars is pumped, the

right one in our case. The blueshift induced by interactions is strongly asymmetric, being much higher on the right pillar, where most of the particles are injected. As sketched in Fig. 4.12 (a), the resulting bonding-antibonding splitting is so high ( $\Delta E \gg 2J$ ) that oscillations are quenched and the system is in a quasi-metastable state, where most of the particles stay on the right pillar. This is clear as we look at the emitted intensity in Fig. 4.12 (b) and at the extracted evolution of the population imbalance (Fig. 4.12 (c)), which stays well above zero. In this regime the phase grows linearly in time, as shown in Fig. 4.12 (c), red curve. Again, later in times, the finite polariton lifetime affects the dynamics. As the number of particles in the system decreases, the induced blueshift progressively reduces, up to a point in which oscillations are recovered and the system is back to the linear regime. As shown in Fig. 4.12 (c) at longer times, both the population imbalance and the phase difference show quasi-harmonic oscillations. This is well reproduced by our simulations as shown in Fig. 4.12 (d).

Something remarkable is that, as the system leaves the self-trapped regime, oscillations in the phase difference take place around  $\pi$ , even if the system was prepared with the initial condition  $\phi(0) = 0$ , since both the pillars are excited in phase by the same laser pulse. This is due to the fact that the self-trapped state results to be very closed to the antibonding state, which is characterized by a  $\pi$  phase difference between the right and left pillar. As the system leaves the self-trapped state, oscillations are recovered around this point in which the phase difference is equal to  $\pi$ . Note also that as the system gets out from the self-trapped regime, the oscillation period is longer than 21 ps, expected from the value of  $h/2J$ . This behaviour is expected from the residual nonlinearity, when oscillations are around  $\phi = \pi$  [124]. This is very different from the case of Fig. 4.10, where the nonlinearity causes oscillations to be shorter than  $h/2J$  around  $\phi = 0$ .

Fig. 4.13 (a) shows the energy resolved emission coming from the left micropillar (the low density one). By measuring the bonding-antibonding splitting we can extract the energy difference  $E_L^* - E_R^*$  of the renormalized left and right states  $E_L^*$  and  $E_R^*$ , shown in Fig. 4.13 (b). At short times a large bonding-antibonding splitting is observed. At around  $\sim 60$  ps, the splitting is reduced to  $2J$ , corresponding to the transition from the self-trapped state to harmonic oscillations, as in Fig. 4.12 (c). The self-trapped regime was observed in atomic BEC [122]. Our experiment reports the first observation of the macroscopic self-trapping regime in a photonic system. Moreover it is the first demonstration of the dynamical formation of  $\pi$  oscillations from the self-trapped regime. This dynamical behaviour is characteristic of our system, in which the high nonlinearity combines with the finite polariton lifetimes.

## 4.7 Polarization rotation

We now discuss the consequences of our cross-polarized detection configuration. Our molecule presents a linear polarization splitting along a non-trivial direction (different from the crystallographic directions) [110]. Similar splittings, with a magnitude between 10-50  $\mu\text{eV}$  were observed in GaAs planar microcavities via their effects on the pseudospin precession of polaritons [144, 76]. The axis of the splitting depends on the exact position on the wafer and it is, thus, molecule dependent. In the polaritonic molecules we have studied, we inject polaritons with linear polarization parallel to the molecule axis, which coincides with one of the highly symmetric crystallographic directions of the GaAs matrix but not necessarily with the splitting axis. Detection is performed selecting a polarization opposite to that of the excita-

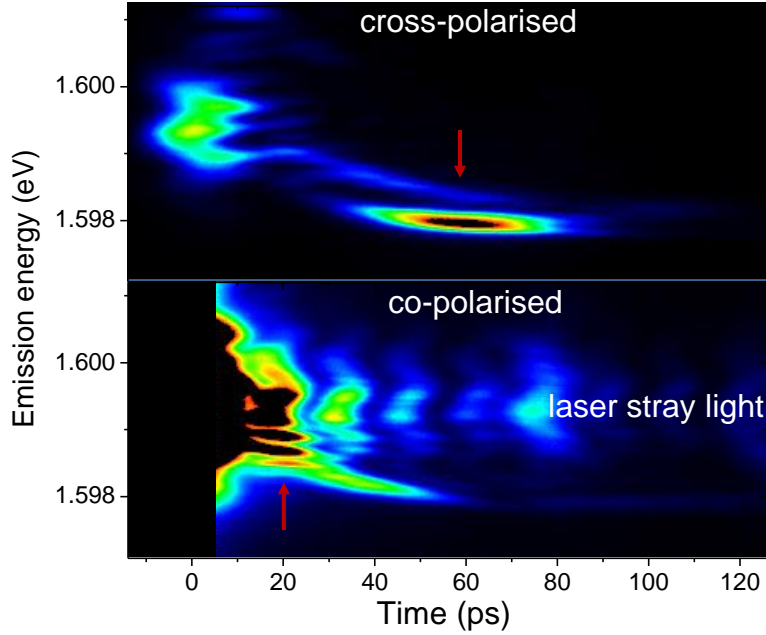


Figure 4.14: Energy resolved emission from the left pillar in the self-trapping conditions (Fig. 4.13). The upper panel shows the emission with detection cross-polarized with respect to the linear polarization of excitation. The maximum intensity is observed at a delay of 56 ps (red arrow). In co-polarized detection (lower panel), the maximum of the emission takes place much earlier (red arrow), evidencing the rotation of the polarization of emission caused by a polarization splitting.

tion in order to avoid a strong stray laser light reflection in the detector. Initially, the injected polariton gas is polarized parallel to the excitation laser. Therefore the observation efficiency is low. The pseudospin precession induced by the linear polarization splitting present in the molecule rotates the axis of polarization allowing us to detect the emission in cross-polarization. We can directly observe the polarization rotation by partially uncrossing the detection polarizer. This is shown in Fig. 4.14 for the left pillar in the self-trapped case. The upper panel shows the emission with detection cross-polarized with respect to the linear polarization of excitation. The maximum intensity is observed at a delay of 56 ps (red arrow). In co-polarized detection (lower panel), the maximum of the emission takes place much earlier (red arrow). From these images we can extract a polarization rotation period of  $\sim 100$  ps corresponding to a polarization splitting of  $\sim 40 \mu\text{eV}$ .

We can now provide an overall picture of the emission dynamics shown in Figs. 4.7-4.13. The time evolution of the emission reflects the interplay between the continuous decay of the density caused by the escape of photons out of the cavity (exponential decay with a lifetime of 30 ps), and the polarization rotation with a period of  $\sim 100$  ps. This interplay results in a detected emission which has an almost constant intensity in the first  $\sim 100$  ps. Indeed, at short times the number of particles in the system is very high but they do not have the time to significantly rotate their polarization. At later times, the number of particles has decreased but their polarization becomes parallel to that of the detection optics. Note that the polarization dynamics does not affect the population imbalance and phase difference dynamics studied in our work and described by Eqs. 4.9 and 4.10. The population imbalance measures the normalized difference in the number of particles in the two micropillars at each instant of time. It is thus not affected by the time evolution

of the total emission. In the same way, the measured phase difference shows the instantaneous phase difference between left and right sites. In order to check this explicitly we have performed experiments with a detection of polarization parallel to that of excitation (not shown). We observe the same phase difference and population imbalance dynamics as those reported in orthogonal polarization.

## 4.8 Conclusion and perspectives

In this chapter we described our experimental study on the dynamical behaviour of a resonantly excited polaritonic diatomic molecule made of two coupled micropillars. Our molecule displays the behaviour typical of a bosonic Josephson junction, characteristic of a system in which two macroscopically occupied modes are weakly coupled through a tunnel barrier. By optically controlling the parameters of the system we explored both the linear and nonlinear regimes of oscillations. We observed Rabi oscillations and the optical analogue of the a.c. Josephson effect. Taking advantage of the high nonlinearities of polaritons, we could reach the regimes of anharmonic oscillations and the macroscopic self-trapping regime. In this regime the nonlinearity is able to drastically affect the dynamics, quenching oscillations and leading the system to a metastable state in which most of the particles stay in one pillar.

We could also observe new dynamical effects, which arise due to the out-of-equilibrium nature of polaritons and hardly achievable for example in atomic systems, like the dynamical transition from the self-trapping regime to  $\pi$  coherent oscillations.

If compared to other optical systems, micropillars have the advantage that they are well coupled to the free space and therefore they allow on one hand a high optical control of their parameters at the single site level, on the other hand the possibility to easily image and detect the temporal evolution of the system. Moreover, this system is easily scalable, the diatomic molecule could be extended to more complex molecules up to two dimensional lattices, in which each site has the same physical properties and the coupling between two sites can be engineered by choosing the center-to-center distance of two micropillars. This is a remarkable advantage of our system if compared for example to micropillar embedded quantum dots, that suffer from the significant drawback that neither the spatial position of individual dots, nor the exact position of the electronic transitions can be controlled during the growth stage, as the different dots self-organize at random positions with random sizes.

The Josephson physics we have studied in the diatomic molecule could be therefore extended to more complex geometries opening the way to the study of nonlinear discrete physics in a polaritonic platform.

The observation of highly nonlinear regimes on one hand opens the way to the study of highly nonlinear many-body effects, such as polarization chaos [125], spontaneous symmetry breaking, pitchfork bifurcations [126, 127, 128] or the formation of highly squeezed macroscopic states [129]. On the other hand, it highlights our polaritonic molecule as a possible system for reaching the quantum regime of strongly interacting particles. A strongly correlated micropillar-based system would be a promising quantum simulator in which for example quantum phase transitions as the superfluid-to-Mott transition could be reached. Moreover it would allow to explore the mostly unexplored physics of out-of-equilibrium strongly correlated particles, with the observation for example of the effects predicted in [37, 38, 145].

The first building step in the study of strongly correlated micropillars would be the experimental demonstration of the photon blockade effect [36], in which nonlinearity

manifests at the single cavity level, inhibiting the presence of two polaritons at the same time inside the cavity. In our case this means in particular a regime where interactions are strong if compared to polariton lifetime ( $U \gg \gamma$ , where  $\gamma$  is the inverse of the polariton lifetime). In the hypothesis of a  $U \propto 1/L^2$  scaling, where  $L$  is the characteristic length of the lateral confinement, it is found that micropillars with a submicron lateral size would be required. It is not obvious that such structures could be realized and would keep the high quality factor typical of our micropillars. Alternative strategies to overcome this difficulty may be to take advantage of the reinforced interaction potential between the hybrid direct/indirect excitons first studied in [146] or of the quantum interference mechanism proposed in [147] or [148]. The extension of this effect to a system of few coupled cavities up to two-dimensional lattices would lead to the realization of strongly correlated photonic systems, with the possibility of observing for example the superfluid-to-Mott-insulator transition [149, 150, 151, 152] or the generation of a Tonks-Girardeau gas of fermionized photons [153].

In the perspective of the realization of strong interactions in micropillars, another road will open, related to the combination of strong interaction effects with artificial gauge fields. In the next chapter we will see how the engineering of coupled micropillar structures with a particular geometry, in the specific case a closed geometry, can lead to the experimental realization of effective spin-orbit couplings and, more in general, artificial magnetic fields. The combination of strong nonlinearities with artificial gauge fields would lead to new and unexpected phenomena.

# Chapter 5

## Spin-orbit coupling in a benzene-like polaritonic molecule

### 5.1 Introduction

In the previous chapter we have studied the physics that arises when we couple two micropillars, creating a polaritonic diatomic molecule. We have studied the temporal dynamics of such a system under resonant pumping conditions, highlighting the role of polariton-polariton interactions, which are able to drive the system to highly nonlinear regimes. Now we will extend our study to more complex structures, in which more than two pillars are coupled together, giving rise to polaritonic analogues of polyatomic molecules and 2D lattices.

Again in this case our system can be described by the discrete nonlinear Schrödinger equations 4.1. In the case of negligible interactions, we can neglect the term  $U |\Psi_j|^2 \Psi_j$ , and these equations reduce to the tight-binding model, which is commonly used to calculate the orbitals of molecules and the electronic bands of solids.

The high scalability of our system allows to design structures with high freedom in the choice of the geometry, and extend them to create 2D lattices in which the engineering of optical analogues of electronic bands in solids can be realized.

An example of such bands in 1D has been recently realized in our group, by modulating transversally a microwire. In such a system, as polariton-polariton interactions are taken into account, highly nonlinear localized states can be observed, such as gap solitons [90].

Coupled micropillars are suited structure in which this physics can be extended to 2D, and in particular 2D lattices can be realized. A remarkable example is a honeycomb lattice [93, 84], i.e. an optical analogue of graphene, which is recently attracting lot of interest due to its peculiar electronic and optical properties [154]. One of the most interesting properties of graphene is its linear dispersion close to the Fermi level. As a consequence, low energy excitations behave as massless, chiral Dirac particles, mimicking the physics of quantum electrodynamics for massless fermions. Hence many of the unusual properties of QED can show up in graphene, such as anomalous integer quantum Hall effect [155, 156], Klein physics [157, 158] or unusual mesoscopic effects [159, 160].

In real two dimensional materials such as graphene, the microscopic properties are hard to access experimentally because of the short length and timescales involved. In this context our polaritonic structures can act as a simulator, in which an analogue system is created, whose typical length and temporal scales allow a direct

manipulation and detection. Compared to other simulators, such as cold atoms in optical lattices, optical based systems have the advantage that they allow experimental access and control over individual lattice sites, and they can be eventually integrated in quantum opto-mechanical devices for quantum information processes. The aforementioned freedom in the design of coupled pillar structures, allows moreover to engineer systems with peculiar topologies and band structures. This opens the possibility to engineer polaritonic structures displaying artificial magnetic fields and spin-orbit couplings, in particular as the spin degree of freedom of polaritons is taken into account.

In this chapter we present an intermediate situation between the diatomic molecule and a 2D lattice, namely a benzene-like molecule, made of six coupled micropillars placed in a hexagonal configuration. We show that the closed geometry combined with the polaritonic spin degree of freedom, gives rise to peculiar molecular eigenstates, which are characterized by non-trivial spin patterns. We show that this observation can be related to the presence of an effective spin-orbit coupling.

## 5.2 Our system: a polaritonic benzene-like molecule

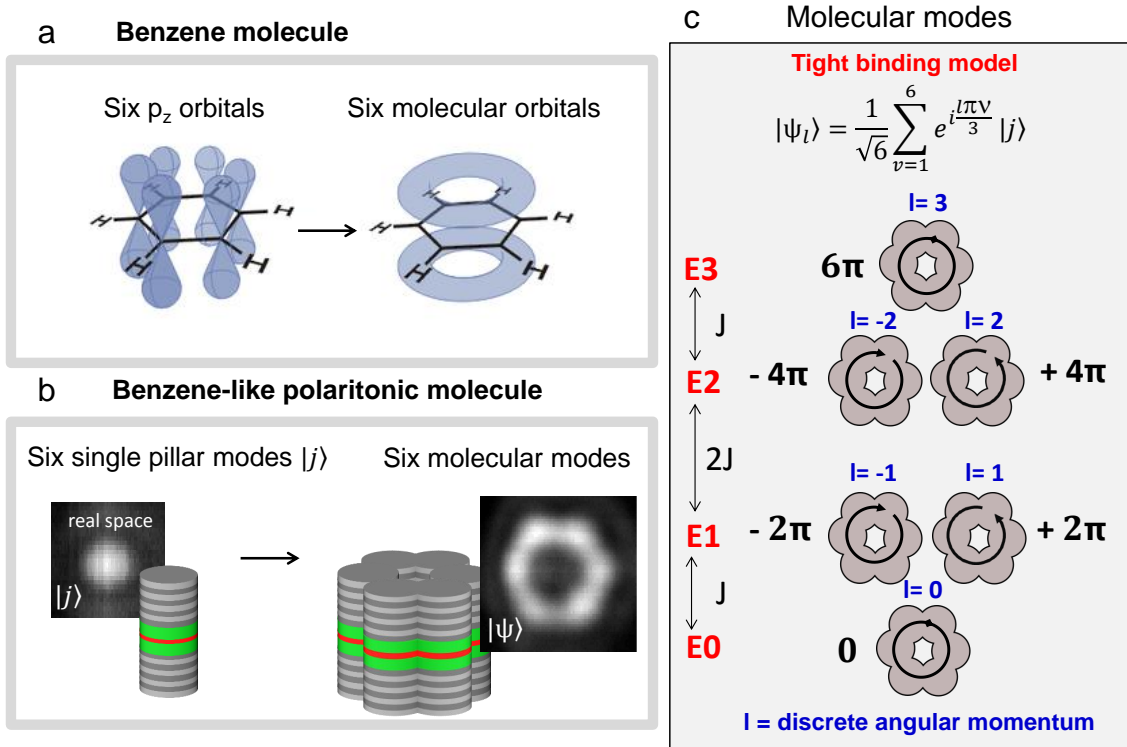


Figure 5.1: (a) Sketch showing the hexagonal structure of the real benzene molecule, with the coupling of the six  $p_z$  orbitals giving rise to delocalized molecular orbitals. (b) Sketch showing our benzene-like polaritonic molecule, made of six coupled micropillars. As for the real molecule, the coupling of the single pillar modes gives rise to molecular modes delocalized over the six pillars. (c) Analytical solution of the molecular eigenmodes in the tight-binding approximation, both for the real benzene molecule and for our polaritonic molecule.

Our system is a polaritonic benzene-like molecule, made of six coupled micropillars placed in a hexagonal structure, as shown in Fig. 5.1 (b). As described in Chapter 2 and in the same way as for the diatomic molecule described in Chapter 4, the

six etched pillars partially overlap, giving rise to a photonic coupling of each pillar with the first neighbours. The choice of the center-to-center distance determines the strength of the coupling, described by the coefficient  $J$ . The molecule we studied is shown in Fig. 5.3 (a). It is made of six pillars with a diameter of  $3 \mu\text{m}$  and a center-to-center separation of  $2.4 \mu\text{m}$ , resulting in a photonic site-to-site coupling of  $J = 0.3 \text{ meV}$ . The coupling between the six pillars gives rise to molecular eigenstates, which are delocalized over the six pillars, as shown in Fig. 5.1 (b).

Our molecule can be considered as a photonic analogue of the real benzene molecule. A benzene molecule is formed by six carbon atoms in a hexagonal structure, as sketched in Fig. 5.1 (a). The  $2s$  and two of the  $2p$  orbitals of the carbon atoms hybridize to form three  $sp^2$  orbitals arranged in the plane of the molecule. They give rise to the rigid hexagonal structure, that is, to the covalent bonding chain of the six carbon atoms, linking each of them to a hydrogen atom. The remaining non-hybridized  $p_z$  orbitals contain the valence electrons, which can tunnel from carbon to carbon. These electrons are responsible for most of the physical properties of the molecule. The coupling of these six  $p_z$  orbitals gives rise to molecular orbitals which are delocalized over the entire molecule, as sketched in Fig. 5.1 (a).

We consider the coupling of the six single pillar fundamental modes  $|j\rangle$ , each of them characterized by a real-space intensity profile radially symmetric, as shown in Fig. 5.1 (b). In our analogue system, each single pillar mode plays the role of one of the  $p_z$  orbitals in the actual benzene molecule. If we use a tight-binding approximation, in which each molecular eigenstate is written as linear superposition of the six single pillar modes and we consider just a linear coupling (with coefficient  $J$ ) between each pillar and its first neighbours, the Hamiltonian of the system has the expression

$$\hat{H} = \epsilon_0 \sum_j |j\rangle \langle j| - J \sum_j |j\rangle \langle j+1|. \quad (5.1)$$

In the single pillar basis  $|j\rangle$ , we can write  $\hat{H}$  in the matricial form

$$\hat{H} = \begin{matrix} & \begin{matrix} 1 & 2 & 3 & 4 & 5 & 6 \end{matrix} \\ \begin{matrix} 1 \\ 2 \\ 3 \\ 4 \\ 5 \\ 6 \end{matrix} & \begin{pmatrix} \epsilon_0 & -J & 0 & 0 & 0 & -J \\ -J & \epsilon_0 & -J & 0 & 0 & 0 \\ 0 & -J & \epsilon_0 & -J & 0 & 0 \\ 0 & 0 & -J & \epsilon_0 & -J & 0 \\ 0 & 0 & 0 & -J & \epsilon_0 & -J \\ -J & 0 & 0 & 0 & -J & \epsilon_0 \end{pmatrix} \end{matrix}. \quad (5.2)$$

The molecular eigenmodes and the corresponding energies can be found diagonalizing such matrix. The eigenmodes have the explicit expression

$$|\Psi_l\rangle = \frac{1}{\sqrt{6}} \sum_{j=1}^6 e^{i\frac{l\pi j}{3}} |j\rangle, \quad (5.3)$$

with eigenvalues

$$E_l = \epsilon_0 - 2J \cos\left(\frac{\pi l}{3}\right). \quad (5.4)$$

They are labeled through the quantum number  $l$  ( $l = 0, \pm 1, \pm 2, 3$ ), defining the eigenvalues of the discrete angular momentum operator  $\hat{L}$ , which commutes with  $\hat{H}$  and which operates on the single pillar basis in the following way

$$\hat{L} |j\rangle = |j+1\rangle. \quad (5.5)$$

A sketch of eigenmodes is shown in Fig. 5.1 (c). The six eigenmodes are distributed in four energy levels, the levels  $E_1$  and  $E_2$  being double degenerate. In the real-space, they are all characterized by intensity distributions with maxima over each site, but they display a different phase profile. As sketched in Fig. 5.1 (c) and explicitly written in the analytical solution 5.3, the ground state mode ( $l=0$ ) is characterized by a constant phase profile over the six sites, while the excited levels display a vortical solution, with the phase turning by an integer number of  $2\pi$  around the molecule. The first excited level  $E_1$  is characterized by two degenerate vortices of order one, in which the phase is turning clockwise (for the mode on the left side) and counterclockwise (for the mode on the right side) by  $2\pi$  around the molecule. The second excited level  $E_2$  is characterized by two degenerate vortices of order two, in which the phase is turning clockwise (for the mode on the left side) and counterclockwise (for the mode on the right side) by  $4\pi$  around the molecule. The third excited level is characterized by a vortex of order three, in which the phase is turning by  $6\pi$  around the molecule. This corresponds to a phase shift of  $\pi$  between adjacent pillars. This level is not degenerate, the clockwise and counterclockwise modes being coincident.

### 5.3 Experimental setup

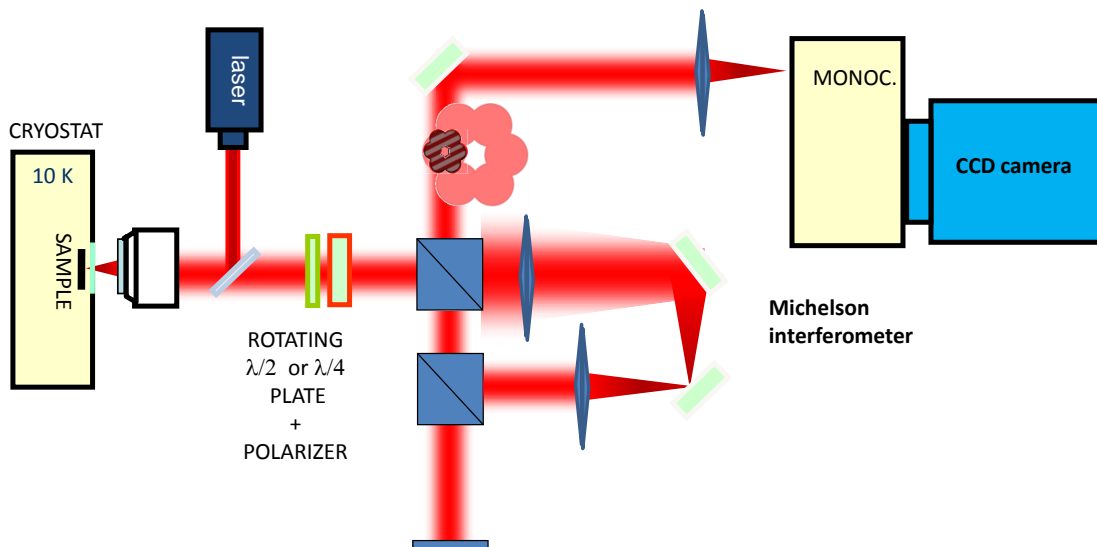


Figure 5.2: *Experimental setup.*

The molecule is etched out from the same planar microcavity described in Chapter 3. The experimental setup is shown in Fig. 5.2. We excite the molecule with a CW monomode laser at a wavelength of 735 nm, at the first reflectivity minimum of the stop band defined by the Bragg mirrors. The laser is well out-of-resonance with respect to the polaritonic modes, which are at  $\sim 780$  nm. We pump the molecule with a laser spot of  $12 \mu\text{m}$  in diameter, pumping entirely and symmetrically the molecule.

We work in reflection geometry, the photoluminescence from the molecule being collected with the same objective we use to excite the system. The collected signal is analysed both in real-, k-space and in energy, by means of a spectrometer coupled to a CCD camera.

To recover the phase distribution of the emission, we use a modified Michelson in-

terferometer, as the one shown in Fig. 5.2. We make the signal from the whole molecule interfere with the magnified emission from just one of the pillars, so that it interferes with just one lobe, which acts as a constant phase reference beam. Since the signal and the reference reach the CCD at different angles, they create an interference pattern. From this interferogram, by means of a Fourier transform analysis, we recover the phase difference between each lobe of the signal and the reference signal. From this measurement we obtain the relative phase of the emission coming from the different micropillars.

As we pump the molecule out-of-resonance at low power, polaritons populate all the energy spectrum. In this case we have therefore the simultaneous emission of signal from different energy levels. In order to have access to the real-space profile of each level, we make use of a tomographic technique. By closing the slit in front of the spectrometer (slit width of  $50 \mu\text{m}$ ), we select just one vertical slice of the real( $k$ ) space. When sending it to a grating, we resolve the emission in energy. We repeat the same procedure for different slices, scanning the full real( $k$ ) space and we reconstruct for each value of energy, the real( $k$ ) space profile.

By means of a half-waveplate or a quarter-waveplate and a polarizing beam-splitter, we can filter the photoluminescence signal and select the different polarization components of the emission. In this way we can measure the six Stokes parameters (linear horizontal, vertical, diagonal, antidiagonal, circular, anticircular polarizations) and fully reconstruct the state of polarization at each point of the molecule.

## 5.4 Low power measurements: characterization of the system

As a first step we pump the system at low power in order to characterize our molecule and find experimentally the molecular modes. We excite the system out-of-resonance (at  $\sim 735 \text{ nm}$ ), much higher in energy than the polaritonic levels. A gas of free electrons and holes is created, which relaxes down populating progressively the full polariton energy spectrum. Fig. 5.3 (b) shows the low power energy spectrum of our molecule, in which we identify the first four energy levels, corresponding to the levels sketched in Fig. 5.1 (c) and reported in Fig. 5.3 (c). By using the tomographic technique described in Section 5.3, we reconstruct the real-space profile of each energy level, which is reported in Fig. 5.3 (d). As expected the modes are all delocalized over the six sites and they share the same hexagonal symmetry. In the same way as for the real-space, we can measure the intensity profile of the modes in the  $k$ -space. The results are shown in Fig. 5.3 (e). We see that, while the modes have almost the same profile in the real-space, they differ substantially in  $k$ -space. This is due to the fact that, being the Fourier transform of the real-space, the  $k$ -space is determined by both the amplitude and phase distribution in the real-space, which is different for the different modes. In Fig. 5.3 (f) we report the numerical simulation of the  $k$ -space profiles, showing a strong agreement with our experimental data. The simulation is performed first by building the modes in the real-space. To this end, we define for each mode a linear superpositions of six gaussians, placed in the vertices of a regular hexagon (the width of the gaussians is chosen in order to reproduce to the best our experimental data). Then, depending on the mode, we associate to each gaussian the phase term given by the analytical solution 5.3. Finally the modes in the  $k$ -space are calculated by performing the spatial Fourier transform of the modes in the real-space.

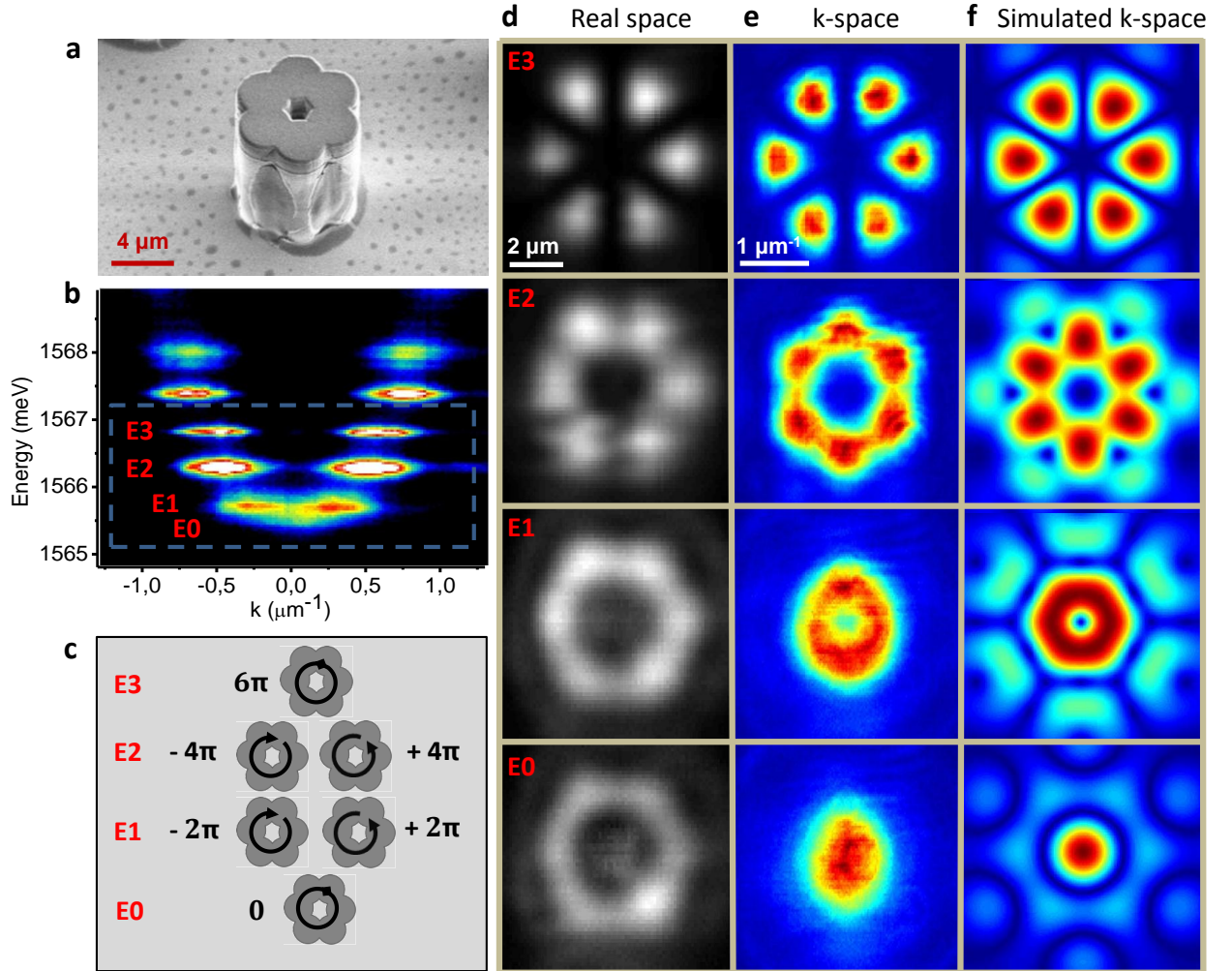


Figure 5.3: (a) Scanning electron microscope image of the benzene-like molecule. (b) Low power energy spectrum in which the first four energy levels are identified, corresponding to the analytical solutions sketched in (c). (d) Real-space emission of the first four energy levels, reconstructed with a tomographic technique. (e), (f) Experimental measurements (e) and numerical simulations (f) of the k-space emission of the first four energy levels.

Fig. 5.4 shows the real- and k-space of the modes corresponding to the higher energy levels  $E_4$  and  $E_5$ . They are two of the modes coming from the coupling of the single pillar p orbitals (first excited single pillar modes). We observe that they are characterized by a real-space intensity distribution with a different symmetry with respect to the modes coming from the coupling of the ground state single pillar modes. In particular, they are characterized by a minimum intensity at the center of each pillar. This is related to the real-space profile of the single pillar p modes, which displays a node in the center.

By using the interferometric technique described in Section 5.3, we can also measure directly the phase profile of the modes in the real-space. As described in Section 5.3 and recalled in Fig. 5.5 (a), we make the signal from the whole molecule interfere with the magnified emission from just one of the pillars, so that it interferes with just one lobe, which acts as constant phase reference beam. At low power, all the polariton energy levels are populated, and the interferogram is the superposition of all the interference patterns, one for each energy level. In order to separate the differ-

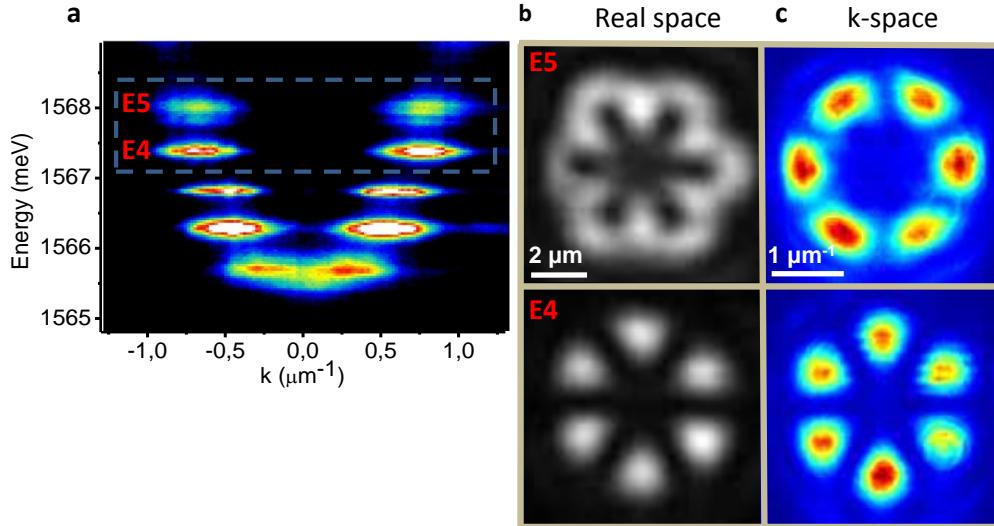


Figure 5.4: Real- and k-space of the two excited modes corresponding to the energy levels  $E_4$  and  $E_5$ . They are two of the modes coming from the coupling of the single pillar  $p$  orbitals.

ent interferograms, we use the same tomographic technique used to reconstruct the real- and k-space profiles. We reduce the width of the slit in front of the spectrometer, selecting just one slice of the interference pattern and we resolve it in energy, obtaining a spectrum as the one shown in Fig. 5.5 (b). After scanning the whole spatial extension of the molecule, we reconstruct tomographically the interferograms for each energy level and we obtain a 2D image. The results of the measurement are shown in Fig. 5.5 (c-f). From each interferogram, by means of Fourier transform analysis, we can extract directly the phase difference between the signal and the reference  $\phi_{diff} = \phi_{sig} - \phi_{ref}$ . The results are shown in Fig. 5.5 (k-n). In order to compare them with the analytical solution 5.3 of Section 5.2, the explicit phase difference profile for each mode is reported in Fig. 5.6.

Accordingly with the analytical solution, the ground state is characterized by a constant phase around the molecule, while the upper mode is characterized by a  $\pi$  phase shift between adjacent pillars, as it is clear as we follow the dashed yellow lines in Fig. 5.5 (n) and (k). For the intermediate levels  $E_1$  and  $E_2$  the situation is more complicated, because in this case each energy level is the superposition of two degenerate modes. The phase profiles (Fig. 5.5 (m) and (l)) can be understood if we consider the superposition of the two degenerate modes (levels  $E_1$  and  $E_2$  of Fig. 5.6) to have a phase difference which changes randomly in time. Such a superposition gives rise to a contrasted interference pattern only when the phase difference with the reference signal is a multiple of  $\pi$ . For intermediate phase differences, the fringes are washed out and the visibility is much lower, as we found experimentally (Fig. 5.5 (i) and (h)).

From the same interferometric measurement used to reconstruct the phase profile of the modes, we can estimate the coherence time of the emission in the low power regime. This is done by progressively varying the delay between the two arms of the interferometer and measuring how the visibility of fringes varies. A plot of the visibility vs delay is shown in Fig. 5.5 (b.1), from which we can estimate a coherence time of  $\tau_c \sim 50$  ps.

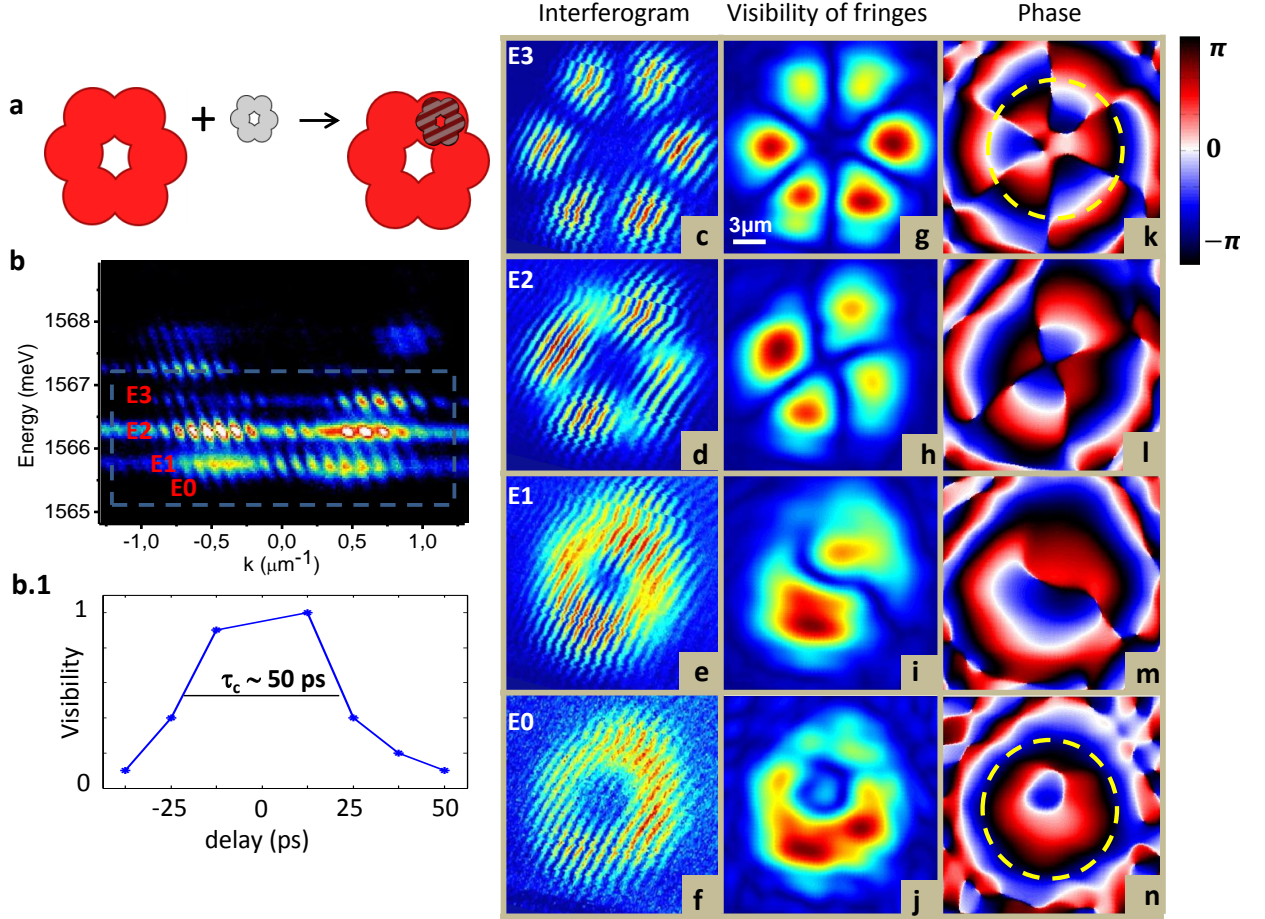


Figure 5.5: (a) Sketch showing the interferometric technique in which the signal is made interfere with a magnified copy of it. (b) Low power energy spectrum obtained during the interferometric measurement. (c)-(f) Interferograms for the first four energy levels obtained by a tomographic technique. (g)-(j) Visibility of the fringes and (k)-(n) phase difference profiles ( $\phi_{diff} = \phi_{sig} - \phi_{ref}$ ), calculated by means of Fourier transform analysis from (c)-(f). (b.1) Visibility of fringes vs temporal delay between the two arms of the interferometer, from which we can estimate a coherence time of  $\tau_c \sim 50$  ps.

## 5.5 High power measurements: polariton condensation in the molecule

In order to study polariton condensation in our benzene-like molecule, we vary the excitation power. As described in Chapter 1, as we increase the pump power, we increase the polariton density in the system, up to a point in which the occupation number in one of the energy levels exceeds one. At this moment bosonic stimulation starts to take place, with more and more polaritons relaxing towards that level. The stimulated process leads to the formation of a condensate, in which a macroscopic population of polaritons is established on the condensate level.

By increasing progressively the pump power, we observe that the system displays two condensation thresholds. As reported in Fig. 5.7, starting from the linear regime, as we increase the excitation power, we find a first threshold at which a condensate forms in the second excited level ( $E_2$  in Fig. 5.7 (b)). By increasing further the excitation power, a new threshold is found, in which the system condenses on the first excited level ( $E_1$  in Fig. 5.7 (c)). Figure 5.7 (d) shows the experimental curves

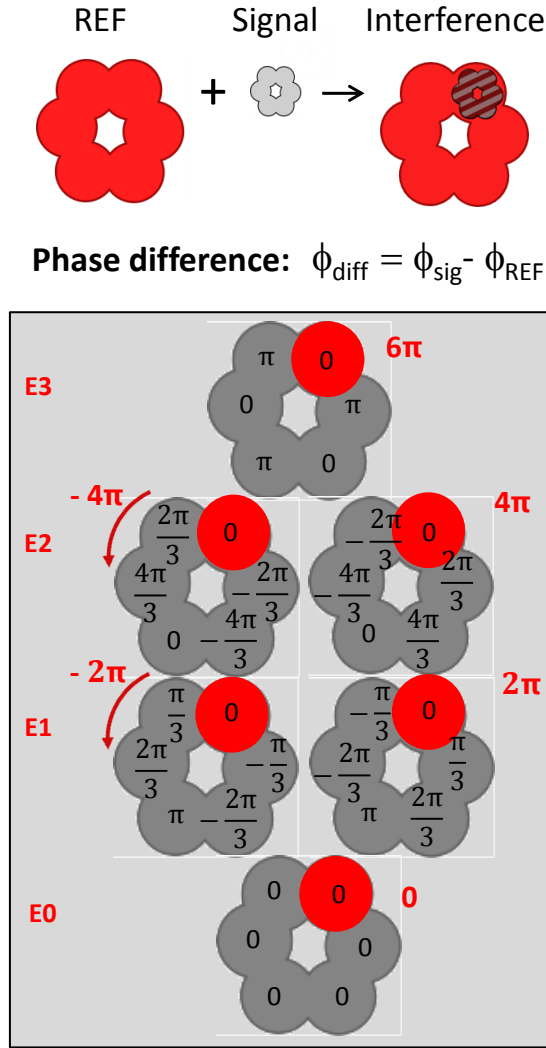


Figure 5.6: Sketch showing the explicit values of the phase difference  $\phi_{diff} = \phi_{sig} - \phi_{ref}$  for each molecular mode, corresponding to the analytical solution 5.3. The red lobe is the one taken as reference beam.

of the emitted intensity vs excitation power for the first and second excited levels, in which the two condensation thresholds are visible. The two black circles on the curves indicate the points at which Figs. 5.7 (b) and (c) are taken.

Something to remark is that condensation does not take place on the fundamental level, but on excited energy levels. This is related to the specific nonequilibrium nature of the polaritonic systems, in which condensation is established not by a thermodynamic equilibrium, but as a stationary state deriving from the balance between pump, relaxation and losses. The choice of the mode at which condensation takes place generates from a mode competition between the different polariton relaxation channels. Not only the relaxation efficiency is important, determined mainly by polariton-polariton and polariton-phonon scattering [161], but also the lifetime of the final state and the overlap with the reservoir play a key role.

We can suppose that at the first threshold (lower excitation power), in which condensation takes place on the second excited level  $E_2$ , the main contribution in the relaxation dynamics is given by the lifetime of the molecular modes, which favours condensation on higher excited modes. In particular there are two reasons why the polariton lifetime is longer for higher excited modes. The first reason is that excited

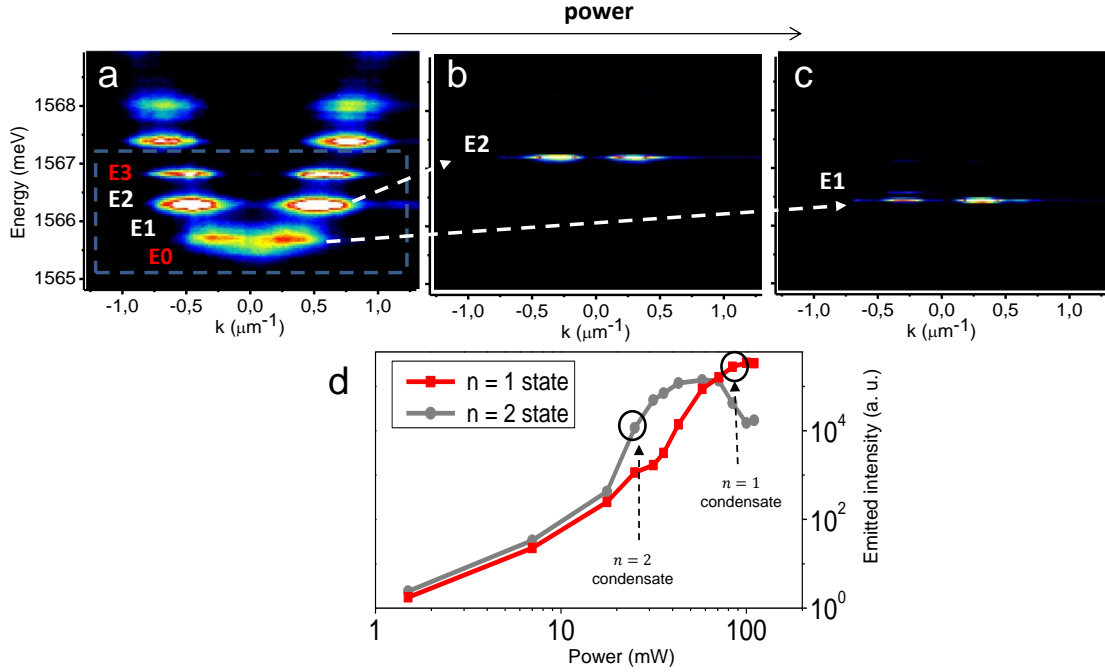


Figure 5.7: Emitted energy spectra taken with increasing pumping power (from left to right). (a) Low power energy spectrum. (b),(c) Energy spectra corresponding to the first (b) and second (c) condensation threshold, in which the second excited level  $E_2$  and the first excited  $E_1$  level are respectively condensing. (d) Curves showing the emitted intensity vs excitation power for the energy levels  $E_1$  (in red) and  $E_2$  (in grey), showing the two condensation thresholds. The black circles highlight the experimental points in which (b) and (c) are taken.

modes are characterized by a wavefunction with a phase profile which varies more rapidly along the molecule (higher number of nodes and antinodes). This translates into patterns in the far-field characterized by regions with destructive interference, corresponding to a lower emission probability (i.e. higher lifetime) [162]. The second reason is that higher excited states are characterized by a wavefunction which is more localized on the center of the six pillars than on the borders and molecular bonds. As a consequence, they are less sensitive to non-radiative recombinations of excitons localized at the edges.

At the second threshold, in which condensation takes place on the first excited level  $E_1$ , the excitation power is higher, corresponding to a higher nonlinearity. We can suppose that in this case the main contribution in the relaxation dynamics is given by the overlap with the excitonic reservoir. Lower excited molecular modes display a better overlap with the reservoir, since they are characterized by a wavefunctions with a more homogeneous intensity distribution along the molecule and in particular with a less number of antinodes.

In conclusion, the competition between lifetime and overlap with the reservoir can explain why condensation takes place first on the second excited level  $E_2$  and then, at higher excitation power, on the first excited level  $E_1$ .

In the next sections we will study the properties of the condensate state at both thresholds.

### 5.5.1 Condensation on the first excited level: a polarization vortex of order 1

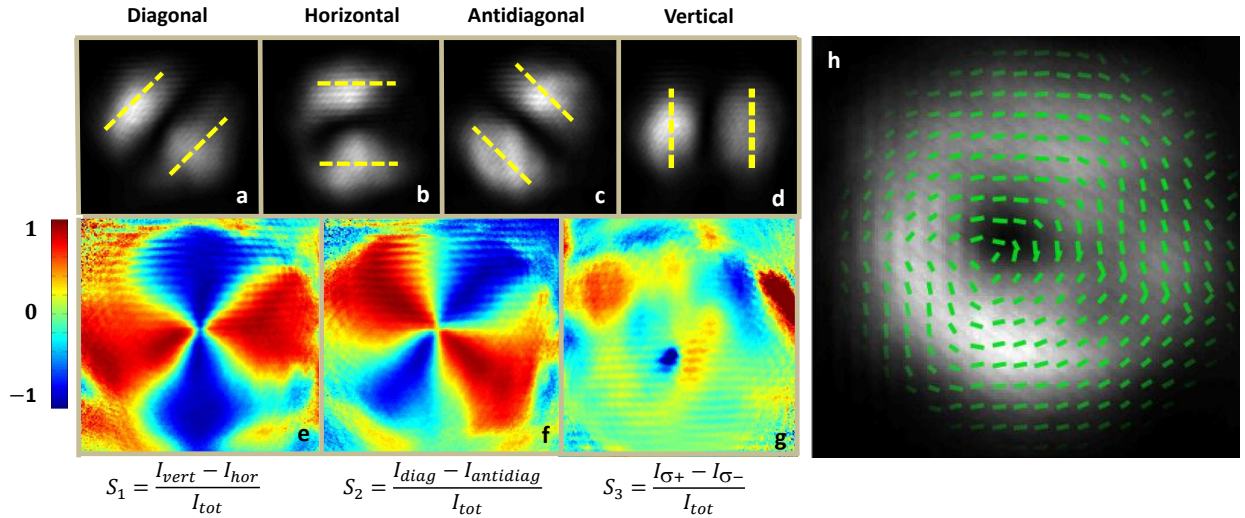


Figure 5.8: Real-space measurements resolved in linear polarization for the condensate on the first excited energy level  $E_1$ . (a)-(d) Real-space emission resolved in the four linear polarizations: diagonal, horizontal, antidiagonal, vertical. The yellow dashed lines help to remark that the emission is turning in the real-space, as we rotate the polarization axis. (e)-(g) Calculated Stockes coefficients  $S_1$ ,  $S_2$  and  $S_3$ , showing that the emission is almost completely linearly polarized. (h) Reconstructed state of the polarization of the emission, showing that the condensate state is azimuthally polarized around the molecule.

We start by studying the condensate which is established at the second threshold (Fig. 5.7 (c)), in which the system condenses on the first excited level.

Since above the condensation threshold most of the particles populate just the condensate level, the photoluminescence coming from the molecule originates mostly from that level, as it is clear from Fig. 5.7. That is why in the condensation regime we do not need to use the tomographic technique described in Section 5.3 in order to recover the real- and k-space of the emission of the single condensate level, a simple measurement with the CCD camera being sufficient.

The real-space emission presents, as expected, an intensity pattern delocalized on the six pillars, similar to the low power emission presented in Fig. 5.3 (d,  $E_1$ ). The interesting features are found as we filter the emitted signal in polarization. By means of a half-waveplate or a quarter-waveplate and a polarizing beam-splitter, we measure the six Stockes parameters (linear horizontal, vertical, diagonal, antidiagonal, circular, anticircular polarization) and fully reconstruct the state of polarization of the molecule.

Fig. 5.8 shows the measurement of the real-space filtered in linear polarization. From Figs. 5.8 (a-d), we see that the signal turns in the real-space, as we rotate the polarization axis. From the calculated Stockes coefficients  $S_1 = \frac{I_{vert} - I_{hor}}{I_{tot}}$ ,  $S_2 = \frac{I_{diag} - I_{antidiag}}{I_{tot}}$  and  $S_3 = \frac{I_{\sigma+} - I_{\sigma-}}{I_{tot}}$ , we see that the molecule is almost completely linearly polarized, the degree of circular polarization being almost zero in every point of the molecule (Fig. 5.8 (g)). The reconstructed state of polarization is shown in Fig. 5.8 (h), in which the green dashes represent the direction of the linear polarization at each point of the molecule. The molecule is azimuthally polarized. In other words we can say that the system condenses on a polarization vortex of order 1, linearly

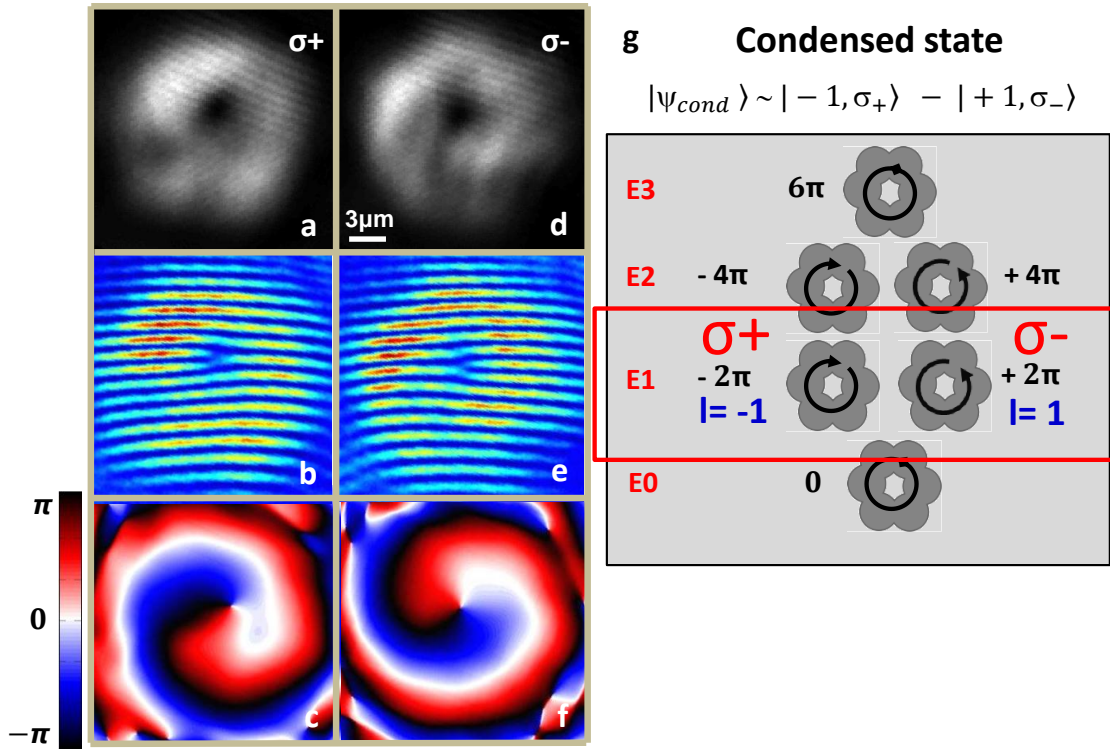


Figure 5.9: Real-space measurements resolved in the  $\sigma+$  and  $\sigma-$  circular polarizations for the condensate on the first excited energy level  $E_1$ . (a), (d) Real-space emission. (b), (e) interferograms obtained with the interferometric technique described in Section 5.2. (c), (f) Phase profiles extracted from (b) and (e) by Fourier transform analysis, showing that the condensate state is a superposition of two counterpropagating phase vortices of order one, one in the  $\sigma+$  and one in the  $\sigma-$  component. These two modes are sketched in (g), where the explicit expression of the superposition is written.

polarized at each point and in which the linear polarization is turning once around the molecule.

The projection of the signal on the basis  $\sigma+$  and  $\sigma-$  gives rise to the data shown in Fig. 5.9. We see that the real-space has the same intensity profile in both the polarizations (Fig. 5.9 (a) and (d)). Something interesting arises as we measure the phase, by means of the interferometric technique explained in Section 5.3. In Fig. 5.9 (c) and (f) we see that the phase is turning by  $2\pi$  around the molecule in both cases, but in the  $\sigma+$  case it is turning clockwise, while in the  $\sigma-$  case is turning counterclockwise. This means that the condensate state is the superposition of a phase vortex of order one and discrete angular momentum  $l=-1$  in the  $\sigma+$  component and a phase vortex of order one and discrete angular momentum  $l=+1$  in the  $\sigma-$  component. This is evident also if we look at the interferograms of Figs. 5.9 (b) and (e), in which we see the fork typical of a quantized vortex [16, 17], which is coming from opposite sides for the  $\sigma+$  and  $\sigma-$  components. In Fig. 5.9 (g) the expression for the condensate state is written explicitly and the two modes which form it are highlighted in the lower sketch.

### 5.5.2 Condensation on a polarization vortex of order 2

We can repeat the same measurements to analyze the condensate at the first condensation threshold, when the system condenses on the second excited level. Figures 5.10 and 5.11 show the experimental data in linear and circular polarizations. From

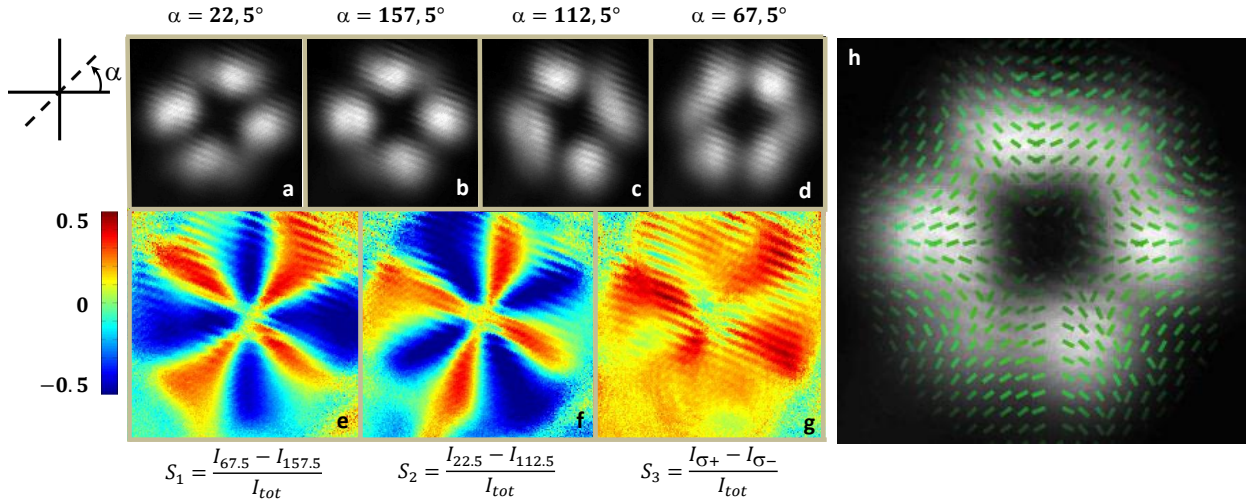


Figure 5.10: Real-space measurements resolved in linear polarization for the condensate on the second excited energy level  $E_2$ . (a)-(d) Real-space emission resolved in four linear Stokes polarizations. (e)-(g) Calculated Stokes coefficients  $S_1$ ,  $S_2$  and  $S_3$ . (h) Reconstructed state of the polarization of the emission. As shown by the green dashes, the linear polarization is pointing towards the six sites of the molecule.

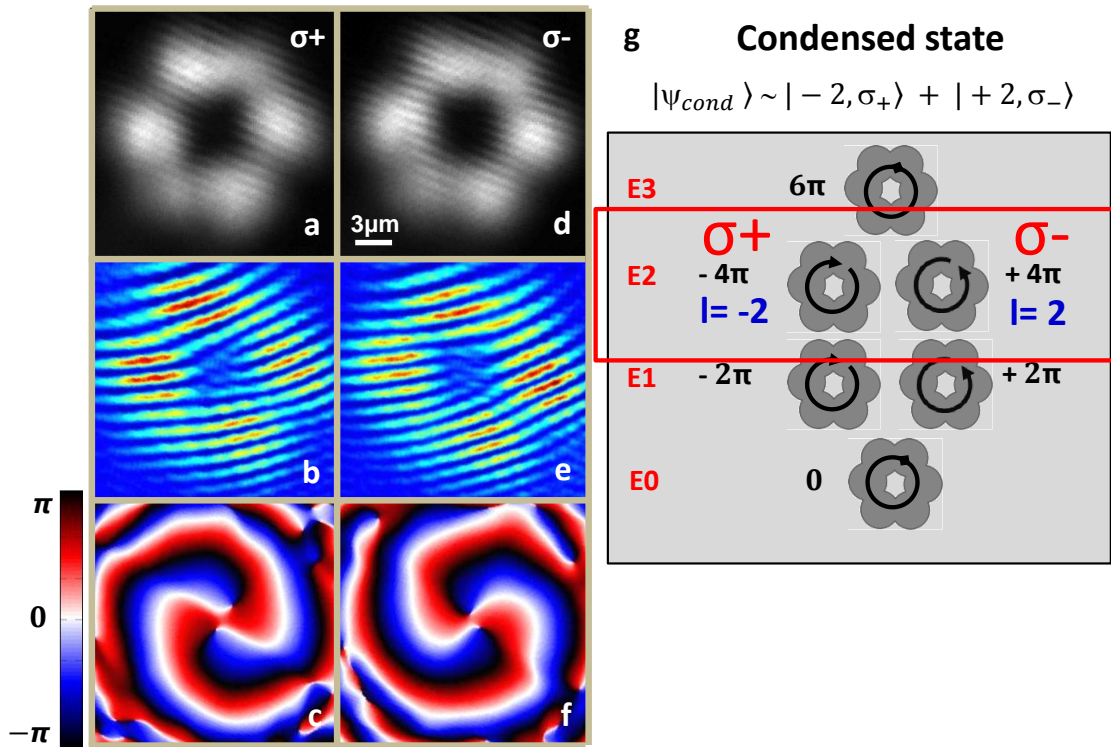


Figure 5.11: Real-space measurements resolved in the  $\sigma+$  and  $\sigma-$  circular polarizations for the condensate on the second excited energy level  $E_2$ . (a), (d) Real-space emission. (b), (e) interferograms obtained with the interferometric technique described in Section 5.2. (c), (f) Phase profiles extracted from (b) and (e) by Fourier transform analysis, showing that the condensate state is a superposition of two counterpropagating phase vortices of order two, one in the  $\sigma+$  and one in the  $\sigma-$  component. These two modes are sketched in (g), where the explicit expression of the superposition is written.

Fig. 5.10 we see that as for the vortex of order one, also in this case the condensate is linearly polarized at each point of the real-space. But this time the linear polar-

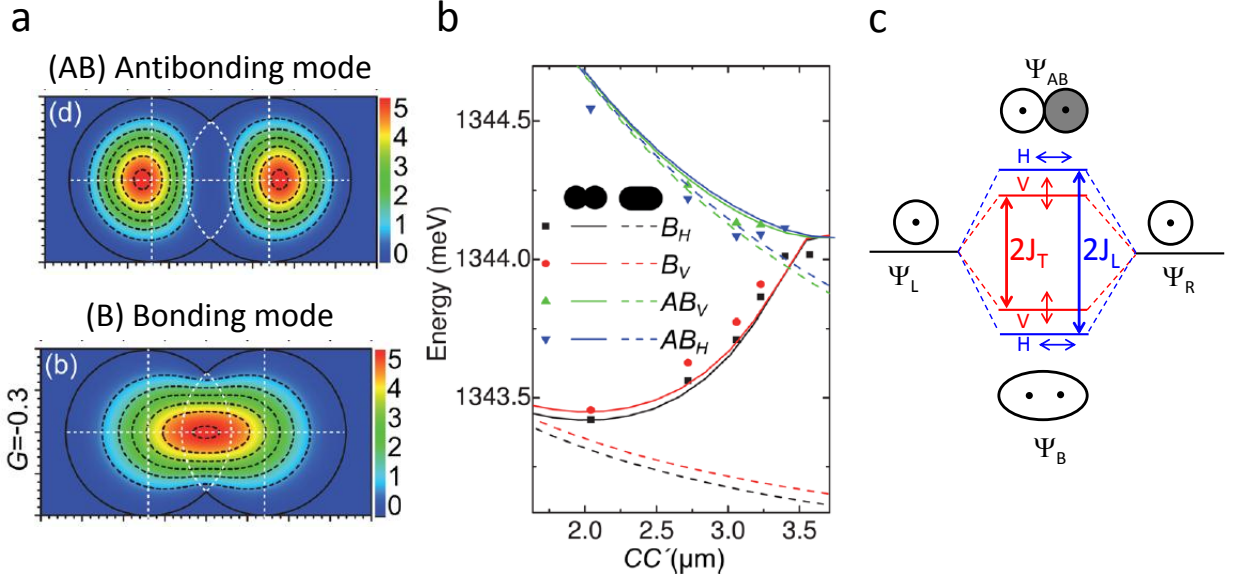


Figure 5.12: (a) Calculated intensity distribution of the electric field for the first bonding and antibonding modes of a diatomic molecule made of two coupled micropillars (data taken from [163]). (b) Polarization resolved energies for the bonding and antibonding modes as a function of the center-to-center (CC') distance (solid lines), showing a polarization splitting between modes polarized along the molecular axis (horizontal, H) and transversally to the molecular axis (vertical, V) (from [163]). (c) Model which partially reproduces the experimental polarization splitting through the introduction of polarization dependent tunneling coefficients ( $J_L$  and  $J_T$ ).

ization is turning twice around the molecule, giving rise to a polarization vortex of order two. As shown in Fig. 5.10 (h) by the green dashes, the linear polarization is pointing towards the six sites of the molecule. In Fig. 5.11 the data in circular polarization are reported. In this case the condensate is formed by the superposition of two phase vortices of order two, with the phase turning by  $4\pi$  clockwise (for the  $\sigma+$  projection) and counterclockwise (for the  $\sigma-$  projection) around the molecule. The explicit expression of the condensate state is reported in Fig. 5.11 (g). In the sketch below, the two modes which form the condensate state are highlighted.

## 5.6 Polarization degree of freedom: real eigenmodes

In order to understand the particular modes in which the system condenses, we have to take into account the polarization-spin degree of freedom. The eigenmodes found in Section 5.2 were calculated using a scalar tight-binding approach. We now need to extend this approach, taking into account polarization.

If we consider each micropillar separately, as we account for the polarization degree of freedom, we will double the number of modes, since for each mode found in the scalar theory, we will have two possible independent polarizations, for example  $\sigma+$  and  $\sigma-$ . If we suppose a single pillar being circular, these two modes will be degenerate in energy.

As we couple two pillars together, building a diatomic molecule as the one described in Chapter 4, we break the circular symmetry, thus inducing a polarization splitting

in the molecular eigenmodes.

Such a polarization splitting in coupled micropillars has been recently studied in [163] and part of the results are reported in Fig. 5.12. In this work, the authors showed both experimentally and numerically that the coupling of two micropillars gives rise to a polarization splitting in both the bonding and antibonding molecular eigenmodes (Fig. 5.12 (a)) respectively along (H) and perpendicularly (V) to the molecular axis (CC'). The polarization splitting depends on the center-to-center distance of the micropillars (Fig. 5.12 (b), black and red curves for the bonding mode, blue and green curves for the antibonding mode) and it is in the range of 10 - 70  $\mu\text{eV}$ . As reported in [163], this splitting seems to be strongly dependent on the shape of the central region of the molecule (molecular bond) and, as we can observe in Fig. 5.12 (b), it is inverted for the two bonding and antibonding modes: for the bonding mode, the mode polarized along the molecular axis (H) is lower in energy with respect to the mode polarized perpendicularly (V), while the situation is inverted for the antibonding mode (Fig. 5.12 (c)). We can explain intuitively this fact by considering the distribution of intensity of the electric field in the two modes, shown in Fig. 5.12 (a). The bonding mode has a shape in the real-space which is more elongated in the horizontal direction, therefore, as it happens in optical waveguides, the horizontally polarized mode results to be less confined than the vertical one and it will have lower energy. On the contrary, the wavefunction of the antibonding mode in the real-space displays two lobes on each pillar which appear to be more elongated in the vertical direction. Therefore, in this case, the vertical polarized mode will be less confined than the horizontal one, and it will have lower energy.

The polarization splitting of the molecular modes, found both theoretically and experimentally in [163], can be modeled considering two pillars coupled through a linear coupling, in which the magnitude of the tunneling coefficient  $J$  (the same defined in Chapter 4) has a different value for a polarization along the molecular bond (horizontal, H) and a polarization perpendicular to the bond (vertical, V), as shown in Fig. 5.12 (c).  $J_L$  corresponds to the tunneling coefficient for particles polarized longitudinally (along the bond),  $J_T$  is for particles polarized transversally to the bond.

We observe that this approximation does not describe completely the experimental data, in fact it predicts equivalent polarization splittings for both the bonding and antibonding modes, while the curves in Fig. 5.12 (b) display a splitting which is higher for the bonding mode than for the antibonding mode.

The experimental data can be reproduced if we consider, additionally to the polarization dependent tunneling, a term which considers a polarization splitting related to the global symmetry of the system. In the diatomic molecule it is related to the elongated shape of the molecule considered in its ensemble and it would give rise again to a splitting along the H - V directions, the H mode having lower energy than the V one. This effect would increase the splitting already present in the bonding mode of Fig. 5.12 (c), while it would decrease the splitting corresponding to the antibonding mode.

Based on these results, we build a model for our benzene-like molecule. This model and the calculation of the eigenstates have been developed by G. Malpuech and D. D. Solnyshkov from Institut Pascal (Clermont-Ferrand), and by I. Carusotto from the BEC-CNR center in Trento, Italy.

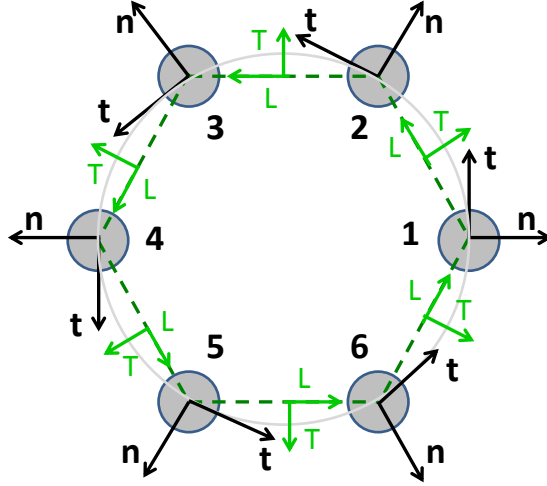


Figure 5.13: Sketch showing the single pillar basis  $\{|j, n\rangle, |j, t\rangle\}$  (in black), i.e. the basis in which for each pillar we take the two independent polarizations, respectively azimuthal and radial with respect to the molecular ring structure. In green the longitudinal and transversal ( $L, T$ ) directions for each molecular bound are shown.

We introduce in the tight-binding scalar Hamiltonian 5.1, the polarization degree of freedom and we take into account both the polarization splittings we just described for the diatomic molecule. On one hand we consider the polarization dependent tunneling, which depends on the direction of the molecular bond. Explicitly we suppose that the tunnel coefficient  $J$  will be different for polarizations along the molecular bond ( $J_L$ ) and transversally to the bond ( $J_T$ ). This directions are shown in Fig. 5.13 (in green) and we remark that they are not conserved along the molecule, i.e. they turn as we consider different bonds. On the other hand we consider the polarization splitting related to the global symmetry of the structure, i.e. in our case to the ring waveguide structure. We introduce therefore a radial-azimuthal splitting, and we consider that a mode polarized azimuthally will be less confined (i.e. lower in energy) than a mode radially polarized.

We remark that the prevalence of one polarization splitting or the other depends on the specific geometry of the structure: the polarization dependent tunneling will dominate when the necklace structure is more pronounced, while the radial-azimuthal splitting will dominate when the waveguide structure is more relevant. A good basis to introduce the radial-azimuthal polarization splitting is the normal-tangential single pillar basis  $\{|j, n\rangle, |j, t\rangle\}$ , i.e. the basis in which for each pillar we take the two independent polarizations, respectively azimuthal and radial with respect to the molecular ring structure. This basis is shown in Fig. 5.13 (in black) and we see that it turns as we consider different pillars.

In the absence of polarization splitting, the Hamiltonian would be the trivial extension of 5.1, with including two degenerate polarizations per mode. Now we want to introduce in this Hamiltonian the tunneling polarization dependence and the “waveguide splitting” expressed as a t-n splitting in each site (using the notation of Fig. 5.13). In particular, as we write the Hamiltonian in the t-n basis, the radial-azimuthal splitting will give rise to different diagonal terms for the n- and t-modes,  $\epsilon_n$  and  $\epsilon_t$ . The polarization dependent tunneling will give rise to non-diagonal terms, which, as explained above, are written explicitly in the T and L directions, i.e. along and transversally to the molecular bound. Therefore, in or-

der to calculate the nondiagonal matrix elements  $\langle j, n(t) | \hat{H} | j+1, n(t) \rangle$ , we need to project the  $\{|j, n\rangle, |j, t\rangle\}$  basis vectors of the two pillars we are considering, on the (T,L) directions of the bond which is connecting them, and then use the known coupling constants  $J_T = \langle j, T | \hat{H} | j+1, T \rangle$  and  $J_L = \langle j, L | \hat{H} | j+1, L \rangle$ , and with  $\langle j, L | \hat{H} | j+1, T \rangle = 0$ .

More explicitly we use the relations:

$$\begin{aligned}
|j, n\rangle &= \frac{\sqrt{3}}{2} |j, T\rangle - \frac{1}{2} |j, L\rangle \\
|j, t\rangle &= \frac{1}{2} |j, T\rangle - \frac{\sqrt{3}}{2} |j, L\rangle \\
|j+1, n\rangle &= \frac{\sqrt{3}}{2} |j+1, T\rangle - \frac{1}{2} |j+1, L\rangle \\
|j+1, t\rangle &= -\frac{1}{2} |j+1, T\rangle + \frac{\sqrt{3}}{2} |j+1, L\rangle.
\end{aligned} \tag{5.6}$$

The resulting Hamiltonian has the explicit expression

$$\hat{H} = \begin{matrix} & \begin{matrix} 1, n & 1, t & 2, n & 2, t & 3, n & 3, t & 4, n & 4, t & 5, n & 5, t & 6, n & 6, t \end{matrix} \\ \begin{matrix} 1, n \\ 1, t \\ 2, n \\ 2, t \\ 3, n \\ 3, t \\ 4, n \\ 4, t \\ 5, n \\ 5, t \\ 6, n \\ 6, t \end{matrix} & \left( \begin{array}{cccccccccccc}
\epsilon_n & 0 & -J_{nn} & J_{nt} & 0 & 0 & 0 & 0 & 0 & 0 & -J_{nn} & -J_{nt} \\
0 & \epsilon_t & -J_{nt} & -J_{tt} & 0 & 0 & 0 & 0 & 0 & 0 & J_{nt} & -J_{tt} \\
-J_{nn} & -J_{nt} & \epsilon_n & 0 & -J_{nn} & J_{nt} & 0 & 0 & 0 & 0 & 0 & 0 \\
J_{nt} & -J_{tt} & 0 & \epsilon_t & -J_{nt} & -J_{tt} & 0 & 0 & 0 & 0 & 0 & 0 \\
0 & 0 & -J_{nn} & -J_{nt} & \epsilon_n & 0 & -J_{nn} & -J_{nt} & 0 & 0 & 0 & 0 \\
0 & 0 & J_{nt} & -J_{tt} & 0 & \epsilon_t & -J_{nt} & -J_{tt} & 0 & 0 & 0 & 0 \\
0 & 0 & 0 & 0 & -J_{nn} & -J_{nt} & \epsilon_n & 0 & -J_{nn} & -J_{nt} & 0 & 0 \\
0 & 0 & 0 & 0 & J_{nt} & -J_{tt} & 0 & \epsilon_t & -J_{nt} & -J_{tt} & 0 & 0 \\
0 & 0 & 0 & 0 & 0 & 0 & -J_{nn} & -J_{nt} & \epsilon_n & 0 & -J_{nn} & J_{nt} \\
0 & 0 & 0 & 0 & 0 & 0 & J_{nt} & -J_{tt} & 0 & \epsilon_t & -J_{nt} & -J_{tt} \\
-J_{nn} & J_{nt} & 0 & 0 & 0 & 0 & 0 & 0 & -J_{nn} & -J_{nt} & \epsilon_n & 0 \\
-J_{nt} & -J_{tt} & 0 & 0 & 0 & 0 & 0 & 0 & J_{nt} & -J_{tt} & 0 & \epsilon_t
\end{array} \right), \tag{5.7}
\end{matrix}$$

where

$$\begin{aligned}
J_{nn} &= \frac{1}{4}(3J_T - J_L) \\
J_{tt} &= \frac{1}{4}(3J_L - J_T) \\
J_{nn} &= \frac{\sqrt{3}}{4}(J_T + J_L).
\end{aligned} \tag{5.8}$$

A more meaningful basis to express Hamiltonian 5.7 is that of circular polarization ( $|+\rangle, |-\rangle$ ) instead of radial-azimuthal ( $|n\rangle, |t\rangle$ ) and, for the spatial component of the wavefunction, the basis of well defined angular momenta  $|l\rangle$  ( $l = 0, \pm 1, \pm 2, 3$ ) instead of that of individual pillars  $|j\rangle$  ( $j = 1, \dots, 6$ ).

First of all we write the basis  $\{|j, n\rangle, |j, t\rangle\}$ , in terms of the  $\{|j, +\rangle, |j, -\rangle\}$  basis, i.e. the single pillar basis, in the circular  $\sigma_+$  and  $\sigma_-$  polarizations:

$$\begin{aligned}
|j, n\rangle &= \frac{1}{\sqrt{2}} \left[ \exp(-i\pi \frac{j-1}{3}) |j, +\rangle + \exp(i\pi \frac{j-1}{3}) |j, -\rangle \right] \\
|j, t\rangle &= \frac{1}{\sqrt{2}} \left[ \exp(-i\pi (\frac{j-1}{3} + \frac{1}{2})) |j, +\rangle + \exp(i\pi (\frac{j-1}{3} + \frac{1}{2})) |j, -\rangle \right].
\end{aligned} \tag{5.9}$$

Then we go to the basis of many-pillar states with left and right circular polarizations:

$$|l, \pm\rangle = \sum_{j=1}^6 \exp(i \frac{l(j-1)\pi}{3}) |j, \pm\rangle. \quad (5.10)$$

In this basis the Hamiltonian takes the form

$$\hat{H} = \begin{pmatrix} 0,+ & 0,- & +1,+ & +1,- & -1,+ & -1,- & +2,+ & +2,- & -2,+ & -2,- & 3,+ & 3,- \\ 0,+ & E-2J & 0 & 0 & 0 & 0 & 0 & -\Delta_E - \Delta_J & 0 & 0 & 0 & 0 \\ 0,- & 0 & E-2J & 0 & 0 & 0 & 0 & 0 & -\Delta_E - \Delta_J & 0 & 0 & 0 \\ +1,+ & 0 & 0 & E-J & 0 & 0 & 0 & 0 & 0 & 0 & 0 & -\Delta_E + \Delta_J \\ +1,- & 0 & 0 & 0 & E-J & -\Delta_E - 2\Delta_J & 0 & 0 & 0 & 0 & 0 & 0 \\ -1,+ & 0 & 0 & 0 & -\Delta_E - 2\Delta_J & E-J & 0 & 0 & 0 & 0 & 0 & 0 \\ -1,- & 0 & 0 & 0 & 0 & 0 & E-J & 0 & 0 & 0 & -\Delta_E + \Delta_J & 0 \\ +2,+ & 0 & 0 & 0 & 0 & 0 & 0 & E+J & 0 & 0 & -\Delta_E + 2\Delta_J & 0 \\ +2,- & -\Delta_E - \Delta_J & 0 & 0 & 0 & 0 & 0 & 0 & E+J & 0 & 0 & 0 \\ -2,+ & 0 & -\Delta_E - \Delta_J & 0 & 0 & 0 & 0 & 0 & 0 & E+J & 0 & 0 \\ -2,- & 0 & 0 & 0 & 0 & 0 & -\Delta_E + 2\Delta_J & 0 & 0 & 0 & E+J & 0 \\ 3,+ & 0 & 0 & 0 & 0 & 0 & 0 & 0 & 0 & 0 & 0 & E+2J \\ 3,- & 0 & 0 & -\Delta_E + \Delta_J & 0 & 0 & -\Delta_E + \Delta_J & 0 & 0 & 0 & 0 & 0 \\ & & & & & & & & & & & E+2J \end{pmatrix} \quad (5.11)$$

where

$$\begin{aligned} E &= \frac{1}{2}(\epsilon_t + \epsilon_n) \\ J &= \frac{1}{2}(J_L + J_T) \\ \Delta_E &= \frac{1}{2}(\epsilon_t - \epsilon_n) \\ \Delta_J &= \frac{1}{2}(J_L - J_T). \end{aligned} \quad (5.12)$$

In this form of the Hamiltonian we very clearly see that states of different angular momentum and polarization are coupled (for instance  $|+1, -\rangle$  and  $|-1, +\rangle$ ). In this matrix the two effects which induce the polarization splitting are clearly highlighted: the term  $\Delta_J$  is related to the polarization dependence of the tunneling coupling between two sites, while  $\Delta_E$  is related to the ring waveguide symmetry.

The molecular eigenstates and energies can be calculated by diagonalizing this matrix. The results are shown in Table 5.1.

In Table 5.1,  $\alpha$ ,  $\beta$  and  $c_i$  are small coefficients which depend on the parameters  $\Delta_E$  and  $\Delta_J$ .

We clearly see that the effect of the polarization dependence, both the one related to  $\Delta_E$  and the one related to  $\Delta_J$ , is to lift the degeneracy of the modes and mix molecular eigenstates with different discrete angular momentum  $l$  and polarization  $\sigma_{\pm}$ . This mixing gives rise to molecular eigenstates with a peculiar polarization texture along the molecule. A sketch for the eigenstates with main  $|l| = 1$  and  $|l| = 2$  is shown in Fig. 5.14. The corresponding numerical calculations are shown in Fig. 5.15.

As shown in Fig. 5.14, the energy level  $E_1$  is splitted into three energy sublevels. In the lowest level we find an azimuthally polarized mode, which is a linear combination of the modes  $|-1, +\rangle$  and  $|+1, -\rangle$ . The upper mode is radially polarized and it is another linear combination of the same modes  $|-1, +\rangle$  and  $|+1, -\rangle$ , orthogonal to the azimuthal one. The two other modes have an intermediate energy, they are degenerate and are linear superpositions of the modes  $|+1, +\rangle$  and  $|-1, -\rangle$ .

State number	Main $ l $	Wavefunction	Energies
1	0	$\frac{1}{\sqrt{1+ \alpha ^2}}( 0, +\rangle - \alpha   +2, -\rangle)$	$E_0 - c_0$
2	0	$\frac{1}{\sqrt{1+ \alpha ^2}}( 0, -\rangle - \alpha   -2, +\rangle)$	$E_0 - c_0$
3	1	$\frac{1}{\sqrt{2}}( -1, +\rangle -   +1, -\rangle)$	$E_1 - c_{11}$
4	1	$\frac{1}{\sqrt{1+ \beta ^2}}(  +1, +\rangle - \beta   -3, -\rangle)$	$E_1 - c_{12}$
5	1	$\frac{1}{\sqrt{1+ \beta ^2}}( -1, -\rangle - \beta   +3, +\rangle)$	$E_1 - c_{12}$
6	1	$\frac{1}{\sqrt{2}}( -1, +\rangle +   +1, -\rangle)$	$E_1 + c_{11}$
7	2	$\frac{1}{\sqrt{2}}(  +2, +\rangle -   -2, -\rangle)$	$E_2 - c_{21}$
8	2	$\frac{1}{\sqrt{1+ \alpha ^2}}(  +2, -\rangle + \alpha   0, +\rangle)$	$E_2 + c_{22}$
9	2	$\frac{1}{\sqrt{1+ \alpha ^2}}(  -2, +\rangle + \alpha   0, -\rangle)$	$E_2 + c_{22}$
10	2	$\frac{1}{\sqrt{2}}(  +2, +\rangle +   -2, -\rangle)$	$E_2 + c_{21}$
11	3	$\frac{1}{\sqrt{1+ \beta ^2}}(\frac{1}{2}   +3, +\rangle + \frac{1}{2}   -3, +\rangle + \beta   -1, -\rangle)$	$E_3 + c_3$
12	3	$\frac{1}{\sqrt{1+ \beta ^2}}(\frac{1}{2}   +3, -\rangle + \frac{1}{2}   -3, -\rangle + \beta   +1, +\rangle)$	$E_3 + c_3$

Table 5.1: Calculated molecular eigenmodes and energies found by diagonalization of the matrix 5.11.

The azimuthal lowest energy mode (highlighted in red) corresponds to the mode in which we observe condensation, as described in Section 5.5.1. As expected it corresponds to the lowest energy level of the triplet.

Something similar happens for the energy level  $E_2$ , whose modes are sketched in Fig. 5.14 (b). For this case we have to do a remark. In fact, while the coefficient  $c_{11}$  in Table 5.1 is always positive, therefore giving rise to molecular eigenmodes for the level  $E_1$  which are disposed in energy as shown in Fig. 5.14, the coefficient  $c_{21}$  is not always positive. Its sign depends on the relative contributions of the two terms  $\Delta_E$  and  $\Delta_J$ , which contribute in opposite directions. In particular it is found that the order in energy of the molecular eigenmodes for the level  $E_2$  is the one sketched in Fig. 5.14 (b) if  $\Delta_J$  is the dominant contribution. On the other hand, if  $\Delta_E$  is the dominant contribution, the upper and lower modes would be inverted.

Our experiment shows that, as the system condenses on level  $E_2$  (section 5.5.2), condensation takes place on the mode highlighted in red in Fig. 5.14, i.e. the mode in which the linear polarization points in the direction of the six lobes. Since it is reasonable to expect condensation to take place on the lowest energy level of the multiplet, our observation seems to indicate that the real disposition of the molecular eigenmodes in energy is the one sketched in Fig. 5.14. This would indicate that the polarization dependence related to  $\Delta_J$  is the dominant one, i.e. the polarization dependent tunneling would dominate over the ring waveguide structure.

We can estimate the polarization energy splitting considering the values measured in [163]. In particular, for our experimental parameters, we expect the energy splitting in each sublevel to be in the range  $\sim 10 - 50 \mu\text{eV}$ .

Note that at low power we populate all the energy levels, but since the linewidth of the modes exceeds the energy splitting related to the polarization splitting, we are

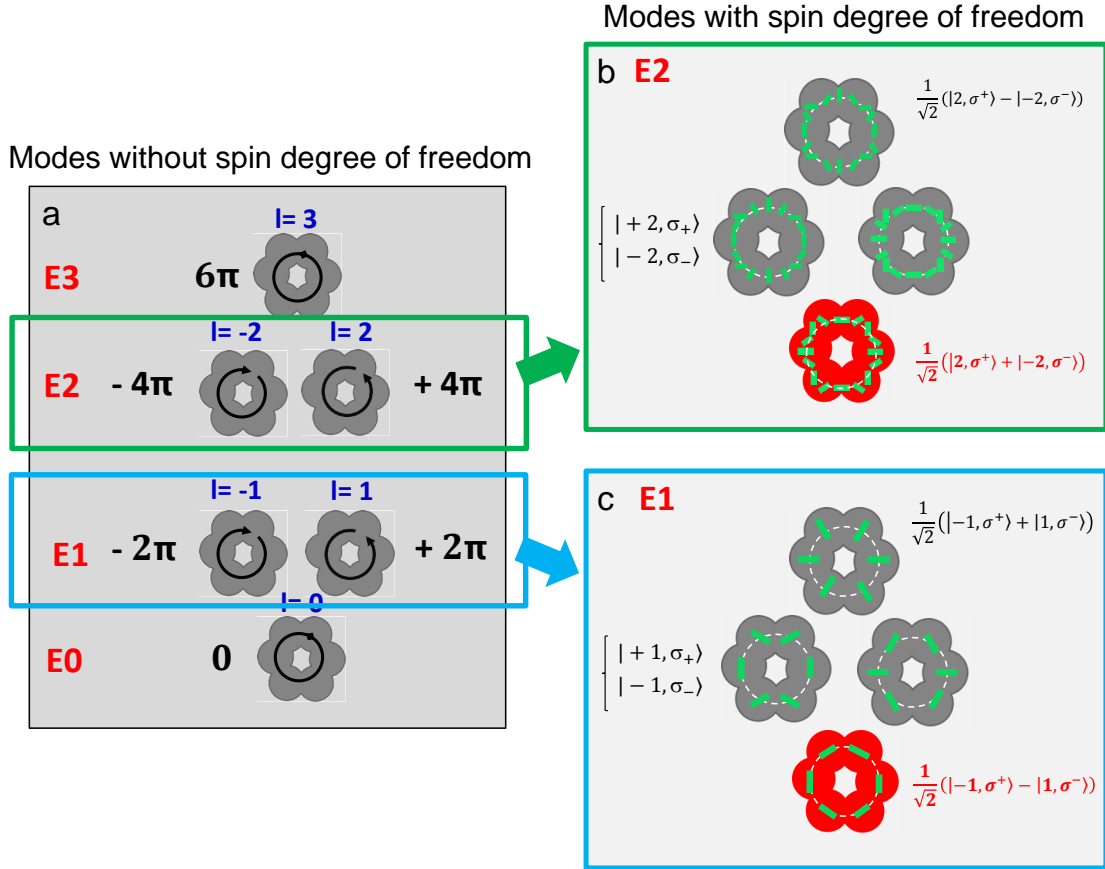


Figure 5.14: Sketch of the molecular eigenmodes as we take polarization into account. The polarization splitting lifts the degeneracy of the energy levels  $E_1$  and  $E_2$ , giving rise to the molecular eigenmodes shown respectively in (c) and (b). The two modes coloured in red are the modes in which the system condenses.

not able to resolve them and we do not observe any polarization pattern. It is as the system condenses, that the macroscopic occupation of one energy level takes place, making it possible for a polarization pattern to emerge.

So the appearance of a polarization pattern is the consequence of two ingredients: polarization splitting and condensation.

## 5.7 Polarization splitting as an effective spin-orbit coupling

In the previous section, we have seen that two polarization dependent effects affect the eigenstates of the system: the first one is a polarization dependence of the site-to-site tunneling for polaritons polarized along and transversally to the molecular bond, the second one is a radial-azimuthal polarization splitting on each site, related to the global ring symmetry of the structure.

Both these terms give rise to nondiagonal elements in the Hamiltonian of the system: the ones which contain the parameter  $\Delta_J$  are related to the polarization tunneling dependence, while the ones which contain the parameter  $\Delta_E$  are related to the global ring symmetry.

These terms lift the degeneracy of the molecular modes and induce a mixing of molecular modes with different discrete angular momentum  $l$  and polarization  $\sigma_{\pm}$

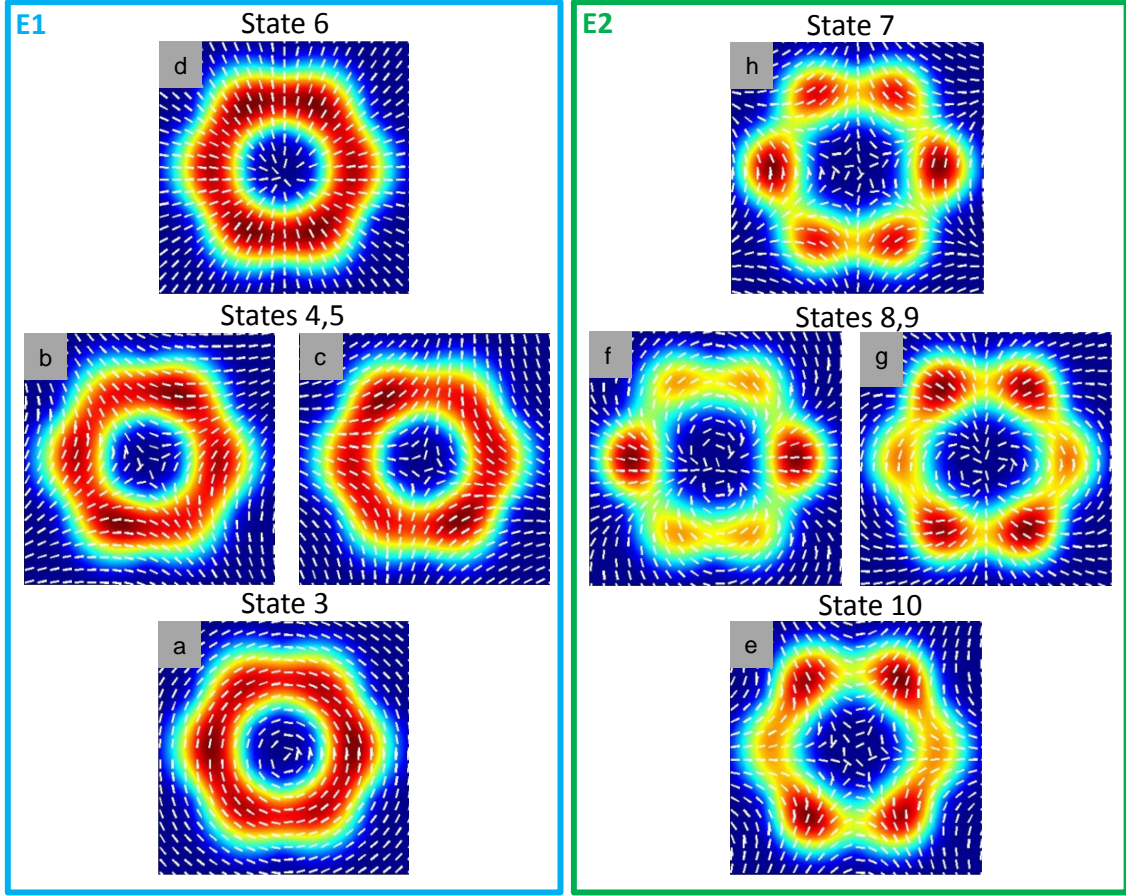


Figure 5.15: Calculated molecular eigenmodes, corresponding to the levels  $E_1$  and  $E_2$ . The white dashes show the direction of the polarization in each point of the molecule.

(i.e. spin-up  $|\uparrow\rangle$ , spin-down  $|\downarrow\rangle$ ). They act therefore as a spin-orbit coupling term. Since spin-orbit coupling acts on the spin degree of freedom, it can be represented through an effective magnetic field. To that end, we express Hamiltonian 5.11 in form of an operator acting on a 1/2 spin particle, i.e. on the spinor  $[\Psi_+(j)\Psi_-(j)]$ , where  $j$  is the generalized integer coordinate ( $j= 1..6$ ) which corresponds to the position of the six sites, as shown in Fig. 5.13.

Hamiltonian 5.11 can be written in the form

$$\hat{H} = \hat{H}_0 - \Delta_E \begin{pmatrix} 0 & e^{-2i\frac{j\pi}{3}} \\ e^{2i\frac{j\pi}{3}} & 0 \end{pmatrix} + \frac{\sqrt{3}\Delta_J}{\pi} \frac{1}{J} \left[ \hat{L}, \begin{pmatrix} 0 & e^{-2i\frac{j\pi}{3}} \\ e^{2i\frac{j\pi}{3}} & 0 \end{pmatrix} \right], \quad (5.13)$$

where the square brackets represent a commutator. If we expand the commutator, we have the explicit expression

$$\hat{H} = \hat{H}_0 - \Delta_E \begin{pmatrix} 0 & e^{-2i\frac{j\pi}{3}} \\ e^{2i\frac{j\pi}{3}} & 0 \end{pmatrix} + \frac{\sqrt{3}\Delta_J}{\pi} \frac{1}{J} \left( \hat{L} \begin{pmatrix} 0 & e^{-2i\frac{j\pi}{3}} \\ e^{2i\frac{j\pi}{3}} & 0 \end{pmatrix} + \begin{pmatrix} 0 & e^{-2i\frac{j\pi}{3}} \\ e^{2i\frac{j\pi}{3}} & 0 \end{pmatrix} \hat{L}^\dagger \right). \quad (5.14)$$

The Hamiltonian 5.14 contains two terms respectively proportional to  $\Delta_E$  and  $\Delta_J$ , corresponding to the two physical mechanisms discussed.

We can define an effective magnetic field whose texture is defined by the matrix

$$\begin{pmatrix} 0 & e^{-2i\frac{j\pi}{3}} \\ e^{2i\frac{j\pi}{3}} & 0 \end{pmatrix}. \quad (5.15)$$

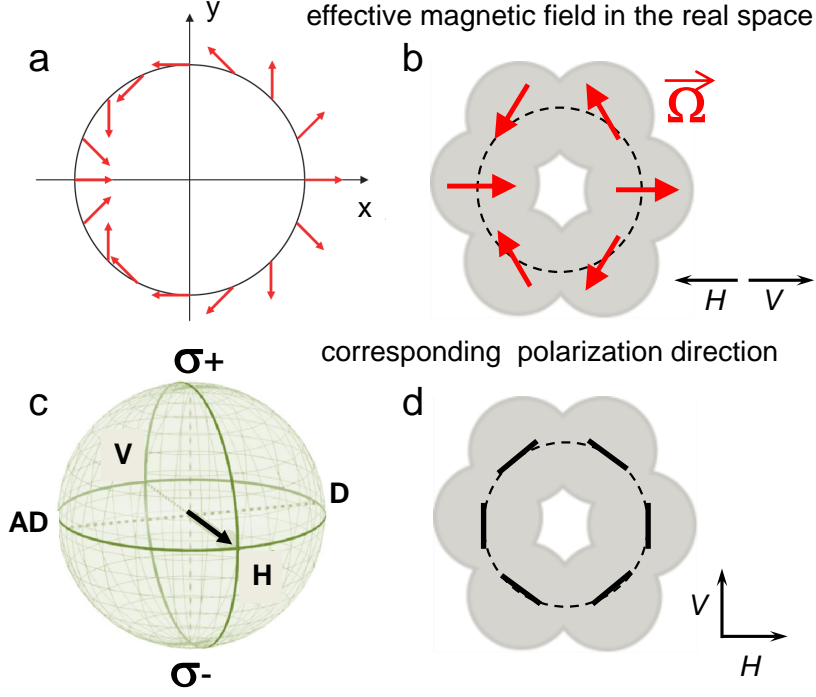


Figure 5.16: Sketch showing the real-space texture, in the plane  $(x,y)$  of the molecule, of the effective magnetic field  $\Omega$  (explicit expression 5.16). (a)  $\Omega$  in the case we had an infinite chain of sites. (b)  $\Omega$  for our molecule, in which (a) is reduced to six coordinates corresponding to the six molecular sites. (d) Polarization texture corresponding to (b), as we consider the one-to-one correspondence between the spin and polarization state (c).

This magnetic field has the explicit form in the  $(x,y)$  plane of the molecule

$$\Omega = \cos\left(2\frac{j\pi}{3}\right)\mathbf{e}_x + \sin\left(2\frac{j\pi}{3}\right)\mathbf{e}_y. \quad (5.16)$$

If our system was characterized by a continuous coordinate (a ring made of infinite sites), this magnetic field would have a texture in  $(x,y)$  plane as the one shown in Fig. 5.16 (a). Since our system is characterized by six sites, such texture reduces to the one shown in Fig. 5.16 (b).

The Hamiltonian can be expressed in function of this magnetic field, by using the Pauli matrices  $\hat{\sigma}$

$$\hat{H} = \hat{H}_0 - \Delta_E \Omega \cdot \hat{\sigma} - \frac{\sqrt{3}\Delta_J}{\pi} \frac{1}{J} [\Omega \cdot \hat{\sigma}, \hat{L}]. \quad (5.17)$$

We see that, while the term containing  $\Delta E$  is proportional to the effective magnetic field, the term containing  $\Delta J$  contains also a dependence on the discrete angular momentum  $\hat{L}$ .

If we consider the motion of a particle around the molecule, this field introduces an interaction between the particle's spin and its motion, because, as the particle moves around the closed trajectory, it sees a varying field, which interacts in a different way with its spin (in this view it is somehow similar to the physics described in [164]). Therefore it is effectively acting as a spin-orbit term.

At this point it is interesting to contextualize our results in the framework of spin-orbit coupling in a larger sense.

## 5.8 Spin-orbit coupling in solids

Spin-orbit coupling is the interaction between a particle spin and its momentum. A textbook example of spin-orbit interaction is the one contributing to the fine structures of atoms. In a classical picture, an electron in orbital motion around the nucleus, sees an effective magnetic field, which is related to the apparent motion of the charged nucleus in the frame where the electron is at rest. This magnetic field has the expression

$$\vec{\Omega} = \frac{\vec{v} \times \vec{E}_{rad}}{c^2}, \quad (5.18)$$

where  $\vec{v}$  is the speed of the electron,  $\vec{E}_{rad}$  is the radial electric field generated by the charged nucleus and  $c$  is the speed of light. Writing  $\vec{E}_{rad} = \left| \vec{E} / r \right| \vec{r}$  and  $\vec{p} = m \vec{v}$ , we have that  $\vec{\Omega} \propto \vec{r} \times \vec{p} \propto \vec{L}$ , where  $\vec{L}$  is the electron angular momentum. It means that the effective field is directed along the  $z$  direction, orthogonal to the plane of motion, and its magnitude depends on  $\vec{L}$ , i.e. on the speed of the electron around the nucleus. This spin-orbit term splits atomic eigenstates which would be otherwise degenerate, with a splitting depending on the values of the spin and angular momentum. This splitting contributes to fine levels in atoms. From this basic example, we see that spin-orbit interaction leads to a dynamics typical of a particle in a magnetic field, even in the absence of an external magnetic field.

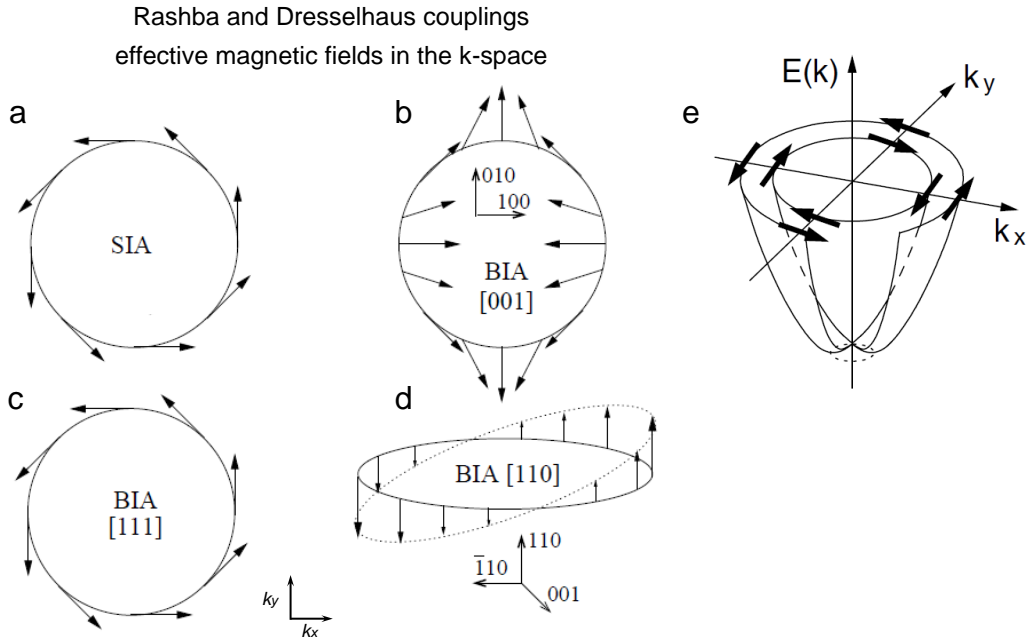


Figure 5.17: Effective magnetic field texture in the  $(k_x, k_y)$  plane for the Rashba (a) and for the Dresselhaus spin-orbit coupling for three different crystallographic directions of growth (b), (c), (d), taken from [165]. (e) Dispersion relation for an electron in the presence of Rashba spin-orbit coupling, showing the spin splitting of the conduction band.

Spin-orbit coupling is also present in solids (see [165]).

In 2D materials with lack of inversion symmetry, as for III-V semiconductors (such as GaAs), there are two main manifestations of spin-orbit coupling: one is related to the bulk inversion asymmetry (Dresselhaus term [166]), the other comes from the structure inversion asymmetry (Rashba term [167]) and it is characteristic of asymmetric structures (asymmetry in the out-of-plane direction, for instance asymmetric

quantum wells or quantum wells in the presence of an electric field). The effective magnetic fields in the  $\mathbf{k}$ -space are represented in Fig. 5.17 for the Rashba term (a) and for the Dresselhaus term for three different crystallographic directions of growth (b), (c), (d). The effective Rashba magnetic field has the expression

$$\boldsymbol{\Omega}(\mathbf{k}) \propto (\mathbf{k} \times \mathbf{n}), \quad (5.19)$$

where  $\mathbf{n}$  is the direction perpendicular to the 2D plane. The spin-orbit term in the Hamiltonian has the expression

$$\hat{H}_R = \alpha_R(k_y\sigma_x - k_x\sigma_y). \quad (5.20)$$

The Dresselhaus term depends on the crystallographic direction of growth of the structure. For the crystallographic direction  $[0,0,1]$  for example (Fig. 5.17 (b)), the effective magnetic field has the expression

$$\boldsymbol{\Omega}(\mathbf{k}) \propto (-k_x, k_y, 0), \quad (5.21)$$

and the spin-orbit term has the expression

$$\hat{H}_D = \alpha_D(k_x\sigma_x - k_y\sigma_y). \quad (5.22)$$

Both the Rashba and the Dresselhaus terms lead to a spin splitting of the conduction band which is linear in  $\mathbf{k}$ , as shown in Fig. 5.17 (e) for the Rashba case.

In semiconductors, spin-orbit interactions lead to the spin Hall effect [168, 169], in which an electrical current results in spin accumulation at the lateral boundaries of the sample.

More recently the possibility of observing a quantum spin Hall effect has been investigated theoretically and soon after observed. This effect is somehow the spinor counterpart of the quantum Hall effect [170, 171], in which a two-dimensional electron system subjected to low temperatures and strong magnetic fields, displays quantized values for the Hall conductivity at the edges. These one dimensional Hall edge channels are very resistant to scattering and charge carriers can be transported without energy dissipation.

It has been proposed that this kind of edge transport could be observed in the absence of an external magnetic field if a suitable spin-orbit coupling is present. In particular it has been predicted [172, 173, 174] that in insulators with suitable electronic structure, edge states would develop, where carriers with opposite spins move in opposite directions on a given edge. Such materials are called topological insulators. In these materials, spin currents are allowed just on the edges of the sample, giving rise to one dimensional transport channels. The transport is characterized by separate channels for spin-up and spin-down particles. The directionality of transport for particles with a fixed spin, results in spin currents which are protected from scattering induced by disorder. The properties of topological insulators have been attributed to the presence of spin-orbit interactions, which lead to self-organization of spin currents in the absence of an external magnetic field. The first experimental realization of a topological insulator has been reported in 2007 in a HgTe quantum well [175] and soon after in a 3D system [176].

The realization of protected edge channels for spin transport, in particular in the case of room temperature realization, is of course very appealing for applications in integrated circuit technology.

These kind of spin related effects are not only object of strong research in the solid-state physics community, but there is an increased interest also from other communities, in particular cold atom physics [177, 178] and optics [179, 180, 181, 182]. This interest goes together with the idea of extending magnetism, and in particular the physics related to spin-orbit coupling, to neutral particles.

As mentioned in the introduction of this chapter, the idea is to develop analogue systems (simulators) in which magnetism and spin-orbit interactions can be studied on length and time scales allowing for a good control and detection of the parameters. Beyond that, this opens the way to observation of new phenomena.

Effective magnetic interactions have been proposed and realized both in Bose-Einstein condensates and photonic systems. In particular this analogy has led to the observation of synthetic magnetic fields and spin-orbit interaction for cold atoms [177, 178], the realization of photonic edge protected states in networks of coupled resonator optical waveguides [179, 180, 181] and to the proposal of photonic topological insulators in metacrystals [182].

The basic idea in the creation of artificial magnetic fields or spin-orbit coupling for neutral particles it to exploit the result of Berry, which describes the dynamics of particles in closed geometries. A particle which is following adiabatically a closed path in a Hamiltonian with position-dependent parameters, will acquire a geometric phase (in addition to a dynamic phase) which is dependent just on the geometry of the parameters along the path and which is called Berry phase. This phase can be reformulated as if arising due to the presence of an effective magnetic field. For instance, one way of doing this is by building a lattice with spin dependent tunneling of particles [183].

In polaritonic systems an effective spin-orbit coupling is naturally present in planar

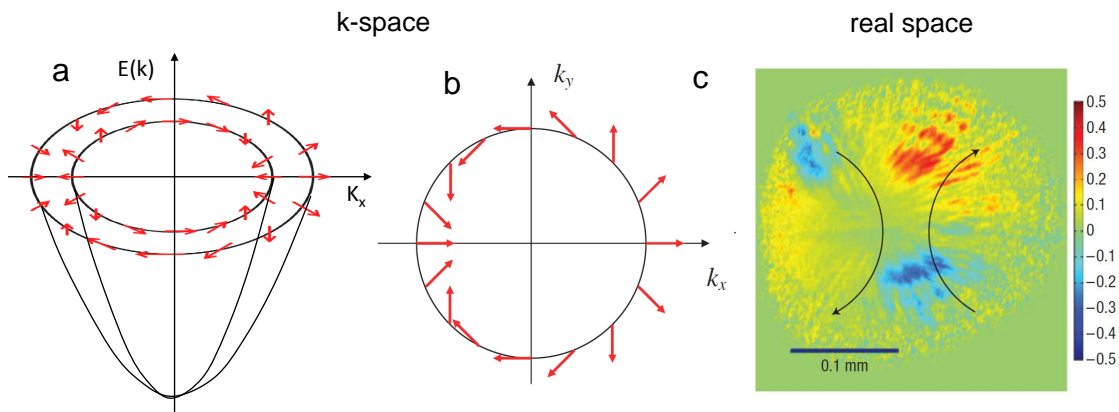


Figure 5.18: (a) TE-TM splitting of the lower polariton band in a 2D microcavity. (b) Corresponding effective magnetic field (taken from [24]). (c) Experimental demonstration of the optical spin Hall effect in a semiconductor microcavity (reported from [23]).

cavities [24]. It arises from the polarization dependence of the electromagnetic field boundary conditions on the microcavity dielectric layers interfaces, which result in a splitting between the transverse electric (TE) and transverse magnetic (TM) polarization modes. This polarization splitting, which translates in pseudospin splitting for polaritons inside the cavity, can be described by an effective magnetic field, which

lies in the microcavity plane and has explicit expression

$$\begin{aligned}\Omega_x &= \frac{\Omega}{k^2}(k_x^2 - k_y^2) \\ \Omega_y &= \frac{2\Omega}{k^2}k_x k_y.\end{aligned}\tag{5.23}$$

The texture of  $\Omega$  in the  $(k_x, k_y)$  plane is shown in Fig. 5.18 (b). The spin-orbit term in the Hamiltonian has the expression

$$\hat{H}_{SO} = \frac{\cos t}{k^2}((k_x^2 - k_y^2)\sigma_x + 2k_x k_y \sigma_y),\tag{5.24}$$

and it gives rise to the TE-TM splitting of the polaritons bands, as described in Chapter 1 and recalled in Fig. 5.18 (a). This spin-orbit coupling term has led for example to the observation of the optical spin Hall effect [23, 75, 184]. In the experiment reported in [23], a polariton wave packet is injected resonantly in the cavity, with fixed momentum and linear polarization. As it propagates, it scatters on the structural disorder of the microcavity in every in-plane direction. The  $k$ -dependent precession of the spin around the effective magnetic field  $\Omega$  results in the appearance, in both real and reciprocal space, of circular polarization domains in the four quarters of the plane, as reported in Fig. 5.18 (c).

In low dimensional polaritonic structures, as 1D wires, a polarization splitting arises between the polarization transversal and longitudinal to the structure. In this case the TE-TM splitting typical of 2D structures, is still present but it is negligible if compared to the polarization splitting due to the elongated geometry of the wire or molecule.

In our benzene-like molecule we take advantage of the specific geometry of the structure, which confines laterally the optical mode, in order to create a spin dependent tunneling plus an on-site polarization splitting. The advantage of this approach is that it can be easily extended to different geometries, as other molecular structures, 1D chains up to 2D lattices. The freedom in designing the geometry of the coupled micropillar structure, opens the way to the engineering of architected spin-orbit couplings.

## 5.9 Conclusion and perspectives

In this chapter we have described our experimental study on a polaritonic benzene-like molecule, made of six coupled micropillars. After characterizing our system in the low power excitation regime (resolving both the intensity and phase profiles of the modes), we have studied polariton condensation on the molecule. Our experiment shows that the system displays two condensation thresholds, the first one in which the system condenses on the second excited energy level, the second one in which the system condenses on the first excited level. In both cases the condensate modes display peculiar polarization-spin textures in the real-space.

These molecular modes have been understood by including in the tight-binding Hamiltonian the polarization degree of freedom and supposing an asymmetry in the tunneling of particles polarized along and transversally to the molecular bond and an onsite linear polarization splitting. Their effect is to lift the degeneracy of molecular modes, introducing a coupling between modes with different discrete angular momentum and spin. Therefore they act as an effective spin-orbit coupling, which

can be described through the introduction of an effective magnetic field, which lies in the  $(x,y)$  plane of the molecule and which has a texture in the real-space. The energy splitting induced by the spin-orbit coupling is small if compared to the modes linewidth, therefore as we excite the system at low power, populating all the energy levels, we are not able to resolve the modes and therefore to detect the polarization patterns. On the contrary, as the system condenses, only one mode is populated, thus allowing a direct visualization of the polarization pattern. Therefore we can say that spin-orbit coupling separates modes with different polarization textures and then condensation allows to have access to them.

As already outlined, a remarkable advantage of our system is the scalability, which allows to extend the few-pillar molecules we have studied to many-pillar systems, where each site has the same properties and the coupling between sites can be engineered. The freedom given by the fabrication technique, allows to design more complex structures, with the possibility of engineering the desired geometry. Our work on one hand goes in the direction of the study of many pillars coupled systems. As nonlinearities are taken into account, our system is a good candidate for the study of the discrete nonlinear physics mentioned in the previous chapter. Additionally our work is placed in the emerging field of artificial magnetism for neutral particles, which is attracting increased interest both in the cold atom and the optics communities. In particular, the approach we used to describe our system in terms of a polarization dependent tunneling, opens the way in polaritonic systems to the engineering of spin-orbit couplings, which was up to now a fixed parameter of the system. This property, together with the high scalability of our system, opens the way to the engineering of architected spin-orbit couplings in 2D pillar lattices, with the perspective of the engineering of artificial magnetic fields, up to the realization of topological insulators. Optical topological insulators are interesting not only for fundamental reasons, but also for applications, since they are characterized by spin edge currents which can propagate just in one direction and are therefore protected from disorder.

As already mentioned, compared to other optical systems, coupled micropillars present some advantages: they allow following directly the temporal dynamics, are a suited systems in which nonlinear effects can be studied and in which the out-of-equilibrium physics can be explored.

The combination of these properties with the realization of artificial gauge fields, could lead to the observation of new phenomena.



# Conclusion and perspectives

In this thesis we presented an experimental study done on microcavity polaritons in GaAs based 0D confining structures, namely micropillars and polaritonic molecules made of coupled micropillars. Three main experiments have been performed:

i) The study of the temporal  $g^2(t,\tau)$  function of polariton condensates in single micropillars. This study has been performed by implementing in our laboratory a streak camera based technique, which allows to measure the  $g^2(t,\tau)$  with a time resolution of  $\sim 4$  ps. Our measurements have shown that at low excitation power the system displays a statistics compatible with thermal emission, while at higher excitation powers the system displays a coherent statistics. Our measurements indicate that interactions play a negligible role on the intensity correlations of a polariton condensate. With this study, we provide new indications in the understanding of the temporal correlation properties of polariton condensates, which is still an open question.

The same technique has been used also to study the dynamical single shot polarization properties of a polariton condensate, providing a new picture in the understanding of the polarization dynamics of the condensates.

ii) The study of Josephson oscillations in a diatomic polaritonic molecule made of two coupled micropillars. By optically controlling the system we could study different dynamical regimes. We studied the linear regime of oscillations with the observation of Rabi oscillations and the a.c. Josephson regime, both characterized by coherent oscillations in the population of the two pillars. By increasing the density of particles in the system, we could reach the nonlinear regime, where polariton-polariton repulsive interactions play an important role. We could observe anharmonic oscillations and macroscopic self-trapping. In the macroscopic self-trapping regime, nonlinearities affects the dynamics so strongly that oscillations are inhibited and the system is found in a quasi-metastable state, where most of the particles stay in one of the two pillars. We studied also the dynamical decrease of the nonlinearities, due to the progressive decrease in the global population density, related to polaritons escaping out of the cavity. We could observe for example the transition from the self-trapped state to the linear regime, in which coherent  $\pi$  oscillations take place. This study highlights polaritonic molecules as a suitable system where highly nonlinear optical effects can be studied.

iii) The study of a benzene-like polaritonic molecule, made of six coupled micropillars in a hexagonal geometry. We have shown that polariton condensation takes place on excited energy levels, on molecular modes displaying nontrivial polarization patterns: condensation on both a polarization vortex of order one and a polarization vortex of order two have been observed. The experimental observations have been interpreted by considering a polarization splitting of the polaritonic modes, aris-

ing from the contribution of two terms: a polarization dependent tunneling term (for adjacent pillars) and an on-site polarization splitting, related to the global ring symmetry. The polarization splitting acts on the system as an effective spin-orbit coupling, which couples together modes with different spin (polarization) and orbital momentum. This work opens the way to the engineering of spin-orbit coupling in polaritonic systems. In particular the scalability of our system, allows to extend the spin-orbit coupling to 2D lattices.

The work done throughout this thesis highlights the potentiality of polariton micropillars and polaritonic molecules for the observation of highly nonlinear phenomena, thanks to enhanced interparticle interactions in 0D confined structures. A further enhancement of the nonlinearities, for example through a reduction in the lateral sizes, could possibly allow to reach a single particle nonlinear regime, with the observation for example of polariton blockade or nonequilibrium strongly correlated polariton gases.

Coupled pillar structures arise also as a system where the polariton properties (non-linearity, spin, condensation) can be combined with nontrivial geometries, giving rise to geometrical dependent effects. Thanks to the high scalability of our system, the few pillar molecules can be extended to many coupled pillar structures, such as 2D lattices (as the honeycomb lattice recently realized in our group), where spin-orbit couplings can be engineered. Artificial magnetism for neutral particles and realization of topological insulators are possible routes for the future.

The combination of these properties with the out-of-equilibrium nature of polaritons, could lead to the observation of new physical effects.

# Publications and conferences

## List of publications

- 1 V. G. Sala, M. Wouters, A. Lemaître, E. Galopin, I. Sagnes, J. Bloch, A. Amo, *Temporal correlation properties of 0D polariton condensates in micropillars*, work in progress
- 2 V. G. Sala, D. D. Solnyshkov, T. Jacqmin, A. Lemaître, M. Abbarchi, E. Galopin, I. Sagnes, J. Bloch, G. Malpuech, A. Amo, *Spin-orbit coupling in a benzene-like polaritonic molecule*, submitted
- 3 M. Abbarchi, A. Amo, V. G. Sala, D. D. Solnyshkov, H. Flayac, L. Ferrier, I. Sagnes, E. Galopin, A. Lemaître, G. Malpuech and J. Bloch, *Macroscopic quantum self-trapping and Josephson oscillations of exciton polaritons*, **Nature Physics**, 9, 275-279 (2013)
- 4 A. Amo, S. Pigeon, D. Sanvitto, V.G. Sala, R. Hivet, I. Carusotto, F. Pisanello, G. Lemenager, R. Houdre, E. Giacobino, C. Ciuti, A. Bramati, *Polariton superfluids reveal quantum hydrodynamic solitons*, **Science**, 332, 1167 (2011)
- 5 D. Sanvitto, S. Pigeon, A. Amo, D. Ballarini, M. De Giorgi, I. Carusotto, R. Hivet, F. Pisanello, V.G. Sala, P.S.S. Guimaraes, R. Houdre, E. Giacobino, C. Ciuti, A. Bramati, G. Gigli, *All-optical control of the quantum flow of a polariton condensate*, **Nature Photonics**, 5, 610 (2011)

## Conferences

**Invited talk:** *Polarization vortices in a benzene-like polariton molecule*  
PLMCN14, 14th Conference on Physics of Light-Matter Coupling in Nanostructures, 27-31/05/2013, Hersonissos, Crete

**Talk:** *Macroscopic self-trapping and nonlinear Josephson oscillations in coupled polariton condensates*  
CLEO/Europe-IQEC 2013, 12-16 May 2013, Munich, Germany

**Talk:** *Dark solitons in polariton superfluids*  
PLMCN11 11th International Conference on Physics of Light-Matter Coupling in Nanostructures, 4-8 April 2011, TU-Berlin



# Bibliography

- [1] C. Weisbuch, M. Nishioka, A. Ishikawa, and Y. Arakawa, “Observation of the coupled exciton-photon mode splitting in a semiconductor quantum microcavity,” *Physical Review Letters*, vol. 69, pp. 3314–3317, Dec. 1992.
- [2] A. Kavokin, J. J. Baumberg, G. Malpuech, and F. P. Laussy, *Microcavities*. Oxford University Press, 2007.
- [3] I. Carusotto and C. Ciuti, “Quantum fluids of light,” *Reviews of Modern Physics*, vol. 85, pp. 299–366, Feb. 2013.
- [4] J. Kasprzak, M. Richard, S. Kundermann, A. Baas, P. Jeambrun, J. M. J. Keeling, F. M. Marchetti, M. H. Szymańska, R. André, J. L. Staehli, V. Savona, P. B. Littlewood, B. Deveaud, and L. S. Dang, “Bose-Einstein condensation of exciton polaritons,” *Nature*, vol. 443, pp. 409–14, Sept. 2006.
- [5] J. Kasprzak, M. Richard, A. Baas, B. Deveaud, R. André, J.-P. Poizat, and L. Dang, “Second-Order Time Correlations within a Polariton Bose-Einstein Condensate in a CdTe Microcavity,” *Physical Review Letters*, vol. 100, p. 067402, Feb. 2008.
- [6] R. Balili, V. Hartwell, D. Snoke, L. Pfeiffer, and K. West, “Bose-Einstein condensation of microcavity polaritons in a trap,” *Science (New York, N. Y.)*, vol. 316, pp. 1007–10, May 2007.
- [7] M. Richard, J. Kasprzak, R. Romestain, R. André, and L. Dang, “Spontaneous Coherent Phase Transition of Polaritons in CdTe Microcavities,” *Physical Review Letters*, vol. 94, p. 187401, May 2005.
- [8] A. P. D. Love, D. N. Krizhanovskii, D. M. Whittaker, R. Bouchekioua, D. Sanvitto, S. A. Rizeiqi, R. Bradley, M. S. Skolnick, P. R. Eastham, R. André, and L. S. Dang, “Intrinsic Decoherence Mechanisms in the Microcavity Polariton Condensate,” *Physical Review Letters*, vol. 101, p. 067404, Aug. 2008.
- [9] E. del Valle, D. Sanvitto, A. Amo, F. Laussy, R. André, C. Tejedor, and L. Viña, “Dynamics of the Formation and Decay of Coherence in a Polariton Condensate,” *Physical Review Letters*, vol. 103, p. 096404, Aug. 2009.
- [10] J. Baumberg, A. Kavokin, S. Christopoulos, A. Grundy, R. Butté, G. Christmann, D. Solnyshkov, G. Malpuech, G. Baldassarri Höger von Högersthal, E. Feltin, J.-F. Carlin, and N. Grandjean, “Spontaneous Polarization Buildup in a Room-Temperature Polariton Laser,” *Physical Review Letters*, vol. 101, p. 136409, Sept. 2008.

- [11] G. Nardin, K. G. Lagoudakis, M. Wouters, M. Richard, A. Baas, R. André, L. S. Dang, B. Pietka, and B. Deveaud-Plédran, “Dynamics of Long-Range Ordering in an Exciton-Polariton Condensate,” *Physical Review Letters*, vol. 103, p. 256402, Dec. 2009.
- [12] C. W. Lai, N. Y. Kim, S. Utsunomiya, G. Roumpos, H. Deng, M. D. Fraser, T. Byrnes, P. Recher, N. Kumada, T. Fujisawa, and Y. Yamamoto, “Coherent zero-state and  $\pi$ -state in an exciton-polariton condensate array,” *Nature*, vol. 450, pp. 529–32, Dec. 2007.
- [13] N. Y. Kim, K. Kusudo, C. Wu, N. Masumoto, A. Löffler, S. Höfling, N. Kumada, L. Worschech, A. Forchel, and Y. Yamamoto, “Dynamical d-wave condensation of exciton-polaritons in a two-dimensional square-lattice potential,” *Nature Physics*, vol. 7, pp. 681–686, June 2011.
- [14] I. Carusotto and C. Ciuti, “Probing Microcavity Polariton Superfluidity through Resonant Rayleigh Scattering,” *Physical Review Letters*, vol. 93, p. 166401, Oct. 2004.
- [15] A. Amo, J. Lefrère, S. Pigeon, C. Adrados, C. Ciuti, I. Carusotto, R. Houdré, E. Giacobino, and A. Bramati, “Superfluidity of polaritons in semiconductor microcavities,” *Nature Physics*, vol. 5, pp. 805–810, Sept. 2009.
- [16] K. G. Lagoudakis, M. Wouters, M. Richard, A. Baas, I. Carusotto, R. André, L. S. Dang, and B. Deveaud-Plédran, “Quantized vortices in an exciton-polariton condensate,” *Nature Physics*, vol. 4, pp. 706–710, Aug. 2008.
- [17] K. G. Lagoudakis, T. Ostatnický, A. V. Kavokin, Y. G. Rubo, R. André, and B. Deveaud-Plédran, “Observation of half-quantum vortices in an exciton-polariton condensate,” *Science (New York, N.Y.)*, vol. 326, pp. 974–6, Nov. 2009.
- [18] D. Sanvitto, F. M. Marchetti, M. H. Szymańska, G. Tosi, M. Baudisch, F. P. Laussy, D. N. Krizhanovskii, M. S. Skolnick, L. Marrucci, A. Lemaître, J. Bloch, C. Tejedor, and L. Viña, “Persistent currents and quantized vortices in a polariton superfluid,” *Nature Physics*, vol. 6, pp. 527–533, May 2010.
- [19] A. Amo, S. Pigeon, D. Sanvitto, V. G. Sala, R. Hivet, I. Carusotto, F. Pisanello, G. Leménager, R. Houdré, E. Giacobino, C. Ciuti, and A. Bramati, “Polariton superfluids reveal quantum hydrodynamic solitons,” *Science (New York, N.Y.)*, vol. 332, pp. 1167–70, June 2011.
- [20] G. Grosso, G. Nardin, F. Morier-Genoud, Y. Léger, and B. Deveaud-Plédran, “Soliton Instabilities and Vortex Street Formation in a Polariton Quantum Fluid,” *Physical Review Letters*, vol. 107, p. 245301, Dec. 2011.
- [21] M. Sich, D. N. Krizhanovskii, M. S. Skolnick, A. V. Gorbach, R. Hartley, D. V. Skryabin, E. A. Cerda-Méndez, K. Biermann, R. Hey, and P. V. Santos, “Observation of bright polariton solitons in a semiconductor microcavity,” *Nature Photonics*, vol. 6, pp. 50–55, Nov. 2011.
- [22] E. A. Cerda-Méndez, D. Sarkar, D. N. Krizhanovskii, S. S. Gavrilov, K. Biermann, M. S. Skolnick, and P. V. Santos, “Exciton-Polariton Gap Solitons in Two-Dimensional Lattices,” *Physical Review Letters*, vol. 111, p. 146401, Oct. 2013.

- [23] C. Leyder, M. Romanelli, J. P. Karr, E. Giacobino, T. C. H. Liew, M. M. Glazov, A. V. Kavokin, G. Malpuech, and A. Bramati, “Observation of the optical spin Hall effect,” *Nature Physics*, vol. 3, pp. 628–631, July 2007.
- [24] A. Kavokin, G. Malpuech, and M. Glazov, “Optical Spin Hall Effect,” *Physical Review Letters*, vol. 95, p. 136601, Sept. 2005.
- [25] R. Hivet, H. Flayac, D. D. Solnyshkov, D. Tanese, T. Boulier, D. Andreoli, E. Giacobino, J. Bloch, a. Bramati, G. Malpuech, and a. Amo, “Half-solitons in a polariton quantum fluid behave like magnetic monopoles,” *Nature Physics*, vol. 8, pp. 724–728, Aug. 2012.
- [26] E. Wertz, L. Ferrier, D. D. Solnyshkov, R. Johne, D. Sanvitto, A. Lemaître, I. Sagnes, R. Grousson, A. V. Kavokin, P. Senellart, G. Malpuech, and J. Bloch, “Spontaneous formation and optical manipulation of extended polariton condensates,” *Nature Physics*, vol. 6, pp. 860–864, Aug. 2010.
- [27] P. Savvidis, J. Baumberg, R. Stevenson, M. Skolnick, D. Whittaker, and J. Roberts, “Angle-Resonant Stimulated Polariton Amplifier,” *Physical Review Letters*, vol. 84, pp. 1547–1550, Feb. 2000.
- [28] J. Baumberg, P. Savvidis, R. Stevenson, A. Tartakovskii, M. Skolnick, D. Whittaker, and J. Roberts, “Parametric oscillation in a vertical microcavity: A polariton condensate or micro-optical parametric oscillation,” *Physical Review B*, vol. 62, pp. R16247–R16250, Dec. 2000.
- [29] C. Diederichs, J. Tignon, G. Dasbach, C. Ciuti, A. Lemaître, J. Bloch, P. Rousignol, and C. Delalande, “Parametric oscillation in vertical triple microcavities,” *Nature*, vol. 440, pp. 904–7, Apr. 2006.
- [30] R. Stevenson, V. Astratov, M. Skolnick, D. Whittaker, M. Emam-Ismaïl, A. Tartakovskii, P. Savvidis, J. Baumberg, and J. Roberts, “Continuous Wave Observation of Massive Polariton Redistribution by Stimulated Scattering in Semiconductor Microcavities,” *Physical Review Letters*, vol. 85, pp. 3680–3683, Oct. 2000.
- [31] J. Karr, A. Baas, R. Houdré, and E. Giacobino, “Squeezing in semiconductor microcavities in the strong-coupling regime,” *Physical Review A*, vol. 69, p. 031802, Mar. 2004.
- [32] A. Baas, J. Karr, H. Eleuch, and E. Giacobino, “Optical bistability in semiconductor microcavities,” *Physical Review A*, vol. 69, p. 023809, Feb. 2004.
- [33] A. Baas, J.-P. Karr, M. Romanelli, A. Bramati, and E. Giacobino, “Optical bistability in semiconductor microcavities in the nondegenerate parametric oscillation regime: Analogy with the optical parametric oscillator,” *Physical Review B*, vol. 70, p. 161307, Oct. 2004.
- [34] N. Gippius, I. Shelykh, D. Solnyshkov, S. Gavrilov, Y. Rubo, A. Kavokin, S. Tikhodeev, and G. Malpuech, “Polarization Multistability of Cavity Polaritons,” *Physical Review Letters*, vol. 98, p. 236401, June 2007.
- [35] T. K. Paraïso, M. Wouters, Y. Léger, F. Morier-Genoud, and B. Deveaud-Plédran, “Multistability of a coherent spin ensemble in a semiconductor microcavity,” *Nature materials*, vol. 9, pp. 655–60, Aug. 2010.

- [36] A. Verger, C. Ciuti, and I. Carusotto, “Polariton quantum blockade in a photonic dot,” *Physical Review B*, vol. 73, p. 193306, May 2006.
- [37] D. Gerace, H. E. Tureci, A. Imamoglu, V. Giovannetti, and R. Fazio, “The quantum-optical Josephson interferometer,” *Nature Physics*, vol. 5, pp. 281–284, Mar. 2009.
- [38] I. Carusotto, D. Gerace, H. Tureci, S. De Liberato, C. Ciuti, and A. Imamoglu, “Fermionized Photons in an Array of Driven Dissipative Nonlinear Cavities,” *Physical Review Letters*, vol. 103, p. 033601, July 2009.
- [39] C. Sturm, D. Tanese, H. S. Nguyen, H. Flayac, E. Galopin, A. Lemaître, I. Sagnes, D. Solnyshkov, A. Amo, G. Malpuech, and J. Bloch, “Giant phase modulation in a Mach-Zehnder exciton-polariton interferometer,” p. 18, Mar. 2013.
- [40] H. S. Nguyen, D. Vishnevsky, C. Sturm, D. Tanese, D. Solnyshkov, E. Galopin, A. Lemaître, I. Sagnes, A. Amo, G. Malpuech, and J. Bloch, “Realization of a Double-Barrier Resonant Tunneling Diode for Cavity Polaritons,” *Physical Review Letters*, vol. 110, p. 236601, June 2013.
- [41] D. Ballarini, M. De Giorgi, E. Cancellieri, R. Houdré, E. Giacobino, R. Cingolani, A. Bramati, G. Gigli, and D. Sanvitto, “All-optical polariton transistor,” *Nature communications*, vol. 4, p. 1778, Jan. 2013.
- [42] T. Gao, P. S. Eldridge, T. C. H. Liew, S. I. Tsintzos, G. Stavrinidis, G. Deligeorgis, Z. Hatzopoulos, and P. G. Savvidis, “Polariton condensate transistor switch,” *Physical Review B*, vol. 85, p. 235102, June 2012.
- [43] C. Antón, T. C. H. Liew, G. Tosi, M. D. Martín, T. Gao, Z. Hatzopoulos, P. S. Eldridge, P. G. Savvidis, and L. Viña, “Dynamics of a polariton condensate transistor switch,” *Applied Physics Letters*, vol. 101, no. 26, p. 261116, 2012.
- [44] T. Liew, A. Kavokin, and I. Shelykh, “Optical Circuits Based on Polariton Neurons in Semiconductor Microcavities,” *Physical Review Letters*, vol. 101, p. 016402, July 2008.
- [45] T. C. H. Liew, A. V. Kavokin, T. Ostatnický, M. Kaliteevski, I. A. Shelykh, and R. A. Abram, “Exciton-polariton integrated circuits,” *Physical Review B*, vol. 82, p. 033302, July 2010.
- [46] M. Liscidini, D. Gerace, D. Sanvitto, and D. Bajoni, “Guided Bloch surface wave polaritons,” *Applied Physics Letters*, vol. 98, no. 12, p. 121118, 2011.
- [47] I. Shelykh, G. Pavlovic, D. Solnyshkov, and G. Malpuech, “Proposal for a Mesoscopic Optical Berry-Phase Interferometer,” *Physical Review Letters*, vol. 102, p. 046407, Jan. 2009.
- [48] C. Cohen-Tannoudji, B. Diu, and F. Laloë, *Mécanique quantique Tome 2*. Hermann.
- [49] R. Thompson, G. Rempe, and H. Kimble, “Observation of normal-mode splitting for an atom in an optical cavity,” *Physical Review Letters*, vol. 68, pp. 1132–1135, Feb. 1992.

- [50] B. Deveaud, F. Clérot, N. Roy, K. Satzke, B. Sermage, and D. Katzer, “Enhanced radiative recombination of free excitons in GaAs quantum wells,” *Physical Review Letters*, vol. 67, pp. 2355–2358, Oct. 1991.
- [51] D. Bajoni, M. Perrin, P. Senellart, A. Lemaître, B. Sermage, and J. Bloch, “Dynamics of microcavity polaritons in the presence of an electron gas,” *Physical Review B*, vol. 73, p. 205344, May 2006.
- [52] J. Hopfield, “Theory of the Contribution of Excitons to the Complex Dielectric Constant of Crystals,” *Physical Review*, vol. 112, pp. 1555–1567, Dec. 1958.
- [53] L. P. Pitaevskii and S. Stringari, *Bose-einstein condensation*. No. 116, Oxford University Press, 2003.
- [54] C. J. Pethick and H. Smith, *Bose-Einstein condensation in dilute gases*. Cambridge university press, 2002.
- [55] M. H. Anderson, J. R. Ensher, M. R. Matthews, C. E. Wieman, and E. A. Cornell, “Observation of bose-einstein condensation in a dilute atomic vapor.,” *Science (New York, N.Y.)*, vol. 269, pp. 198–201, July 1995.
- [56] K. Davis, M. Mewes, M. Andrews, N. van Druten, D. Durfee, D. Kurn, and W. Ketterle, “Bose-Einstein Condensation in a Gas of Sodium Atoms,” *Physical Review Letters*, vol. 75, pp. 3969–3973, Nov. 1995.
- [57] H. Deng, H. Haug, and Y. Yamamoto, “Exciton-polariton Bose-Einstein condensation,” *Reviews of Modern Physics*, vol. 82, pp. 1489–1537, May 2010.
- [58] A. Imamoglu and R. Ram, “Quantum dynamics of exciton lasers,” *Physics Letters A*, vol. 214, pp. 193–198, May 1996.
- [59] A. Imamoglu, R. Ram, S. Pau, and Y. Yamamoto, “Nonequilibrium condensates and lasers without inversion: Exciton-polariton lasers,” *Physical Review A*, vol. 53, pp. 4250–4253, June 1996.
- [60] H. Deng, G. Weihs, C. Santori, J. Bloch, and Y. Yamamoto, “Condensation of semiconductor microcavity exciton polaritons,” *Science (New York, N.Y.)*, vol. 298, pp. 199–202, Oct. 2002.
- [61] D. Bajoni, P. Senellart, E. Wertz, I. Sagnes, A. Miard, A. Lemaître, and J. Bloch, “Polariton Laser Using Single Micropillar GaAs-GaAlAs Semiconductor Cavities,” *Physical Review Letters*, vol. 100, p. 047401, Jan. 2008.
- [62] G. Malpuech, A. Di Carlo, A. Kavokin, J. J. Baumberg, M. Zamfirescu, and P. Lugli, “Room-temperature polariton lasers based on GaN microcavities,” *Applied Physics Letters*, vol. 81, no. 3, p. 412, 2002.
- [63] S. Christopoulos, G. von Högersthal, A. Grundy, P. Lagoudakis, A. Kavokin, J. Baumberg, G. Christmann, R. Butté, E. Feltn, J.-F. Carlin, and N. Grandjean, “Room-Temperature Polariton Lasing in Semiconductor Microcavities,” *Physical Review Letters*, vol. 98, p. 126405, Mar. 2007.
- [64] G. Malpuech, Y. G. Rubo, F. P. Laussy, P. Bigenwald, and A. V. Kavokin, “Polariton laser: thermodynamics and quantum kinetic theory,” *Semiconductor Science and Technology*, vol. 18, pp. S395–S404, Oct. 2003.

- [65] C. Ciuti, V. Savona, C. Piermarocchi, A. Quattropani, and P. Schwendimann, “Role of the exchange of carriers in elastic exciton-exciton scattering in quantum wells,” *Physical Review B*, vol. 58, pp. 7926–7933, Sept. 1998.
- [66] K. M. Birnbaum, A. Boca, R. Miller, A. D. Boozer, T. E. Northup, and H. J. Kimble, “Photon blockade in an optical cavity with one trapped atom.,” *Nature*, vol. 436, pp. 87–90, July 2005.
- [67] G. Nardin, G. Grosso, Y. Léger, B. Pitka, F. Morier-Genoud, and B. Deveaud-Plédran, “Hydrodynamic nucleation of quantized vortex pairs in a polariton quantum fluid,” *Nature Physics*, vol. 7, pp. 635–641, Apr. 2011.
- [68] A. Amo, D. Sanvitto, F. P. Laussy, D. Ballarini, E. del Valle, M. D. Martín, A. Lemaître, J. Bloch, D. N. Krizhanovskii, M. S. Skolnick, C. Tejedor, and L. Viña, “Collective fluid dynamics of a polariton condensate in a semiconductor microcavity.,” *Nature*, vol. 457, pp. 291–5, Jan. 2009.
- [69] D. Sanvitto, S. Pigeon, A. Amo, D. Ballarini, M. De Giorgi, I. Carusotto, R. Hivet, F. Pisanello, V. G. Sala, P. S. S. Guimaraes, R. Houdré, E. Giacobino, C. Ciuti, A. Bramati, and G. Gigli, “All-optical control of the quantum flow of a polariton condensate,” *Nature Photonics*, vol. 5, pp. 610–614, Sept. 2011.
- [70] I. Shelykh, Y. Rubo, G. Malpuech, D. Solnyshkov, and A. Kavokin, “Polarization and Propagation of Polariton Condensates,” *Physical Review Letters*, vol. 97, p. 066402, Aug. 2006.
- [71] A. Amo, T. C. H. Liew, C. Adrados, R. Houdré, E. Giacobino, A. V. Kavokin, and A. Bramati, “Exciton–polariton spin switches,” *Nature Photonics*, vol. 4, pp. 361–366, Apr. 2010.
- [72] D. Sarkar, S. S. Gavrilov, M. Sich, J. H. Quilter, R. A. Bradley, N. A. Gippius, K. Guda, V. D. Kulakovskii, M. S. Skolnick, and D. N. Krizhanovskii, “Polarization Bistability and Resultant Spin Rings in Semiconductor Microcavities,” *Physical Review Letters*, vol. 105, p. 216402, Nov. 2010.
- [73] C. Adrados, A. Amo, T. C. H. Liew, R. Hivet, R. Houdré, E. Giacobino, A. V. Kavokin, and A. Bramati, “Spin Rings in Bistable Planar Semiconductor Microcavities,” *Physical Review Letters*, vol. 105, p. 216403, Nov. 2010.
- [74] K. Kavokin, I. Shelykh, A. Kavokin, G. Malpuech, and P. Bigenwald, “Quantum Theory of Spin Dynamics of Exciton-Polaritons in Microcavities,” *Physical Review Letters*, vol. 92, p. 017401, Jan. 2004.
- [75] M. Maragkou, C. E. Richards, T. Ostatnický, A. J. D. Grundy, J. Zajac, M. Hugues, W. Langbein, and P. G. Lagoudakis, “Optical analogue of the spin Hall effect in a photonic cavity.,” *Optics letters*, vol. 36, pp. 1095–7, Apr. 2011.
- [76] A. Amo, T. C. H. Liew, C. Adrados, E. Giacobino, A. V. Kavokin, and A. Bramati, “Anisotropic optical spin Hall effect in semiconductor microcavities,” *Physical Review B*, vol. 80, no. 16, p. 165325, 2009.

- [77] E. A. Cerda-Méndez, D. N. Krizhanovskii, M. Wouters, R. Bradley, K. Biermann, K. Guda, R. Hey, P. V. Santos, D. Sarkar, and M. S. Skolnick, “Polariton Condensation in Dynamic Acoustic Lattices,” *Physical Review Letters*, vol. 105, p. 116402, Sept. 2010.
- [78] G. Tosi, G. Christmann, N. G. Berloff, P. Tsotsis, T. Gao, Z. Hatzopoulos, P. G. Savvidis, and J. J. Baumberg, “Sculpting oscillators with light within a nonlinear quantum fluid,” *Nature Physics*, vol. 8, no. 3, pp. 190–194, 2012.
- [79] E. A. Cerda-Méndez, D. N. Krizhanovskii, K. Biermann, R. Hey, M. S. Skolnick, and P. V. Santos, “Dynamic exciton-polariton macroscopic coherent phases in a tunable dot lattice,” *Physical Review B*, vol. 86, p. 100301, Sept. 2012.
- [80] A. Amo, S. Pigeon, C. Adrados, R. Houdré, E. Giacobino, C. Ciuti, and A. Bramati, “Light engineering of the polariton landscape in semiconductor microcavities,” *Physical Review B*, vol. 82, p. 081301, Aug. 2010.
- [81] G. Tosi, G. Christmann, N. G. Berloff, P. Tsotsis, T. Gao, Z. Hatzopoulos, P. G. Savvidis, and J. J. Baumberg, “Geometrically locked vortex lattices in semiconductor quantum fluids,” *Nature communications*, vol. 3, p. 1243, 2012.
- [82] R. Cerna, D. Sarchi, T. Paraiso, G. Nardin, Y. Léger, M. Richard, B. Pietka, O. El Daif, F. Morier-Genoud, V. Savona, M. Portella-Oberli, and B. Deveaud-Plédran, “Coherent optical control of the wave function of zero-dimensional exciton polaritons,” *Physical Review B*, vol. 80, p. 121309, Sept. 2009.
- [83] M. Bayer, T. Gutbrod, A. Forchel, T. Reinecke, P. Knipp, R. Werner, and J. Reithmaier, “Optical Demonstration of a Crystal Band Structure Formation,” *Physical Review Letters*, vol. 83, pp. 5374–5377, Dec. 1999.
- [84] N. Y. Kim, K. Kusudo, A. Löffler, S. Höfling, A. Forchel, and Y. Yamamoto, “Exciton-polariton condensates near the Dirac point in a triangular lattice,” *New Journal of Physics*, vol. 15, p. 035032, Mar. 2013.
- [85] R. I. Kaitouni, O. El Daif, A. Baas, M. Richard, T. Paraiso, P. Lugan, T. Guillet, F. Morier-Genoud, J. Ganière, J. Staehli, V. Savona, and B. Deveaud, “Engineering the spatial confinement of exciton polaritons in semiconductors,” *Physical Review B*, vol. 74, p. 155311, Oct. 2006.
- [86] O. El Daif, A. Baas, T. Guillet, J.-P. Brantut, R. I. Kaitouni, J. L. Staehli, F. Morier-Genoud, and B. Deveaud, “Polariton quantum boxes in semiconductor microcavities,” *Applied Physics Letters*, vol. 88, no. 6, p. 061105, 2006.
- [87] G. Dasbach, M. Bayer, M. Schwab, and A. Forchel, “Spatial photon trapping: tailoring the optical properties of semiconductor microcavities,” *Semiconductor Science and Technology*, vol. 18, pp. S339–S350, Oct. 2003.
- [88] G. Dasbach, M. Schwab, M. Bayer, D. Krizhanovskii, and A. Forchel, “Tailoring the polariton dispersion by optical confinement: Access to a manifold of elastic polariton pair scattering channels,” *Physical Review B*, vol. 66, p. 201201, Nov. 2002.

- [89] A. Kuther, M. Bayer, T. Gutbrod, A. Forchel, P. Knipp, T. Reinecke, and R. Werner, “Confined optical modes in photonic wires,” *Physical Review B*, vol. 58, pp. 15744–15748, Dec. 1998.
- [90] D. Tanese, H. Flayac, D. Solnyshkov, A. Amo, A. Lemaître, E. Galopin, R. Braive, P. Senellart, I. Sagnes, G. Malpuech, and J. Bloch, “Polariton condensation in solitonic gap states in a one-dimensional periodic potential,” *Nature communications*, vol. 4, p. 1749, Jan. 2013.
- [91] E. Wertz, *Formation spontanée de condensats de polaritons dans des microcavités à base de GaAs*. PhD thesis, Université Paris - Sud 11, 2010.
- [92] L. Ferrier, E. Wertz, R. Johne, D. D. Solnyshkov, P. Senellart, I. Sagnes, A. Lemaître, G. Malpuech, and J. Bloch, “Interactions in Confined Polariton Condensates,” *Physical Review Letters*, vol. 106, p. 126401, Mar. 2011.
- [93] T. Jacqmin, I. Carusotto, I. Sagnes, M. Abbarchi, D. Solnyshkov, G. Malpuech, E. Galopin, A. Lemaître, J. Bloch, and A. Amo, “Direct observation of Dirac cones and a flatband in a honeycomb lattice for polaritons,” Oct. 2013.
- [94] M. Galbiati, L. Ferrier, D. D. Solnyshkov, D. Tanese, E. Wertz, A. Amo, M. Abbarchi, P. Senellart, I. Sagnes, A. Lemaître, E. Galopin, G. Malpuech, and J. Bloch, “Polariton Condensation in Photonic Molecules,” *Physical Review Letters*, vol. 108, p. 126403, Mar. 2012.
- [95] M. Abbarchi, A. Amo, V. G. Sala, D. D. Solnyshkov, H. Flayac, L. Ferrier, I. Sagnes, E. Galopin, A. Lemaître, G. Malpuech, and J. Bloch, “Macroscopic quantum self-trapping and Josephson oscillations of exciton polaritons,” *Nature Physics*, vol. 9, pp. 275–279, Apr. 2013.
- [96] R. Glauber, “Coherent and Incoherent States of the Radiation Field,” *Physical Review*, vol. 131, pp. 2766–2788, Sept. 1963.
- [97] F. Laussy, G. Malpuech, a. Kavokin, and P. Bigenwald, “Spontaneous Coherence Buildup in a Polariton Laser,” *Physical Review Letters*, vol. 93, p. 016402, June 2004.
- [98] T. Doan, H. Cao, D. Thoai, and H. Haug, “Coherence of condensed microcavity polaritons calculated within Boltzmann-Master equations,” *Physical Review B*, vol. 78, p. 205306, Nov. 2008.
- [99] M. Wouters and V. Savona, “Stochastic classical field model for polariton condensates,” *Physical Review B*, vol. 79, p. 165302, Apr. 2009.
- [100] P. Schwendimann and A. Quattropani, “Statistics of the polariton condensate,” *Physical Review B*, vol. 77, p. 085317, Feb. 2008.
- [101] T. Horikiri, P. Schwendimann, A. Quattropani, S. Höfling, A. Forchel, and Y. Yamamoto, “Higher order coherence of exciton-polariton condensates,” *Physical Review B*, vol. 81, p. 033307, Jan. 2010.
- [102] R. Hanbury Brown and R. Q. Twiss, “The Question of Correlation between Photons in Coherent Light Rays,” *Nature*, vol. 178, pp. 1447–1448, Dec. 1956.

- [103] J.-S. Tempel, F. Veit, M. Assmann, L. E. Kreilkamp, A. Rahimi-Iman, A. Löffler, S. Höfling, S. Reitzenstein, L. Worschech, A. Forchel, and M. Bayer, “Characterization of two-threshold behavior of the emission from a GaAs microcavity,” *Physical Review B*, vol. 85, p. 075318, Feb. 2012.
- [104] J. Wiersig, C. Gies, F. Jahnke, M. Assmann, T. Berstermann, M. Bayer, C. Kistner, S. Reitzenstein, C. Schneider, S. Höfling, A. Forchel, C. Kruse, J. Kalden, and D. Hommel, “Direct observation of correlations between individual photon emission events of a microcavity laser.,” *Nature*, vol. 460, pp. 245–9, July 2009.
- [105] M. Assmann, F. Veit, M. Bayer, M. van der Poel, and J. M. Hvam, “Higher-order photon bunching in a semiconductor microcavity.,” *Science (New York, N. Y.)*, vol. 325, pp. 297–300, July 2009.
- [106] M. Assmann, J.-S. Tempel, F. Veit, M. Bayer, A. Rahimi-Iman, A. Löffler, S. Höfling, S. Reitzenstein, L. Worschech, and A. Forchel, “From polariton condensates to highly photonic quantum degenerate states of bosonic matter.,” *Proceedings of the National Academy of Sciences of the United States of America*, vol. 108, pp. 1804–9, Feb. 2011.
- [107] M. Maragkou, A. J. D. Grundy, E. Wertz, A. Lemaître, I. Sagnes, P. Senellart, J. Bloch, and P. G. Lagoudakis, “Spontaneous nonground state polariton condensation in pillar microcavities,” *Phys. Rev. B*, vol. 81, p. 81307, Feb. 2010.
- [108] R. Loudon, *The quantum theory of light*. Oxford university press, 2000.
- [109] I. Shelykh, K. V. Kavokin, A. V. Kavokin, G. Malpuech, P. Bigenwald, H. Deng, G. Weihs, and Y. Yamamoto, “Semiconductor microcavity as a spin-dependent optoelectronic device,” *Phys. Rev. B*, vol. 70, no. 3, p. 35320, 2004.
- [110] L. Klotkowski, M. Martín, A. Amo, L. Viña, I. Shelykh, M. Glazov, G. Malpuech, A. Kavokin, and R. André, “Optical anisotropy and pinning of the linear polarization of light in semiconductor microcavities,” *Solid State Communications*, vol. 139, pp. 511–515, Sept. 2006.
- [111] S. Fölling, S. Trotzky, P. Cheinet, M. Feld, R. Saers, A. Widera, T. Müller, and I. Bloch, “Direct observation of second-order atom tunnelling.,” *Nature*, vol. 448, pp. 1029–32, Aug. 2007.
- [112] D. Gerace and I. Carusotto, “Analog Hawking radiation from an acoustic black hole in a flowing polariton superfluid,” *Physical Review B*, vol. 86, p. 144505, Oct. 2012.
- [113] F. Lederer, G. I. Stegeman, D. N. Christodoulides, G. Assanto, M. Segev, and Y. Silberberg, “Discrete solitons in optics,” *Physics Reports*, vol. 463, pp. 1–126, July 2008.
- [114] J. C. Eilbeck and M. Johansson, “The discrete nonlinear Schrödinger equation—20 years on,” in *Conference on Localization and Energy Transfer in Nonlinear Systems*, p. 44, 2003.
- [115] A. S. Davydov, “The theory of contraction of proteins under their excitation,” *Journal of Theoretical Biology*, vol. 38, no. 3, pp. 559–569, 1973.

- [116] W. P. Su, J. R. Schrieffer, and A. J. Heeger, “Solitons in polyacetylene,” *Physical Review Letters*, vol. 42, no. 25, pp. 1698–1701, 1979.
- [117] A. J. Heeger, S. Kivelson, J. R. Schrieffer, and W.-P. Su, “Solitons in conducting polymers,” *Reviews of Modern Physics*, vol. 60, no. 3, p. 781, 1988.
- [118] J. Hubbard, “Electron Correlations in Narrow Energy Bands,” *Proceedings of the Royal Society A: Mathematical, Physical and Engineering Sciences*, vol. 276, pp. 238–257, Nov. 1963.
- [119] D. N. Christodoulides, F. Lederer, and Y. Silberberg, “Discretizing light behaviour in linear and nonlinear waveguide lattices,” *Nature*, vol. 424, pp. 817–23, Aug. 2003.
- [120] I. L. Garanovich, S. Longhi, A. A. Sukhorukov, and Y. S. Kivshar, “Light propagation and localization in modulated photonic lattices and waveguides,” *Physics Reports*, vol. 518, pp. 1–79, Sept. 2012.
- [121] O. Morsch and M. Oberthaler, “Dynamics of Bose-Einstein condensates in optical lattices,” *Reviews of Modern Physics*, vol. 78, pp. 179–215, Feb. 2006.
- [122] M. Albiez, R. Gati, J. Fölling, S. Hunsmann, M. Cristiani, and M. K. Oberthaler, “Direct Observation of Tunneling and Nonlinear Self-Trapping in a Single Bosonic Josephson Junction,” *Physical Review Letters*, vol. 95, p. 010402, June 2005.
- [123] A. Smerzi, S. Fantoni, S. Giovanazzi, and S. R. Shenoy, “Quantum Coherent Atomic Tunneling between Two Trapped Bose-Einstein Condensates,” *Physical Review Letters*, vol. 79, pp. 4950–4953, Dec. 1997.
- [124] S. Raghavan, A. Smerzi, S. Fantoni, and S. Shenoy, “Coherent oscillations between two weakly coupled Bose-Einstein condensates: Josephson effects,  $\pi$  oscillations, and macroscopic quantum self-trapping,” *Physical Review A*, vol. 59, pp. 620–633, Jan. 1999.
- [125] D. D. Solnyshkov, R. Johne, I. a. Shelykh, and G. Malpuech, “Chaotic Josephson oscillations of exciton-polaritons and their applications,” *Physical Review B*, vol. 80, p. 235303, Dec. 2009.
- [126] C. Cambournac, T. Sylvestre, H. Maillotte, B. Vanderlinden, P. Kockaert, P. Emplit, and M. Haelterman, “Symmetry-Breaking Instability of Multimode Vector Solitons,” *Physical Review Letters*, vol. 89, p. 083901, July 2002.
- [127] T. Zibold, E. Nicklas, C. Gross, and M. K. Oberthaler, “Classical Bifurcation at the Transition from Rabi to Josephson Dynamics,” *Physical Review Letters*, vol. 105, p. 204101, Nov. 2010.
- [128] C. S. Gerving, T. M. Hoang, B. J. Land, M. Anquez, C. D. Hamley, and M. S. Chapman, “Non-equilibrium dynamics of an unstable quantum pendulum explored in a spin-1 Bose-Einstein condensate,” *Nature communications*, vol. 3, p. 1169, Jan. 2012.
- [129] B. Juliá-Díaz, T. Zibold, M. K. Oberthaler, M. Melé-Messeguer, J. Martorell, and a. Polls, “Dynamic generation of spin-squeezed states in bosonic Josephson junctions,” *Physical Review A*, vol. 86, p. 023615, Aug. 2012.

- [130] B. Josephson, “Possible new effects in superconductive tunnelling,” *Physics Letters*, vol. 1, pp. 251–253, July 1962.
- [131] B. Josephson, “The discovery of tunnelling supercurrents,” *Reviews of Modern Physics*, vol. 46, pp. 251–254, Apr. 1974.
- [132] Y. Yu, S. Han, X. Chu, S.-I. Chu, and Z. Wang, “Coherent temporal oscillations of macroscopic quantum states in a Josephson junction.,” *Science (New York, N.Y.)*, vol. 296, pp. 889–92, May 2002.
- [133] S. V. Pereverzev, A. Loshak, S. Backhaus, and J. C. Davis, “letters to nature Quantum oscillations between two weakly coupled reservoirs of superfluid  $^3\text{He}$ ,” vol. 388, no. July, pp. 449–451, 1997.
- [134] J. Javanainen, “Oscillatory exchange of atoms between traps containing Bose condensates,” *Physical Review Letters*, vol. 57, pp. 3164–3166, Dec. 1986.
- [135] G. J. Milburn, J. Corney, E. M. Wright, and D. F. Walls, “Quantum dynamics of an atomic Bose-Einstein condensate in a double-well potential,” *Physical Review A*, vol. 55, pp. 4318–4324, June 1997.
- [136] S. Levy, E. Lahoud, I. Shomroni, and J. Steinhauer, “The a.c. and d.c. Josephson effects in a Bose-Einstein condensate.,” *Nature*, vol. 449, pp. 579–83, Oct. 2007.
- [137] F. S. Cataliotti, S. Burger, C. Fort, P. Maddaloni, F. Minardi, A. Trombettoni, A. Smerzi, and M. Inguscio, “Josephson junction arrays with Bose-Einstein condensates.,” *Science (New York, N.Y.)*, vol. 293, pp. 843–6, Aug. 2001.
- [138] T. Anker, M. Albiez, R. Gati, S. Hunsmann, B. Eiermann, A. Trombettoni, and M. Oberthaler, “Nonlinear Self-Trapping of Matter Waves in Periodic Potentials,” *Physical Review Letters*, vol. 94, p. 020403, Jan. 2005.
- [139] P. Kevrekidis, Z. Chen, B. Malomed, D. Frantzeskakis, and M. Weinstein, “Spontaneous symmetry breaking in photonic lattices: Theory and experiment,” *Physics Letters A*, vol. 340, pp. 275–280, June 2005.
- [140] D. Sarchi, I. Carusotto, M. Wouters, and V. Savona, “Coherent dynamics and parametric instabilities of microcavity polaritons in double-well systems,” *Physical Review B*, vol. 77, p. 125324, Mar. 2008.
- [141] I. Shelykh, D. Solnyshkov, G. Pavlovic, and G. Malpuech, “Josephson effects in condensates of excitons and exciton polaritons,” *Physical Review B*, vol. 78, p. 041302, July 2008.
- [142] S. Schmidt, D. Gerace, A. A. Houck, G. Blatter, and H. E. Türeci, “Nonequilibrium delocalization-localization transition of photons in circuit quantum electrodynamics,” *Physical Review B*, vol. 82, p. 100507, Sept. 2010.
- [143] K. G. Lagoudakis, B. Pietka, M. Wouters, R. André, and B. Deveaud-Plédran, “Coherent Oscillations in an Exciton-Polariton Josephson Junction,” *Physical Review Letters*, vol. 105, p. 120403, Sept. 2010.

- [144] D. N. Krizhanovskii, D. Sanvitto, I. A. Shelykh, M. M. Glazov, G. Malpuech, D. D. Solnyshkov, A. Kavokin, S. Ceccarelli, M. S. Skolnick, and J. S. Roberts, “Rotation of the plane of polarization of light in a semiconductor microcavity,” *Physical Review B*, vol. 73, no. 7, p. 73303, 2006.
- [145] A. Le Boité, G. Orso, and C. Ciuti, “Steady-State Phases and Tunneling-Induced Instabilities in the Driven Dissipative Bose-Hubbard Model,” *Physical Review Letters*, vol. 110, p. 233601, June 2013.
- [146] P. Cristofolini, G. Christmann, S. I. Tsintzos, G. Deligeorgis, G. Konstantinidis, Z. Hatzopoulos, P. G. Savvidis, and J. J. Baumberg, “Coupling quantum tunneling with cavity photons,” *Science (New York, N.Y.)*, vol. 336, pp. 704–7, May 2012.
- [147] T. C. H. Liew and V. Savona, “Single Photons from Coupled Quantum Modes,” *Physical Review Letters*, vol. 104, p. 183601, May 2010.
- [148] M. Bamba and C. Ciuti, “Counter-polarized single-photon generation from the auxiliary cavity of a weakly nonlinear photonic molecule,” *Applied Physics Letters*, vol. 99, no. 17, p. 171111, 2011.
- [149] A. D. Greentree, C. Tahan, J. H. Cole, and L. C. L. Hollenberg, “Quantum phase transitions of light,” *Nature Physics*, vol. 2, pp. 856–861, Nov. 2006.
- [150] M. J. Hartmann, F. G. S. L. Brandão, and M. B. Plenio, “Strongly interacting polaritons in coupled arrays of cavities,” *Nature Physics*, vol. 2, pp. 849–855, Nov. 2006.
- [151] D. Angelakis, M. Santos, and S. Bose, “Photon-blockade-induced Mott transitions and XY spin models in coupled cavity arrays,” *Physical Review A*, vol. 76, p. 031805, Sept. 2007.
- [152] M. Hartmann, F. Brandão, and M. Plenio, “Quantum many-body phenomena in coupled cavity arrays,” *Laser & Photonics Review*, vol. 2, pp. 527–556, Dec. 2008.
- [153] D. E. Chang, V. Gritsev, G. Morigi, V. Vuletić, M. D. Lukin, and E. A. Demler, “Crystallization of strongly interacting photons in a nonlinear optical fibre,” *Nature Physics*, vol. 4, pp. 884–889, Sept. 2008.
- [154] A. H. Castro Neto, N. M. R. Peres, K. S. Novoselov, and A. K. Geim, “The electronic properties of graphene,” *Reviews of Modern Physics*, vol. 81, pp. 109–162, Jan. 2009.
- [155] K. S. Novoselov, A. K. Geim, S. V. Morozov, D. Jiang, M. I. Katsnelson, I. V. Grigorieva, S. V. Dubonos, and A. A. Firsov, “Two-dimensional gas of massless Dirac fermions in graphene,” *Nature*, vol. 438, pp. 197–200, Nov. 2005.
- [156] Y. Zhang, Y.-W. Tan, H. L. Stormer, and P. Kim, “Experimental observation of the quantum Hall effect and Berry’s phase in graphene,” *Nature*, vol. 438, pp. 201–4, Nov. 2005.
- [157] A. Calogeracos and N. Dombey, “History and physics of the Klein paradox,” *Contemporary Physics*, vol. 40, pp. 313–321, Sept. 1999.

- [158] C. Itzykson and J. B. Zuber, “Quantum Field Theory Dover Publications, New York,” 2006.
- [159] M. I. Katsnelson, “Conductance quantization in graphene nanoribbons: adiabatic approximation,” *The European Physical Journal B*, vol. 57, pp. 225–228, June 2007.
- [160] N. Peres, A. Castro Neto, and F. Guinea, “Conductance quantization in mesoscopic graphene,” *Physical Review B*, vol. 73, p. 195411, May 2006.
- [161] M. Maragkou, A. J. D. Grundy, T. Ostatnický, and P. G. Lagoudakis, “Longitudinal optical phonon assisted polariton laser,” *Applied Physics Letters*, vol. 97, no. 11, p. 111110, 2010.
- [162] I. L. Aleiner, B. L. Altshuler, and Y. G. Rubo, “Radiative coupling and weak lasing of exciton-polariton condensates,” *Physical Review B*, vol. 85, p. 121301, Mar. 2012.
- [163] S. Michaelis de Vasconcellos, A. Calvar, A. Dousse, J. Suffczynski, N. Dupuis, A. Lemaître, I. Sagnes, J. Bloch, P. Voisin, and P. Senellart, “Spatial, spectral, and polarization properties of coupled micropillar cavities,” *Applied Physics Letters*, vol. 99, no. 10, p. 101103, 2011.
- [164] D. Loss, P. Goldbart, and A. Balatsky, “Berry’s phase and persistent charge and spin currents in textured mesoscopic rings,” *Physical Review Letters*, vol. 65, pp. 1655–1658, Sept. 1990.
- [165] I. Žutić and S. Das Sarma, “Spintronics: Fundamentals and applications,” *Reviews of Modern Physics*, vol. 76, pp. 323–410, Apr. 2004.
- [166] G. Dresselhaus, “Spin-orbit coupling effects in zinc blende structures,” *Physical Review*, vol. 100, no. 2, pp. 580–586, 1955.
- [167] E. I. Rashba, “Properties of semiconductors with an extremum loop. 1. Cyclotron and combinational resonance in a magnetic field perpendicular to the plane of the loop,” *Sov. Phys. Solid State*, vol. 2, pp. 1109–1122, 1960.
- [168] Y. K. Kato, R. C. Myers, a. C. Gossard, and D. D. Awschalom, “Observation of the spin Hall effect in semiconductors.,” *Science (New York, N.Y.)*, vol. 306, pp. 1910–3, Dec. 2004.
- [169] J. Wunderlich, B. Kaestner, J. Sinova, and T. Jungwirth, “Experimental Observation of the Spin-Hall Effect in a Two-Dimensional Spin-Orbit Coupled Semiconductor System,” *Physical Review Letters*, vol. 94, p. 047204, Feb. 2005.
- [170] T. Ando, Y. Matsumoto, and Y. Uemura, “Theory of Hall Effect in a Two-Dimensional Electron System,” *Journal of the Physical Society of Japan*, vol. 39, pp. 279–288, Feb. 1975.
- [171] K. Klitzing, G. Dorda, and M. Pepper, “New Method for High-Accuracy Determination of the Fine-Structure Constant Based on Quantized Hall Resistance,” *Physical Review Letters*, vol. 45, pp. 494–497, Aug. 1980.
- [172] J. Sinova, D. Culcer, Q. Niu, N. A. Sinitsyn, T. Jungwirth, and A. H. MacDonald, “Universal intrinsic spin Hall effect,” *Physical review letters*, vol. 92, no. 12, p. 126603, 2004.

- [173] S. Murakami, N. Nagaosa, and S.-C. Zhang, “Spin-Hall Insulator,” *Physical Review Letters*, vol. 93, p. 156804, Oct. 2004.
- [174] C. L. Kane and E. J. Mele, “Z<sub>2</sub> Topological Order and the Quantum Spin Hall Effect,” *Physical Review Letters*, vol. 95, p. 146802, Sept. 2005.
- [175] M. König, S. Wiedmann, C. Brüne, A. Roth, H. Buhmann, L. W. Molenkamp, X.-L. Qi, and S.-C. Zhang, “Quantum spin hall insulator state in HgTe quantum wells,” *Science (New York, N.Y.)*, vol. 318, pp. 766–70, Nov. 2007.
- [176] Y. L. Chen, J. G. Analytis, J.-H. Chu, Z. K. Liu, S.-K. Mo, X. L. Qi, H. J. Zhang, D. H. Lu, X. Dai, Z. Fang, S. C. Zhang, I. R. Fisher, Z. Hussain, and Z.-X. Shen, “Experimental realization of a three-dimensional topological insulator, Bi<sub>2</sub>Te<sub>3</sub>,” *Science (New York, N.Y.)*, vol. 325, pp. 178–81, July 2009.
- [177] Y.-J. Lin, R. L. Compton, K. Jiménez-García, J. V. Porto, and I. B. Spielman, “Synthetic magnetic fields for ultracold neutral atoms.,” *Nature*, vol. 462, pp. 628–32, Dec. 2009.
- [178] Y.-J. Lin, K. Jiménez-García, and I. B. Spielman, “Spin-orbit-coupled Bose-Einstein condensates.,” *Nature*, vol. 471, pp. 83–6, Mar. 2011.
- [179] M. Hafezi, E. A. Demler, M. D. Lukin, and J. M. Taylor, “Robust optical delay lines with topological protection,” *Nature Physics*, vol. 7, pp. 907–912, Aug. 2011.
- [180] M. Hafezi, J. Fan, A. Migdall, and J. M. Taylor, “Observation of photonic edge states in a versatile Silicon platform,” pp. 1–16.
- [181] M. C. Rechtsman, J. M. Zeuner, Y. Plotnik, Y. Lumer, D. Podolsky, F. Dreisow, S. Nolte, M. Segev, and A. Szameit, “Photonic Floquet topological insulators.,” *Nature*, vol. 496, pp. 196–200, Apr. 2013.
- [182] A. B. Khanikaev, S. H. Mousavi, W.-K. Tse, M. Kargarian, A. H. MacDonald, and G. Shvets, “Photonic topological insulators.,” *Nature materials*, vol. 12, pp. 233–9, Mar. 2013.
- [183] M. Aidelsburger, M. Atala, S. Nascimbène, S. Trotzky, Y.-A. Chen, and I. Bloch, “Experimental Realization of Strong Effective Magnetic Fields in an Optical Lattice,” *Physical Review Letters*, vol. 107, p. 255301, Dec. 2011.
- [184] E. Kammann, T. C. H. Liew, H. Ohadi, P. Cilibrizzi, P. Tsotsis, Z. Hatzopoulos, P. G. Savvidis, A. V. Kavokin, and P. G. Lagoudakis, “Nonlinear Optical Spin Hall Effect and Long-Range Spin Transport in Polariton Lasers,” *Physical Review Letters*, vol. 109, p. 036404, July 2012.